The photodissociation of ClNO: a computational approach

Kiera Megan Jones

Submitted in accordance with the requirements for the

degree of Doctor of Philosophy

The University of Leeds

School of Chemistry

August 2014

The candidate confirms that the work submitted is her own, except where work which has formed part of jointly authored publications has been included. The contribution of the candidate and the other authors to this work has been explicitly indicated below. The candidate confirms that appropriate credit has been given within the thesis where reference has been made to the work of others.

Chapter 3 contains work which has been included in the publication:

'Photodissociation of ClNO in the 2 ^{1}A$'$ State: Computational and Experimental NO Product State Distributions'
Kiera M. Jones, Jadwiga A. Milkiewicz, Benjamin J. Whitaker, Alan G. Sage and Graham A. Worth
Chem. Phys. Chem., Vol. 14, p. 1479 - 1487

I was responsible for the computational work. Alan Sage and Jadwiga Milkiewicz performed the experiments, and Graham Worth and Ben Whitaker provided advice.

To my family

Acknowledgements

PhDs are hard. Doing a PhD alone at home several hundred miles away from a research group whilst in pain is even harder. Luckily, I have been surrounded by many lovely people who have helped me get through it.

Firstly, thanks to Ben Whitaker for supervision, for giving me the project and for being incredibly tolerant of the difficulties brought about by my health problems. Thanks to Mike Nix for many helpful discussions on my trips up north, without which my understanding of the science would be much poorer. Thanks also to Jadwiga Milkiewicz, Ingvar Kraatz and Alan Sage for being friendly faces in the office and working hard on the experimental data. Back in the mists of time when I was an experimentalist, Nick Form helped to get me started and Iain Wilkinson was a limitless source of useful advice for which I am very grateful.

This project would not even have got off the ground without the help of Graham Worth, who has always been willing to give me a hand and has been patient with me on the many occasions when I turned up in Birmingham confused and clasping a long list of questions. George McBane helped considerably with the classical trajectory calculations, adding an extra dimension to the project.

On the personal side, huge thanks are due to Richard Gilham for always looking after me when I was struggling and keeping a roof over my head for many years. Heather from Pain Concern was instrumental in convincing me that having painful wrists didn't mean I was completely useless. Many other great friends have helped to keep me sane over the past few years: thanks to KEF for messing around in the mountains with me, to Isca hash house harriers for all the fun times rampaging round the Devon countryside, and to the Exeter Collective Writers' group for saying nice things about my writing.

Thanks to my partner Alan Sage, who has been a great source of support, in both work and life. I have no doubt of his dedication to me: he even read this thesis. Finally, none of this would have been possible without my parents and family, who have always been there for me, whatever the situation. I am very lucky to have had their inspiration and encouragement throughout my life.

Abstract

The detailed photodissociation dynamics of ClNO on the $2\,^{1}A'$ and $1\,^{3}A''$ states have been investigated using computational methods. Chapter 3 concerns the photodissociation of the $2\,^{1}A'$ state. New, purely *ab initio* potential energy surfaces are described, calculated using the MRCI method. Transition dipole moments and non-adiabatic coupling matrix elements have been calculated across the extent of the surface. To investigate the dissociation dynamics, wavepacket propagations using the MCTDH method have been performed, yielding NO product state distributions which match extremely well with experimental results. In addition, classical trajectory calculations incorporating surface hopping have modelled transitions through a conical intersection in the asymptotic region of the surfaces, and have allowed anisotropy parameters to be obtained.

In chapter 4 the photodissociation dynamics of the $1\,^{3}A''$ state are described. A new potential energy surface and set of transition dipole moments have been calculated, and these have been used in quantum and classical dynamics calculations. In this case, whilst the quantum results agree well with experiment, the classical results do not.

In chapter 5, coherent control on the $1\,^{3}A''$ state is discussed. Using the MCTDH method, both transform limited and shaped ultrashort laser pulses at a series of energies have been used to influence the dynamics. The NO vibrational and rotational state distributions can be changed considerably using femtosecond pulse pairs separated by a variable delay.

Finally, chapter 6 examines the effect of spin-orbit coupling on the states of ClNO and surfaces taking this into account have been obtained at the CASSCF level. These surfaces are used to qualitatively explain experimental product state distributions. Further to this, dissociation on the spin-orbit equivalent of the $2\,^{1}A'$ state has been studied using a preliminary wavepacket propagation; the predicted spin-orbit product state distributions agree well with experiment.

Contents

Conclusions 241

Appendices 243

A SOCME sign-sorting algorithm 243

References 247

List of Figures

List of Tables

List of acronyms

AO	Atomic orbital
au	Atomic units
AVQZ	aug-ccpVQZ, augmented correlation consistent polarised quadruple zeta
AVTZ	aug-ccpVTZ, augmented correlation consistent polarised triple zeta
BO	Born-Oppenheimer
CAP	Complex absorbing function
CASSCF / CAS	Complete active space self-consistent field
CCSD	Coupled cluster singles and doubles
CGTO	Contracted Gaussian-type orbital
CI	Configuration interaction
CoIn	Conical intersection
CSF	Configuration state function
cw	continuous wave
DVR	Discrete variable representation
EOM-CC	Equations of motion coupled cluster
EOM-CCSD	Equations of motion coupled cluster singles and doubles
FBR	Finite basis representation
FC	Franck-Condon
fs	femtosecond
FWHM	Full-width half maximum
HF	Hartree Fock
KE	Kinetic energy
LIF	Laser induced fluorescence
MCSCF	Multi configuration self-consistent field
MCTDH	Multi configuration time dependent Hartree
MO	Molecular orbital

MR-ACPF	Multi-reference averaged coupled pair functional
MRCI	Multi-reference configuration interaction
NACME	Non-adiabatic coupling matrix element
NK88	3,3-diethyl-2,2-thiacyanine iodide
ns	nanosecond
PES	Potential energy surface
PGTO	Primitive Gaussian-type orbital
RAS	Restricted active space
REMPI	Resonance enhanced multiphoton ionisation
SD	Slater determinant
SOC	Spin-orbit coupling
SOCME	Spin-orbit coupling matrix element
SOM	Spin-orbit matrix
SPF	Single particle function
TDH	Time dependent Hartree
TDM	Transition dipole moment
TDSE	Time-dependent Schrödinger equation
TISE	Time-independent Schrödinger equation
TL	Transform-limited
TOF	Time-of-flight
TSH	Trajectory surface hopping
UV-vis	Ultraviolet - visible

Chapter 1

Introduction

1.1 Photodissociation dynamics

1.1.1 Overview

Photodissociation is the process by which a molecule fragments following the absorption of one or more photons of light. The fragmentation may occur in the ground electronic state, following excitation to a vibrational level above the dissociation threshold, or it may occur from a higher energy electronic state. For the photodissociation of ClNO, it is the latter case that is of interest, with a visible or UV photon triggering the fragmentation. The overall process is:

$$AB + h\nu \rightarrow (AB)^* \rightarrow A + B \tag{1.1}$$

Depending on the molecule in question, the products A and B can be formed in a variety of quantum states, be they electronic, vibrational or rotational, and the dissociation can occur via a range of mechanisms.

Many important atmospheric processes involve the photodissociation of small molecules [1, 2]. For example, NO_2 absorbs near-UV light and dissociates yielding NO and radical O:

$$NO_2 + h\nu \, (\lambda < 398\text{nm}) \rightarrow NO + O(^3P) \tag{1.2}$$

This O then goes on to react with O_2 and produce O_3 (ozone). O_3 is a crucial species in atmospheric chemistry, as it photolyses at $\lambda < 320$ nm to form excited O ^1D. This in turn reacts with water to produce the OH radical, which is the most important atmospheric oxidising agent.

For some species such as formaldehyde there are multiple photodissociation pathways; which is followed will depend on the precise state(s) accessed and how the system evolves once excited.

$$H_2CO + h\nu \, (\lambda < 370\text{nm}) \rightarrow HCO + H$$
$$H_2CO + h\nu \, (\lambda < 370\text{nm}) \rightarrow CO + H_2.$$

(1.3)
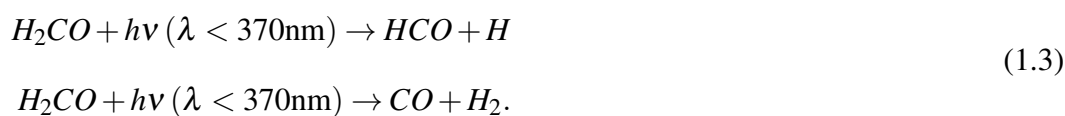
The latter process has received considerable recent interest as it can occur via a 'roaming' mechanism [3, 4]. In this, the reaction does not proceed via a typical transition state; instead one of the H atoms roams at a long C-H bond distance, leaving the HCO almost as a separate radical species, before returning to abstract the remaining H. The H_2 thus formed is highly vibrationally excited, whereas that produced from the more usual transition state mechanism is not. A detailed understanding of such reactions is therefore key to the accurate modelling of atmospheric photochemistry. Other important processes which depend intimately upon photodissociation range from photosynthesis in plants to the decomposition of molecules in interstellar chemistry [5, 6].

Photodissociation is also of great interest because it provides an excellent opportunity to study molecular dynamics in an extremely detailed fashion. If narrow bandwidth lasers are used, the excited complex can be prepared in a specific electronic and vibrational (and in small molecules, rotational) state. State-specific dynamics can therefore be elucidated, with the state accessed varied simply by varying the wavelength of the photon used. Alternatively, ultrafast, wide bandwidth lasers can be used to probe the photodissociation process. Although in this case the state specificity can be lost, additional information can be gained by following the fragmentation in time. The broad range of states excited can also be exploited in coherent control schemes, as discussed later. Photodissociation can also be viewed as a half-scattering reaction, and hence can be used to gain insights into more complicated processes.

Potential energy surfaces

The key to understanding the photodissociation process is the concept of the potential energy surface (PES). To understand what a PES is, firstly the Born-Oppenheimer (BO) approximation needs to be invoked [7]. This states that as the mass of the electrons is so small compared to those of the nuclei, their movement can be considered to be instantaneous as the nuclei are displaced. It follows that the Hamiltonian operator used in the Schrödinger equation can be split into separate terms for the electrons and nuclei, i.e.

$$\hat{H} = \hat{T}_n + \hat{T}_e + \hat{V}_{ne} + \hat{V}_{ee} + \hat{V}_{nn}. \tag{1.4}$$

Here, $\hat{T}_n$ and $\hat{T}_e$ are the kinetic energy operators for the nuclei and electrons respectively, and $\hat{V}_{ne}$, $\hat{V}_{ee}$ and $\hat{V}_{nn}$ are the potential energy operators for the nuclei-electron, electron-electron and nuclei-nuclei interactions. Keeping the nuclei fixed (i.e. setting $\hat{T}_n$ to zero) and using this Hamiltonian (now labelled $\hat{H}_e$ as it is electronic) to solve the time-independent Schrödinger equation (TISE) for the electrons will then give the energy at a particular geometry. If the energy is calculated at a range of geometries then these can be combined to produce a 'surface' showing how the energy of a particular electronic state of the system varies as the bond lengths and angles are varied; this is the adiabatic PES. Different electronic states will have different energies, leading to different PESs. Clearly, the topology of the PES determines the dynamics: the system will tend to follow the lowest energy path, and so any barriers or other features will force it in a particular direction. PESs for diatomics are conceptually simple, being just a one dimensional curve showing how the energy varies as the bond length between the two atoms changes. For triatomics the situation is more complicated as there are two bonds and an angle that can be varied; for larger molecules the PESs become rather harder to picture.

Direct vs indirect photodissociation

There are two basic categories describing photodissociation. The first is known as direct dissociation, and occurs extremely rapidly. The molecule is excited to a repulsive state and falls apart immediately, giving no time for any vibrations or rotations to occur in the

excited complex. The second form of photodissociation is known as indirect dissociation. In this case there is some kind of barrier preventing immediate fragmentation, and so the excited complex has an increased lifetime, allowing multiple oscillations of vibrational and rotational modes. The barrier could derive from the interaction of bound and repulsive electronic states, giving rise to electronic predissociation, or there could be a barrier on the PES of the excited electronic state, in which case the process is known as vibrational predissociation. For electronic predissociation the rate of fragmentation depends on the coupling between the two electronic states involved. For vibrational predissociation the rate instead depends on tunnelling or intra-molecular vibrational energy redistribution.

Investigating photodissociation processes

The first port of call when attempting to unravel the dynamics of a photodissociation process is to look at the absorption spectrum of the relevant molecule. Although this is a time-independent measurement averaged across all the possible absorbing states it can still furnish some useful information. For example, if a peak is broad and free of structure it implies that the corresponding excited state dissociates in a direct fashion. Alternatively, if distinct vibrational (or even rotational) structure can be seen in a peak the associated excited complex must exist for several vibrational periods, and therefore the dissociation must be indirect.

The absorption spectrum can be split up to give partial photodissociation cross-sections for specific states. These partial spectra can be measured experimentally using techniques such as photofragment yield spectroscopy [8], and are useful as they allow the dynamics for one specific state to be seen without interference from all the others. Any vibrational or rotational structure is hence likely to become clearer.

Studying the products of the photodissociation process can also yield useful data. The vibrational and rotational product state distributions, as well as the angular distribution of the photofragments, can provide a wealth of information about the dynamics in the exit channel. From this it may be possible to learn about the shape of the PES. Experimental techniques such as velocity map or ion imaging are ideal for obtaining these types of data [9].

An experimental advance that has revolutionised the study of photodissociation has been the development of ultrafast lasers [10]. Bond breaking normally occurs on a femtosecond (10^{-15} s, fs) timescale, and so by using lasers which produce pulses of light that are only a few fs in duration the process can be studied in 'real-time' [11, 12]. In a typical pump-probe experiment, the molecule of interest is excited to a higher electronic state by an initial ultrashort laser pulse, allowed to evolve for a period of time and then ionised by a second ultrashort pulse. By varying the time delay between the pump and probe pulses the dynamics of the system can be followed.

An example of how this can be achieved experimentally is given by the work of Ahmed Zewail, for which he was awarded the 1999 Nobel Prize for chemistry [13]. In a seminal experiment, he studied the photodissociation of ICN [14, 15] using femtosecond transition-state spectroscopy. The ICN was first excited to a repulsive state using a pulse at 306 nm, then a variable time delay later the resulting CN was detected by laser-induced fluorescence (LIF). From the results it was found that the dissociation process takes 205 ± 30 fs. Since these early experiments the field has flourished, with ever more complicated systems being studied, both in the gas and solution phases [16, 17].

Reflection principles

The reflection principle can help to explain absorption spectra and product state distributions for simple systems [18]. It applies primarily to direct photodissociation, which can be considered an essentially classical process. According to the principle, the absorption spectrum for a system is determined by the coordinate distribution of the wavepacket on the ground state. This wavepacket is then 'reflected' by the dissociative excited state, as illustrated in figure 1.1, with each position corresponding to a particular energy. For purely direct dissociation the gradient of the excited state is large, resulting in a broad absorption spectrum. For dissociation with more indirect character, where the gradient of the excited state is shallower, the absorption spectrum will display a narrower peak. Figure 1.2 illustrates the situation when there is more than one excited state, which leads to multiple peaks. Note how for direct dissociation all structure resulting from the presence of three states may be hidden under the broad curve of the spectrum.
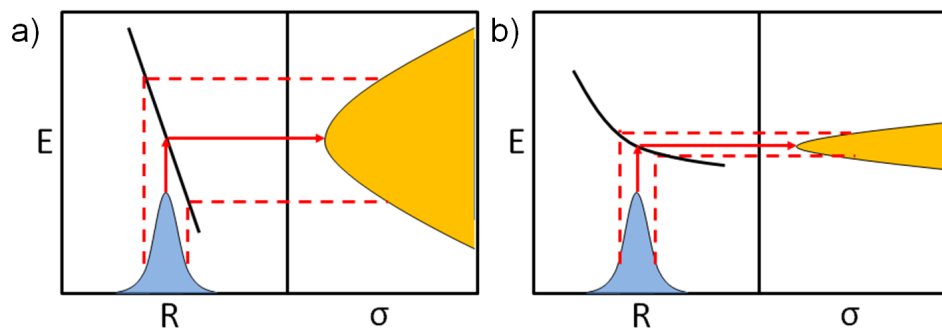
Figure 1.1: An illustration of the reflection principle for both purely direct dissociation (panel a)) and dissociation with some indirect character (panel b)).
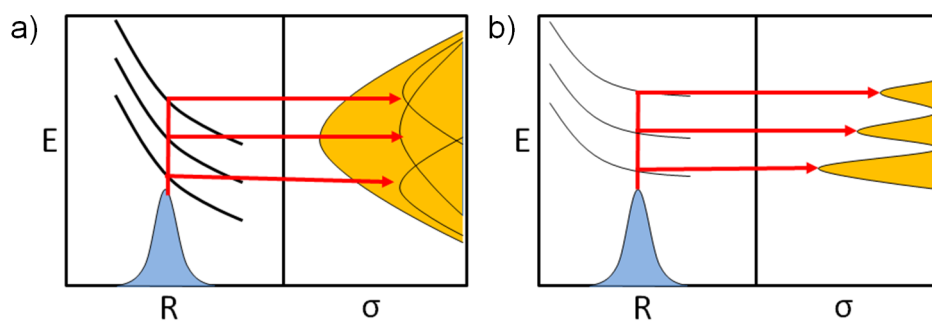
Figure 1.2: An illustration of the reflection principle when multiple excited states are present, for purely direct dissociation (panel a)) when the peaks are completely overlapping and for dissociation with some indirect character (panel b)) when separate peaks are clearly visible.

The reflection principle can in some cases be extended to explain rotational distributions. To do this, the effect of the excited state PES on the initial wavepacket needs to be considered. For example, a cut along the angular coordinate of the PES can give an idea of how much torque will be imparted upon each part of the wavepacket: areas in which the PES changes considerably in the angular coordinate will impart a large amount of torque, whereas areas where the PES is flatter will not. The wavepacket can then be reflected taking this into account, resulting in a rotational distribution which should match qualitatively with that observed experimentally. Similar arguments can be used to obtain vibrational distributions [19].

1.1.2 Adiabatic vs non-adiabatic dynamics

The BO approximation is often valid and considerably facilitates the computation of PESs and the dynamics occurring on them. However, if multiple, coupled electronic states are involved the approximation may break down and no longer accurately describe the physics of the system. For example, consider the reaction of a halogen molecule X_2 with an alkali metal atom M. This occurs via the 'harpoon' mechanism [20]: as the halogen molecule approaches the metal atom it draws away an electron to leave the ions M^+ and X_2^-. The system therefore transfers from a purely-covalent picture to a purely-ionic one. Close to the crossing point a small change in geometry results in a sudden change in the electronic configuration. The motion of the electrons and the nuclei are therefore strongly coupled in this region and the BO approximation is not valid. Instead, the system can be viewed as a pair of intersecting potential energy curves, one corresponding to the covalent species and the other to the ionic. There will be a critical distance at which these curves cross and the ionic species become more energetically favourable than the covalent. This situation is illustrated in figure 1.3.

The eigenvalues which arise from solving the TISE under the BO approximation are combined to give what are termed the adiabatic PESs. If there are couplings between different states these adiabatic surfaces will not necessarily appear as fully smooth functions. In this case it may be helpful to look instead at the diabatic surfaces: these are
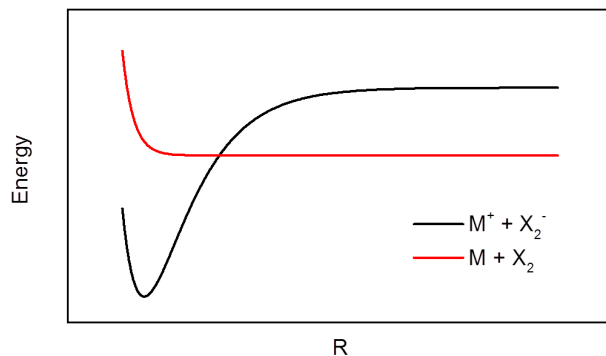
Figure 1.3: Sketched potential energy curves for the reaction between a metal atom M and a halogen molecule X_2. As the distance R between the two species decreases, the ionic species $M^+ + X_2^-$ become more energetically favourable than the covalent species $M + X_2$. The curves cross, meaning the system will behave nonadiabatically.
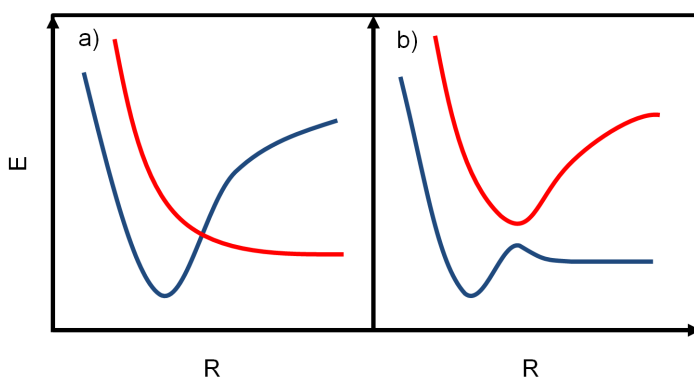
Figure 1.4: Sketched potential energy curves for two interacting electronic states. a) shows diabatic curves which cross; b) shows adiabatic curves which avoid each other.

the surfaces in which the electronic characters of the states are maintained, as opposed to simply ordering them by energy. Figure 1.4 gives a sketch of how the same states would appear in the adiabatic and diabatic representations.

Nonadiabatic couplings

When applying the BO approximation to the Schrödinger equation the nuclear part of the kinetic energy operator is set to zero. However, when nonadiabatic coupling occurs this is no longer the case, and instead the total wavefunction needs to be written in the Born

representation as follows [20, 21]:

$$\Psi(R,r) = \sum_i \psi_i(R)\phi_i(R,r), \tag{1.5}$$

where the i designates the current electronic state. Here, the $\phi_i(R,r)$ are the functions found from $\hat{H}_e$ (see equation 1.1.1) which act as a basis set for the expansion, and the $\psi_i(R)$ are nuclear functions, which act as coefficients. Inserting this into the time-dependent Schrödinger equation (TDSE), multiplying by $\phi_j(R,r)$ and integrating over the electronic coordinates gives

$$(\hat{T}_n + V_j)\psi_j - \sum_i \hat{\Lambda}_{ji}\psi_i = i\hbar \frac{\partial \psi_j}{\partial t} \tag{1.6}$$

where the V_j are the adiabatic (i.e. derived from $\hat{H}_e$) potentials and $\hat{\Lambda}_{ji}$ is the nonadiabatic coupling operator. This is equal to

$$\hat{\Lambda}_{ji} = \delta_{ji}\hat{T}_n - \langle\phi_j|\hat{T}_n|\phi_i\rangle. \tag{1.7}$$

From this it can be seen that in the adiabatic picture the nonadiabatic couplings will be present in the off-diagonal terms of the kinetic energy matrix. The potential energy matrix however remains diagonal.

Taking the kinetic energy operator to be

$$\hat{T}_n = -\frac{1}{2M}\nabla^2 \tag{1.8}$$

allows $\hat{\Lambda}_{ji}$ to alternatively be expressed in terms of derivative couplings as

$$\hat{\Lambda}_{ji} = \frac{\hbar^2}{2M}(2\boldsymbol{F}_{ji}\cdot\nabla + G_{ji}). \tag{1.9}$$

The first-derivative coupling between the states is

$$\boldsymbol{F}_{ji} = \langle\phi_j|\nabla|\phi_i\rangle = \frac{\langle\phi_j|\nabla\hat{H}_e|\phi_i\rangle}{V_i - V_j} \tag{1.10}$$

i.e. when the adiabatic states become close in energy the derivative coupling will increase, and if they become degenerate it will become infinite. The scalar coupling term is

$$G_{ji} = \langle \phi_j | \nabla^2 | \phi_i \rangle \tag{1.11}$$

but this is normally negligible and so can usually be ignored.

Diabatic states

Diabatic states can be expressed as linear combinations of adiabatic states [20], i.e.

$$\phi_i^d = \sum_j d_{ji} \phi_j. \tag{1.12}$$

There is not one unique set of diabatic states; rather they can be chosen in order to eliminate the nonadiabatic coupling vectors, i.e. to ensure that

$$\boldsymbol{F}_{ji}^d = \langle \phi_j^d | \nabla | \phi_i^d \rangle = 0. \tag{1.13}$$

However, it is impossible for this to be achieved for all i and j without including an infinite number of electronic states. Instead, so-called 'quasidiabatic' states are used, whereby the derivative couplings are made as small as possible. Unitary transformations of the adiabatic states can also give rise to what are termed 'mixed' states, in which the states are neither fully adiabatic or diabatic.

In the diabatic picture the nonadiabatic couplings appear simpler. The TDSE gives

$$(\hat{T}_n + \boldsymbol{V}^d)\psi = i\hbar \frac{\partial \psi}{\partial t}. \tag{1.14}$$

Here, $\boldsymbol{V}^d$ is the diabatic potential energy matrix. Unlike in the adiabatic representation, this is not diagonal: the off-diagonal elements give the nonadiabatic couplings. These tend to vary more smoothly than the adiabatic couplings, and so are often easier to handle computationally. When states become degenerate the diabatic couplings go to zero.
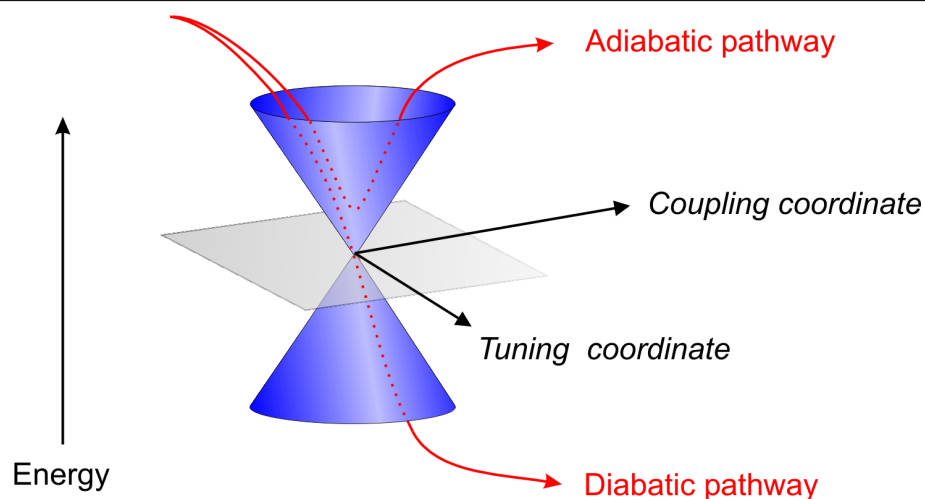
Figure 1.5: An illustration of a conical intersection in its branching space. The tuning and coupling coordinates are shown, and potential adiabatic and diabatic pathways are indicated. Figure courtesy of Alan Sage.

Conical intersections

Conical intersections (CoIns) are a particular type of nonadiabatic interaction between two or more electronic states [21, 22]. CoIns occur when the states are degenerate in an $(N-2)$-dimensional subspace known as the 'seam space', where N is the number of internal degrees of freedom of the molecule ($N = 3n - 5$ for linear molecules containing n atoms, $N = 3n - 6$ for non-linear). The degeneracy is lifted in the remaining two degrees of freedom, which are termed the 'branching space' or 'g-h plane'. The name 'conical' refers to the shape of the adiabatic states in the region of the intersection when viewed in the branching space; figure 1.5 illustrates this. Where CoIns are present radiationless transitions between surfaces can occur very rapidly. Originally thought to be rare, CoIns have been found to be a fairly ubiquitous feature in polyatomic molecules.

In the diabatic picture, at a 2-state CoIn V_{11}^d is equal to V_{22}^d as the states are at that point degenerate. In addition, the potential couplings must be zero, i.e. $V_{12}^d = V_{21}^d = 0$. The two coordinates in the branching space are known as the 'tuning' and 'coupling' coordinates. The first is the direction along which these nuclei have to move in order to bring the adiabatic states close in energy, and is totally symmetric to maintain $V_{12}^d = 0$. The second is the direction, orthogonal to the first, in which degeneracy is lifted, and is non-totally symmetric. Note that these coordinates may well not correspond to the normal modes of

the molecule, and so may be difficult to identify.

CoIns can occur between states of different symmetry within the same point group as in this case V_{12}^d must be zero. Symmetry-induced CoIns occur when the electronic states transform as different irreducible representations of the point group; in this case moving along the tuning and coupling coordinates can make $V_{12}^d = 0$. CoIns can also in some cases occur between states of the same symmetry (except for in diatomics where the non-crossing rule applies), and these are known as 'accidental' [20].

1.1.3 Spin-orbit coupling

Spin-orbit coupling (SOC) is the most common mechanism by which adiabatic PESs for electronic states of different spin can be coupled [20]. Its effects are most prominent in heavy atoms, but are also relevant to an extent for lighter atoms such as Cl and molecules such as NO, and so in a full treatment of ClNO photodissociation dynamics spin-orbit effects need to be included.

All angular momentum vectors have with them an associated magnetic moment, which lies along the same line but points in the opposite direction. In quantum mechanical systems there are electron spin (quantum number S), electron orbital (L for atoms or Λ for molecules) and nuclear orbital angular momenta; these can interact both with each other and with any external field. SOC specifically results from the interaction between the magnetic moment of an electron, which arises from its spin, and the magnetic field produced by the electronic orbital motion. The total angular momentum vector J is obtained from the combination of S and L or Λ. This can have a number of orientations depending on the relative orientations of S and L or Λ.

As an example, the chlorine atom in its ground electronic state has one unpaired electron in a 2p orbital. It therefore has the values $L = 1$ and $S = \frac{1}{2}$. Combining these gives $J = \frac{1}{2}$ or $\frac{3}{2}$; in the first case the individual angular momenta (and hence magnetic moments) are aligned antiparallel and in the second they are parallel. The term symbols for the resulting states are $^2P_{1/2}$ and $^2P_{3/2}$.

In this study of ClNO, a transition from a singlet to a triplet state will be considered.

Such transitions can occur due to SOC: once the spin and orbital angular momenta couple, S is no longer a good quantum number and states cannot be fully described as singlet and triplets, and so, if symmetry allows, transitions can take place between them. These transitions can be considered as follows. In the presence of a magnetic field, a triplet state will split into 3 sub-levels, one for each value of M_s, which gives the direction of the electron spin angular momentum vector relative to the field. These sub-levels can be denoted as T_+ for $M_s = 1$, T_0 for $M_s = 0$ and T_- for $M_s = -1$. The magnetic moments of the different spin states precess in cones around the magnetic field axis. The interaction with the orbital angular momentum introduces a torque which acts on the individual spins and can cause them to change direction; for a triplet to singlet transition the process is analogous to longitudinal (T_+ or T_-) or transverse (T_0) relaxation in NMR, for a singlet to triplet transition the reverse process occurs.

SO coupled surfaces and the SOC matrix elements between these can be found using the Breit-Pauli spin-orbit operator. This can be derived from the relativistic Dirac Hamiltonian, and then added as a perturbation onto the Hamiltonian $\hat{H}_e$ used earlier [23]. The operator has the form:

$$\hat{H}_{SO} = \frac{\alpha^2}{2} \left(\sum_{ia} \frac{Z_a}{r_{ia}^3} (\boldsymbol{r}_{ia} \times \boldsymbol{p}_i) \cdot \hat{s}_i - \sum_{i \neq j} \frac{1}{r_{ij}^3} (\boldsymbol{r}_{ij} \times \boldsymbol{p}_i) \cdot (\hat{s}_i + 2\hat{s}_j) \right) \tag{1.15}$$

where α is the fine-structure constant, the i, j are electrons and the a denote nuclei, Z_a is the nuclear charge, r_{ia} is the distance between electron i and nucleus a, r_{ij} is the distance between electron i and electron j, and the $\boldsymbol{r}$, $\boldsymbol{p}$ and $\hat{s}$ correspond to position, momentum and spin respectively. The Z_a dependence shows why the magnitude of SOC is greater for heavier atoms. The first part of operator contains one electron terms whereas the second contains two electron terms. The magnitude of the one electron part increases rapidly as Z_a increases, whereas the two electron part increases only slowly, and so approximations can be made whereby the two electron part is neglected, with its contribution incorporated into an effective charge Z_{eff} which replaces Z_a.

1.2   Ultrashort laser pulses

Key to studying ultrafast dynamics and coherent control are ultrashort laser pulses, which normally have durations on the order of femtoseconds. As mentioned earlier in section 1.1.1, such pulses allow chemical reactions to be studied in real time, so that bond breaking and formation can be 'watched' as the processes occur. Coherent control takes this one step further: instead of simply observing the process, the light is used to make it happen in the first place. More detail is given in the following section, 1.3.

Due to the time-energy uncertainty relation, the shorter a pulse length in time, the broader its spectrum, i.e. the greater its bandwidth. Many frequencies are therefore contained in one ultrashort pulse, a property that is of great use for control experiments. The relative position in time of each of these frequencies may vary, for example lower frequencies may arrive at the beginning of the pulse, with higher frequencies arriving at the end (a situation known as positive chirp). This variation arises from the phase difference between the different frequencies. Therefore, to describe a pulse fully the amplitude and phase of each component, be it temporal or frequency, need to be specified.

In order to understand these pulses their mathematical description needs to be considered in more detail [24, 25]. Femtosecond light pulses can be described in a similar way to ordinary continuous wave (cw) laser light, but with one important difference. Ultrashort pulses contain only a few complete optical cycles; for example a 20 fs Gaussian pulse centred at 800 nm contains $\sim$15 cycles. Whereas the electric field of cw light can be described as a sine wave, an ultrashort pulse needs to be described as a sine wave multiplied by a pulse-envelope function. In the time domain this gives

$$E(t) = A(t)\cos(\omega_0 t - \phi(t)) \tag{1.16}$$

where $A(t)$ is the temporal amplitude, ω_0 is the central, or carrier, frequency and $\phi(t)$ is the temporal phase. This can alternatively, via Euler's formula, be written as

$$E(t) = \frac{1}{2}(A(t)\exp\{-i(\omega_0 t - \phi(t))\} + c.c) = \frac{1}{2}(E^+(t) + E^-(t)). \tag{1.17}$$
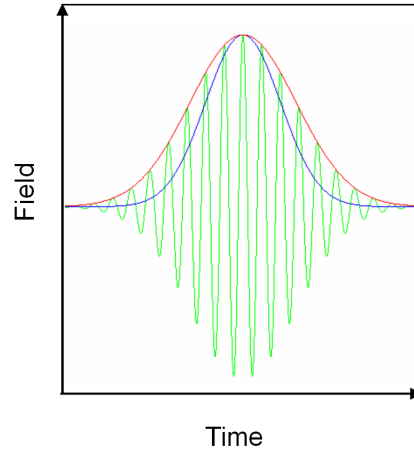
Figure 1.6: An ultrashort Gaussian pulse. The green line shows the real electric field, the red line shows the electric field amplitude $|E(t)|$ and the blue line shows the electric field intensity, $|E(t)|^2$.

$E^+(t)$ can be considered as the component of the field leading to absorption, whereas $E^-(t)$ can be considered to lead to emission. $A(t)$ will have different forms depending on the type of pulse used. A Gaussian is often a good choice, and leads to simpler calculations than alternatives such as sech^2 or Lorentzian functions. In this case, the temporal amplitude is

$$A(t) = \exp\left(-2\ln 2 \left(\frac{t}{\tau}\right)^2\right) \tag{1.18}$$

where τ is the full-width half maximum (FWHM) of the pulse. The intensity of a pulse can be obtained from the square of the electric field as

$$I(t) = |E(t)|^2. \tag{1.19}$$

Note that this gives the intensity in atomic units rather than its absolute magnitude. For a Gaussian this gives a temporal intensity of

$$I(t) = \exp\left(-4\ln 2 \left(\frac{t}{\tau}\right)^2\right). \tag{1.20}$$

In this case the intensity is $\sqrt{2}$ narrower than the amplitude. Figure 1.6 illustrates the difference.

The temporal phase can be found using the following relation:

$$\phi(t) = \arctan\left(\frac{Im(E(t))}{Re(E(t))}\right).$$

(1.21)

If this yields a constant phase then the pulse is said to be 'transform limited', i.e. it has the minimum possible pulse length for its bandwidth and all frequencies have the same arrival time. For a Gaussian pulse the transform limit is achieved if $\tau \Delta \omega = 4 \ln 2$.

If the phase varies smoothly, with no sudden jumps, it is often easier to consider it in terms of a Taylor expansion around time zero, t_0.

$$\phi(t) = \phi_0 + \phi_1(t - t_0) + \frac{\phi_2}{2!}(t - t_0)^2 + \frac{\phi_3}{3!}(t - t_0)^3 + \dots$$

(1.22)

where

$$\phi_n = \frac{\partial^n \phi(t)}{\partial t^n}\Big|_{t=0}$$

(1.23)

Each component of the expansion has a different effect. The absolute phase, ϕ_0, controls the offset between the carrier wave and the pulse envelope. As illustrated in figure 1.7, this is unlikely to be of importance unless the pulse is only a handful of cycles long - not normally the case in control experiments. The first order phase, ϕ_1, corresponds to a shift of the carrier frequency ω_0.

More interesting is the second order phase, ϕ_2, which controls the amount of linear chirp in the pulse, i.e. the extent to which the instantaneous frequency varies linearly with time, as illustrated in figure 1.8. The instantaneous frequency is defined as

$$\omega_{inst}(t) = \omega_0 - \frac{d\phi}{dt}.$$

(1.24)

If the frequency increases with time the pulse has positive chirp, if the frequency decreases with time the pulse has negative chirp. Most ultrashort pulses have a degree of positive chirp as propagation through materials (for which the refractive index is a decreasing function of λ) will impart this, lengthening the pulse. Figure 1.9 shows the electric fields
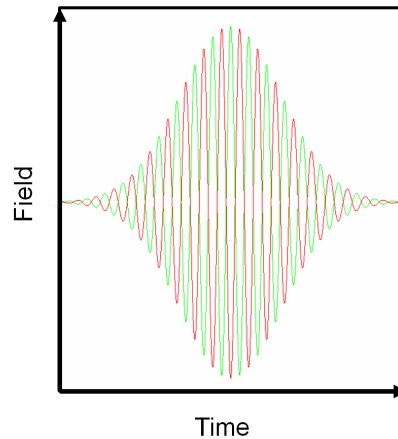
Figure 1.7: The variation of absolute phase. The green line shows the full real electric field of a pulse with zero ϕ_0 and the red line shows the full electric field of a pulse with π ϕ_0.
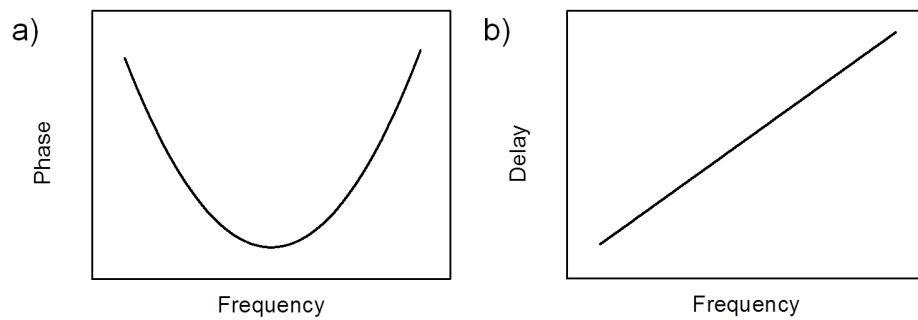
Figure 1.8: The variation of phase (panel a)) and delay (panel b)) with frequency for a linearly chirped pulse.

of pulses with considerable positive and negative linear chirp.

Third order phase, ϕ_3, is termed quadratic chirp as it corresponds to a quadratic variation in frequency with time, as shown in figure 1.10. The central frequency of the pulse will therefore arrive first (or last, depending on the sign), with the other frequencies tailing behind (or in front). Figure 1.11 gives a Wigner plot (frequency versus time and intensity) of a pulse with quadratic chirp. The intensity of the pulse also displays beats.

Variations in higher order phases are more difficult to describe as the distortions introduced can give rise to extremely complex pulse shapes. In situations where coherent control is achieved by a pulse with large amounts of higher order chirp, the mechanism of control will therefore be much more difficult to extract.
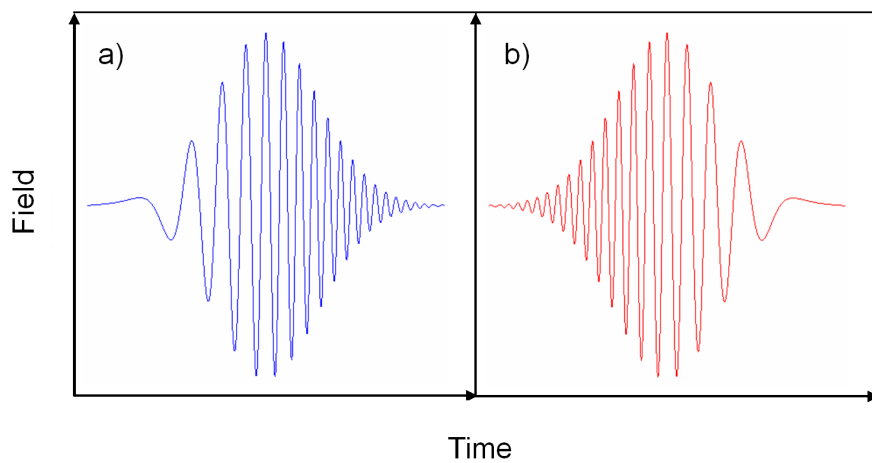
Figure 1.9: The electric fields of ultrashort pulses with positive (blue pulse, panel a)) and negative (red pulse, panel b)) linear chirp.
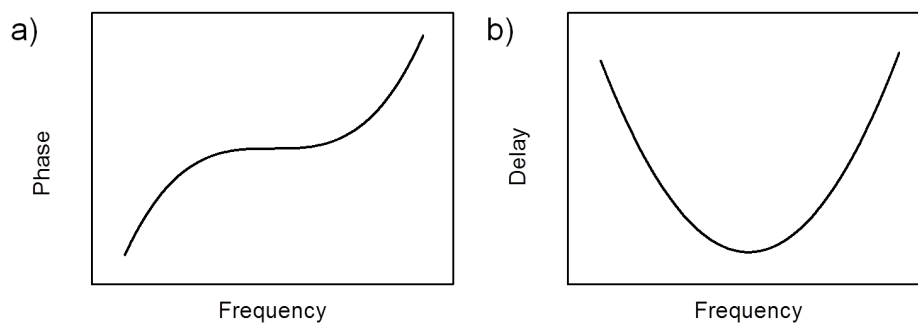
Figure 1.10: The variation of phase (panel a)) and delay (panel b)) with frequency for a quadratically chirped pulse.
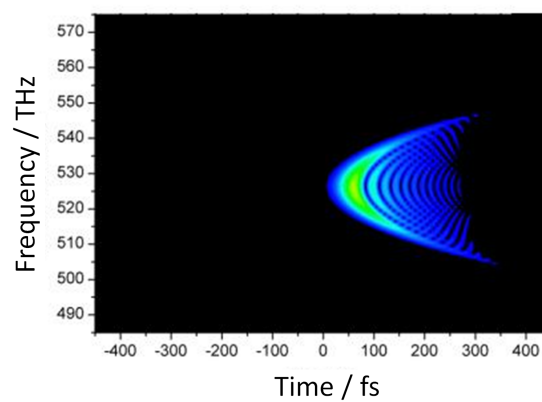
Figure 1.11: A Wigner representation of a pulse with significant quadratic chirp. Figure courtesy of Nicholas Form.

The electric field can be defined in either the time domain or the frequency domain, and changing from one to the other can be achieved by Fourier transformation. For example, taking $E^+(t)$ and applying a Fourier transformation gives $\tilde{E}^+(t)$, the frequency domain equivalent:

$$\tilde{E}^+(\omega) = \frac{1}{2\pi} \int_{-\infty}^{+\infty} E^+(t) \exp(-i\omega t)\, dt. \tag{1.25}$$

Once again, this part of the electric field can be written as the product of an envelope function, this time the spectral amplitude $\tilde{A}(\omega)$, and a phase term, this time involving the spectral phase $\varphi(\omega)$:

$$\tilde{E}^+(\omega) = \tilde{A}(\omega) \exp(i\varphi(\omega)). \tag{1.26}$$

An equivalent transformation can be done for $\tilde{E}^-(t)$. In the frequency domain, squaring the electric field yields not the intensity but the spectrum:

$$S(\omega) = |\tilde{E}(\omega)|^2. \tag{1.27}$$

For a Gaussian pulse, the frequency amplitude is

$$\tilde{A}(\omega) = \sqrt{\frac{\pi}{2\ln 2}}\, \tau \exp\left(-\frac{\tau^2(\omega - \omega_0)^2}{8\ln 2}\right) \tag{1.28}$$

and the frequency intensity is

$$S(\omega) = \frac{\pi}{2\ln 2}\, \tau \exp\left(-\frac{\tau^2(\omega - \omega_0)^2}{4\ln 2}\right). \tag{1.29}$$

For practical reasons, to shape the phase of the pulse in experiments the electric field must be manipulated in the frequency domain. The spectral phase can, like the temporal phase, be expanded as a Taylor series, but this time the expansion is around the carrier frequency:

$$\varphi(\omega) = \varphi_0 + \varphi_1(\omega - \omega_0) + \frac{\varphi_2}{2!}(\omega - \omega_0)^2 + \frac{\varphi_3}{3!}(\omega - \omega_0)^3 + \dots \tag{1.30}$$

The zeroth-order spectral phase, φ_0, has the same effect as the zeroth-order temporal phase. The first order phase, φ_1 can also be referred to as the group delay as it corresponds to the pulse arrival time. Generally, the shape of the pulse is more interesting than when it arrives, and so φ_1 is again of little importance in most cases. φ_2, the quadratic variation of $\varphi(\omega)$, is termed the group delay dispersion. Higher order terms give the third, fourth and so on orders of dispersion.

1.3   Coherent control

1.3.1   Overview

The goal of much of chemistry is to synthesize new molecules, to manipulate atoms such that they bond together in a desired way. Organic chemists have made considerable inroads towards achieving this with new reaction schemes and conditions; however they are limited by the thermodynamics and kinetics of their bulk systems. Some reaction pathways are simply not accessible no matter how much a sample is heated, pressurised or concentrated. In a few cases catalysts can be used, but finding one can be difficult, and a catalyst that works for one reaction will not necessarily be applicable to another. What is required is a universal catalyst that can directly manipulate the propagation of reagents along a PES and hence circumvent the thermodynamic and kinetic limitations. This was the original aim of coherent control, to steer reactions to a desired conclusion using light as the catalyst or reagent.

The idea of using light to directly control chemical reactions has a long history. Mode-selective chemistry, whereby energy is selectively partitioned into one mode of a molecule thus promoting reaction in that area, was initially thought to be a viable method of control. Indeed, there was some success with small molecules, notably the control of HOD dissociation by putting quanta of vibrational energy into either the H-O or O-D stretches [26]. However, upon moving to larger molecules the problem of intramolecular vibrational redistribution is encountered: the energy simply does not stay in the required mode long enough. In fact, mode-selective chemistry is only viable for molecules in which the react-
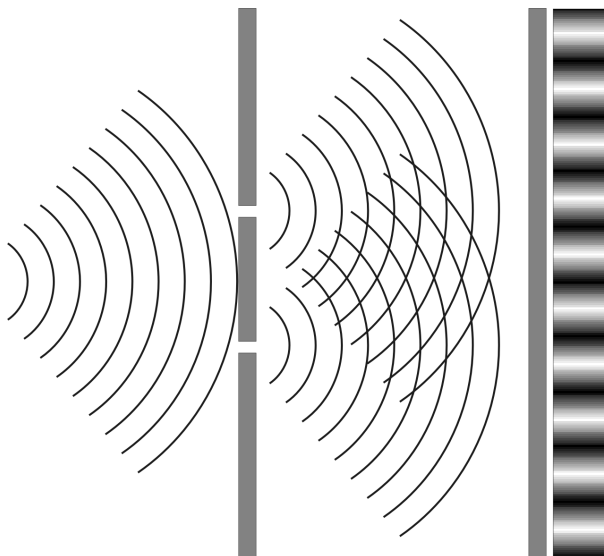
Figure 1.12: An illustration of Young's double slit experiment. A light source passes through 2 slits and the resulting waves interfere with each other to produce an interference pattern on the screen.

ing mode is only very weakly coupled to all the others, meaning energy will stay localised for long enough for a reaction to occur. This is only true for a handful of species, and hence this approach has very limited applicability.

Coherent control seeks to overcome these problems and to allow light to be used in all cases. The basic idea is that of wavepacket interference, where a wavepacket is a coherent superposition of states. If a system is coherently excited from an initial state to a final state via more than one pathway an interference pattern can be created between different components of the wavepacket, allowing it to be steered towards a desired outcome. Perhaps the simplest way in which to consider coherent control is by analogy with Young's famous double slit experiment in which a single particle (be it a photon, an electron [27], or even a C_{60} molecule [28]) passing through two slits results in an interference pattern. This experiment is illustrated in figure 1.12.

The interference pattern will change if more slits, i.e. more possible pathways for the particles to follow, are added. The pattern will also change if the phase of one or more of these pathways is changed, for example by putting a glass slide over one of the slits. By doing this the interference pattern can be manipulated such that most of the intensity lies in one particular fringe.
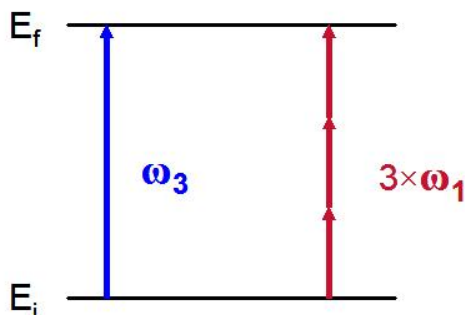
Figure 1.13: An illustration of Brumer-Shapiro control theory. To get from the initial state E_i to the final state E_f either one photon of ω_3 or three photons of ω_1 can be absorbed.

Now consider performing the experiment within a molecule. There is an initial state E_i and a final state E_f, from which several product channels are open. There is more than one pathway between these two states, and these are indistinguishable from each other. These pathways are equivalent to the slits in Young's experiment, and so by varying their relative phases they can be made to interfere, hence controlling which product channel the molecule ends up in. Two ways of performing this control were postulated theoretically before any experiments were attempted: these will now be considered.

1.3.2 Brumer-Shapiro control theory

Brumer-Shapiro control [29, 30], developed in 1986, is the theory most clearly analogous to the double slit experiment. As illustrated in figure 1.13, there are two possible pathways between the initial and final states of a system: the absorption of one photon of frequency ω_3, or the absorption of three photons of frequency ω_1. These photons are provided by two cw lasers as this allows the narrow bandwidth necessary to be obtained. At E_f more than one product channel is available; for example, a molecule could ionise or dissociate. By varying the relative phase of the two lasers the interference between the two pathways and hence the branching ratio of ionisation to dissociation can be manipulated.

Although this idea seems relatively simple, it took until 1995 before it was realised experimentally. The group of Robert Gordon used cw lasers to control the ratio of photoionisation versus photodissociation initially in the HI molecule [31], and later in DI as

well [32, 33]. The HI or DI was held in a chamber containing a variable pressure of H_2 gas and was excited using the fundamental and third harmonic of an excimer-pumped dye laser. The refractive index of the H_2 gas was very different for the two wavelengths used, and hence by varying the pressure their relative phases could be changed. The results from this experiment clearly showed a phase-lag between the two product channels, with the yield of I^+ increasing as that of DI^+ decreased, and *vice-versa*. However, whereas calculations had suggested a 100% depth of modulation would be seen, in the experiment only about 20% was obtained.

1.3.3   Tannor-Rice control theory

Whereas Brumer-Shapiro control theory considers control from a frequency perspective, Tannor-Rice-Kosloff control theory looks at it in the time-domain [34, 35]. Figure 1.14 illustrates the scheme. First, a wavepacket is excited from an initial PES to a higher energy PES using an ultrashort laser pulse. The wavepacket then evolves along this PES until a second ultrashort pulse sends it back down to the initial PES. By changing the delay between the 'pump' and 'dump' pulses, the part of the initial PES that the wavepacket falls down to can be controlled. Different areas of the PES may correspond to different products. It should be noted that in practice the 'dump' pulse does not normally bring the wavepacket down to the initial PES; rather it excites it to a still higher energy PES. The effect is the same regardless.
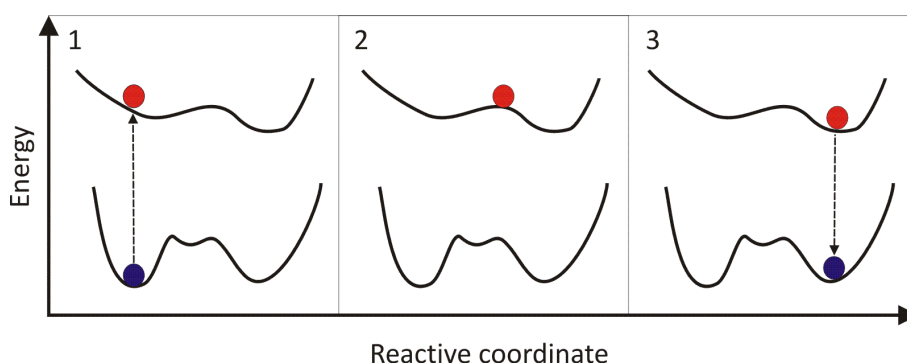
Figure 1.14: The Tannor-Rice-Kosloff control scheme. 1. A wavepacket is pumped by an ultrafast pulse onto an excited PES. 2. The wavepacket evolves on the excited PES. 3. A second ultrafast pulse 'dumps' the wavepacket back down to the lower PES, but in a different location to where it started from.

The first experimental achievement of pump-dump control was by Baumert *et al.* using the dissociation and ionisation of Na_2 [36, 37]. They found that if the probe laser came when the wavepacket excited by the pump pulse was at its inner turning point Na_2^+ was produced, and if the wavepacket was at its outer turning point Na^+ was produced.

1.3.4 Control experiments

Closed loop control

The publication of a key article by Judson and Rabitz in 1992 [38] led to much greater success in experimental control. Their idea was to use a learning algorithm, such as a genetic algorithm, in combination with a pulse shaper. Briefly, a transition or reaction of the molecule of interest is chosen, and an experimental way of measuring this is found. Several guess pulses are generated, and then are used on the molecule in question to attempt to maximise the desired process. The signals from the experimental probe, which could be time-resolved photoelectron spectroscopy, fluorescence, or some other technique, are then used to determine the fitness of each pulse. The algorithm uses these results to form a new set of pulses, which will hopefully have higher fitness than the previous generation. This process continues until the algorithm converges.

The first experimental demonstration of this closed-loop coherent control was achieved a few years later by Gerber *et al.* [39]. They managed to control the branching ratio between two possible bond cleavages in the organometallic compound $CpFe(CO)_2Cl$, where $Cp = C_5H_5$. The same group built upon this first success, controlling various processes in an array of molecules, as reviewed in an article by Gerber and Brixner [40]. A learning algorithm has even been used to control energy transfer in a light harvesting bacterium in the liquid phase [41].

A closed-loop system can therefore yield very impressive results, however there are drawbacks. Firstly, it is crucial that the algorithm has been parameterised carefully. For example, it is of no use trying to increase the ratio of one product with respect other if its absolute yield is not also maintained at a sensible level. Secondly, there is no way of knowing if the pulse returned by the algorithm is the global optimum pulse. To find

that with certainty, a grid search has to be performed, however given the potential size of the search space this is unlikely to be feasible. Most importantly, the optimum pulses produced by these algorithms are often extremely complex, making it very difficult to work out what the pulse is actually doing. In other words, the control occurs, but the mechanism by which it does so is still a mystery.

Example studies

Many studies, both experimental and theoretical, have been undertaken into coherent control. Review articles covering some of these are given in references [42–44]. In order to give an idea of the types of study that are possible, two very different examples are considered here in more detail.

One coherent control investigation was performed by Silberberg and co-workers [45]. Their aim was to control a two-photon transition in atomic caesium by simple changes in the spectral phase of their ultrashort pulse. As opposed to running the experiment and then trying to interpret the results, they performed theoretical calculations first, and then carried out the experiments.

The calculations had predicted that the position of a π-step in the spectral phase (making in effect a pulse pair) would have a large effect upon the two-photon transition probability, and the experiments confirmed this. The shortest possible pulse gave a high probability simply because it was the most intense pulse, but moving slightly away from this resulted in complete suppression of the transition. Moving to even longer pulses however resulted in probabilities as high as those for the shortest pulse. This can be explained by considering that in a two-photon transition using ultrashort pulses there are actually a whole range of intermediate (virtual) levels that the system can pass via to facilitate the transition. If the pulse had a narrow bandwidth with a central frequency of ω_0, then the only pathway available would be ω_0 plus ω_0. However, as ultrashort pulses have a wider bandwidth, pathways of $\omega_0 + \Delta\omega$ plus $\omega_0 - \Delta\omega$ are also possible. If the phases of these two different frequency components are opposite then the phase terms will cancel each other out and the system will behave in the same way as a transform-limited pulse, despite being spread out further in time. It is possible to manipulate the phases in other ways so

that there is spectral interference, cancelling out some frequencies and hence significantly reducing the probability of the two photon absorption.

To test these predictions, the 2-photon $6S_{1/2} \leftarrow 8S_{1/2}$ transition in caesium was investigated. A Ti:Sapphire laser was used to produce 31 fs long pulses centred at 822 nm, and π-steps were then introduced at variable wavelengths in the spectral phases of these using a spatial light modulator. No amplitude shaping was undertaken. The resulting light was focused down into a cell containing the gaseous caesium with a photomultiplier tube attached to collect fluorescence at 460 nm. The results from the experiment matched the theoretical results extremely well.

In a completely different approach, Gerber *et al.* studied the *cis-trans* isomerisation of a large molecule, 3,3-diethyl-2,2-thiacyanine iodide (NK88), in methanol solution [46]. Control in the liquid phase presents more difficulties than that in the gas phase as dephasing occurs rapidly, but as most synthetic chemistry takes place in solution it is an important area for study. The *trans* form of NK88 is stable at room temperature, whereas the *cis* is not. In the photoisomerisation process used, a pump pulse centred at 400 nm excites the molecule from its ground state to the first excited state, S_1, which has a twisted configuration. This then relaxes down to one of the two isomers via a conical intersection. The aim of the experiment was therefore to use a shaped 400 nm pulse to control the dynamics on S_1 in order to preferentially form the *cis* isomer.

An 800 nm pump pulse with a duration of 80 fs was shaped using a spatial light modulator and then frequency doubled. This was then focused down into a flow cell containing the NK88 in methanol. For the probe pulse, a portion of the 800 nm light was focused into a sapphire plate to generate a continuum which could then be used to measure the absorption spectrum of the sample. The light was then passed to two monochromators, allowing two wavelengths to be monitored at the same time. One of these was representative of the number of molecules excited, the other was proportional to the number of molecules undergoing *trans-cis* isomerisation. The ratio of these could therefore be used as the fitness function in an evolutionary algorithm to try to optimise the amount of *cis*-isomer formed.

The algorithm found pulses which minimized and maximized the amount of pho-

toisomerisation occurring. The optimum pulses were very different: for maximization, the pulse was hardly modified, whereas for the minimization it consisted of a train of pulses with reduced energy. It was postulated that this was due to higher excited states being involved: with the more intense, little-modified pulse, these states would be more accessible. However, no concrete explanation was possible without considerably more theoretical work being undertaken.

Some theoretical work was performed by Brumer and Hoki [47], who disputed the degree of coherent control achieved. By using a simple model consisting of one degree of freedom plus decoherence to describe the results, the optimum pulse for the formation of the *cis* isomer was found merely to ensure that none of the *trans* species was initially excited due to its low intensity. Conversely, the optimum pulse for the formation of the *trans* isomer was shown to lead to more efficient excitation. This case illustrates the major problem of closed-loop methods.

1.4 ClNO

1.4.1 Overview

The photodissociation of nitrosyl chloride, ClNO, has been studied as a prototypical example of bond rupture since the 1930s [48]. The molecule's small size, ease of synthesis and high reactivity has made it an ideal candidate for both experimental and theoretical investigations. Although only properly identified by Edmund Davy in the 1830s, it has been used by chemists for centuries as it is a major component of aqua regia [49]. This mixture of hydrochloric and nitric acids readily affords ClNO by the following solution-phase reaction:

$$3HCl_{(aq)} + HNO_{3(aq)} \rightarrow Cl_{2(aq)} + 2H_2O_{(aq)} + ClNO_{(aq)} \tag{1.31}$$

Alternatively, the highly corrosive gas can be synthesized by the direct interaction of chlorine and nitric oxide:

$$Cl_{2(g)} + 2NO_{(g)} \rightleftharpoons 2ClNO_{(g)}. \tag{1.32}$$

ClNO has an important role in the chemistry of the troposphere, where it acts as a precursor for radical Cl which goes on to initiate photochemical oxidations. It also hydrolyses to HONO, which in turn produces radical OH, the major atmospheric oxidising agent. ClNO is therefore implicated in the production of tropospheric ozone and HNO_3, as well as other pollutants, and it has been proposed that the species is responsible for around 10% of organic oxidations in coastal areas [50]. Short-lived, its lifetime in the atmosphere has been estimated at between 5 and 30 minutes [51]. Especially prevalent in urbanised sections of the coast, ClNO arises from the interaction of NO_2 gas and marine aerosol. The heterogeneous reaction occurs as follows [52, 53]:

$$2NO_{2(g)} + NaCl_{(s)} \rightarrow ClNO_{(g)} + NaNO_{3(s)} \tag{1.33}$$
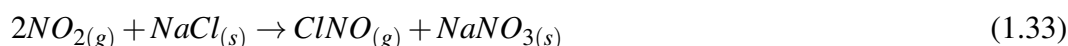
It has also been proposed that ClNO can be formed via a mechanism whereby the NO_2 becomes bound to the surface and forms N_2O_4, which then reacts with HCl [54].
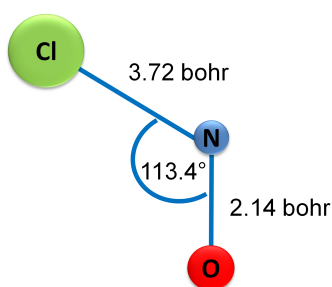
Figure 1.15: The equilibrium geometry of the ClNO molecule. $r_{NO} = 2.146$ bohr, $r_{ClN} = 3.72$ bohr and $\theta_{ClNO} = 113.4°$ [55].

The equilibrium geometry of the electronic ground state of ClNO, shown in figure 1.15, was found by Cazzoli *et al.* using spectroscopic methods [55]. The bond lengths and bond angle are:

- r_{NO} = 1.136 Å (2.146 bohr)

- r_{ClN} = 1.97 Å (3.72 bohr)

- θ_{ClNO} = 113.4°

These values are in very good agreement with those calculated using *ab initio* methods [56–58]. Note that the Cl-N bond is long, reflecting its weakness. The bond dissociation energy D_0 calculated from enthalpies of formation is small, being only 1.614 eV [59]. As a bent triatomic, ClNO has three normal modes of vibration. The fundamental frequencies of these were determined from infrared (IR) absorption studies by Jones *et al.* [60]. The N-O stretch occurs at 1836 cm^{-1}, the Cl-N stretch at 336 cm^{-1} and the bend at 603 cm^{-1}.

The photodissociation of ClNO would initially appear to be rather simple. In the UV-vis region (2 to 7 eV) ClNO exhibits strong absorption, the Cl-N bond readily dissociating to yield Cl and NO fragments in their ground electronic states as follows:

$$ClNO + h\nu \rightarrow Cl(^2P_{3/2,1/2}) + NO(X^2\Pi_{1/2,3/2}). \tag{1.34}$$
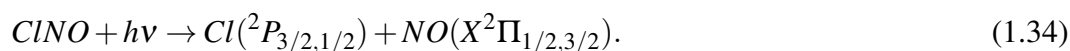
However, the picture is complicated by the wealth of easily-accessible excited electronic states and the various non-adiabatic interactions between these [61]. In addition, the photodissociation products can be formed in a variety of electronic, vibrational, rotational and spin-orbit states.

ClNO belongs to the C$_s$ point group and hence its electronic states are of either A$'$ or A$''$ symmetry. Ignoring spin-orbit coupling, there are 12 states which correlate to the ground electronic states of NO and Cl ($^2\Pi$ and ^2P respectively) on dissociation: $3 \times {}^1$A$'$, $3 \times {}^1$A$''$, $3 \times {}^3$A$'$ and $3 \times {}^1$A$''$. All of these barring the 1 ^{1}A$'$ are dissociative, but there is some variation in their lifetimes, with the 1 ^{1}A$''$ and 1 ^{3}A$''$ in particular existing long enough to exhibit structured absorption bands [62–64].

The UV-vis absorption spectrum of ClNO is given in figure 1.16. This was first taken in 1939 by Goodeve and Katz [65], who assigned each peak a letter as shown in the figure, a nomenclature that is still sometimes used today despite the fact that not all peaks correspond to separate electronic states. The spectrum is dominated by one band, labelled
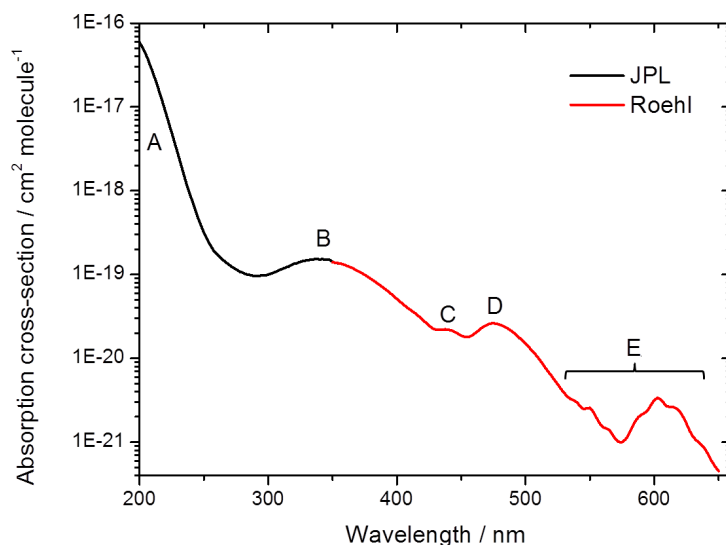
Figure 1.16: The UV-vis spectrum of gas-phase ClNO. The data for the lower wavelength portion labelled 'JPL' is taken from reference [66], and the data for the longer wavelength portion labelled 'Roehl' is taken from [67].

A, that is broad and featureless. The lack of structure implies photodissociation in this region is very rapid. However, moving towards longer wavelengths some structure becomes evident, showing that the state(s) excited at these low energies exist for longer than a vibrational period. In fact, all the peaks labelled E (originally labelled E to K in reference [65]) derive from excitation to the first triplet state, $1\,^3A''$.

Peaks A to D are all due to singlet states. A is mostly due to the absorption to the $4\,^1A'$ state, which has ion-pair character. It cannot dissociate directly but instead decays non-adiabatically into different final states, thought to be the 1 and $3\,^1A'$ [68]. Peak B is due mostly to the $2\,^1A'$ state [69] and Peaks C and D arise from excitation to the $1\,^1A''$ state [70]. These excited states all arise from the excitation of an electron from a Cl p orbital to an orbital with NO π^* character. In this study, the $2\,^1A'$ and $1\,^3A''$ states are of most interest, and so these will be considered in more detail below.

1.4.2 $2\,^1A'$ state

The $2\,^1A'$ state absorbs light between 280 and 400 nm (3 to 4.5 eV) with a peak at 335 nm (3.72 eV) [69]. The primary excitation is from a Cl $3p_x$ to an NO $(2p_x)$ π^* orbital. Although not quite as comprehensively studied as some of the other electronic states, there

is still plenty in the literature referring to its photodissociation. It did however take considerable investigation into the nature of the B band before the precise identity of the state was confirmed. Back in 1972, Busch and Wilson obtained the photofragment spectrum of ClNO at 347 nm [71]. From this they were not able to identify the relevant state but did conclude that it must have A′ symmetry. Considerably later, the group of Huber combined their results from photofragment laser-induced fluorescence (LIF) spectroscopy [72, 73] with previous *ab initio* calculations [74] to conclude incorrectly that the B band was due to the $3\,^1$A′ state.

The problem was solved when Reisler and co-workers conducted photofragment yield spectroscopy experiments [69, 75]. The ClNO was jet-cooled then photodissociated using a tunable dye laser system across the region 620 to 180 nm. The resulting NO was then detected by LIF via the A $^2\Sigma^+$ ← X $^2\Pi$ transition at around 226 nm. From the results at 355 nm they concluded that the B band transition must indeed be parallel, i.e. A′ to A′. The NO rotational distribution at this wavelength was also measured, and was found to be bell-shaped with a peak at $J = 43.5$ (later updated to $J = 46.5$ [75]). This high degree of rotational excitation implied that the NO must experience considerable torque during the photodissociation process. By comparing the rotational populations obtained from the Q and P or R branches of the NO spectrum the group was able to determine the Λ doublet populations. In contradiction to Huber's earlier results, it was found that the Π(A″) doublet was 10 to 15 times more populated than the Π(A′), depending on the precise value of J. This implied that the NO π^* orbital perpendicular to the ClNO molecular plane was preferentially populated, which would not be the case with the $3\,^1$A′ state.

To aid with the interpretation of their results, Reisler's group also carried out some *ab initio* calculations of their own. These were at the MRCI level with a CSF threshold of 10% using a compact Dunning double zeta basis set. Rather than the full PESs, which would have been very expensive at the time, least energy paths were calculated. These had several inaccuracies (such as predicting that the $1\,^3$A″ and $1\,^1$A″ states had shallow minima), but produced an excitation energy for the $2\,^1$A′state of 3.70 eV which matched very well with the experimental B band peak. The predicted orbital populations supported

Excitation wavelength / nm	Cl*/(Cl* + Cl) / %	NO*/(NO* + NO) / %	NO Λ doublet ratio	Ref.
355	45	-	-	[61]
355	-	-	$A'' \gg A'$	[75]
355	-	45	$A'' \gg A'$	[69]
355	-	50	-	[77]
351	90	-	-	[76]

Table 1.1: Summary of experimental spin-orbit and Λ-doublet product state distributions following photodissociation of ClNO via the $2\,^1A'$ state.

this assignment.

With the correct electronic state for the B band confirmed, more detailed experiments could be performed. For example, Cao *et al.* dissociated ClNO at a variety of wavelengths including 355 nm in order to find the Cl product fine structure state distributions [61]. Cl was detected by resonance-enhanced multiphoton ionisation combined with a time-of-flight spectrometer (REMPI-TOF), using a (2+1) REMPI scheme at around 235 nm. From these results, the NO rotational distribution was again found to be narrow, peaking at $J = 49.5$ for Cl $^2P_{3/2}$ and $J = 44.5$ for Cl $^2P_{1/2}$. Anisotropy parameters (β) were also extracted, and found to be 1.63 and 1.78 for Cl $^2P_{3/2}$ + Cl $^2P_{1/2}$ respectively, implying the photodissociation process was rapid. The ratio of (Cl $^2P_{1/2}$) / (Cl $^2P_{3/2}$ + Cl $^2P_{1/2}$) obtained was 45 ± 4%. This disagreed with earlier work by Chichinin [76], who used a slightly different wavelength of 351 nm. The ratio of (NO $^2\Pi_{3/2}$) / (NO $^2\Pi_{3/2}$ + NO $^2\Pi_{1/2}$) has also been investigated. It was reported by Reisler's group [69] to be 45 ± 5 %, i.e. the spin-orbit states are produced in essentially equal proportions. The same result was found in more recent, detailed state-selected experiments carried out by Torres *et al.* at 355 nm, which also found a narrow NO rotational distribution peaking at $J = 46$ for NO in its ground vibrational state [77]. The experimental product state distributions, including spin-orbit ratios and NO vibrational and rotational distributions, are given in tables 1.1 and 1.2.

Yamashita and Kato used electronic structure calculations at the MRCI level with various basis sets to produce analytical potential energy surfaces (PESs) for the first six singlet excited states [68]. Combining these with quantum dynamics calculations they were able to assign all the peaks in the absorption spectrum barring those (much weaker)

Excitation wave-length / nm	NO vibrational state	NO rotational state	β	Ref.
355	-	$J_{max} = 44.5$, $\Delta J = 12$; (Cl*), $J_{max} = 49.5$, $\Delta J = 9$ (Cl)	1.63 (Cl*); 1.78 (Cl)	[61]
355	-	$J_{max} = 46.5$	-	[75]
355	v=0	$J_{max} = 44.5$, $\Delta J \sim 10$	1.8	[69]
355	v=0	$j_{max} = 46$, $\Delta j \sim 8$	1.85	[77]

Table 1.2: Summary of experimental NO vibrational and rotational distributions, and anisotropy parameters, following photodissociation of ClNO via the $2\,^1A'$ state.

arising from triplet states. The results for the B band matched very well with experiment: the absorption maximum was found to be at $\sim$3.7 eV, with the major contribution from the $2\,^1A'$ state. At energies above $\sim$3.8 eV transitions to the $3\,^1A'$ and $3\,^1A''$ states also contribute, and there is a small overlap with the $1\,^1A''$ state below $\sim$3.2 eV.

1.4.3 $1\,^3A''$ state

The $1\,^3A''$, or T_1, state of ClNO absorbs in the visible region from around 650 to 500 nm, and displays an absorption spectrum with several features. As a triplet state, absorption from the ground state is technically forbidden, and so the peaks in the E band are rather weak. The primary excitation is from a Cl $3p_z$ to an NO $(2p_x)$ π^* orbital.

The E band was first convincingly assigned by the group of Reisler following their photofragment yield spectroscopy experiments on jet-cooled ClNO [69]. The low oscillator strength of the E band in comparison with other peaks suggested that it was due to a triplet state, and electronic structure calculations on the $1\,^3A''$ state gave an excitation energy which matched very well with experimental results. Further work by this group [78–80] endeavoured to explain the structure by monitoring the NO product in different vibrational states. The NO fragments were detected by LIF 80 ns post dissociation by a photolysis laser tuned between 625 and 500 nm. Some of these results are given in figure 1.17.

A number of observations can be made from these spectra. Firstly, there are spacings between the main peaks of about 1580 cm^{-1}, and between the sub-peaks of 380 cm^{-1}. These correspond to the NO stretching and Cl-N-O bending vibrations respectively. The
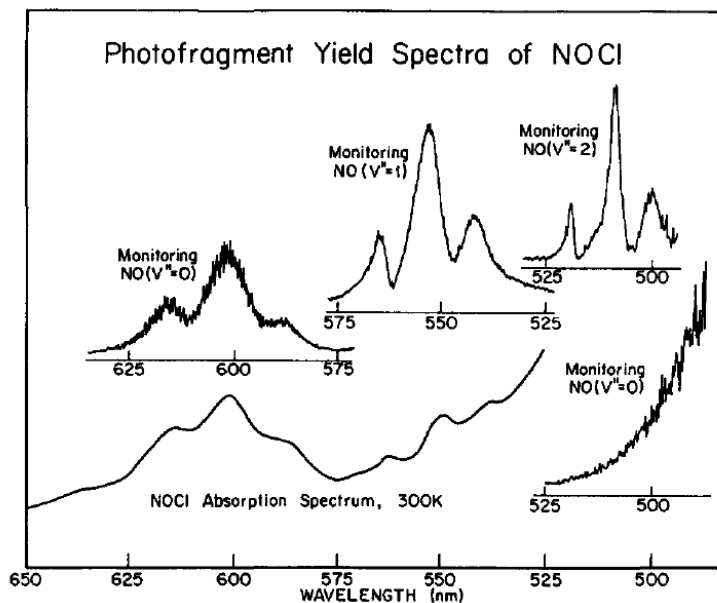
Figure 1.17: Photofragment yield spectra of ClNO following photodissociation on the $1\,^3A''$ state. Taken from [79].

$1\,^3A''$ state therefore exists long enough for several vibrational oscillations to occur, but the lack of rotational structure shows the lifetime must be less than a rotational period. The absorption linewidths decrease with increasing NO stretch and increase with increasing Cl-N-O bend. This implies, counter-intuitively, that the more vibrational quanta of NO are excited, the longer the excited complex lives. The peaks also display a degree of asymmetry.

Reisler *et al.* also obtained product NO rotational distributions. These were found to be multimodal with considerable population at low J, with the exact structure being highly dependent upon the wavelength of the photolysis laser. A modified Franck-Condon model for predissociation [81, 82] treating the bending mode as a harmonic oscillator was used to help explain these results, but for a complete description *ab initio* calculations were required.

Such calculations were carried out by Schinke *et al.* [64]. Firstly orbitals were optimised at the CASSCF level with a full-valence active space. These were then used in further calculations using the Multi-Reference Averaged Coupled Pair Functional (MR-ACPF) technique, which produces results of a quality between MRCI and CASSCF. Initial MRCI calculations were run, but were found to be overly expensive. The basis set

used was a variation of the Dunning cc-pVQZ set, augmented with a selection of diffuse functions. A complete 3D PES was calculated consisting of more than 300 points. Once formed, a scaling factor was applied to decrease the gradient in the exit channel and improve the dissociation energy, and then the PES was fitted using a 3D cubic spline and converted into Jacobi coordinates for use in time-dependent dynamics calculations. The wavepacket propagations were carried out using discrete variable representations (DVRs), and the total angular momentum was kept as 0.

The shape of the calculated PES immediately explained some of the experimental results. Firstly, the gradient in the exit channel is very shallow, meaning the wavepacket moves relatively slowly down the slope towards the products, hence allowing enough time for full vibrations to occur. Secondly, the exit channel is almost parallel to the dissociative *R* coordinate (see figure 2.4 later for a definition of this), implying that there is little to no coupling between the NO stretch and the bending vibrations. The dissociation would therefore be expected to be adiabatic with respect to the NO stretch. Thirdly, there is a slight well in the r_{NO} coordinate near the Franck-Condon region. This can explain the increased lifetime of the excited state complex for higher NO stretch excitation: the more energy in the vibration, the more likely the wavepacket will become temporarily caught in this well.

From the wavepacket dynamics Schinke was able to calculate an autocorrelation function (see equation 2.96) which showed two series of partial recurrences: one, with a period of about 18.5 fs, corresponds to the NO stretching vibration; the other, with a period of about 70 fs, corresponds to the bending vibration. The amplitudes of these drop-off reasonably rapidly as the wavepacket density leaches out of the exit channel, but as has been seen already there is still sufficient time for oscillations to be completed in each mode. This leads to an absorption spectrum comprising two progressions, as seen experimentally. The major peaks are due to the NO stretch; these are then split into three sub-peaks, each corresponding to a different number of quanta in the bending vibration.

To explain the NO rotational distributions, Schinke used a more advanced variation of the rotation-reflection principle [18]. A 'transition line', past which the excited wavepacket was considered to move irreversibly into the exit channel, was drawn onto

the PES and stationary (i.e. time-independent) wavefunctions were calculated from this line onwards. Due to the limited rotational-translational coupling, the initial structures of the wavefunctions persist even to the end of the exit channel.

The NO rotational distributions were therefore highly dependent upon the bending vibration in the excited state complex, with the number of nodes corresponding to the level of bending excitation. For example, for n* = 0, where n* is the number of quanta in the excited state bending vibration, the wavefunction consists of just one component, giving a unimodal distribution. For n = 1, the wavefunction has a central node, and the distribution is correspondingly bimodal, for n* = 2, the wavefunction has two nodes and so on. It should be noted that a degree of averaging had to be used to produce rotational distributions to compare with experiment; quantum mechanical oscillations were also present due to interference effects that are not observed experimentally. Overall, however the agreement with experiment is good, at least in a qualitative sense. The peak for the n* = 0 distribution occurs at around $j = 8$ rather than the observed $j = 0$, implying there were still some deficiencies with either the photodissociation model or the *ab initio* PES used.

The 1 $^3A''$ state of ClNO has also been studied using purely time-independent quantum dynamics. One example of this is the quantum flux method used by Vegiri and Alexander [83]. Both adiabatic and diabatic states were used in order to model the process, with the diabatic picture found to be more appropriate further out in the exit channel. For slightly smaller values of the r_{ClN} bond distance they observed quantum interference between different photofragmentation pathways in nearby adiabatic channels. Despite this added complexity, broadly the same conclusions were reached as in Reisler and Schinke's earlier work. A certain level of vibrational excitation in the NO stretch was found to occur during the dissociation process, but by the time the Cl and NO have fully separated the bulk of this excitation has disappeared. For example, for an initial excitation to v* = 0 in the excited state complex, about 11% of the total flux moves to v* = 1, before returning to give v = 0 in the product NO.

Vegiri and Alexander also calculated the product NO rotational state distributions. The modality seen in these reflected the shape of the calculated flux distributions in the excited

state complex, as had been shown previously. However, they provided an alternative explanation for the high-j shoulders of the rotational distributions, finding them to be due to the relaxation of excited vibrational states not seen by Schinke.

Another approach was taken by Grinberg *et al.*, [84–86] although this met with considerably less success in reproducing experimental results. The technique, known as analytical infinite order sudden quantum theory, is an extension of Franck-Condon models but with fewer approximations. For example, it does not make the assumption that the initial bending and stretching vibrations are uncoupled, and it allows for an anisotropic repulsive PES. However, despite these apparent advantages it was relatively poor in reproducing both NO product rotational distributions and absorption spectra. The authors suggested that this was most likely due to deficiencies in the potentials they used to construct the surfaces.

Chapter 2

Methodology

2.1 Electronic structure methods

2.1.1 Overview

In electronic structure calculations the time-independent Schrödinger equation (TISE),

$$\hat{H}\Psi = E\Psi, \tag{2.1}$$

is solved. The methods are referred to as *ab initio*, meaning they come from quantum mechanics directly and do not incorporate empirical parameters. Here, such calculations will be used to build up PESs of the relevant electronic states. To form a PES it is necessary to obtain the energies of the state in question over a range of molecular geometries. These points are then fitted by potential energy functions to give the complete surface.

As discussed earlier, the concept of the PES is valid only in the framework of the BO approximation and thus the assumption is made that there is no coupling between the nuclei and electronic motion. The Schrödinger equation can then be separated into nuclear and electronic parts and solved for each molecular geometry. This leads to adiabatic surfaces; if non-adiabatic transitions are to be investigated the situation becomes rather more complex.

It is impossible to solve the Schrödinger equation exactly for any but the simplest of systems and so approximations have to be made. There are many different electronic

structure methods available, all of which make different approximations. The main variation is the way in which so-called 'electron correlation' is dealt with. This is the energy arising from the instantaneous (as opposed to average) interactions of each electron with all the others, and although it only accounts for a relatively small amount of the total energy it is essential to describe the system with chemical accuracy. However, methods returning a large proportion of the electron correlation are very computationally expensive. There is hence always a trade-off between accuracy and calculation time.

Four different methods will be considered briefly here. The first, Hartree Fock, acts as the basis for all others. Multi configuration self consistent field (MCSCF) is a more accurate method, and is still relatively cheap to run. Multi reference configuration interaction (MRCI) is a yet more advanced method, and is correspondingly expensive. The descriptions here follow a similar line as in reference [87]. A few calculations have been run using the equations of motion coupled cluster method (EOM-CCSD), and so a short overview of this is also given. Other crucial concepts are basis sets and variational theory; these will be discussed first of all.

Several suites of programs exist for carrying out electronic structure calculations. In this work, the Molpro package has been used [88] extensively, with occasional calculations using Gaussian [89].

2.1.2 Variational theory

The variational principle is crucial to Hartree Fock theory and many other electronic structure methods. In essence, it states that for any approximate wavefunction, the energy calculated is always greater than or equal to the true ground state energy. i.e.

$$E = \frac{\int \Psi^* \hat{H} \Psi d\tau}{\int \Psi^* \Psi d\tau} \geq E_0 \qquad (2.2)$$

which can be written in the more compact bra-ket notation as

$$E = \frac{\left\langle \Psi^* \left| \hat{H} \right| \Psi \right\rangle}{\left\langle \Psi^* \middle| \Psi \right\rangle} \geq E_0 \tag{2.3}$$

The solution of the Schrödinger equation can therefore be treated as a minimisation problem, with the wavefunctions varied until the minimum energy is reached.

The proof of the principle is as follows. First, consider the total wavefunction to be an expansion of eigenfunctions of the energy operator such that

$$\Psi = \sum_n c_n \psi_n, \tag{2.4}$$

where the ψ_n are an orthonormal set. Substitution of this wavefunction into the TISE gives:

$$E = \frac{\left\langle \sum_n c_n^* \psi_n \middle| \hat{H} \middle| \sum_m c_m \psi_m \right\rangle}{\left\langle \sum_n c_n^* \psi_n \middle| \sum_m c_m \psi_m \right\rangle} \tag{2.5}$$

$$E = \frac{\sum_{n,m} c_n^* c_m \left\langle \psi_n \middle| \hat{H} \middle| \psi_m \right\rangle}{\sum_{n,m} c_n^* c_m \left\langle \psi_n \middle| \psi_m \right\rangle} \tag{2.6}$$

The ψ_n are orthogonal, leading to

$$E = \frac{\sum_{n,m} c_n^* c_m E_n \delta_{n,m}}{\sum_{n,m} c_n^* c_m \delta_{n,m}} = \frac{\sum_n E_n |c_n^2|}{\sum_n |c_n^2|} \tag{2.7}$$

Two observations can be made from equation 2.7. Firstly, the ground state E_0 is the lowest possible energy, and so $E_n \geq E_0$. Secondly, the $|c_n|^2$ must all be positive. Hence it follows

$$E = \frac{\sum_n E_n |c_n^2|}{\sum_n |c_n^2|} \geq \frac{E_0 \sum_n |c_n^2|}{\sum_n |c_n^2|} = E_0 \tag{2.8}$$

from which equation 2.3 is obtained.

2.1.3   Orbitals and basis sets

In order to run an electronic structure calculation, molecular orbitals (MOs) need to be formed for each electron. The MOs are formed of linear combinations of atomic orbitals (AOs), which in turn are represented by a function, or set of functions, known as a basis set. One type of function which models orbitals very well is the Slater type orbital:

$$\chi_{\zeta,n,l,m}(r,\theta,\varphi) = N Y_{l,m}(\theta,\varphi) r^{n-1} e^{-\zeta r}, \tag{2.9}$$

where the $Y_{l,m}$ are the spherical harmonics, n is the principal quantum number, ζ is a constant reflecting the effective nuclear charge and N is a normalisation constant. These functions give the majority of electron density near the nucleus and tail off as the distance increases. However, they have the disadvantage of being computationally cumbersome. Much more convenient are Gaussian functions, but a single Gaussian reflects the shape of an orbital poorly. To get around this issue a linear combination of Gaussian functions (individually known as primitives) can be used together to imitate the shape of a Slater-type orbital. This leads to the STO-NG family of basis sets, with the N denoting the number of Gaussians included.

Basis sets are contracted to avoid most of the calculation time being spent optimising the energetically-important, but chemically unimportant, core orbitals. To do this, fixed linear combinations of primitive Gaussian-type orbitals (PGTOs) are used to form contracted GTOs (CGTOs). Only the coefficients of these CGTOs then have to be optimised. In some basis sets a general contraction method is used. This means that every PGTO in the basis set is included in each CGTO; the coefficients of the linear combination are however different in each.

The exponents of each Gaussian function are fixed, and so each orbital of a given type ends up being exactly the same size. This also means that the orbitals all have the same shape, which is clearly not physically realistic. To counter this size problem double-zeta basis sets were introduced. In these, each valence atomic orbital is now represented by one smaller and one bigger contracted function. The larger function is multiplied by a

constant d, and so by varying d the size of the orbital can be tuned:

$$\chi(r) = \chi(r, \zeta_1) + d\chi(r, \zeta_2) \tag{2.10}$$

If three basis functions are used to represent each atomic orbital then the basis set is termed triple-zeta, if four are used it is termed quadruple-zeta, and so on.

In most cases it is the valence orbitals which are most important for molecular bonding. This means it is often valid to use multiple basis functions to represent the valence orbitals, but to just use a single contracted basis function (which itself may of course be comprised of several primitives) to represent the core orbitals. Such basis sets are known as 'split-valence'. The Pople-style family of double-zeta, split-valence basis sets serves as a good illustration. These are labelled N-MPG, where N is the number of primitive Gaussians used for inner-shell orbitals, the hyphen denotes that the basis set is split-valence, M is the number of primitive Gaussians describing the smaller orbital, P is the number describing the larger orbital and G denotes that we are using Gaussian functions.

The fact that atomic orbitals distort when atoms are brought together can be modelled by including 'polarisation effects'. This is done by adding higher-l functions to the atomic orbital in question. Examples of such basis sets are the Pople-style series such as N-MPG* and N-MPG**. In the first of these, $3p$ functions have been added to the $2p$ orbitals, and in the second $2p$ functions have additionally been added to H $1s$ orbitals. If processes involving bond-breaking, or other situations where the electron density extends a long way from the nucleus, are being investigated then it is normally imperative to include diffuse functions. In Pople-style basis sets these are denoted by a '+'; an example is 6-31+G. Well-balanced basis sets contain both polarisation and diffuse functions.

The Pople-style basis sets described here are commonly used, but many others are available. Of most relevance to this work are the correlation consistent basis sets first produced by Dunning and co-workers [90]. These have been designed to aid the recovery of the correlation energy due to the valence electrons, and tend to provide better results than more simple basis sets. The names are of the form cc-pVNZ, where the cc stands for correlation consistent, the p signifies that polarisation functions are included, the V stands

for valence and the NZ denotes the number of zeta. The addition of the prefix aug- shows that diffuse functions are also present. As these are important for accurate modelling of dissociation processes they are essential to this study.

2.1.4 The Hartree-Fock method

As mentioned earlier, the Hartree Fock (HF) method is the starting point for all the other methods considered here. The key to HF theory is the Slater determinant [87], which is a way of representing a total, many electron, wavefunction as a product of single electron wavefunctions (orbitals). These single electron orbitals are the columns of the determinant, and the rows represent the electron coordinates. The molecular orbitals (MOs, or spin-orbitals $\phi_a(i)$) are the product of a spatial orbital and a spin (α or β). The advantages of this representation are that firstly the Pauli exclusion principle is satisfied (if more than one electron is put into the same orbital the determinant becomes 0) and secondly it fulfills the antisymmetry principle (the wavefunction changes sign if any of the orbitals are switched). Thirdly, all the electrons are indistinguishable. These facts can be seen clearly if a simple system containing just two electrons is considered:

$$
\begin{aligned}
\Phi(1,2) &= \frac{1}{\sqrt{2}}(\phi_1(1)\phi_2(2) - \phi_1(2)\phi_2(1)) \\
&= \frac{1}{\sqrt{2}}\begin{vmatrix} \phi_1(1) & \phi_2(1) \\ \phi_1(2) & \phi_2(2) \end{vmatrix}
\end{aligned}
\tag{2.11}
$$

Swapping ϕ_1 and ϕ_2 gives $-\Phi(1,2)$ and if $\phi_1 = \phi_2$ then $\Phi(1,2) = 0$. Extending to the general case of n electrons gives the full Slater determinant:

$$
\Phi_{SD} = \frac{1}{\sqrt{n!}}\begin{vmatrix} \phi_1(1) & \phi_2(1) & \cdots & \phi_n(1) \\ \phi_1(2) & \phi_2(2) & \cdots & \phi_n(2) \\ \ldots & \ldots & \ldots & \ldots \\ \phi_1(n) & \phi_2(n) & \cdots & \phi_n(n) \end{vmatrix}
\tag{2.12}
$$

The individual MOs are orthonormal, i.e. they are both orthogonal ($\langle \phi_i | \phi_j \rangle = \delta_{ij}$) and normalised.

In HF theory it is assumed that the many electron wavefunction can be represented by a single Slater determinant. The aim is then to take this single determinant and adjust the orbitals in such a way as to minimise the energy of the system at hand, thereby getting as close to the 'real' energy as possible by the variational theorem.

By applying the BO approximation, the electronic Hamiltonian can be written as follows:

$$\hat{H}_e = \hat{T}_e + \hat{V}_{ne} + \hat{V}_{ee} + \hat{V}_{nn} \tag{2.13}$$

where $\hat{V}_{nn}$ is constant for a given molecular geometry, $\hat{T}_e$ and $\hat{V}_{ne}$ depend only on single electron coordinates, and $\hat{V}_{ee}$ depends on two electron coordinates. Each term is defined as follows:

$$\hat{T}_e = -\sum_{i=1}^{n} \frac{1}{2} \nabla_i^2 \tag{2.14}$$

$$\hat{V}_{ne} = -\sum_{i=1}^{n} \sum_{a}^{N} \frac{Z_a}{|R_a - r_i|} \tag{2.15}$$

$$\hat{V}_{ee} = -\sum_{i=1}^{n} \sum_{j>i}^{n} \frac{1}{|r_i - r_j|} \tag{2.16}$$

$$\hat{V}_{nn} = -\sum_{a=1}^{N} \sum_{b>a}^{N} \frac{Z_a}{Z_b} |R_a - R_b|. \tag{2.17}$$

The indices i and j refer to electrons (of which there are n in total), and the indices a and b refer to nuclei (of which there are N in total). Gathering these terms together gives the single electron operator

$$\hat{h}_i = -\frac{1}{2} \nabla_i^2 - \sum_{a=1}^{N} \frac{Z_a}{R_a - r_i} \tag{2.18}$$

and the two electron operator

$$\hat{g}_{ij} = \frac{1}{|r_i - r_j|}. \tag{2.19}$$

$\hat{H}_e$ then becomes

$$\hat{H}_e = \sum_{i=1}^{n} \hat{h}_i + \sum_{i=1}^{n} \sum_{j>i}^{n} \hat{g}_{ij} + \hat{V}_{nn}. \tag{2.20}$$

$\hat{V}_{nn}$ is easily dealt with as it is constant for a fixed set of nuclear coordinates. To see the effects of $\hat{h}_i$ and $\hat{g}_{ij}$ it is helpful to write the Slater determinant as

$$\Phi_{SD} = \hat{A}\Pi \tag{2.21}$$

where $\hat{A}$ is an antisymmetrising operator defined below and Π is the diagonal product of the Slater determinant.

$$\hat{A} = \frac{1}{\sqrt{n!}} \sum_{p=0}^{n-1} (-1)^p \hat{P} = \frac{1}{\sqrt{n!}} \left[\hat{1} - \sum_{ij} \hat{P}_{ij} + \sum_{ijk} \hat{P}_{ijk} - \cdots \right] \tag{2.22}$$

Here, the $\hat{P}$ are permutation operators that act on the electron coordinates. As $\hat{h}_i$ involves only single electrons it follows that the operator will only give nonzero values on the diagonal product of the Slater determinant, where the indices of the electron coordinate and the orbital are the same. i.e. for $i = 1$ this gives

$$\begin{aligned} \langle \Pi | \hat{h}_1 | \Pi \rangle &= \langle \phi_1(1)\phi_2(2)\phi_3(3) \ldots | \hat{h}_1 | \phi_1(1)\phi_2(2)\phi_3(3) \ldots \rangle \\ &= \langle \phi_1(1) | \hat{h}_1 | \phi_1(1) \rangle = h_1 \end{aligned} \tag{2.23}$$

In contrast, for $\hat{g}_{ij}$ both the identity operator $\hat{1}$ and $\hat{P}_{ij}$ in $\hat{A}$ above come into play. For $i = 1$ and $j = 2$ the identity leads to

$$\begin{aligned} \langle \Pi | \hat{g}_{12} | \Pi \rangle &= \langle \phi_1(1)\phi_2(2)\phi_3(3) \ldots | \hat{g}_{12} | \phi_1(1)\phi_2(2)\phi_3(3) \ldots \rangle \\ &= \langle \phi_1(1)\phi_2(2) | \hat{g}_{12} | \phi_1(1)\phi_2(2) \rangle = J_{12} \end{aligned} \tag{2.24}$$

This result is known as the Coulomb integral, and directly relates to the classical electron-electron repulsion as it gives the coulombic repulsion between electrons 1 and 2. The

permutation operator $\hat{P}_{ij}$ leads, for $i = 1$ and $j = 2$, to

$$
\begin{aligned}
\langle \Pi | \hat{g}_{12} | P_{12} \Pi \rangle &= \langle \phi_1(1) \phi_2(2) \phi_3(3) \ldots | \hat{g}_{12} | \phi_2(1) \phi_1(2) \phi_3(3) \ldots \rangle \\
&= \langle \phi_1(1) \phi_2(2) | \hat{g}_{12} | \phi_2(1) \phi_1(2) \rangle = K_{12}
\end{aligned}
\tag{2.25}
$$

This result is known as the exchange integral and is purely quantum mechanical, stemming from the wavefunction's antisymmetry requirement. Combining these terms allows the energy to be written as:

$$
E = \sum_{i=1}^{n} \hat{h}_i + \frac{1}{2} \sum_{i=1}^{n} \sum_{j=1}^{n} \left(\hat{J}_{ij} - \hat{K}_{ij} \right) + V_{nn}
\tag{2.26}
$$

where $\hat{J}_{ij}$ and $\hat{K}_{ij}$ are the Coulomb and exchange operators yielding the matrix elements given above.

In order to solve the electronic Schrödinger equation this energy needs to be minimised with respect to changes in the orbitals. It is known from the variational principle that minimising the energy will give the best representation of the wavefunction possible using a single Slater determinant. However, in minimising the energy there exists an important constraint, namely that the orbitals remain orthonormal. This can be achieved using Lagrange's method of undetermined multipliers. This minimisation results in the set of Hartree Fock equations which define the orbitals:

$$
\hat{F}_i \phi_i = \varepsilon_i \phi_i
\tag{2.27}
$$

where $\hat{F}$ is the Fock operator

$$
\hat{F}_i \phi_i = \hat{h}_i + \sum_{j}^{n} (\hat{J}_j - \hat{K}_j).
\tag{2.28}
$$

The Hartree Fock equations are pseudo-eigenvalue equations, meaning that their solutions can be found by diagonalising the Fock matrix. However, to form the Fock matrix, and hence produce the desired MOs, initial MOs are needed. The process is therefore iterative, and termed 'Self-Consistent', meaning the optimisation stops when the input and output

MOs are the same. The Hartree Fock equations can be solved numerically, or a basis set can be used, in which case they become the Roothaan equations. The MOs can be written as an expansion of the atomic orbital basis functions (χ_k),

$$\phi_i = \sum_{k=1}^{K} c_{ki}\chi_k \tag{2.29}$$

where the c_{ki} are the coefficients, and then inserted into equation 2.27 above. In the Self-Consistent Field method the coefficients are varied until the optimal set of orbitals are found.

An important point to emphasise is that although electron-electron repulsion is accounted for in the HF method, it is only done so in an averaged way. Each electron sees the other electrons as a 'mean field', and there are no individual electron-electron interactions. The additional energy provided by these interactions is the correlation energy, and to get better results than HF it needs to be recovered. The HF energy is however the best energy that can be obtained from a single Slater determinant.

2.1.5 Electron correlation and configuration interaction

Each electron in the system will interact with all the others. It will interact most strongly with those sharing its spatial MO, but the interactions with those in different MOs are also important, particularly in larger molecules. Interactions with electrons of the same spin are termed 'Fermi correlations', and those with electrons of opposite spin are termed 'Coulomb correlations'. Instantaneous interactions are known as 'dynamic correlation' (important for lowering the energy) and more permanent interactions are known as static correlation (important to get a qualitatively correct description of the system). For example, if two electrons are well separated spatially the correlation will be mostly static, but if they are close, e.g. sharing the same MO, it will be mostly dynamic.

To recover the correlation energy the HF method needs to be improved upon. In order to do this the wavefunction can no longer be considered as a single Slater determinant;
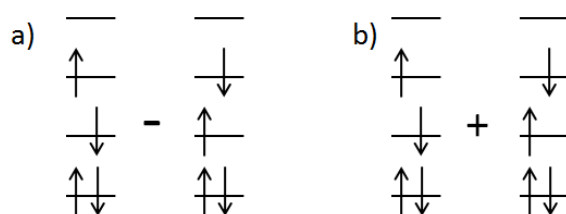
Figure 2.1: An example of how CSFs are formed from Slater determinants. a) shows a singlet state and b) shows the $S_Z = 0$ component of a triplet state [87].

instead it comprises a collection of Slater determinants each with a different coefficient:

$$\Psi = a_0\Phi_{HF} + \sum_{i=1} a_i\Phi_i \tag{2.30}$$

This is analogous to basis sets in which the more functions that are included, the more flexible the description of the orbital. Here, the more determinants that are included, the better the description of the overall wavefunction for the system.

To generate additional Slater determinants, electrons are excited from occupied MOs into unoccupied MOs in a process known as configuration interaction (CI). In the simplest case only single excitations are considered. This allows excited states to be modelled but makes no difference to the energy of the ground state. To improve upon this double, triple and even quadruple excitations out of the original HF determinant can be added. Not every new Slater determinant will be a proper spin eigenfunction of the system under consideration. However, these eigenfunctions can be found by taking linear combinations of the individual determinants. Such combinations are termed configuration state functions (CSFs), an example of which is given in figure 2.1.

In the limit of full CI, i.e. with all the possible excited Slater determinants included, the wavefunction will be exact (at least for the given basis set). However, this is far too computationally expensive to be practical, and so only single and double excitations are routinely used. The iterative procedure then adjusts the coefficients in front of each new determinant until an energy minimum is reached.
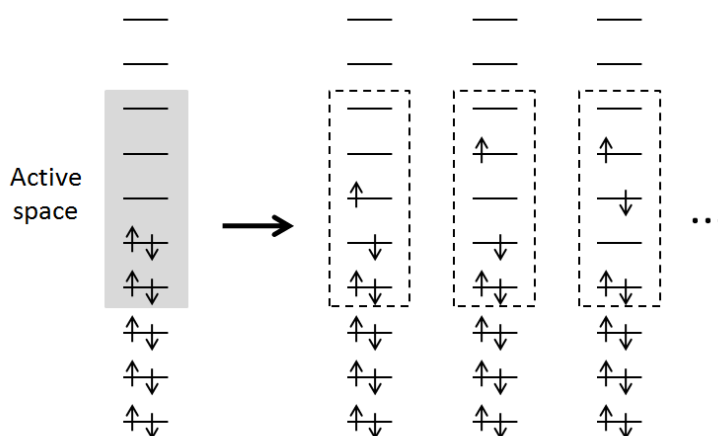
Figure 2.2: An illustration of the CASSCF process. In the active space all possible excitations are allowed, leading to the creation of new Slater determinants. Everywhere else the occupation numbers are kept to be 0 or 2.

2.1.6   The Multi-Configuration Self-Consistent Field method

The MCSCF method is one way of recovering the static part of the electron correlation [87]. MCSCF wavefunctions therefore often give a good, qualitative picture but are not so useful for determining energies with high accuracy. The general idea is as follows: as in the CI method, excitations are made out of the HF Slater determinant. Then, in addition to the a_i coefficients of the new determinants, the MOs in each are also optimised. Obviously, if this was done for all possible excitations out of all possible MOs the problem would be prohibitively large. Instead, the orbitals are partitioned into 'active' and 'inactive' spaces. In the inactive, or closed region below the active space all MOs are kept to be doubly occupied. In the inactive space the MOs are kept to have an occupation of zero, and in the active space itself excitations are allowed. This setup is illustrated in figure 2.2.

If all possible excitations are allowed in the active space the method is known as complete active space SCF (CASSCF); if some restrictions on the occupancies of certain orbitals are made it is instead termed restricted active space SCF (RASSCF). Clearly, the selection of the active space will have a huge influence on the resulting wavefunction, and hence deciding which MOs and how many electrons to include is often a difficult problem. All MOs likely to be involved in the process being studied need to be included.

A safe option is to include all valence orbitals and electrons, but this space is often large and so is too computationally expensive for all but the smallest molecules. For larger molecules the natural orbitals (those for which the density matrix is diagonal) from a HF calculation should be examined and inferences about their importance made.

2.1.7 The Multi-Reference Configuration Interaction method

Once a good qualitative wavefunction has been generated by the MCSCF method steps need to be taken to make it more accurate quantitatively. One way to do this is by using the MRCI method [87]. As the name suggests, this is equivalent to the standard CI method, but instead of including only excitations out of the original HF Slater determinant the MCSCF wavefunction is used as the starting point. This means that excitations are made out of every determinant included in the MCSCF calculation, generating even more determinants, the coefficients of which all need to be optimised. Figure 2.3 gives a schematic representation of the MRCI process.

The MRCI method can produce extremely accurate wavefunctions, but only for an extremely high computational cost. In practice therefore only single and double excitations are commonly used. Even with this restriction the calculation may still be unfeasible. To reduce the expense further, it is possible to restrict the number of CSFs involved by only including those which contribute more than a given percentage to the final MCSCF wavefunction. The threshold so chosen should not be more than about 3% or the risk is that important configurations will be missed.

It should be noted that the HF, full valence CASSCF and full CI methods are variational, i.e. they will always converge downwards towards the 'true' energy. MRCI however is not in most cases variational as the excitations are truncated at doubles.

2.1.8 The Coupled Cluster method

The coupled cluster method [87, 91] is a way of obtaining accurate ground state wavefunctions. In the method an excitation operator works on a single reference function, usually the HF Slater determinant Φ_0. The overall excitation operator $\hat{T}$ is the sum of in-
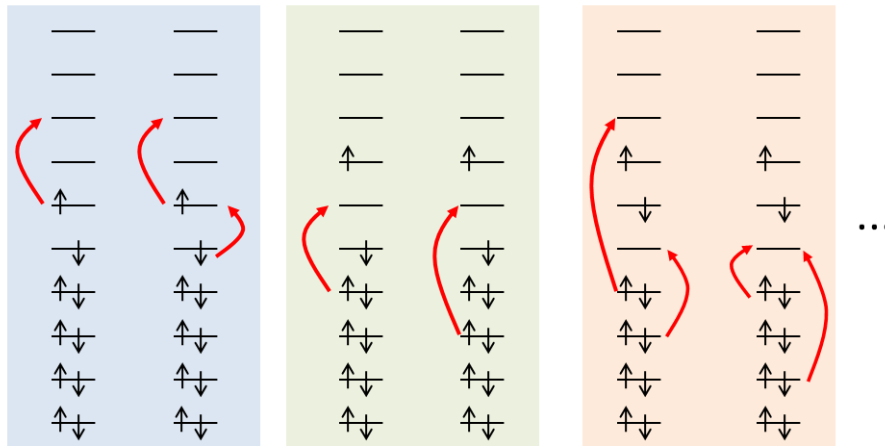
Figure 2.3: An illustration of the MRCI process. Single and double excitations are made out of the Slater determinants from figure 2.2.

dividual operators $\hat{T}_i$, where i is the level of excitation. The coupled cluster wavefunction is written as

$$\Psi_{cc} = e^{\hat{T}}\Phi_0, \tag{2.31}$$

where

$$e^{\hat{T}} = \hat{1} + \hat{T} + \frac{1}{2}\hat{T}^2 + \frac{1}{6}\hat{T}^3 \cdots = \sum_{k=0}^{\infty}\frac{1}{k!}\hat{T}^k. \tag{2.32}$$

Re-writing this so that terms leading to the same number of electrons excited are grouped together gives:

$$e^{\hat{T}} = \hat{1} + \hat{T}_1 + (\hat{T}_2 + \frac{1}{2}\hat{T}_1^2) + (\hat{T}_3 + \hat{T}_1\hat{T}_2 + \frac{1}{6}\hat{T}_1^3)\ldots. \tag{2.33}$$

The first term in this expansion is the HF Slater determinant, the second gives the singly excited configurations, the third gives the doubly excited configurations, the fourth gives the triply excited configurations, and so on. Note that the doubly and triply excited configurations contain both true doubles/triples (simultaneously excited interacting electrons) and product doubles/triples (combinations of interacting and non-interacting electrons).

In contrast, the CI wavefunction would just be:

$$\Psi_{CI} = (\hat{1} + \hat{T}_1 + \hat{T}_2 + \hat{T}_3 \dots)\Phi_0 \tag{2.34}$$

It is normally too computationally expensive to find the amplitudes of each excited Slater determinant using the variational principle. Instead, the coupled cluster Schrödinger equation is projected onto Φ_0 to give

$$E_{cc} = \left\langle \Phi_0 | \hat{H} e^{\hat{T}} | \Phi_0 \right\rangle \tag{2.35}$$

As the Hamiltonian only contains 1 and 2 electron operators the expansion of $e^{\hat{T}}$ ends at $\hat{T}_2$. Using the HF orbitals the following can be derived:

$$E_{cc} = E_0 + \sum_{i<j}^{occ} \sum_{a<b}^{vir} (t_{ij}^{ab} + t_i^a t_j^b - t_i^b t_j^a)(\langle \phi_i \phi_j | \phi_a \phi_b \rangle - \langle \phi_i \phi_j | \phi_b \phi_a \rangle) \tag{2.36}$$

To find the amplitudes (t_i etc) the Schrödinger equation is projected onto the excited determinants. This is done using the de-excitation operator $e^{-\hat{T}}$, eventually obtaining:

$$E_{cc} = \left\langle \Phi_m^{ex} | e^{-\hat{T}} \hat{H} e^{\hat{T}} | \Phi_0 \right\rangle \tag{2.37}$$

The method would be too expensive if all possible parts of $\hat{T}$ were included. Hence it is usually truncated at the singles and doubles level, a method referred to as CCSD. However, note that higher excitations are included by means of product excitations e.g. quadruples are included via the $\hat{T}_{22}$ operator. This means CCSD is size extensive and better than CISD.

Equations of motion coupled cluster (EOM-CC) is a variant in which a whole spectrum of excited states is obtained in a single calculation. The excited electronic states are generated when a wave operator acts on a CCSD reference state, with a common set of MOs used for all. The method is less reliable for systems where static correlation effects

are most important as it is single reference. The final state wavefunction is given by:

$$|\Psi_x\rangle = \hat{R}|\Psi_g\rangle, |\Psi_g\rangle = e^{\hat{T}}|\Phi_0\rangle \tag{2.38}$$

where $\hat{R}$ is a linear excitation operator. From the Schrödinger equation,

$$\hat{H}\hat{R}e^{\hat{T}}|\Phi_0\rangle = E\hat{R}e^{\hat{T}}|\Phi_0\rangle \tag{2.39}$$

the eigenvalue equation

$$[e^{-\hat{T}}\hat{H}e^{\hat{T}} - E]\hat{R}|\Phi_0\rangle = 0 \tag{2.40}$$

can be derived, leading to the effective Hamiltonian

$$\tilde{H} = e^{-\hat{T}}\hat{H}e^{\hat{T}} \tag{2.41}$$

$\tilde{H}$ contains the Fock matrix elements and the two electron integrals. It is not Hermitian however, and so each root has two eigenvectors corresponding to bra and ket states:

$$\begin{aligned}\langle\tilde{\Psi}| &= \langle\Phi_0|\hat{L}e^{\hat{T}} \\ |\Psi\rangle &= e^{\hat{T}}\hat{R}|\Phi_0\rangle.\end{aligned} \tag{2.42}$$

$\hat{L}$ is a de-excitation operator. If only energies are required, the bra states do not need to be calculated. However, to get other properties both states need to be evaluated. Generally,

$$\theta = \langle\tilde{\Psi}|\Theta|\Psi\rangle. \tag{2.43}$$

where θ is the property of interest and Θ is a linear operator. Transition moments are not well defined in EOM-CC. However, as the experimental observable is the square of these, a combination of the left and right transition moments can be taken instead.

Many other electronic structure methods, such as those based on perturbation theory and density functional theory, are also available. These have not been used beyond quick

test calculations in this work and so are not described here.

2.1.9 Non-adiabatic coupling

It is possible to calculate non-adiabatic coupling matrix elements (NACMEs) between different electronic states in various ways depending on the system at hand. Here, as ClNO is a small molecule, it is feasible to calculate them using the 'DDR' method in Molpro at the CASSCF level to obtain the derivative couplings as in equation 1.10 [88]. In this, the wavefunction is calculated at the geometry of interest, and then at either one or two points slightly displaced from it. The orbitals and transition density matrices from these different geometries are then used to derive the NACMEs using finite difference methods.

2.1.10 Spin-orbit coupling

In Molpro [88] spin-orbit coupling matrix elements and eigenstates can be calculated at the CASSCF level using the Breit-Pauli operator given in equation 1.15. Both the one and two-electron terms are calculated. The spin-orbit eigenstates are found by diagonalising $\hat{H}_e + \hat{H}_{SO}$ using a basis of the eigenfunctions of $\hat{H}_e$. The resulting spin-orbit matrices are outputted in terms of both the zeroth-order and symmetry-adapted wavefunctions; in this latter representation the different contributions from each of the triplet sub-levels can be seen more explicitly.

2.2   Computational dynamics

2.2.1   Quantum dynamics

The time-dependent Schrödinger equation

At the heart of quantum dynamics methods lies the time-dependent Schrödinger equation (TDSE). This is

$$i\hbar\frac{\partial}{\partial t}\Psi(q,t) = \hat{H}\Psi(q,t),\tag{2.44}$$

where the Hamiltonian operator $\hat{H} = \hat{T} + \hat{V}$. In fact, the TISE considered previously represents a particular solution of this, and can be derived from it as follows. Firstly, assume that the wavefunction Ψ can be written as a product of time- and position-dependent components:

$$\Psi(x,t) = \psi(x)\chi(t).\tag{2.45}$$

Here just one coordinate (x) is considered for simplicity, but the argument stands whatever the dimensionality of q. Next, substitute this into equation 2.44 to give

$$i\hbar\psi(x)\frac{\partial\chi(t)}{\partial t} = -\frac{\hbar^2}{2m}\frac{\partial^2\psi(x)}{\partial x^2}\chi(t) + V(x)\psi(x)\chi(t).\tag{2.46}$$

Note that the potential V here is not time-dependent. Dividing throughout by $\chi(t)\psi(x)$ leads to

$$i\hbar\frac{1}{\chi(t)}\frac{\partial\chi(t)}{\partial t} = -\frac{\hbar^2}{2m}\frac{1}{\psi(x)}\frac{\partial^2\psi(x)}{\partial x^2} + V(x).\tag{2.47}$$

Now all the terms on the left hand side of the equation are dependent only on time, and all those on the right hand side are dependent only on position. In order for this equation to work, both sides must be therefore be equal to a constant: E, the energy, yielding a pair

of equations. The first,

$$i\hbar \frac{1}{\chi(t)} \partial \chi(t) = E \partial t, \tag{2.48}$$

can easily be solved to give the general solution

$$\chi(t) = \chi_0 \exp\left(-\frac{iEt}{\hbar}\right) \tag{2.49}$$

where χ_0 is the solution at $t = 0$. The second,

$$-\frac{\hbar^2}{2m} \frac{\partial^2 \psi(x)}{\partial x^2} + V(x)\psi(x) = \hat{H}\psi(x) = E\psi(x) \tag{2.50}$$

is the familiar TISE, with the wavefunction $\psi(x)$ as its eigenstate. Combining these two parts gives a single solution of the TDSE represented as

$$\Psi(q,t) = \psi(q)\chi_0 \exp\left(-\frac{iEt}{\hbar}\right). \tag{2.51}$$

To make this simpler the constant χ_0 is normally absorbed into $\psi(q)$.

The general solution to the TDSE is therefore a linear combination of the individual solutions, i.e. a superposition of eigenstates, commonly known as a wavepacket.

$$\Psi(q,t) = \sum_{j=1}^{\infty} a_j \psi_j(q) \exp\left(-\frac{iE_j t}{\hbar}\right) \tag{2.52}$$

By propagating this wavepacket in time, the dynamics of the system can be followed. Note that it is also possible to investigate dynamics using time-independent methods, but time-dependent methods are often preferable. This is because, due to the multi-eigenstate nature of wavepackets, information about a range of energies can be obtained at once, and such methods are often mathematically easier as they involve initial value problems rather than eigenvalue problems. Hence, the time-dependent approach has been used in this study [20, 92, 93].

Preparing the Hamiltonian

When using time-dependent methods to investigate chemical processes, the idea is as follows: prepare a wavepacket for a given set of initial conditions, propagate this wavepacket across the PES(s) for the system until the asymptotic region is reached, then perform analyses to find the properties of interest. Firstly, however, the full Hamiltonian for the system needs to be defined. The potential energy operator $\hat{V}$ is normally a PES, or set of PESs, that has been calculated earlier using electronic structure methods, possibly converted to a more suitable coordinate set and then fitted with some kind of potential energy function. The kinetic energy operator $\hat{T}$ will depend on the exact nature of the system at hand, and the coordinate set used. When looking at the photodissociation of a triatomic ABC, the PESs are usually calculated in binding coordinates, i.e. terms of the bond lengths A-B and B-C, and the angle θ_{ABC}. However, the kinetic energy operator using these coordinates is rather complicated, even when the assumption that the total angular momentum is zero, i.e. $J = 0$, is made:

$$
\begin{aligned}
\hat{T}(r_1, r_2, \theta) = {} & -\frac{\hbar^2}{2\mu_1}\frac{\partial^2}{\partial r_1^2} - \frac{\hbar^2}{2/mu_2}\frac{\partial^2}{\partial r_2^2} - \frac{\hbar^2}{\mu_B}\cos\frac{\partial^2}{\partial r_1 \partial r_2} \\
& -\frac{\hbar^2}{2}\left(\frac{1}{\mu_1 r_1^2} + \frac{1}{\mu + 2r_2^2} - \frac{2\cos\theta}{m_B r_1 r_2}\right)\left(\frac{\partial^2}{\partial\theta^2} + \cot\theta\frac{\partial}{\partial\theta}\right) \\
& -\frac{\hbar^2}{m_B}\frac{1}{r_1 r_2}\left(\sin\frac{\partial}{\partial\theta} + \cos\theta\right) \\
& +\frac{\hbar^2}{m_B}\left(\sin\theta\frac{\partial}{\partial\theta} + \cos\theta\right)\left(\frac{1}{r_1}\frac{\partial}{\partial r_2} + \frac{1}{r_2}\frac{\partial}{\partial r_1}\right).
\end{aligned}
\tag{2.53}
$$

r_1 is the length of the AB bond, r_2 is the length of the BC bond and μ_1 and μ_2 are the corresponding reduced masses.

A better alternative is to use Jacobi coordinates. These are easily converted from Cartesian coordinates, and are illustrated in figure 2.4. The kinetic energy operator is considerably more straightforward, being

$$
\hat{T}(R, r, \gamma) = -\frac{\hbar^2}{2\mu_R}\frac{\partial^2}{\partial R^2} - \frac{\hbar^2}{2\mu_r}\frac{\partial^2}{\partial r^2} + \frac{(\hat{J} - \hat{j})^2}{2\mu_R R^2} + \frac{\hat{j}^2}{2\mu_r r^2}
\tag{2.54}
$$

where $\hat{J}$ is the total angular momentum operator and $\hat{j}$ is the rotational angular momentum
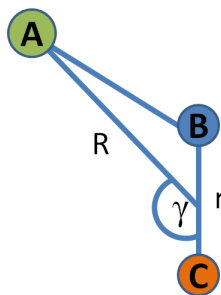
Figure 2.4: Jacobi coordinates for a triatomic molecule. The R coordinate goes from atom A to the centre of mass of the B-C bond.

operator for BC. For $J = 0$, this can be simplified further to

$$\hat{T}(R, r, \gamma) = -\frac{\hbar^2}{2\mu_R}\frac{\partial^2}{\partial R^2} - \frac{\hbar^2}{2\mu_r}\frac{\partial^2}{\partial r^2} - \frac{1}{2}\left(\frac{1}{\mu_R R^2} + \frac{1}{\mu_r r^2}\right)\frac{1}{\sin\gamma}\frac{\partial}{\partial\gamma}\sin\gamma\frac{\partial}{\partial\gamma}. \quad (2.55)$$

If multiple states are involved then the Hamiltonian becomes more complicated. Potentials need to be included for each state of interest, and any couplings between these also need to be incorporated. For larger molecules the picture becomes more complex still: it is often too computationally expensive to include every mode, so those deemed most relevant to the process under investigation need to be part of the Hamiltonian, but others have to be neglected or treated in a general sense.

The discrete variable representation

Once the Hamiltonian has been specified, the form of the wavepacket needs to be chosen. In some cases the coordinates will lend themselves well to a basis set representation, such as harmonic oscillator-like vibrational modes. In photodissociation however, when molecules are broken apart, this is not physically realistic and so a grid method needs to be used, whereby the wavefunction is considered only at discrete points. Clearly, the grid needs to extend over the whole region of interest, to be placed along physically-sensible modes, and to be dense enough that the wavepacket is accurately represented.

At each step in a propagation the wavefunction Ψ at each grid point needs to be acted upon by the potential, $\hat{V}$, and kinetic energy, $\hat{T}$, operators. It turns out the first step is trivial, but the latter is more complicated: derivatives are needed, but a set of numbers

at grid points is no longer a differentiable function. Finite-difference methods could be used, but these are rarely sufficiently accurate. Instead, the definite integrals that need to be evaluated are approximated by a weighted sum of function values at the grid points, i.e. quadrature methods are used. One commonly-used method which employs quadrature is the discrete variable representation (DVR).

The DVR method works as follows. Firstly, consider a wavefunction in one dimension, $\Psi(x)$. This needs to be expanded in a set of N orthonormal basis functions, φ_j, known as the Finite Basis Representation (FBR).

$$\Psi(x) = \sum_{j=1}^{N} a_j \varphi_j(x) \tag{2.56}$$

To find the expansion coefficients a_j, it is necessary to use an N-point quadrature method. The positions of the quadrature points (abscissae) hence need to be decided upon. To do this, the matrix representation of the coordinate operator $\hat{Q}$ is diagonalised in the FBR basis. The matrix elements of $\boldsymbol{Q}$ are:

$$Q_{jk} = \langle \varphi_j | \hat{x} | \varphi_k \rangle \tag{2.57}$$

and it is diagonalised to $\boldsymbol{X}$ using the unitary matrix $\hat{U}$ via

$$\boldsymbol{Q} = \boldsymbol{U}\boldsymbol{X}\boldsymbol{U}^{\dagger}. \tag{2.58}$$

The elements of the diagonalised matrix are then

$$X_{\alpha\beta} = x_{\alpha}^2 \delta_{\alpha\beta} \tag{2.59}$$

where α and β denote the DVR points. These points can be used to find the a_j by quadrature as follows:

$$a_j = \int \varphi_j^*(x)\Psi(x)dx \approx \sum_{\alpha=1}^{N} w_{\alpha}\varphi_j(x_{\alpha})\Psi(x_{\alpha}) \tag{2.60}$$

where w_α is a weight. Note that if $\boldsymbol{Q}$ is tridiagonal the DVR is termed a 'proper' DVR and the weights are simple, being

$$w_\alpha = \left(\frac{U_{k\alpha}}{\varphi_k^*(x_\alpha)}\right)^2. \tag{2.61}$$

Using $\hat{U}$, the DVR functions can now be defined as

$$\chi_\alpha(x) = \sum_{j=1}^N \varphi_j(x)U_{j\alpha}. \tag{2.62}$$

These functions are orthonormal, and are zero-valued at every DVR point on the grid except one. This has a fortunate consequence when calculating potential matrix elements:

$$\langle\chi_\alpha|\hat{V}|\chi_\beta\rangle = \sum_{\gamma=1}^N \chi_\alpha^*(x_\gamma)V(x_\gamma)\chi_\beta(x_\gamma) = V(x_\gamma)\delta_{\alpha\beta} \tag{2.63}$$

i.e. the wavefunction at the grid point x_γ simply needs to be multiplied by the value of V at that point.

Finding the kinetic energy operator is much easier once the DVRs have been found. If the FBR functions have been well-chosen, it will be possible to calculate the KE matrix elements analytically. If this is the case, moving from the FBR to the DVR picture is simply a matter of a unitary transformation using the matrix $\mathbf{U}$ found above.

$$T_{jk}^{FBR} = \langle\varphi_j|\hat{T}|\varphi_k\rangle \tag{2.64}$$

$$\boldsymbol{T}^{DVR} = \boldsymbol{U}^\dagger\boldsymbol{T}^{FBR}\boldsymbol{U} \tag{2.65}$$

Ideally, the FBR functions are chosen to be those which link directly to Gaussian quadrature, thus providing known weights and optimum DVR grid points. The most commonly used functions depend on the nature of the mode the DVR is representing. For vibrational modes, the harmonic oscillator is often chosen. For bonds which break this would not be appropriate and so exponential DVRs, which use plane waves as basis functions, and sine DVRs, which use the particle in a box eigenfunctions, are better. For angular coordinates it is often best to use the Legendre polynomials as these are the

eigenfunctions of the angular momentum operator.

Propagating the wavepacket

In order to follow the course of the dynamics the wavepacket needs to be propagated across the PES(s). To see how this is commonly achieved, the TDSE first needs to be re-written (in a form similar to equation 2.51) as

$$\Psi(q, t + \Delta t) = \exp\left(-\frac{i\hat{H}(q)\Delta t}{\hbar}\right)\Psi(q, t) \tag{2.66}$$

where Δt is the time-step. $\exp\left(-\frac{i\hat{H}(q)\Delta t}{\hbar}\right)$ is known as the time-evolution operator, and there are several ways it can be dealt with [94]. One option is to use approximate eigenvalues and vectors of $\hat{H}$. Another is to use a split-operator method, whereby the time-evolution operator can be split into kinetic and potential parts, such as:

$$\exp\left(-\frac{i\hat{H}\Delta t}{\hbar}\right) \approx \exp\left(-\frac{i\hat{T}\Delta t}{\hbar}\right)\exp\left(-\frac{i\hat{V}\Delta t}{\hbar}\right) \tag{2.67}$$

A third common method is to approximate the operator as a sum of Chebyshev polynomials [95], i.e.

$$\exp\left(-\frac{i\hat{H}\Delta t}{\hbar}\right) \approx \sum_{n=0}^{N} c_n C_n\left(-\frac{i\hat{H}\Delta t}{\hbar}\right) \tag{2.68}$$

where the c_n are expansion coefficients and C_n is the nth Chebyshev polynomial. This is a very accurate and widely-applicable model, and so has been used in this study.

Preparing an initial wavepacket

The initial wavepacket needs to be specified on the grid in the chosen coordinate set. In many cases a Gaussian wavepacket is adequate, but other functions can also be used. For example, in a vibrational mode the wavepacket could be described by a harmonic oscillator. For photodissociation processes the initial wavepacket will normally be a bound state of the molecule in question. This can then be acted on by the transition dipole moment operator in order to get the wavepacket onto an excited state.

One way to prepare an initial wavepacket in the ground state is to run a 'relaxation' [96]. This is essentially the opposite of a normal propagation and involves propagating the wavepacket in imaginary time, $i\tau$. Equation 2.52 then becomes

$$\Psi(q,\tau) = \sum_{j=1}^{\infty} a_j \psi_j(q) \exp\left(-\frac{E_j \tau}{\hbar}\right) \qquad (2.69)$$

i.e. each eigenstate will decay exponentially. However, each state will decay at a rate which is proportional to its energy, with the higher energy states tailing off fastest. If the relaxation runs far enough back in imaginary time only the lowest-energy eigenfunction of the PES used will be left. The norm of the wavepacket needs to be maintained so that it does not disappear completely. Note that it is also possible to produce wavepackets in higher-energy eigenstates using this method if the lowest ones are filtered out in some way. The starting wavepacket should be a reasonable guess to the desired one, but does not need to be particularly accurate as long as the relaxation time is long enough, making this a very good method by which to produce high-quality initial wavepackets.

Standard methods of solving the TDSE

In standard methods for solving the TDSE, the wavefunction is expanded as a product of time-independent basis functions:

$$\Psi(Q_1,...,Q_f,t) = \sum_{j_1=1}^{N_1} ... \sum_{j_f=1}^{N_f} C_{j_1...j_f}(t) \times \prod_{\kappa=1}^{f} \chi_{j_\kappa}^{(\kappa)}(Q_\kappa). \qquad (2.70)$$

Here, there are f degrees of freedom, the $Q_1,...,Q_f$ are the nuclear coordinates, the $C_{j_1...j_f}(t)$ are time-dependent expansion coefficients and the $\chi_{j_\kappa}^{(\kappa)}$ are the one-dimensional basis functions for degree of freedom κ. These basis functions, of which there are N_κ, are generally the DVR functions described earlier. The equations of motion of the expansion coefficients are found by application of the Dirac-Frenkel time-dependent variational principle, which states that

$$\langle \delta\Psi | H - i\frac{\partial}{\partial t} | \Psi \rangle = 0. \qquad (2.71)$$

The details will not be covered here, but the following can be derived:

$$i\dot{C}_J = \sum_L \langle \chi_J | H | \chi_L \rangle C_L \tag{2.72}$$

where J denotes $j_1...j_f$ and L denotes $l_1...l_f$. The solution to this is

$$C(t) = \exp\left(-i\hat{H}t\right) C(0). \tag{2.73}$$

Unfortunately, this is rather difficult to solve for systems with more than a handful of degrees of freedom due to the sheer number of coupled differential equations involved: the computational expense scales exponentially with f. It is therefore necessary in many cases to make use of non-exact methods, of which the Multi-Configuration Time-Dependent Hartree (MCTDH) is one of the most successful.

Time-dependent Hartree method

Before considering the MCTDH method, first consider its predecessor, the simpler time-dependent Hartree (TDH) method. In this, the wavefunction is written as

$$\Psi(Q_1,...,Q_f,t) = a(t) \prod_{\kappa=1}^{f} \varphi_\kappa(Q_\kappa,t) = a(t) \cdot \Phi(t) \tag{2.74}$$

where $\Phi(t) = \varphi_1 \ldots \varphi_f$, and the φ_κ are known as single particle functions (SPFs). The SPFs are time-dependent, which has a major advantage: if the functions are allowed to adapt during a wavepacket propagation then fewer are needed for an accurate description of the dynamics. Each SPF comprises a linear combination of time-independent functions known as the primitive basis. The form of the primitive basis functions is dependent upon the nature of the corresponding degree of freedom; they are usually represented by appropriate DVRs. Note that herein lies a disadvantage of the method: as each degree of freedom has its own set of functions the different modes are no longer coupled except in an average sense, i.e. each mode sees a 'mean field' of the others, rather as each electron moves in the mean field of all the others in HF theory.

The problem with the formulation in equation 2.74 is that the representation of the

wavefunction is not unique; the SPFs could be modified by a complex constant b and still represent the same wavefunction, e.g.

$$\varphi_1 \cdot \varphi_2 = \left(\frac{\varphi_1}{b}\right) \cdot (\varphi_2 \cdot b). \tag{2.75}$$

Note that $\varphi_1 \cdot \varphi_2$ is termed a Hartree product. To get around this problem, and therefore be able to derive unique equations of motion, constraints need to be introduced, namely

$$i\langle \varphi_\kappa(t) | \dot{\varphi}_\kappa(t) \rangle = g_\kappa(t). \tag{2.76}$$

g_κ is the constraint for degree of freedom κ and is arbitrary; its form can be chosen in order to generate equations of motion that are as simple as possible. If g_κ is real then the norm of the SPFs is maintained. Again, the equations of motion are derived from the Dirac-Frenkel variational principle, yielding

$$i\dot{a} = \left(E - \sum_\kappa^f g_\kappa \right) a \tag{2.77}$$

and

$$i\dot{\varphi}_\kappa = \left(\left\langle \prod_{v=1, v \neq \kappa}^f \varphi_v \middle| H \middle| \prod_{v=1, v \neq \kappa}^f \varphi_v \right\rangle - E + g_\kappa \right) \varphi_\kappa. \tag{2.78}$$

The TDH method is quite accurate if the potential V is 0, or if it doesn't vary much in the region occupied by the wavepacket. It works best for Hamiltonians which can be split into separable and non-separable terms, with the separable terms working on one degree of freedom only. It is much cheaper computationally than the standard method as a huge, f-dimensional partial differential equation has been reduced to f one-dimensional equations.

MCTDH method

The TDH method can be improved upon considerably by writing the wavefunction as a linear combination of Hartree products instead of just one. This gives the MCTDH

method, the underlying equation of which is:

$$\Psi(Q_1,...,Q_f,t) = \sum_{j_1=1}^{N_1} ... \sum_{j_f=1}^{N_f} A_{j_1...j_f}(t) \times \prod_{\kappa=1}^{f} \varphi_{j_\kappa}^{(\kappa)}(Q_\kappa,t)$$

$$= \sum_J A_J \Phi_J$$

(2.79)

where the $Q_1,...,Q_f$ are again the nuclear coordinates, the $A_{j_1...j_f}$ are the expansion coefficients and the $\varphi_{j_\kappa}^{(\kappa)}$ are again the SPFs for each degree of freedom κ. In the simplified notation, the A vector $A_J = A_{j_1...j_f}(t)$ and the product of SPFs is $\Phi_J = \prod_{\kappa=1}^{f} \varphi_{j_\kappa}^{(\kappa)}(Q_\kappa,t)$. When more than one PES is included in the calculation multiple, distinct sets of these SPFs can be used.

To find the equations of motion for the method, two constraints need to be imposed. The first is that the SPFs are orthonormal, i.e.

$$\langle \varphi_j^{(\kappa)}(0) | \varphi_l^{(\kappa)}(0) \rangle = \delta_{jl}.$$

(2.80)

The second is similar to equation 2.76, but now a constraint operator $\hat{g}^{(\kappa)}$ is used:

$$i\langle \varphi_l^{(\kappa)} | \dot{\varphi}_j^{(\kappa)} \rangle = \langle \varphi_l^{(\kappa)} | \hat{g}^{(\kappa)} | \varphi_j^{(\kappa)} \rangle$$

(2.81)

The operator works on degree of freedom κ, and is arbitrary as long as it is Hermitian. It is normally chosen to be 0 or $h^{(\kappa)}$, where the latter is the separable part of the Hamiltonian acting only on degree of freedom κ; from here on $\hat{g}^{(\kappa)} = 0$ is assumed.

There are several quantities which need to be considered. The first are termed 'single-hole functions', and are equal to the complete wavefunction but without the SPFs for the coordinate Q_κ:

$$\Psi_l^{(\kappa)} = \langle \varphi_l^{(\kappa)} | \Psi \rangle = \sum_J^\kappa A_{J_l^\kappa} \prod_{v \neq \kappa} \varphi_{j_v}^{(v)}.$$

(2.82)

Here, the index J_l^κ is equivalent to J but with the κth entry set at l; the index J^κ is also equivalent to J, but this time without the κth entry included. The sum in this case is over

all degrees of freedom except the κth. These single-hole functions can then be used to calculate further quantities. Namely, the 'mean field' can be defined as

$$\langle H \rangle_{kl}^{(\kappa)} = \langle \Psi_j^{(\kappa)} | H | \Psi_l^{(\kappa)} \rangle, \tag{2.83}$$

and the density matrices are given by

$$\rho_{jl}^{(\kappa)} = \langle \Psi_j^{(\kappa)} | \Psi_l^{(\kappa)} \rangle = \sum_{J^\kappa} A_{J_j^\kappa}^* A_{J_l^\kappa}. \tag{2.84}$$

Another important operator is the projector onto the space covered by the SPFs, which has the form

$$P^{(\kappa)} = \sum_{j=1}^{N_\kappa} | \varphi_j^{(\kappa)} \rangle \langle \varphi_j^{(\kappa)} |. \tag{2.85}$$

This projector ensures that the constraints stated above are adhered to.

Finally, the Hamiltonian is split up as far as possible into a set of terms which apply to a single degree of freedom only, and the left-over correlated terms are gathered together as H_R:

$$H = \sum_{\kappa=1}^{f} h^{(\kappa)} + H_R. \tag{2.86}$$

Note that for maximum efficiency all the terms should be separable. This is often not true for the potential part of the Hamiltonian, however methods have been developed to re-formulate PESs in product form [97, 98] and hence make them easily usable.

Using all these terms, the equations of motion are then found variationally to be

$$i\dot{A}_J = \sum_L \langle \Phi_J | H | \Phi_L \rangle A_L \tag{2.87}$$

and

$$\dot{\varphi}_j^{(\kappa)} = (1 - P^{(\kappa)}) \left[h^{(\kappa)} \varphi_j^{(\kappa)} + \sum_{k,l} (\boldsymbol{\rho}^{(\kappa)^{-1}})_{jk} \langle H_R \rangle_{kl}^{(\kappa)} \varphi_l^{(\kappa)} \right] \tag{2.88}$$

These are a set of non-linear coupled differential equations, which are complicated to solve and so integrators have been developed for this purpose. Examples for calculating the mean fields are the constant mean field (CMF) and variable mean field (VMF) integrators [93, 99]. To calculate the A vector and the SPFs other integration schemes such as Short-Iterative Lanczos and Bulirsch-Stoer are used [100, 101].

The MCTDH method has been used with considerable success on a variety of systems. For molecules with only a few degrees of freedom such as ClNO, the MCTDH results are very close to the exact results [102]. For larger systems, such as pyrazine [103], modes can often be combined. A range of processes have been studied, including photodissociation, reactive scattering, isomerisation and molecule-surface scattering amongst others [104]. For a full review of the MCTDH method, see reference [93]. Note that many alternative quantum dynamics methods exist, such as Coupled Coherent States [105, 106] which uses a trajectory guided grid of Gaussian wavepackets, and *ab initio* multiple spawning [107], which was designed to treat non-adiabatic dynamics, but these have not been used here.

Flux analysis

A standard method for obtaining elements of the scattering matrix, or S-matrix, following wavepacket propagations is to take the time-dependent wavefunction in the asymptotic region and then project it onto the eigenstates of the individual product species. To do this, the quantum flux in the asymptotic region needs to be recorded in some way. One method is to place a complex absorbing potential (CAP) [108, 109] onto the dissociative coordinate, R. This absorbs the wavepacket, allowing the flux to be analysed and also preventing it from 'bouncing' off the edges of the grid and interfering with itself in a non-physical fashion. Here, CAPs have been used with the form

$$-iW\left(R\right) = -i\eta\left(R - R_{cap}\right)^{b}h\left(R - R_{cap}\right) \tag{2.89}$$

where R_{cap} is the start point, η is the strength (values of $\sim$0.3 are common), b is the order (often $\sim$3) and $h(R - R_{cap})$ is a Heaviside step function. The start point, strength and order need to be optimised to ensure the CAP only absorbs parts of the wavepacket

which will no longer be influenced by the potential(s) and that none of the wavepacket is reflected instead of absorbed. The CAP can then be combined with the flux operator, $\hat{F}$, as outlined in reference [110].

Briefly, the amount of quantum flux in the asymptotic region varies as

$$\frac{d}{dt}\langle\Psi|h(R-R_{cap})|\Psi\rangle = i\langle\Psi|[H,h(R-R_{cap})]|\Psi\rangle \tag{2.90}$$

Including the CAP modifies the Hamiltonian to give

$$\tilde{H} = \hat{H} - iW. \tag{2.91}$$

Using these two equations implies the flux operator should have the form

$$\hat{F} = i[\tilde{H}, h(R-R_{cap})] = i[H, h(R-R_{cap})] + 2W. \tag{2.92}$$

If the total flux going into the CAP is all that is required, this can be calculated easily using

$$\int_0^T \langle\Psi(t)|\hat{F}|\Psi(t)\rangle dt = \langle\Psi(t)|h(R-R_{cap})|\Psi(t)\rangle dt + 2\int_0^T \langle\Psi(t)|W|\Psi(t)\rangle dt$$

$$= 2\int_0^T \langle\Psi(t)|W|\Psi(t)\rangle dt \tag{2.93}$$

The first term disappears as at the beginning of the propagation none of the wavepacket is in the asymptotic region and at the end it will all have been absorbed by the CAP.

Obtaining detailed product state distributions is more complicated and requires the use of projectors. To calculate the S-matrix from a ClNO photodissociation channel a into a NO product state b using the flux operator, the working equations are

$$|S_{NO_b,ClNO_a}(E)|^2 = \frac{2}{\pi|\Delta(E)|^2}Re\int_0^T g_{NO_b}(\tau)e^{iE\tau}d\tau \tag{2.94}$$

and

$$g_{NO_b}(\tau) = \int\limits_0^{T-\tau} \langle \Psi(t)|P_{NO_b}WP_{NO_b}|\Psi(t+\tau)\rangle dt \qquad (2.95)$$

where T is the final propagation time, ΔE is the energy spread of the initial wavepacket, and P_{NO_b} is the projector onto the b state of NO. The form of the projector will vary depending upon the state in question. It is also possible to apply multiple projectors, for example to find out the amount of NO produced in a particular rotational state *and* a particular vibrational state.

Absorption spectra

Absorption spectra are one of the most basic, yet most revealing pieces of data that can be obtained from both experiments and calculations. It is simple to calculate them from wavepacket propagations: due to the Fourier relationship between time and frequency, the spectrum is equal to the Fourier transform of the autocorrelation function [111, 112]. The autocorrelation function gives the overlap of the wavepacket at time t with that at time 0, i.e.

$$c(t) = \langle \Psi(0)|\Psi(t)\rangle. \qquad (2.96)$$

The total absorption spectrum is then:

$$\sigma(E) \propto \int e^{iEt}c(t)dt. \qquad (2.97)$$

2.2.2 Classical trajectories

In classical dynamics calculations, instead of propagating a wavepacket according to the time-dependent Schrödinger equation, individual trajectories are propagated across the PES(s) following the rules of classical, rather than quantum, mechanics. The starting position and momenta are chosen based on a representation of the probability density of an initial wavepacket on the ground state surface (often using the Wigner distribution

function), and the trajectory is then allowed to run. In other words, a classical trajectory is much like putting a ball on the PES, giving it an initial push and watching where it ends up. Because each trajectory only represents one set of starting conditions and one energy, in order to get a full picture of the dynamics many (1000s) trajectories need to be calculated and their results averaged. This is feasible because the calculations are, in most cases, several orders of magnitude faster than their quantum equivalents.

Classical trajectories are perhaps most useful for larger systems in which quantum dynamics are prohibitively computationally expensive. However, it is still instructive to look at classical results for smaller systems such as ClNO: the method can work very well in the case of rapid processes such as direct photodissociation and so can serve as a useful comparison. In addition, with the use of surface-hopping techniques, trajectories can move between different electronic states, and so some non-adiabatic processes can be investigated more simply than in quantum calculations, where the adiabatic states calculated using standard electronic structure methods would have to be diabatised.

To propagate the trajectories, Hamilton's equations of motion are used. These are:

$$\frac{d}{dt}Q_i = \frac{\partial H}{\partial P_i}$$
$$\frac{d}{dt}P_i = \frac{\partial H}{\partial Q_i}$$

(2.98)

where P is the momentum, Q is the position and H, the classical Hamilton function, is

$$H = \frac{P^2}{2\mu_R} + \frac{p^2}{2\mu_r} + \left(\frac{1}{2\mu_r r^2} + \frac{1}{2\mu_R R^2}\right) j^2 + V(R, r, \gamma).$$

(2.99)

This is in Jacobi coordinates for ClNO, with P and p as the momenta and μ_R and μ_r as the reduced masses in the R and r coordinates respectively. j is the classical angular momentum of the NO fragment, and is not quantised. Here it is assumed that the total angular momentum J is zero. The trajectory can then be described by a vector defined by the values of R, r, γ, P, p and j at each moment in time. To calculate how the trajectory

moves, Hamilton's equations are used as follows:

$$\frac{dR}{dt} = \frac{\partial H}{\partial P} = \frac{P}{\mu_R} \tag{2.100}$$

$$\frac{dr}{dt} = \frac{\partial H}{\partial p} = \frac{p}{\mu_r} \tag{2.101}$$

$$\frac{d\gamma}{dt} = \frac{\partial H}{\partial j} = 2\left(\frac{1}{2\mu_R R^2} + \frac{1}{2\mu_r r^2}\right) j \tag{2.102}$$

$$\frac{dP}{dt} = -\frac{\partial H}{\partial R} = \frac{j^2}{\mu_R R^3} - \frac{\partial V_I}{\partial R} \tag{2.103}$$

$$\frac{dp}{dt} = -\frac{\partial H}{\partial r} = \frac{j^2}{\mu_2 r^3} - \frac{\partial V_{NO}}{\partial r} - \frac{\partial V_I}{\partial r} \tag{2.104}$$

$$\frac{dj}{dt} = \frac{\partial H}{\partial \gamma} = -\frac{\partial V_I}{\partial \gamma} \tag{2.105}$$

V_I is the interaction potential, and is the difference between the potential of the whole system and that of the NO fragment for a given set of coordinates. This potential is key to the evolution of the trajectory: from it the forces acting upon the system, and hence its future movements, are derived. In this work, the PES is known and has been calculated using *ab initio* methods, and so the dynamics can be termed 'semi-classical'. For larger systems where this is not feasible it can be found using alternative methods such as direct dynamics, whereby the potential is calculated 'on the fly' at each point of the trajectory, or by placing quantum mechanics aside completely and using a force-field approximation.

At the end of the trajectory V_I will tend to a constant, namely the dissociation energy of the relevant state of the ClNO, and the trajectory can then be considered complete: the Cl has no further effect upon the NO and they can be treated independently. Once the trajectory is over, the partitioning of the energy can be worked out. The internal energy of the NO is

$$E_{int,NO} = E_{vib} + E_{rot} + V_{NO} = \frac{p^2}{2\mu_r} + \frac{j^2}{2\mu_r r^2} + V_{NO} \tag{2.106}$$

and the translational energy of the system is

$$E_{trans} = \frac{P^2}{2\mu_R}. \tag{2.107}$$

To find the rotational quantum state distribution of the NO the values of j can simply be sorted into integer bins, thus transforming them from continuous to discrete values. The vibrational quantum state can either be calculated directly from the value of E_{vib}, or can, more accurately, be found by comparing the internal energy of the NO to tabulated (experimental) energies.

Surface hopping

The major disadvantage of classical trajectories is that they cannot accurately model purely quantum phenomena, such as non-adiabatic transitions, tunnelling and interference. The trajectory surface-hopping (TSH) idea first introduced by Tully and Preston [113–115] attempts to remedy this first deficiency and allow the trajectories to transfer between electronic states in regions where the coupling is strong. The overall idea is this: the trajectory propagates classically on the adiabatic surfaces for the majority of the time, but at each point the probability of a transition between states is also calculated. When this probability is high, such as when the states become close in energy, a stochastic algorithm is used to decide whether the trajectory 'hops' instantaneously from one state to another. If enough such trajectories are run then the overall results should reflect those of a wavepacket which becomes split over multiple states.

There are several ways in which the transition probability can be calculated. In very basic methods the probability can be entirely linked to the energy difference between states; if the difference falls below a threshold value then the 'hop' will most likely take place. A better method to use is that of 'fewest-switches' [114], which, as its name suggests, seeks to minimise the number of hops taking place in each trajectory whilst retaining the correct state populations - it is easy to imagine how using a simpler prescription the trajectory could end up hopping back and forth with every single step, which would not be physically realistic. For a two state system the algorithm works as follows:

- Start with a trajectory in state X. Integrate the semi-classical time-dependent Schrödinger equation [114] using information from the PESs and nonadiabatic coupling terms. From the resulting density matrix, obtain the state populations a_X and a_A.

- Move on one time step, Δt, recalculate the state populations and hence yield $\frac{da_X}{dt}$ and $\frac{da_A}{dt}$.

- Produce a random number, κ, between 0 and 1.

- Calculate

$$p_{hop} = \frac{\Delta t \frac{da_A}{dt}}{a_X}. \tag{2.108}$$

  If $\kappa < p_{hop}$ then the trajectory will hop to state A; if not then it will remain on state X.

- Move to the next time-step and repeat, but change the state labels over in equation 2.108 if a hop has occurred.

It is also possible to use this algorithm in terms of electronic state amplitudes rather than the electronic density matrix [116].

Once a hop has occurred it is likely that the energy of the system will have changed as the potentials for each state will not be the same. In order for energy to be conserved, some other adjustment must therefore be made. The energy needs to be distributed amongst the momenta in each coordinate; it could be distributed evenly, in the direction of the non-adiabatic coupling vector or in some other way. If this is not possible, e.g. if the hop is to a higher-energy state and there is insufficient momentum that can be removed from one or more coordinates to compensate for the gain in energy, then the hop fails and is said to be frustrated.

The coupling required for TSH can be obtained by calculating non-adiabatic kinetic coupling matrix elements (NACMEs, as described earlier) for each coordinate using an *ab initio* method. For a triatomic considered in Jacobi coordinates the overall coupling between the ground (adiabatic) state *X* and an excited (adiabatic) state *A* can then be taken

as:

$$\chi = \frac{dR}{dt}\langle\Psi_X|\frac{\partial}{\partial R}|\Psi_A\rangle + \frac{dr}{dt}\langle\Psi_X|\frac{\partial}{\partial r}|\Psi_A\rangle + \frac{d\gamma}{dt}\langle\Psi_X|\frac{\partial}{\partial\gamma}|\Psi_A\rangle \tag{2.109}$$

Disadvantages of the TSH method include the fact that the trajectories are all independent, and therefore cannot interact with each other in the way that different portions of a quantum wavepacket could. This means that coherence effects cannot be accurately modelled, and so it is not suitable for investigating coherent control. Also, the best way to conserve energy after hops occur can be ambiguous.

Beta parameters

The anisotropy parameter, β, can provide information about the photodissociation mechanism. It is easily extracted from velocity map images [9] and so is a valuable quantity to derive from dynamics calculations as it can be compared with experiment. β is defined as

$$\beta = 2P_2(cos(\theta_m)) \tag{2.110}$$

where $P_2(x)$ is a Legendre polynomial and θ_m is the angle between the direction of the transition dipole moment (TDM) between the ground and excited states at the starting point of the trajectory and the velocity vector of the Cl atom at the end of the trajectory, relative to the initial R vector [117, 118]. This angle is shown in figure 2.5. The value of β can therefore be calculated for each trajectory, then averaged for the entire set to give an overall value. Alternatively, β can be averaged for different final product states, and so may illuminate differences in the dynamics leading to each of these.

A β of 2 implies that the velocities are parallel to the polarisation direction, whereas a β of -1 implies the velocities are perpendicular. Intermediate values indicate a process somewhere in between. There are also higher-order anisotropy parameters yielding further dynamical information for multi-photon processes which can be extracted from experimental results but which have not been calculated here.
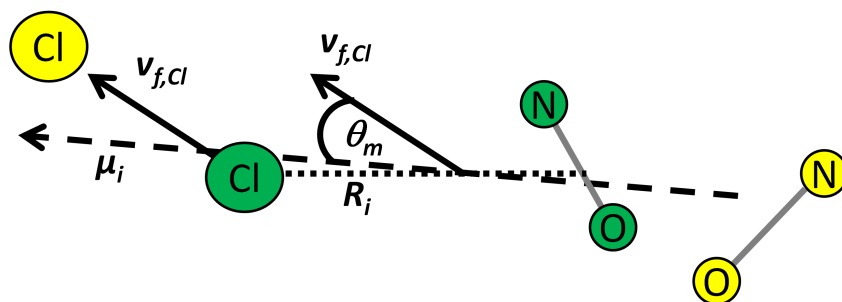
Figure 2.5: An illustration of the angle θ_m used to calculate β. $v_{f,Cl}$ is the velocity vector of the Cl atom at the end of the trajectory, μ_i is the initial TDM and R_i gives the initial R vector. The atoms shaded green are the positions at the beginning of the trajectory and the atoms shaded yellow represent their positions at the end of the (hypothetical) trajectory. [117, 118]

Chapter 3

Photodissociation on the 2 ^{1}A$'$ state of ClNO

3.1 Summary

The initial aim of the investigation into the photodissociation of ClNO via the 2 ^{1}A$'$ state was to provide theoretical support for velocity map imaging investigations undertaken by the Whitaker group. Using the 3D-REMPI technique [9, 119] the NO product vibrational and rotational state distributions were collected across a range of energies. By calculating these product state distributions using computational methods, more information about the dynamics can be determined. To this end, new PESs have been constructed for the ground (1 ^{1}A$'$) and 2 ^{1}A$'$ states of ClNO, and quantum wavepacket dynamics have been run on these to yield the absorption spectrum, autocorrelation and NO product state distributions. In order to more accurately model the excitation process from the ground to excited state, the transition dipole moment 'surface' between them has been calculated and included in the dynamics; this has not been done before for this system. Some of this work has been published in reference [120].

In the course of the investigation an accidental conical intersection was discovered between the two states, and so this has also been modelled. The NACMEs between the states have been calculated and incorporated into classical trajectory calculations including surface-hopping. The effect of this CoIn has been shown to be small, but not negligi-

ble, as the NO rotational distribution of trajectories ending on the ground state is shifted compared to that for trajectories remaining on the excited state surface. In addition, the variation of the β parameter for the photodissociation with NO rotational state has been calculated, and has been found to be close to 2, as expected for a direct, parallel process.

3.2 Potential energy surfaces

To calculate PESs, electronic structure calculations were performed. All of the results described below were obtained using the Molpro suite of programs [88].

3.2.1 Choosing a method

In order to calculate PESs, a suitable method needs to be decided upon. Both accuracy and computational time are important considerations. As ClNO is a relatively small molecule it is possible to use electronic structure methods which return electron correlation energy reliably. As a first step, MCSCF calculations were used. In order to provide the best possible results, a complete active space, rather than one with restricted occupancies, was chosen. In larger systems choosing an active space can be a difficult problem, but for ClNO it was feasible to use a full-valence active space, i.e. all the molecular orbitals derived from the N 2s and 2p, O 2s and 2p, and Cl 3s and 3p atomic orbitals were included. Such active spaces tend to be well-balanced, 'safe' choices. A few test calculations were run with larger active spaces including additional orbitals, but these took much longer and gave erroneous results.

Table 3.1 lists the lowest-energy orbitals for ClNO in its ground state. The ordering and identities come from a calculation at the CASSCF level using the small STO-3G basis set to allow for easier identification. Note that the orbital character and ordering changes very little if larger basis sets are used. In the full-valence active space, the 7 lowest energy orbitals corresponding to all the 1s orbitals and the Cl 2s and 2p were kept 'closed', i.e. still optimised but always doubly-occupied. The next 12 orbitals were included in the active space, incorporating 9 'occupied' and 3 'virtual' orbitals. The CASSCF space is therefore defined as (18,12), meaning 18 electrons are distributed throughout 12 orbitals.

Orbital label	Symmetry	Dominant contribution(s)
1.1	A'	Cl 1s
2.1	A'	O 1s
3.1	A'	N 1s
4.1	A'	Cl 2s
5.1	A'	Cl $2p_z$
1.2	A''	Cl $2p_x$
6.1	A'	Cl $2p_y$
9.1	A'	O 2s
7.1	A'	Cl 3s
10.1	A'	N-O 2s σ^*
11.1	A'	N-O $2p_{y,z}$ π^*
12.1	A'	N-O $2p_{y,z}$ π
3.2	A''	N-O $2p_x$ π
8.1	A'	Cl $3p_y$
2.2	A''	N-O $2p_x$ π
13.1	A'	Cl-N-O $p_{y,z}$ π^*
4.2	A''	N-O $2p_x$: π^*
14.1	A'	N-O $2p_{y,z}$ π^*, Cl-N $p_{y,z}$ π
15.1	A'	N-O 2s σ^*, NO $2p_{y,z}$ π

Table 3.1: The lowest orbitals of ClNO in its ground state listed in order of occupation, calculated at the CASSCF/STO-3G level. The orbital labels are the identifiers given by Molpro, with the '.1' referring to A' symmetry and the '.2' referring to A'' symmetry. The dominant contributions have been found from inspection of the coefficients for each basis function in the set. Orbitals set to be doubly occupied are shaded grey, those in the active space with occupation values close to 2 are shaded orange and those in the active space with occupation values close to 0 are shaded green.
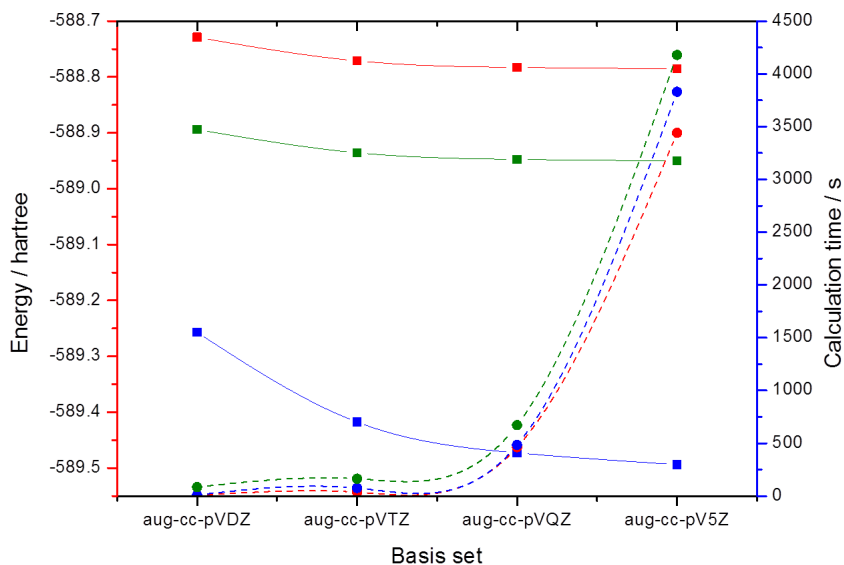
Figure 3.1: An illustration of how the calculation time increases rapidly with increasing basis set size. The corresponding energy gains are ever-decreasing. The squares show the energies and the circles show the calculation times. The methods are: red - HF; blue - MP2, green - CASSCF.

The basis set also needs to be selected. The Dunning correlation-consistent basis sets [87, 90] are commonly used when studying this type of system, and so were also chosen for this work. In many cases researchers make small changes to the standard basis sets but this was considered unnecessary and unlikely to have much impact upon the results. As a photodissociation process is being studied, the basis sets used must include diffuse functions. These diffuse functions spread over a wide volume and so are needed to model geometries with long r_{ClN} distances. The two main basis sets used have therefore been:

- Augmented Dunning correlation consistent triple zeta, aug-cc-pVTZ (also abbreviated here to AVTZ)

- Augmented Dunning correlation consistent quadruple zeta, aug-cc-pVQZ (also abbreviated here to AVQZ)

Quintuple-zeta basis sets were found to be excessively expensive. An illustration of how the calculation time increases with the size of the basis set is given in figure 3.1.

Method	Basis set	rClN / bohr	rNO / bohr	ClNO angle / ^{o}	Energy / hartree
HF	AVTZ	3.63	2.07	113.02	-588.7743394
HF	AVQZ	3.63	2.08	113.06	-588.7863873
CASSCF	AVTZ	3.88	2.14	113.17	-588.9366948
CASSCF	AVQZ	3.87	2.14	113.18	-588.9485558
MRCI	AVTZ	3.75	2.16	113.42	-589.3955137
MRCI	AVQZ	3.74	2.15	113.39	-589.4414372
Experiment [55]	-	3.72	2.14	113.4	-

Table 3.2: Optimised geometries and energies for the ground state of ClNO at various levels of theory. Note that in the MRCI results no state-averaging was used in the preceding CASSCF step.

Geometry optimisations

As a test of the quality of potential methods, geometry optimisations for the ground state were run using Molpro [88, 121, 122]. Both the AVTZ and AVQZ basis sets were used, with methods ranging from simple HF to single-state CASSCF and MRCI. The results are given in table 3.2. Unsurprisingly, the MRCI/AVQZ results are closest to the experimental geometry, but even the HF results are reasonably accurate.

State-averaged CASSCF

To obtain excited states state-averaging can be used, whereby several states are calculated at the same time [123]. The CI vectors for each state are found, and from these averaged density matrices and hence orbitals are obtained. It is possible to adjust the weighting of each state in the averaging process, however interpreting the results can then become more difficult and so all states here have been given equal weighting throughout. The orbitals produced in the calculation are optimised for the whole set of states, i.e. each state is described using the same orbitals, but with different occupations. To obtain the best possible ground state surface, state-averaging should not be used. However, to calculate energies for excited states state-averaging is essential, often to avoid 'root flipping' near a degeneracy. The choice of states included in the averaging has a significant effect upon the nature of the final orbitals. Problems can arise if states which affect the state of interest are not included, or if states of a very different character are included. For example,
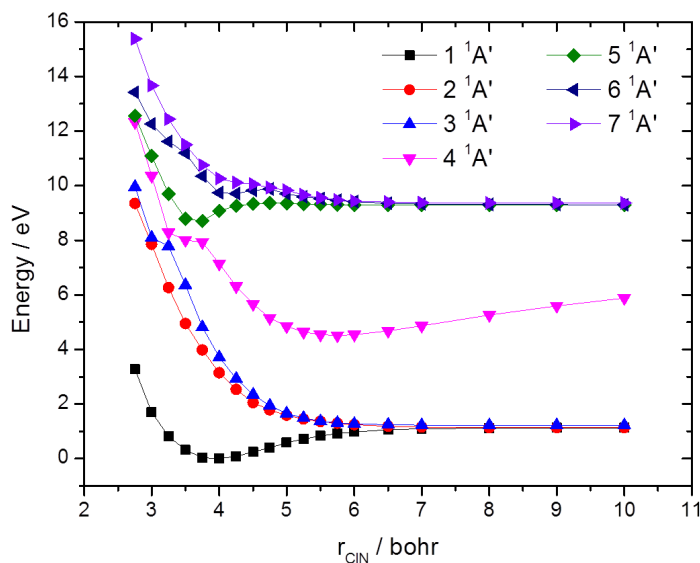
Figure 3.2: Cuts through the PESs for the first 7 states of $^1A'$ symmetry for a fixed bond angle of $113°$ and a r_{NO} bond length of 2.14 bohr, calculated at the CAS/AVQZ level.

figure 3.2 shows the first 7 states of $^1A'$ symmetry for ClNO, which all have excitation energies below about 12 eV. The fourth state is very different to the others, having ion-pair character, and so its inclusion risks distorting the second state which is more simply dissociative. The highest 3 states converge on a different asymptote, corresponding to Cl with NO in its first excited electronic state. Therefore, the best option is to state-average over the first 3 states in order to obtain good results for the first 2. Figure 3.3 shows cuts through the first 3 surfaces for the AVTZ basis set when 3 and 7 states are included in the averaging. The energies are lower, and the surfaces are slightly smoother when just 3 states are included.

MRCI

Although CASSCF results are often qualitatively correct, in order to obtain reliable energies MRCI is needed. MRCI calculations do however use CASSCF wavefunctions as their basis, and so are very dependent upon the quality of this first step. Disadvantages of the MRCI method are that it is not variational, size-extensive or size-consistent. These issues arise because it is a truncated method: only single and double excitations out of the reference Slater determinants are allowed. This can be improved on using a David-
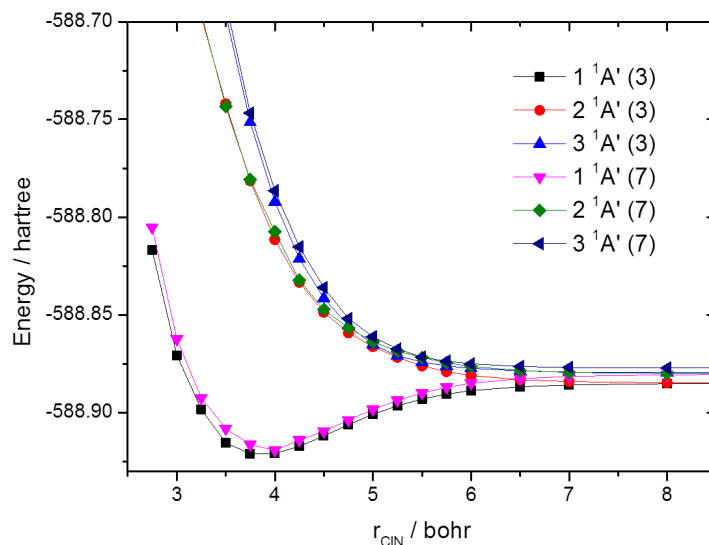
Figure 3.3: Cuts through the PESs for the first 3 states of $^1A'$ symmetry for a fixed bond angle of $110°$ and a r_{NO} bond length of 2.2 bohr, calculated at the CAS/AVTZ level. The results when 3 states have been included in the averaging have been labelled (3), those where 7 states have been included are labelled (7).

son correction, which estimates the contribution of quadruple excitations to the overall energy [124]. MRCI is a computationally expensive method, but is nonetheless feasible for a small system such as ClNO. As the most accurate readily usable method, it has been chosen for calculating surfaces here.

Problems with MRCI calculations at long r_{ClN} bond lengths

In the region of long r_{ClN} bond lengths, from about $r_{ClN} = 6.0$ bohr outwards, the MRCI energy was found to jump hugely and unrealistically. An example of this is shown in figure 3.4 for a cut through the first 3 states of $^1A'$ symmetry. It was initially thought this could be due to root flipping, but this turned out not to be the case. Similar problems had been found by others for FNO [125], but were not solved. Eventually the cause was found in the underlying CASSCF calculation: at long r_{ClN} bond distances the N 1s orbital is rotated into the active space, replacing the 7th orbital of A' symmetry. The underlying reason for the problem is likely due to the fact that the 7th A' orbital always has an occupation extremely close to 2 at long r_{ClN} distances, and hence it can be swapped for a different orbital also with an occupation of 2 with little effect on the CAS calculation.
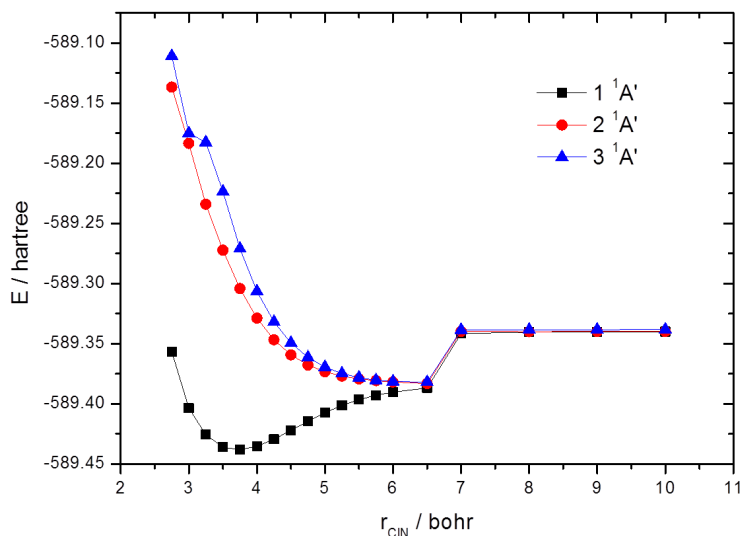
Figure 3.4: A cut through the MRCI/AVQZ surfaces for the 1, 2 and 3 $^1A'$ states of ClNO for a fixed angle of 110° and fixed r_{NO} bond distance of 2.2 bohr. At $r_{ClN} = 6.5$ bohr the energy jumps to a much higher level, which is not realistic behaviour.

Indeed, this change in active space makes virtually no difference to the energy of any of the CAS states, which remain smooth.

To solve the problem, several approaches were attempted. It was not possible to force Molpro's selection of the active space orbitals: whatever orbitals were initially selected, the N 1s was always rotated back in. Instead, the most successful approaches were either to freeze the core orbitals in the CAS step, i.e. not optimising them beyond the HF level, or to restrict the active space. In this latter solution the 7th orbital of A' symmetry was forced to always have an occupation of 2, in effect taking it out of the active space. With this restriction in place the orbitals in the active space retained the correct identity. These two solutions lead to very similar energies, and so either could have been used. The RAS approach was implemented when re-calculating the affected parts of the surfaces as it was felt that as the 7th A' orbital always had an occupation extremely close to 2 this was a less drastic approximation.

Vertical excitation

Table 3.3 shows the change in orbital occupation following excitation from the 1 to 2 $^1A'$ state. The orbitals are simply numbered from 1 to 19 and listed in order of occupation. The primary excitation is from a Cl $3p_x$ to an NO $(2p_x)$ π^* orbital. These orbitals,

Orbital number	Character	Occupation		
		$1\,^1A'$	$2\,^1A'$	Difference
1	Cl 1s	2	2	0
2	O 1s	2	2	0
3	N 1s	2	2	0
4	Cl 2s	2	2	0
5	Cl $2p_z$	2	2	0
6	Cl $2p_x$	2	2	0
7	Cl $2p_y$	2	2	0
8	O 2s	2	2	0
9	Cl 3s	2	2	0
10	N-O 2s σ^*	1.99	1.99	0
11	N-O $2p_{y,z}$ π^*	1.98	1.98	0
12	N-O $2p_{y,z}$ π	1.97	1.97	0
13	N-O $2p_x$ π	1.92	1.95	0.03
14	Cl $3p_{y,z}$	2.00	2.00	0.00
15	Cl $3p_x$	1.98	1.90	-0.08
16	Cl-N-O $2p_{y,z}$ π^*	1.86	1.08	-0.78
17	N-O $2p_x$ π^*	0.11	0.96	0.85
18	N-O $2p_{y,z}$ π^*, Cl-N $p_{y,z}$ π	0.17	0.16	-0.01
19	N-O 2s σ^*, NO $2p_{y,z}$ π	0.03	0.03	0.00

Table 3.3: The occupation number of each orbital in the 1 and 2 $^1A'$ states. The values are from a calculation at the experimental minimum energy geometry at the CASSCF/STO-3G level, state-averaged equally over the first 3 states of $^1A'$ symmetry. The orbitals which change occupation significantly are highlighted in green.

visualised using Molden [126] following a calculation at the FC geometry using state-averaged CAS/AVTZ, are shown in figure 3.5.

The excitation energies for various methods were calculated and compared with the experimental value, as shown in table 3.4. The CASSCF energies are all too high, but the MRCI values are closer to the experimental values. The Davidson-corrected values for the AVQZ basis set are just 0.016 eV lower than the experimental value. In addition, the 1 $^1A'$ dissociation energy for this method, obtained by taking the difference between the energies at the 1 $^1A'$ minimum and out in the asymptotic region (using the same r_{NO} and angular values but with $r_{ClN} = 20.0$ bohr), is 1.619 eV. This agrees very well with the experiment-based value of 1.615 eV [73, 127]. The excitation energy for MRCI with the AVTZ basis set is also close to the experimental value, but the dissociation energy for this method is too low, being 1.435 eV.
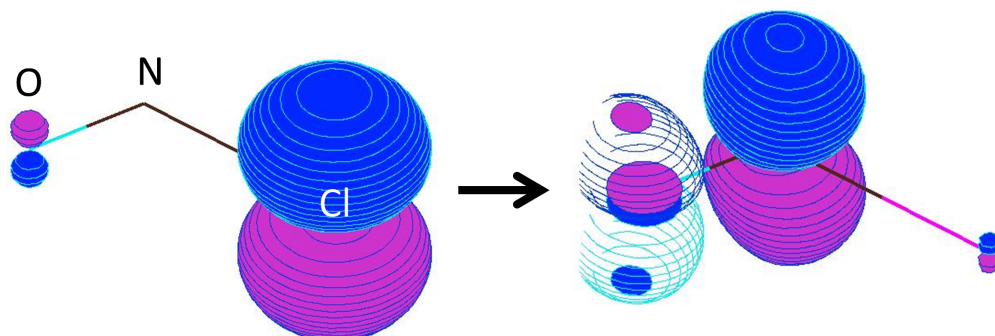
Figure 3.5: A visualisation of the orbitals involved in the excitation from the 1 to 2 ^{1}A$'$ state, pictured using Molden [126] following a single-point calculation at the CASSCF/AVTZ level. The predominant excitation is from a Cl $3p_x$ orbital into an NO ($2p_x$) π^* orbital.

Method	Basis set	Excitation energy / eV
CAS	AVTZ	3.888
CAS	AVQZ	3.888
MRCI	AVTZ	3.702 3.651 (Davidson)
MRCI	AVQZ	3.768 3.704 (Davidson)
Experiment	-	3.72 [69]

Table 3.4: The vertical excitation energies between the 1 and 2 ^{1}A$'$ states at the optimised FC geometry for each method.

3.2.2 Calculated surfaces

PESs for the 1 and 2 ^{1}A$'$ states were constructed using state-averaged CASSCF [128, 129] followed by 2 state MRCI [130–132] with the AVQZ basis set. The Davidson correction using relaxed reference functions was used. 2464 *ab initio* points were calculated across the following binding coordinates:

- r_{NO}: every 0.2 bohr from 1.95 to 2.95

- r_{ClN}: every 0.25 bohr from 2.75 to 6.0, then every 0.5 bohr to 10.0

- **bond angle** θ: every 10° from 20° to 170°.

To improve the quality of the initial wavepackets created, the PES for the ^{1}A$'$ state was calculated in a denser grid in the FC region:

- r_{NO}: every 0.1 bohr from 1.75 to 2.95

- r_{ClN}: every 0.125 bohr from 2.75 to 5.0

- **bond angle** θ: every 5° from 90° to 130°.

Fitting functions such as many-body expansions [133–135] and Aguado and Paniagua functions [136] were investigated. However, the quality of the *ab initio* points was sufficiently good that the surfaces could be smoothly fitted using 3D cubic splines.

1 ^{1}A$'$ surface

A cut through the 1 ^{1}A$'$ PES at a bond angle θ of 110° (close to the equilibrium value of 113.4°) is given in figure 3.6. Note that the well is not uniform, but instead extends slightly into the r_{NO} coordinate at lower r_{ClN} distances. In figure 3.7 another cut is given for a r_{NO} bond length of 2.15 bohr. The key features here are the two wells, with the first at the FC geometry and the other further out centred at around $r_{ClN} = 5.7$ bohr, $r_{NO} = 2.1$ bohr and $\theta = 40°$, which corresponds to the ClON isomer [127]. This second well arises from an interaction with the 2 ^{1}A$'$ state, occurring at around $\theta = 70°$ throughout the surface. The states are extremely close in energy at this angle from about $r_{ClN} = 5.75$ bohr outwards for a r_{NO} bond length of 2.15 bohr. A one-dimensional cut at $r_{NO} = 2.15$ bohr and $r_{ClN} = 6$ bohr is given in figure 3.8 to illustrate this. It is rather unusual to find conical
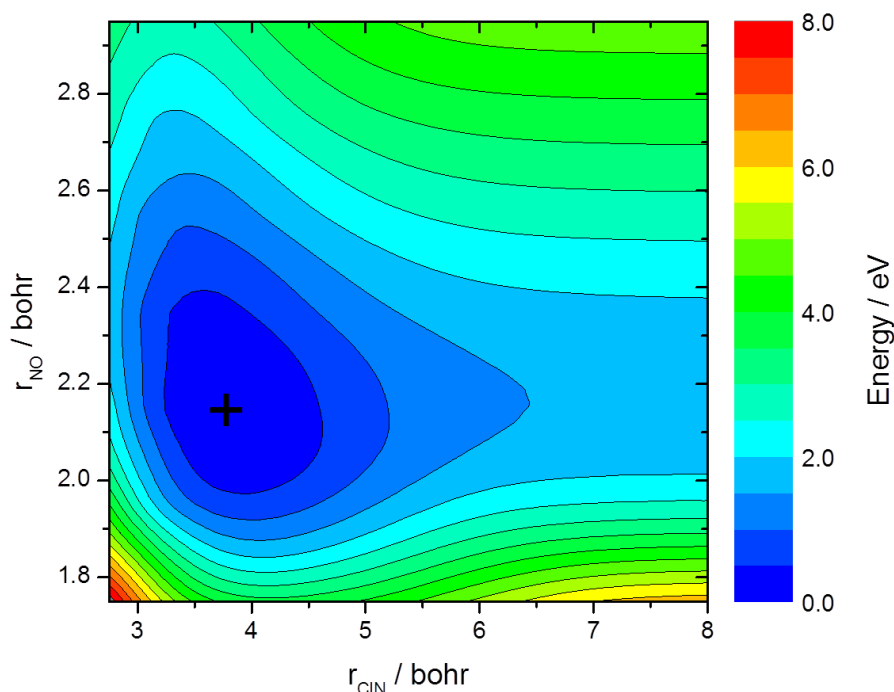
Figure 3.6: A cut through the 1 ^{1}A$'$ PES for a fixed bond angle θ of 110°. The cross marks the FC point.

intersection seams in asymptotic regions, and so this has been investigated further, as described later in sections 3.4.2 and 2.2.2.

2 ^{1}A$'$ surface

Cuts through the 2 ^{1}A$'$ surface are given in figures 3.9 to 3.11. Figure 3.9 gives a cut at $\theta = 110°$ which shows the considerable steepness of the slope from the FC to asymptotic regions. The cut in figure 3.10 at $r_{NO} = 2.15$ bohr shows clearly the kink at an angle of around $\theta = 70°$ due to the intersection with the 1 ^{1}A$'$ state. In figure 3.11, the equivalent cut plotted in Jacobi coordinates shows how the slope of the surface at the FC geometry points steeply towards smaller γ.

The features of both PESs agree well with previous calculations performed by Yamashita and Kato [68, 137], and as shown earlier in section 3.2.1, the associated energies for the vertical excitation and dissociation are very close to the experimental values. Therefore, the PESs can be viewed as an accurate representation and used in dynamics calculations with confidence.
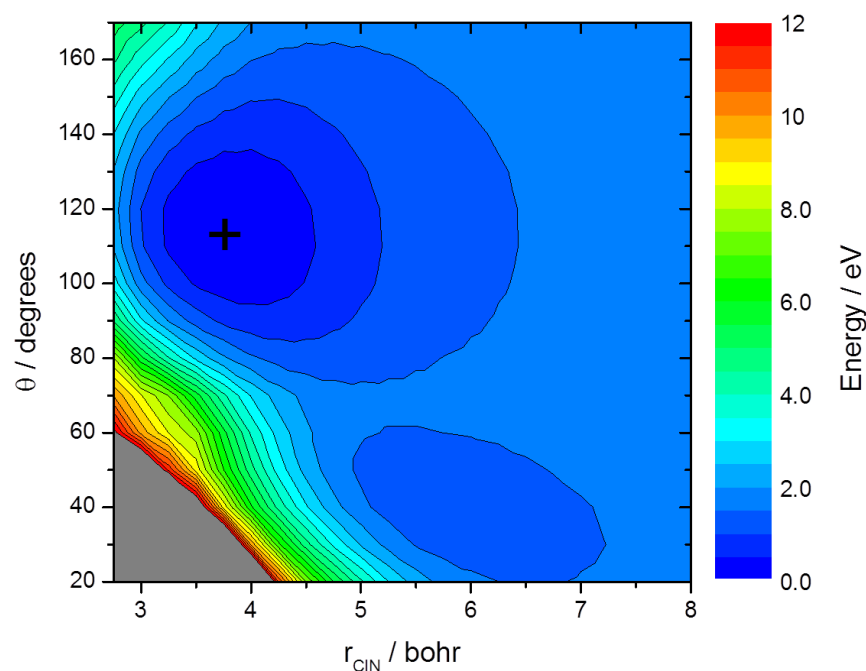
Figure 3.7: A cut through the 1 $^1A'$ PES for a fixed r_{NO} bond distance of 2.15 bohr. The cross marks the FC point. Note the second minimum, corresponding to the ClON isomer.
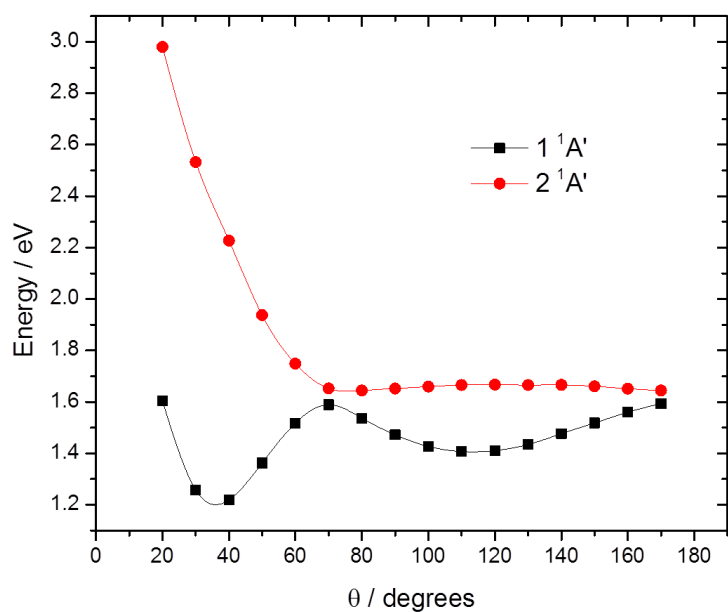
Figure 3.8: Cuts through the 1 and 2 $^1A'$ surfaces close to the asymptotic region at a constant r_{NO} bond length of 2.15 bohr and a constant r_{ClN} bond length of 6 bohr. Note the interaction between the two states at around $\theta = 70°$.
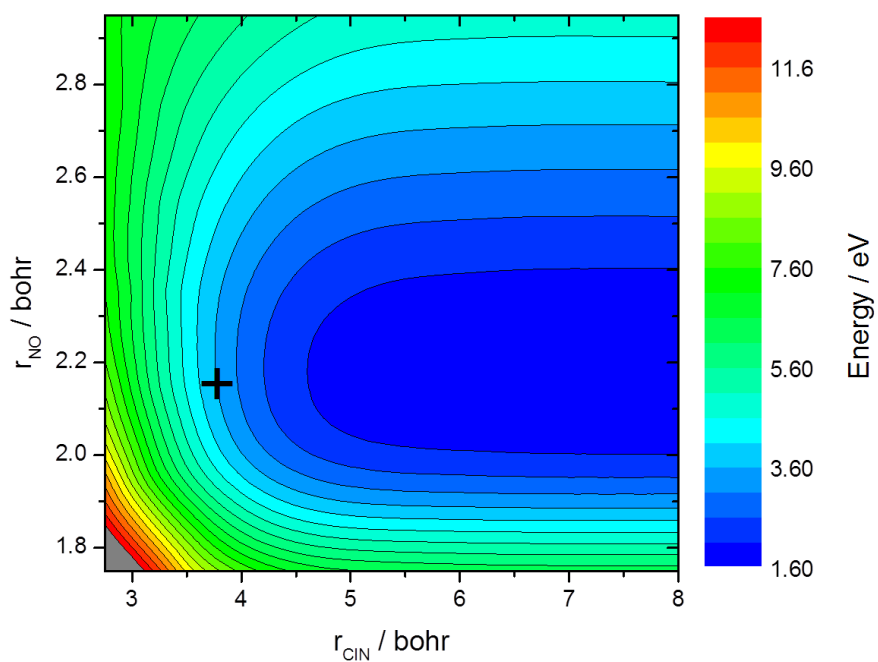
Figure 3.9: A cut through the $2\,^1A'$ PES for a fixed bond angle θ of $110°$. The cross marks the FC point.
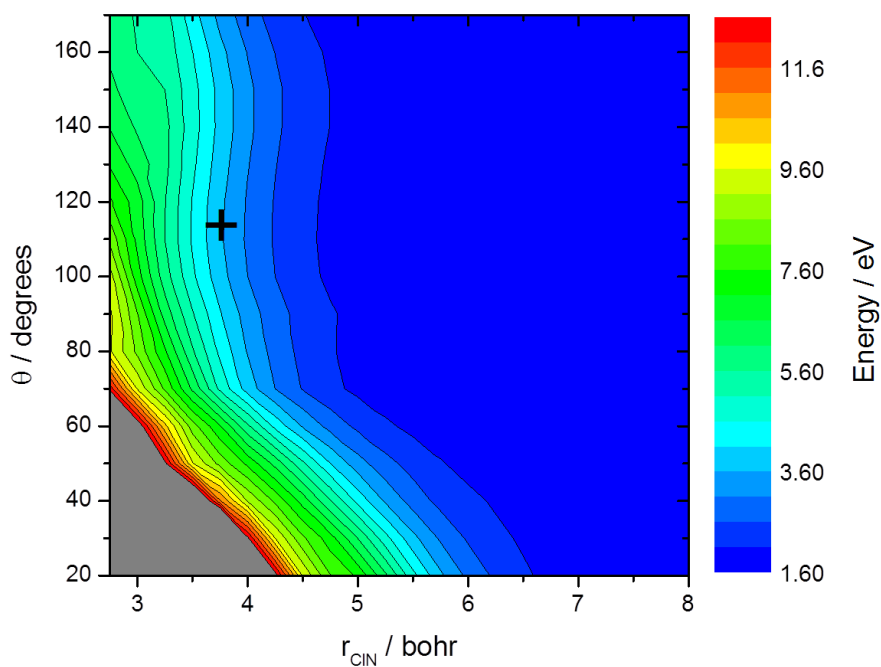
Figure 3.10: A cut through the $1\,^1A'$ PES for a fixed r_{NO} bond distance of 2.15 bohr. The cross marks the FC point.
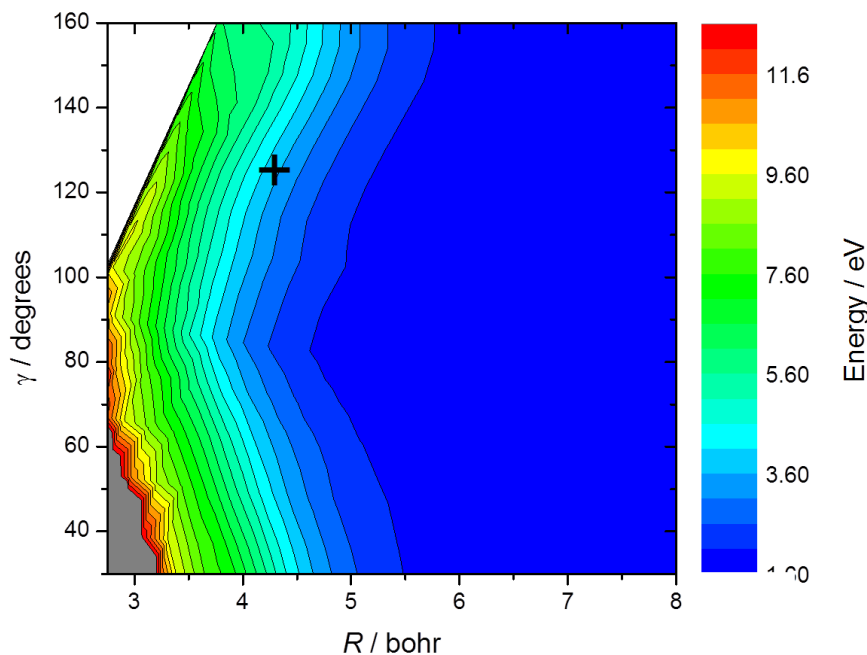
Figure 3.11: A cut through the 1 ^{1}A$'$ PES for a fixed r_{NO} bond distance of 2.15 bohr, in Jacobi coordinates. The cross marks the FC point. The PES slopes steeply downhill towards smaller values of γ.

3.3 Transition dipole moments

3.3.1 Choosing a method

Transition dipole moments (TDMs) for the transition between the 1 and 2 ^{1}A$'$ states were calculated and found to vary significantly depending on the method used. The TDMs as calculated using Molpro comprise two perpendicular in-plane components (here labelled y and z) aligned along the eigenvectors of the inertia tensor matrix. This gives a body-fixed view, which then needs to be transformed for use in dynamics calculations. For the wavepacket dynamics, instead of considering the two in-plane components separately they have been treated together by calculating their resultant, as the bulk of these resultants lie along the Jacobi R coordinate. This is expected as the excitation from the 1 ^{1}A$'$ to the 2 ^{1}A$'$ states involves promotion of an electron from a Cl $3p$ orbital to an NO π^* orbital. Note that the x component of the TDM, which points out of the plane of the molecule, is always 0 on symmetry grounds.

Calculated TDMs are rarely reliable outside of the FC region. Here, they have been

found to vary smoothly across a limited region of the PES, from approximately $r_{ClN} = 3.5$ to 5.0 bohr and from $\theta = 90°$ to 130°. Outside this region the values are much less smooth, but as transitions are not likely to occur at such geometries they can be disregarded.

Recent work on OCS [117] found that the level of theory used, and importantly the number of states averaged over in the CAS step, had a large effect on the calculated TDMs, much more so than on the energy. In order to see if this was the case for ClNO, cuts through the TDM 'surfaces' were calculated for a range of methods. Figure 3.12 shows the y and z components of the TDMs for CAS calculations in which the states included in the averaging were varied. For comparison, the MRCI results obtained from the same calculations as the PESs (i.e. based on a CAS wavefunction averaged over the first 3 states of $^1A'$ symmetry) are also shown. The combinations of states averaged over were:

- 1-2 $^1A'$
- 1-3 $^1A'$
- 1-4 $^1A'$
- 1-5 $^1A'$
- 1-6 $^1A'$
- 1-2 $^1A'$, 1 $^1A''$
- 1-2 $^1A'$, 1-2 $^1A''$
- 1-3 $^1A'$, 1-3 $^1A''$
- 1-4 $^1A'$, 1-3 $^1A''$

All states were given equal weighting, and the AVQZ basis set was used throughout.

The shapes of the curves in figure 3.12 are reasonably consistent, but the absolute values of the TDMs vary considerably depending on the combination of states included in the averaging. For the larger z component, the biggest difference comes from the inclusion of the 3 $^1A'$ state, without which the values are shifted significantly lower. Including the 4 $^1A'$ ion-pair state shifts the values higher initially, but this effect disappears when additional states are added. The MRCI values are similar to the central group of curves. For the smaller y component the ordering is similar, but the clustering is less pronounced. It might be expected that including the 4 $^1A'$ state in the state-averaging would be important: this is the ion-pair state which has a huge oscillator strength with the ground state,
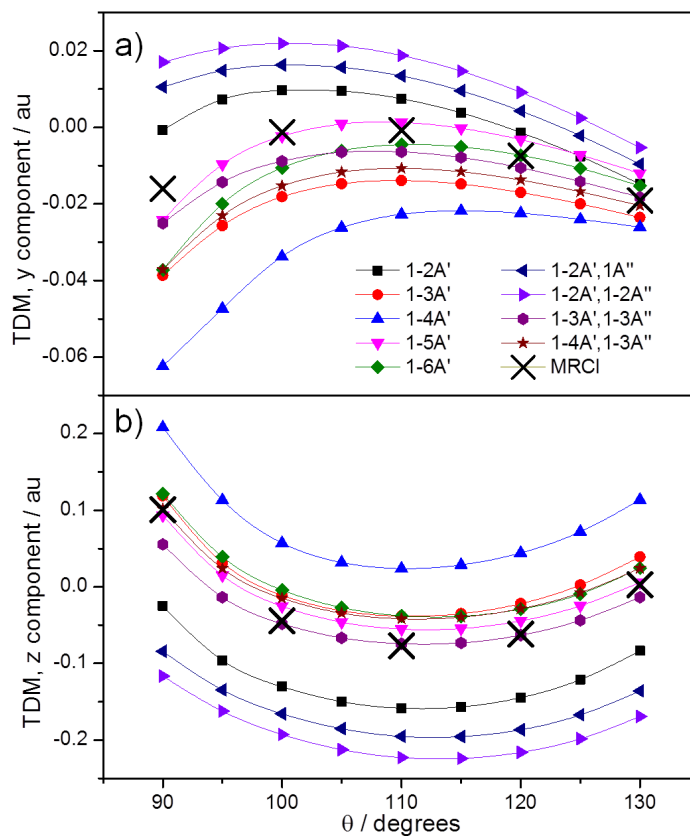
Figure 3.12: TDM values for the transition between the 1 and 2 $^1A'$ states of ClNO, for a cut at r_{ClN} = 3.75 bohr and r_{NO} = 2.15 bohr. The y components of the TDMs are given in panel a), and the z components are given in panel b). The results are from CAS calculations, state-averaged over various combinations of singlet states as shown in the legend. The results from MRCI calculations based on a CAS wavefunction averaged over the first 3 $^1A'$ states are also shown.

and so other states may borrow intensity from it. However, as discussed earlier, its inclusion may lead to a rather unbalanced set of orbitals as it is so different in character to the lower energy states.

The calculations shown in figure 3.12 were repeated at the MRCI level. The same patterns were seen as for the CAS method, and so the results are not shown here. Given the variation in these results, other methods were attempted. It was postulated that calculating the $1\,^1A'$ state wavefunction in a separate CAS step, i.e. without using state-averaging, would improve its description and therefore could lead to more reliable TDMs. As shown in figure 3.13, the results are rather different to those obtained when just one step-averaged CAS step is used. It is unclear which set of results is more valid.

As it was not obvious which method gave rise to the most reliable TDM values, the MRCI values based on a CAS wavefunction averaged over the first $3\,^1A'$ states were chosen for use in the dynamics calculations. These values lie fairly centrally between those for the other methods, and are at the same level of theory as the PESs. They also compare reasonably well with previous calculations at the FC geometry [68], with the component of the TDM aligned in the same direction as the Jacobi R coordinate being 0.076 atomic units (au), and the component in the perpendicular coordinate being -0.0071 au.

3.3.2 MRCI TDMs

The MRCI/AVQZ TDMs were calculated across the FC region in the same range as the denser $1\,^1A'$ PES. The TDMs at each geometry were combined to create a surface, which was then converted to Jacobi coordinates and used in the dynamics calculations. Figure 3.14 shows cuts through the TDM surfaces close to the FC geometry, for both the y and z components and for the resultants. From this it can be seen that the z components dominate the y, as the z coordinate is more closely aligned to the Jacobi R coordinate. The TDM has the largest magnitude close to the FC r_{ClN} bond length of 3.75 bohr, and the FC angle θ of 113°. However, the magnitude of the TDM peaks at an r_{NO} bond length of around 2.7 bohr, which is a significant distance away from its FC value.
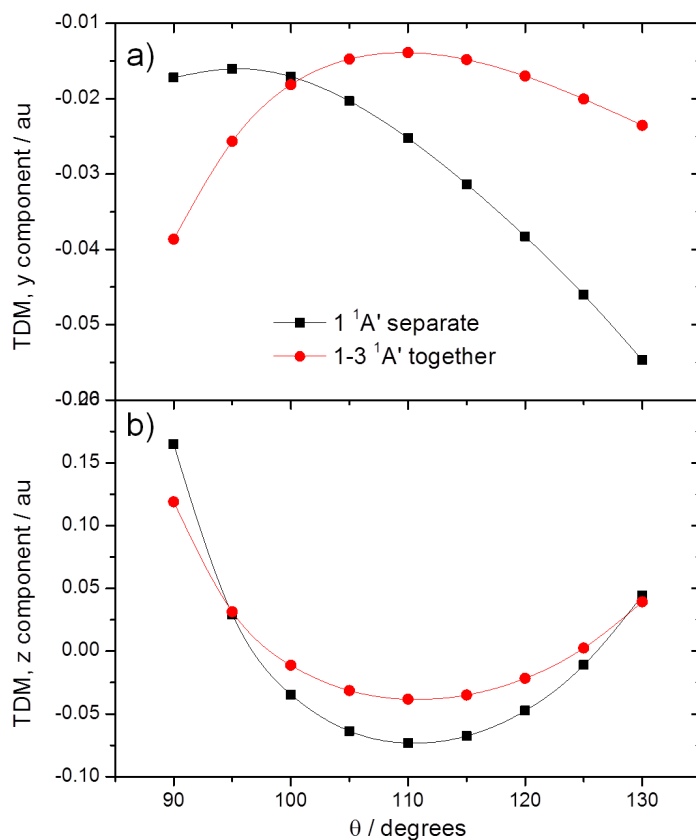
Figure 3.13: TDM values for the transition between the 1 and 2 ^{1}A$'$ states of ClNO, for a cut at a fixed r_{ClN} bond length of 3.75 bohr and a fixed r_{NO} bond length of 2.15 bohr. The y components of the TDMs are given in panel a), and the z components are given in panel b). The results labelled '1 ^{1}A$'$ separate' are from calculations where the TDM is calculated between the 1 ^{1}A$'$ state obtained from a single-state CAS wavefunction and the 2 ^{1}A$'$ from a CAS step averaged over the first 3 states of ^{1}A$'$ symmetry.
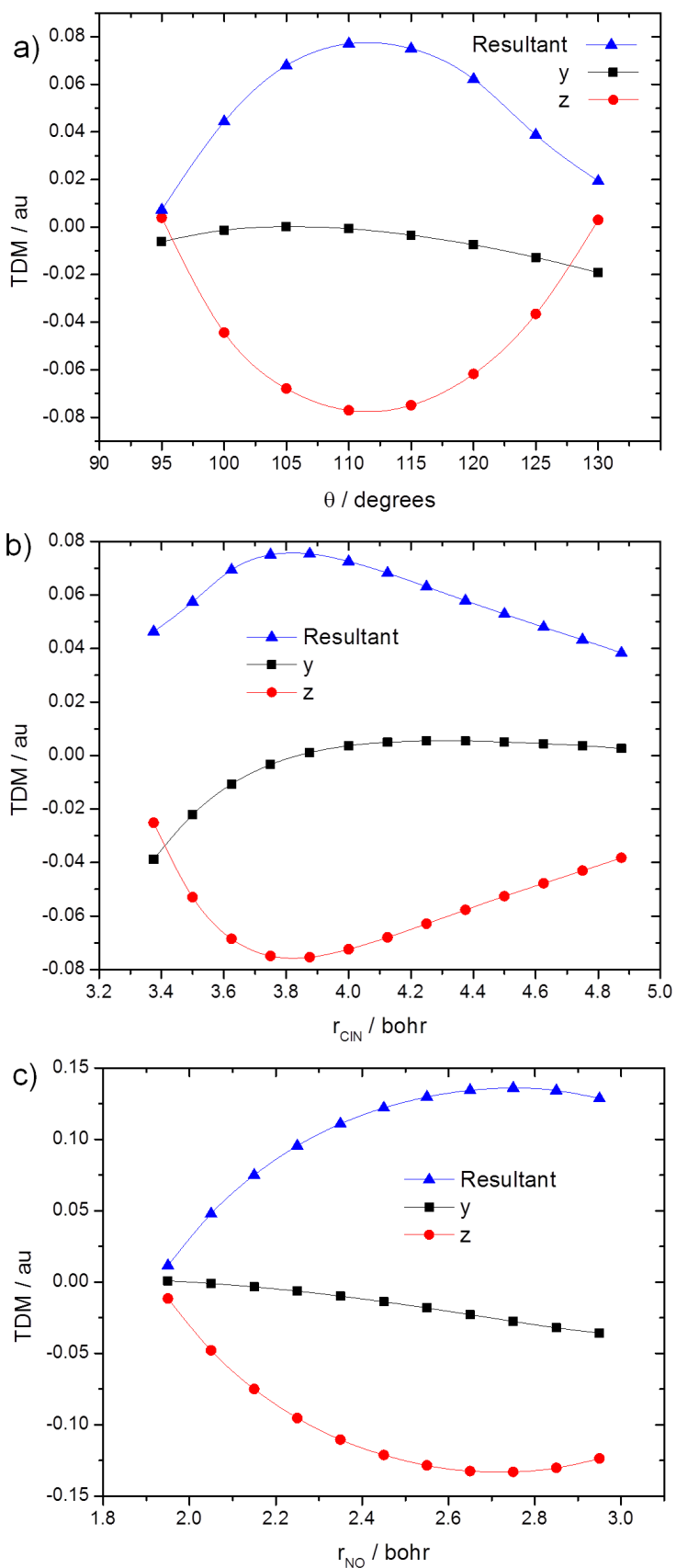
Figure 3.14: TDM surfaces for the transition between the 1 and 2 $^1A'$ states of ClNO, calculated at the MRCI/AVQZ level. The y and z components of the TDMs, as well as their resultants, are shown. Panel a) shows a cut at r_{ClN} = 3.75 bohr and r_{NO} = 2.15 bohr; panel b) shows a cut at r_{NO} = 2.15 and θ = 115°; panel c) shows a cut at r_{ClN} = 3.75 bohr and θ = 115°.

Coefficient	Orbitals involved in excitation
-0.77282	$3.2 \rightarrow 4.2$
-0.39039	$13.1 \rightarrow 14.1$
-0.18673	$3.2 \rightarrow 4.2$ $13.1 \rightarrow 14.1$
-0.17936	$13.1 \rightarrow 16.1$
0.14057	$13.1 \rightarrow 15.1$
-0.11505	$3.2 \rightarrow 7.2$
-0.10649	$3.2 \rightarrow 4.2$ $13.1 \rightarrow 16.1$

Table 3.5: The coefficients of the orbital excitations moving from the 1 to 2 ^{1}A$'$ state. The results are from an EOM-CCSD calculation at the FC geometry, and the orbitals are labelled according to order and symmetry, with '.1' corresponding to A$'$ and '.2' corresponding to A$''$.

3.3.3 EOM-CCSD TDMs

The coupled cluster method, specifically equations-of-motion CCSD, may be a better way of calculating transition dipole moments than CAS or MRCI. It has been shown to give good agreement with full CI calculations in cases where the excited state of interest can be well-described by the promotion of a single electron from the ground state, and where the ground state can be well-represented by a single-reference calculation [117]. Molpro [138, 139] produces transition moments for both the left and right operators, and the signs of these are not consistent across the full range of geometries. To find the overall TDM, the resultant of these two moments needs to be calculated.

The EOM-CCSD method may be valid for ClNO. At the FC point, the dominant electron configuration for the 1 ^{1}A$'$ state contributes 0.9459 of the whole wavefunction in CAS calculations, and so although it has some multi-reference character it is not a large amount. In addition, for an EOM-CCSD calculation at the FC point, the excitation to the 2 ^{1}A$'$ state is mostly due to the promotion of an electron from the orbital labelled 3.2 to that labelled 4.2, although other excitations also contribute, as shown in table 3.5.

EOM-CCSD/AVQZ TDMs were calculated over the same geometries as the MRCI TDMs. Cuts through the TDM surfaces are given in figure 3.15, for the y and z components and the resultants. The magnitudes of the TDMs are significantly larger than the
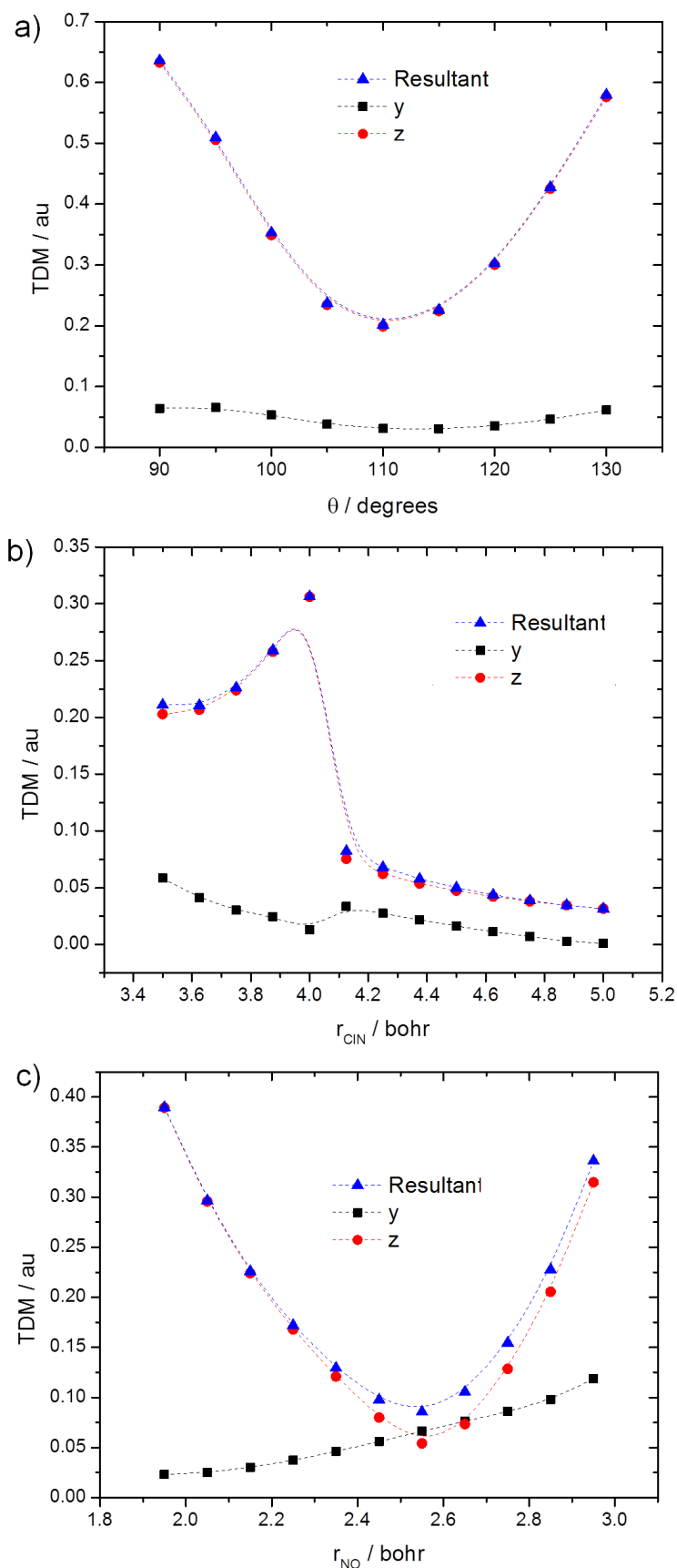
Figure 3.15: TDM surfaces for the transition between the 1 and 2 $^1A'$ states of ClNO, calculated at the EOM-CCSD/AVQZ level. The y and z components of the TDMs, as well as their resultants, are shown. Panel a) shows a cut at r_{ClN} = 3.75 bohr and r_{NO} = 2.15 bohr; panel b) shows a cut at r_{NO} = 2.15 and θ = 115°; panel c) shows a cut at r_{ClN} = 3.75 bohr and θ=115°.

MRCI values, and the shapes of the curves are very different. The main similarity is that the z components are still much larger than the y components. The TDM has a maximum value close to the FC r_{ClN} bond length, but then there is a sharp kink towards zero as the bond stretches. The cut in which θ varies, panel a) of figure 3.15, displays completely the opposite behaviour to that in the MRCI cut: the TDM is at a minimum close to the FC geometry. The variation with r_{NO} is also markedly different, displaying a minimum at around $r_{NO} = 2.55$ bohr. As the TDMs for the MRCI/CAS and EOM-CCSD methods are so different both were used in dynamics calculations to see their effect. How well the results of these calculations agree with experiment should provide an indication of which method is most reliable.

3.4 Non-adiabatic coupling

3.4.1 Conical intersection optimisations

Examination of the PESs for the 1 and 2 ^{1}A$'$ states suggested the presence of a conical intersection seam between them in the asymptotic region at a bond angle θ of approximately 70°. In order to confirm this, CoIn optimisations were run using Molpro at the CAS level [88, 122]. If successful, these would provide a geometry for the CoIn and show the directions of the tuning and branching vectors. However, various problems were encountered.

Firstly, the CAS gradient code in Molpro requires segmented rather than generally contracted basis sets, and the Dunning basis sets used in the PES calculations are generally contracted. The AVTZ basis set was manually segmented, and gave sensible results for a standard energy calculation, but then contained too many PGTOs to be used in gradient calculations. Pople basis sets use segmented contraction and so a series of calculations were run with these. The 6-31G, 6-311G and 6-311++G(3df,3pf) basis sets were chosen, with the latter being the largest commonly-used Pople basis set available. However, most calculations did not converge on any geometry. The only optimisation which did converge used the smallest 6-31G basis set and required 32 iterations. The optimised geometry was

at $r_{ClN} = 6.53$ bohr, $r_{NO} = 2.32$ bohr and $\theta = 74.4°$. From inspection of the PESs, this geometry seems reasonable, but the failure of other calculations to converge casts doubt upon its validity.

These convergence problems derive from the fact that in the asymptotic region the states are all very flat and close together in energy. The CoIn optimisation algorithm is attempting to find the point at which the energy difference between two states is zero, by looking at the energy gradients of the states as the geometry is varied. However, as these gradients are close to zero, and the coupling and tuning coordinates are not known, the problem is poorly-defined.

Attempts were made to improve convergence, by varying the state-averaging in the CAS and by using Gaussian's CoIn optimisation routine [89], however these did not meet with much success. In many cases, the optimisation algorithm moved a long way into the asymptotic region. One further calculation converged at a reasonable geometry, using the 6-311++G(3df,3pd) basis set and state-averaging over the first 6 states of $^1A'$ symmetry. The optimised geometry of $r_{ClN} = 7.29$ bohr, $r_{NO} = 2.14$ bohr and $\theta = 70.85°$ is different to that found in the previous converged calculation. This could be due to basis-set differences, or could be down to chance given the unreliability of these optimisations.

3.4.2   NACMEs

To allow radiationless transitions between states to be incorporated into dynamics calculations, NACMEs need to be calculated. There are three ways in which this can be done using Molpro. Using the CAS method they can be found analytically [88], giving as an output a matrix of energy gradients for each individual atom along the Cartesian axes. However, the disadvantage of this is that, as with the CoIn optimisation routine, gradients are again computed and so Dunning basis sets cannot be used. An alternative is to use quasi-diabatisation, which attempts to formulate diabatic states and the associated potential coupling matrix elements and mixing angles. The disadvantage of this is that it is very computationally demanding and therefore time-consuming to run at the MRCI level.

The third option is to use the numerical DDR method mentioned in section 2.1.9, us-

ing the adiabatic states and generating the kinetic couplings. As in order to obtain reliable gradients it is necessary to calculate the geometry of interest and two points slightly displaced from it, this is also quite expensive. In addition, as NACMEs change very rapidly as the geometry changes, it is necessary to calculate them over a very dense grid, further adding to the expense. However, as the CoIn appears at similar geometries in both the MRCI and CAS level PESs, it was considered valid to perform these calculations at the CAS level. The AVTZ basis set was used as the differences between results for this and the larger AVQZ basis set in test calculations were very small.

Ideally, the NACMEs would be calculated in the direction of the branching and tuning coordinates of the CoIn, however as these were not known the Jacobi coordinates were used instead. Jacobi were chosen rather than binding as these are the coordinates used preferentially in dynamics calculations due to the simplification of the kinetic energy part of the Hamiltonian and the greater ease of analysis. Gradients in all three Jacobi coordinates were calculated in order to provide as complete a picture of the intersection as possible.

The DDR method works as follows [88, 130] for calculating the NACME in the coordinate of interest x:

1. The wavefunction is calculated at the reference geometry.

2. The wavefunction is calculated at a positively displaced geometry, x + increment.

3. The wavefunction is calculated at a negatively displaced geometry, x - increment.

4. The transition density matrices between the reference and displaced geometries are calculated.

5. The NACME is computed.

The increment chosen for the R and r coordinates was 0.01 bohr, and the increment chosen for the angle γ was 0.1°. The grid over which the NACMEs were calculated was:

- $\boldsymbol{R}$: every 0.25 bohr from 5.5 to 9.5 bohr

- $\boldsymbol{r}$: every 0.05 bohr from 1.95 to 2.45 bohr

- Jacobi angle $\boldsymbol{\gamma}$: every 1° from 50° to 100°.

If less dense grids were used, particularly in the angular coordinate, key features of the NACMEs were lost.

One issue with the NACMEs produced by this method is that the signs are not consistent across the 'surfaces'. If the branching and tuning vectors were known, this would not be a problem as it would be possible to assign the signs unambiguously. However, as the results from the CoIn optimisations were not reliable, the signs have been chosen in order to keep the variation of the NACMEs as smooth as possible. Another issue is that as the Jacobi coordinates do not correspond to the branching and tuning vectors, the behaviour of the NACMEs at points where the surfaces cross cannot be predicted so easily: the NACMEs will not necessarily go to infinity or zero at the point of intersection.

NACMEs in the R coordinate

Figure 3.16 shows cuts through the NACME surfaces for the gradients in the R direction. Panel a) shows how the NACME varies with R at a fixed γ of $80°$. The NACMEs are highest for $r = 2.2$ bohr, around $R = 7.25$ bohr, as expected from inspection of the PESs. Panel b) shows how the NACME varies with γ at a fixed r bond length of 2.2 bohr. Note here that the signs of the NACMEs change, with a minimum at lower γ preceding a maximum. As R increases, these maxima appear at lower γ, showing that the intersection seam does not occur at a fixed angle. Panel c) shows how the NACME varies with r at a fixed γ of $80°$. Again there is a change in sign at around $r = 2.2$ bohr, and the maxima shift according to the value of R.

NACMEs in the γ coordinate

Figure 3.17 shows cuts through the NACME surfaces for the gradients in the γ direction. The behaviour is very similar to that for the NACMEs in the R coordinate, but the magnitudes of the NACMEs are rather smaller.
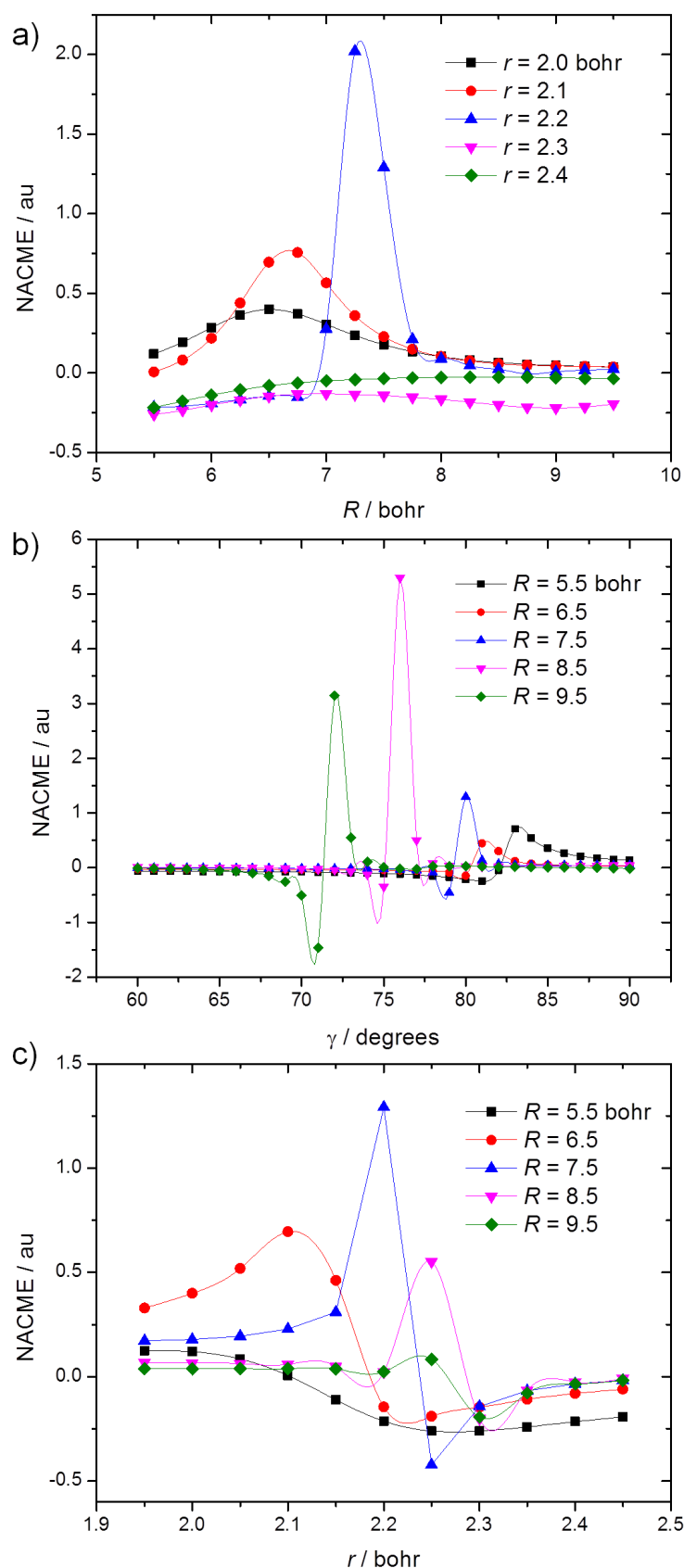
Figure 3.16: Cuts through NACME surfaces between the 1 and 2 ^{1}A$'$ states of ClNO in the *R* coordinate, calculated at the CASSCF/AVTZ level. Panel a) shows a cut at $\gamma = 80°$, showing the variation with *R* for several values of *r*. Panel b) shows a cut at *r* = 2.2 bohr, showing the variation with γ for several values of *R*. Panel c) shows a cut at $\gamma = 80°$, showing the variation with *r* for several values of *R*.
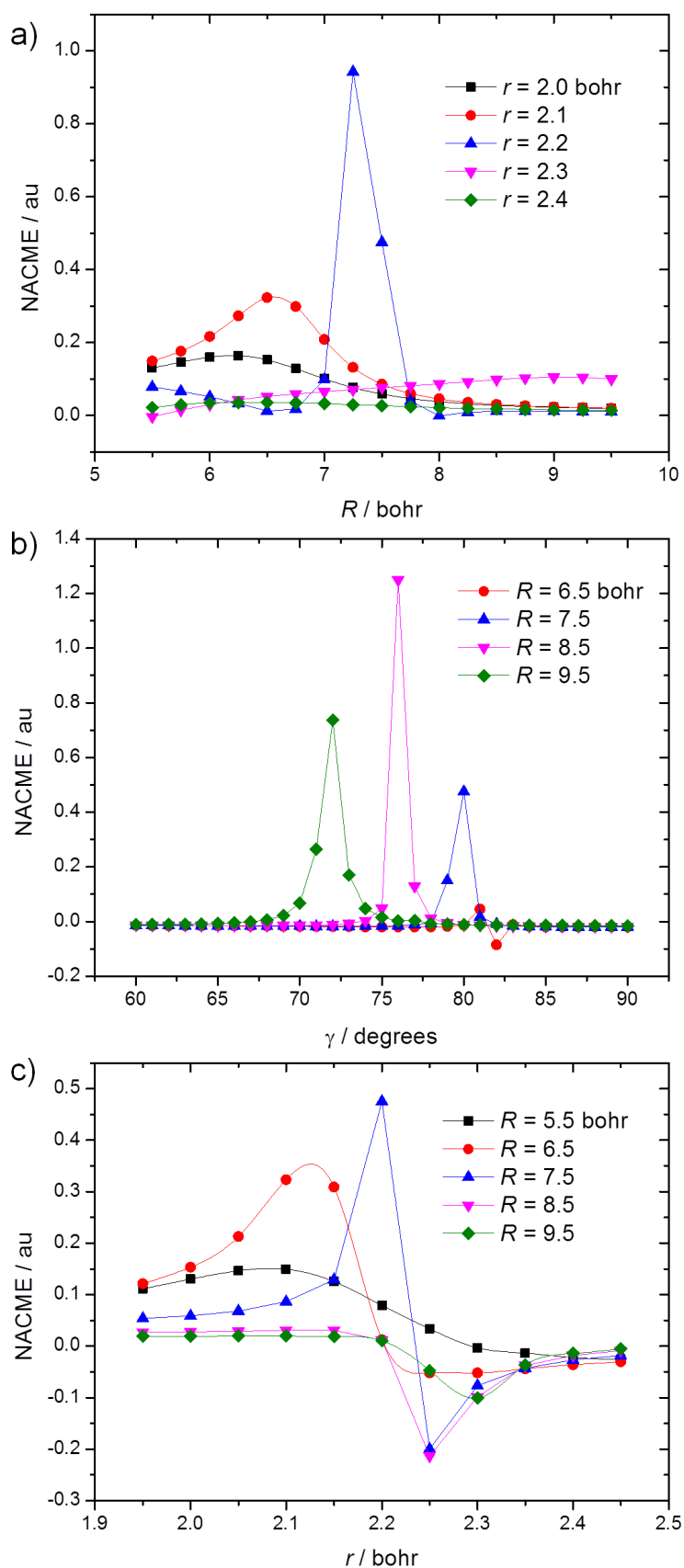
Figure 3.17: Cuts through NACME surfaces between the 1 and 2 ^{1}A$'$ states of ClNO in the γ coordinate, calculated at the CASSCF/AVTZ level. Panel a) shows a cut at $\gamma = 80°$, showing the variation with R for several values of r. Panel b) shows a cut at $r = 2.2$ bohr, showing the variation with γ for several values of R. Panel c) shows a cut at $\gamma = 80°$, showing the variation with r for several values of R.

NACMEs in the *r* coordinate

Figure 3.18 shows cuts through the NACME surfaces for the gradients in the *r* direction. The first thing to note about these NACMEs is that their magnitudes are much larger than those in the γ and *R* coordinates. This is unexpected, as from the PESs it appears that the CoIn should be facilitated mostly via the angular coordinate. However, as the momenta in each coordinate as well as the size of the NACMEs are key to determining the probability of a transition between the electronic states, motion in the *r* coordinate may not after all be the most important. The behaviour of the NACMEs is also a little different in the *r* direction. As well as being larger, the NACMEs change sign in a more pronounced manner, and the values at $r = 2.2$ bohr are more dominant.
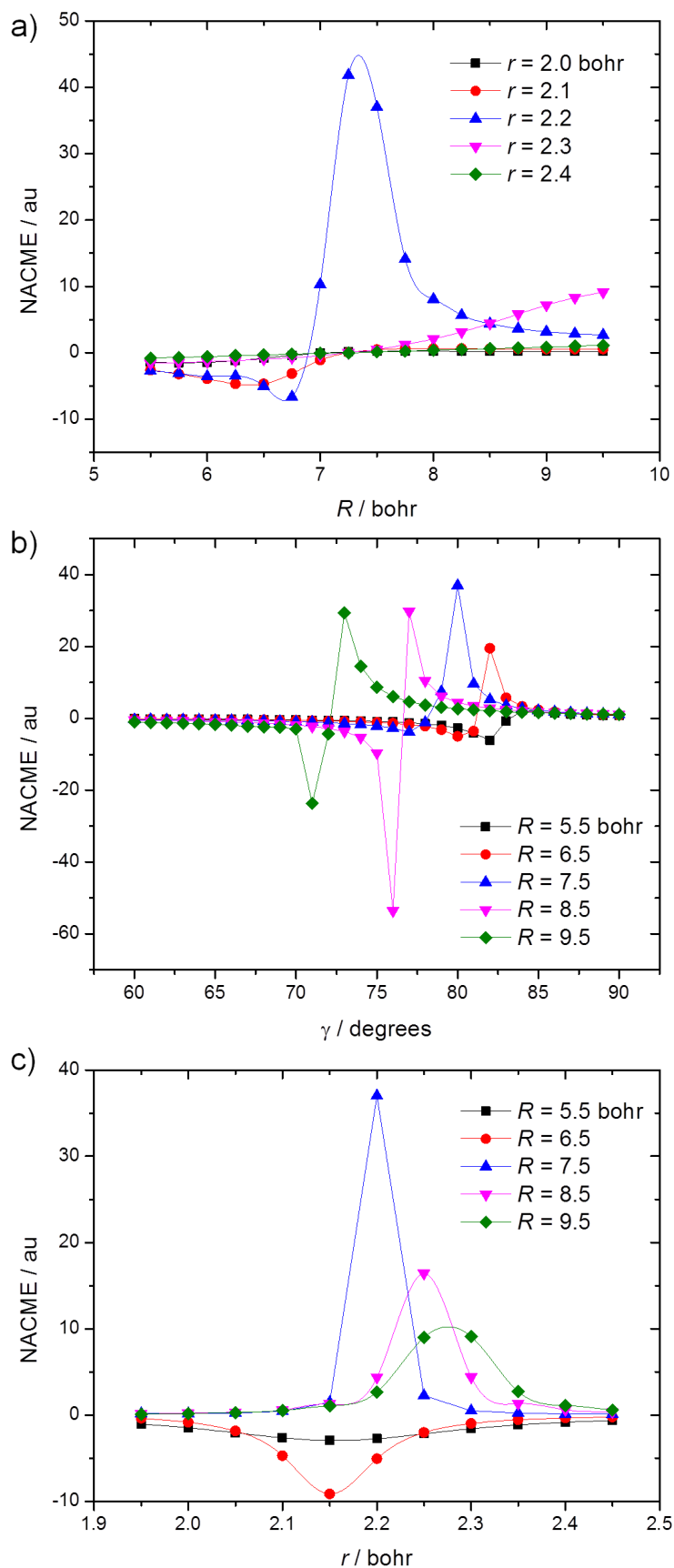
Figure 3.18: Cuts through NACME surfaces between the 1 and 2 $^1\mathrm{A}'$ states of ClNO in the r coordinate, calculated at the CASSCF/AVTZ level. Panel a) shows a cut at $\gamma = 80°$, showing the variation with R for several values of r. Panel b) shows a cut at $r = 2.2$ bohr, showing the variation with γ for several values of R. Panel c) shows a cut at $\gamma = 80°$, showing the variation with r for several values of R.

3.5 Wavepacket dynamics

The MCTDH method [93, 104, 140, 141] as implemented in the Heidelberg suite of programs (version 90) [142] was used throughout to run wavepacket propagations. When running such calculations the Hamiltonian needs to be determined, as do the SPF basis size and the number and form of the primitive basis functions. Ten SPFs for each mode (R, r and γ) were chosen for each electronic state. Fewer were needed to accurately describe the ground state, but the same number were chosen for each to give a more balanced calculation. To ensure the accuracy of the calculation, the populations of the highest natural orbital should be very small, at least below 1%. When 10 natural orbitals are used in each SPF basis in this system, the populations of the highest orbitals are all of the order 10^{-6} or lower.

To improve computational efficiency the Discrete Variable Representation (DVR) has been used for the primitive basis functions, allowing the wavefunction to be localised onto a grid. For the γ coordinate, the Legendre DVR was chosen, with a sine DVR for the dissociative R coordinate and a harmonic oscillator for the bound r coordinate. The number of grid points for each mode needs to be chosen such that the maximum population on the end grid points is minimal, and that the grid is dense enough so that no features of the dynamics are lost. For this system, these criteria were satisfied using 288 points on the R coordinate, 48 on the r, and 200 on the γ. Large numbers of points were required on the R coordinate as the PES extends a long way in this direction, and large numbers were needed on the γ coordinate as this changes rapidly as the molecule dissociates.

The PESs need to be transformed from binding to Jacobi coordinates. This can be done simply using the following transformations:

$$R = \sqrt{r_{ClN}^2 + (ar_{NO})^2 - 2ar_{NO}r_{ClN}\cos\theta} \tag{3.1}$$

$$\gamma = \pi - \mathrm{acos}\left(\frac{R^2 + (ar_{NO})^2 - r_{ClN}^2}{2ar_{NO}R}\right) \tag{3.2}$$

The constant a represents the centre of mass of the r_{NO} bond, and is equal to 0.533205.

The *r* coordinate is the same as r_{NO}, and so remains unchanged. The resulting Jacobi surfaces are fitted with a 3D spline, and then converted into product form using the POTFIT program [97, 98].

A complex absorbing potential (CAP) of the form described in section 2.2.1 needs to be placed on the 2 ^{1}A$'$ PES in order to stop the wavepacket hitting the edge of the grid in the *R* coordinate. The CAP needs to be positioned far enough out on the *R* coordinate such that the PES is essentially flat and so will have no further effect upon the dynamics of the wavepacket. Positions between *R* = 7.5 and 8.5 bohr were found to be suitable to achieve this. The strength and order of the CAP are found by trial and error: they need to be such that no back-reflections occur, but at the same time the wavepacket needs to be absorbed sufficiently so that none of it reaches the end of the grid. Values of 0.3 and 3 for the strength and order respectively were found to be optimum in this case.

The approximation that the total angular momentum *J* = 0 was made, giving the overall Hamiltonian for the system as

$$\hat{H}_n = -\hat{T} + V_n(R, r, \gamma), \tag{3.3}$$

with $\hat{T}$ being the kinetic energy operator stated previously in equation 2.55 and V_n being the PES for the desired state *n*. The integrator used also needed to be chosen. Here, the Short-Iterative Lanczos method was used for propagating the expansion coefficients and the Bulirsch-Stoer extrapolation integrator was used for the SPFs, as these have been succesfully used before with ClNO and similar systems [141].

The calculations proceeded as follows: first, an initial wavepacket was formed on the 1 ^{1}A$'$ PES by propagating it in imaginary time. Second, this initial wavepacket was transferred to 2 ^{1}A$'$ PES, either directly or by being operated on by a TDM function (calculated at the MRCI or EOM-CCSD level). Thirdly, this excited wavepacket was allowed to propagate until it had been completely absorbed by the CAP.
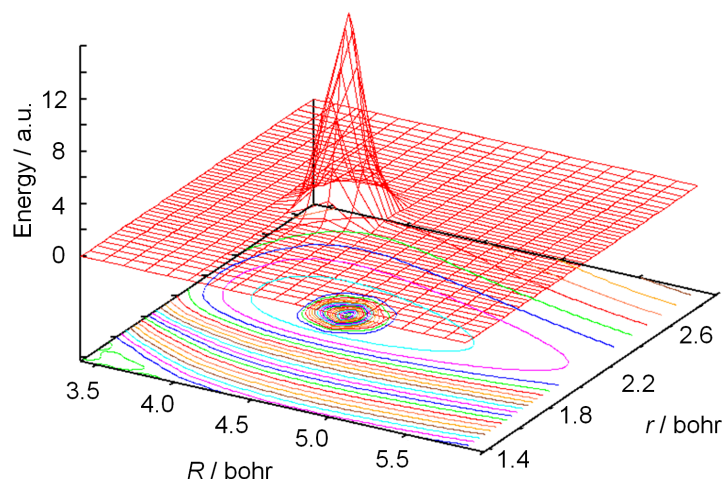
Figure 3.19: A snapshot of the fully-relaxed initial wavepacket. The 2D cut of the 1 ^{1}A$'$ PES shown is for a constant γ of 127°.

3.5.1   Initial wavepacket

To form the initial wavepacket, it was relaxed on the 1 ^{1}A$'$ PES for 80 fs. After this time it was stable and had the following mode expectation values and variances:

- $\boldsymbol{R}$ = 4.344, dR = 0.104 bohr
- $\boldsymbol{r}$ = 2.152, dr = 0.068 bohr
- $\boldsymbol{\gamma}$ = 127.6°, $d\gamma$ = 3.3°

This mean geometry is equivalent to r_{CIN} = 3.755 bohr, θ = 113.6°, showing that the wavepacket is accurately finding the minimum of the PES. Figure 3.19 gives an view of the initial wavepacket, showing that it has a uniform, Gaussian-like shape.

3.5.2   Propagation on 2 ^{1}A$'$ state

In the wavepacket propagation the entire ground state wavepacket is projected up onto the excited state. It therefore contains all possible excitation energies in one calculation. If results for a particular energy, for example that corresponding to a laser pulse in an experiment, are required, this can be extracted from the overall results. The results shown in this section are for the complete wavepacket; those for individual energies will be considered later in section 3.7. Three wavepacket propagations have been run: one without a TDM function, one using the MRCI level TDMs and one using the EOM-CCSD TDMs.

Snapshots of the wavepacket every 10 fs as it propagates on the 2 ^{1}A′ surface when the MRCI level TDMs were used are shown in figure 3.20. As can be seen in the cut at $\gamma = 127°$ in panel a), the wavepacket receives only a small impetus in the NO coordinate as its starting position is very close to the energy minimum. The NO product would therefore be expected to have little to no vibrational excitation. The cut at $r_{NO} = 2.15$ bohr given in panel b) is more interesting: the wavepacket is initially high on a steep wall angled towards lower γ, and so proceeds rapidly downhill in this direction. The NO product would therefore be expected to have significant rotational excitation.
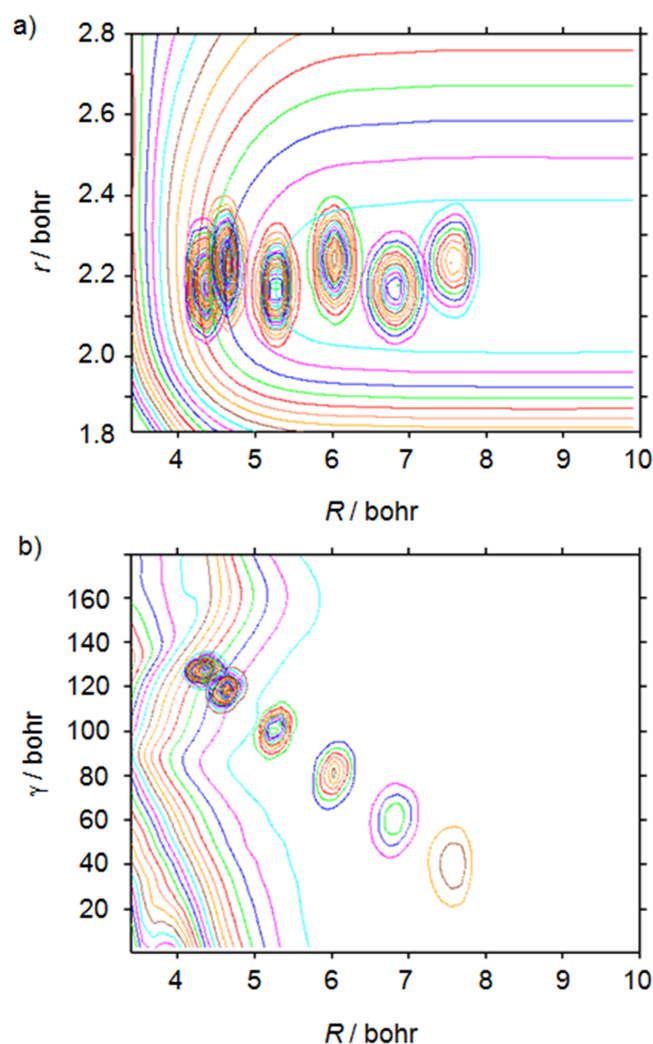
Figure 3.20: Snapshots of the wavepacket propagation on the 2 ^{1}A′ state of ClNO, a) for a constant γ of 127° and b) for a constant r_{NO} bond length of 2.15 bohr. Jacobi coordinates are used. The wavepackets are shown at 0, 10, 20, 30, 40 and 50 fs after excitation. The dotted arrows reflect the wavepacket's path. Contour lines on the surfaces are 0.5 eV apart.
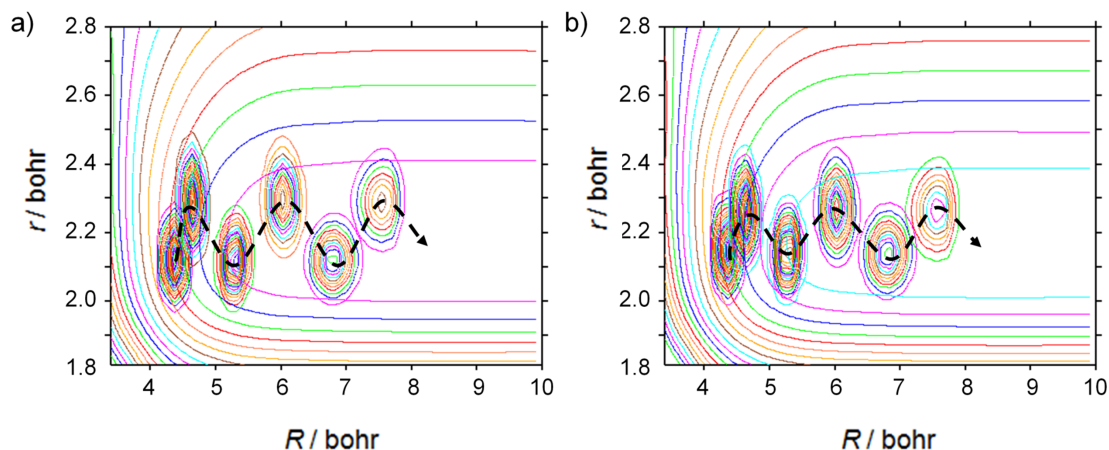
Figure 3.21: Snapshots of the wavepacket propagation on the 2 ^{1}A$'$ state of ClNO for a constant γ of 127°. Panel a) shows the results when the EOM-CCSD TDM function is used, and panel b) shows the results when no TDM function is used. The wavepackets are shown at 0, 10, 20, 30, 40 and 50 fs after excitation. The dotted arrows reflect the wavepacket's path.

Figure 3.21 shows the paths of the wavepackets when the EOM-CCSD TDMs and no TDMs are used, for a cut at $\gamma = 127°$. In both cases, the initial wavepacket on the 2 ^{1}A$'$ surface is centred at a lower r_{NO} bond length than that for the MRCI TDMs. This means the wavepacket is further away from the minimum in the r_{NO} coordinate in the exit channel, and hence the slope of the PES in this direction is steeper. The amplitude of the oscillation in this coordinate is therefore greater, implying a greater degree of NO product vibrational excitation will be found, especially when the EOM-CCSD TDMs are used. This behaviour is expected given the shapes of the TDM functions in the r_{NO} coordinate: for the MRCI TDMs, their magnitude increases as r_{NO} increases, and for the EOM-CCSD TDMs their magnitude increases as r_{NO} decreases, at least in the region in which the ground state wavepacket has greatest density. Note that the path of the wavepacket in the angular coordinate is affected very little by the TDM function, and so these plots are not shown.

Autocorrelation and absorption spectrum

The autocorrelation functions for each propagation are shown in figure 3.22. These are very simple and tail off almost immediately with no real structure, showing that the
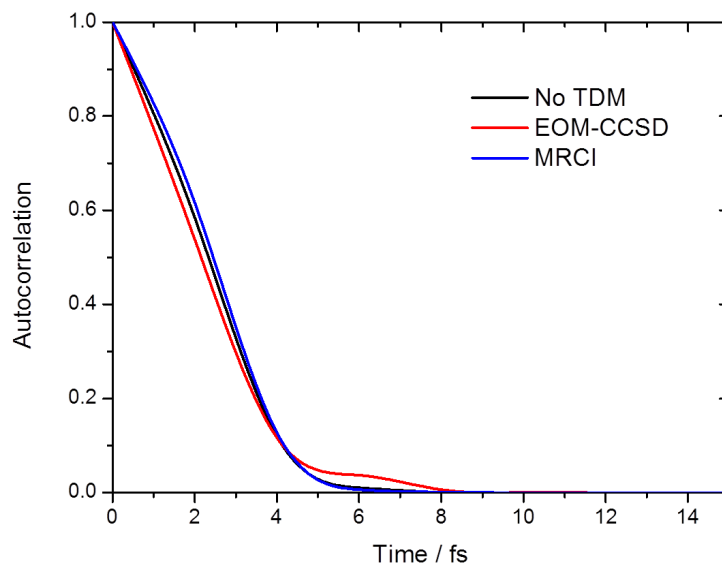
Figure 3.22: Autocorrelations calculated from wavepacket propagations on the 2 $^1A'$ state. The black line is from when no TDM function was used, the red is with EOM-CCSD TDMs and the blue is with MRCI TDMs.

wavepacket moves rapidly away from the FC point and does not return. The autocorrelations for the propagations without TDMs and with the MRCI TDMs are nearly identical. When EOM-CCSD TDMs are used there is a small hump at around 6 fs, indicating that a tiny portion of the wavepacket returns, most likely due to movement in the r_{NO} coordinate.

Figure 3.23 shows the absorption spectra derived from Fourier transformations of the autocorrelation data. As expected from such simple autocorrelation functions, the spectra consist of a single, broad peak. Both the spectra for no TDM and the MRCI TDMs peak at around 3.79 eV and have similar widths of around 0.8 eV. The spectrum for the EOM-CCSD TDMs is shifted slightly to lower energy, peaking at 3.70 eV, and is less symmetrical, extending further out to higher energies. This asymmetry is due to the vibrational excitation in the NO bond. The spectra for no TDM and with the MRCI values agree better with that calculated by Yamashita and Kato [68], who included the TDM just at the FC point. The spectra can also be compared with the experimental spectrum given in figure 1.16.
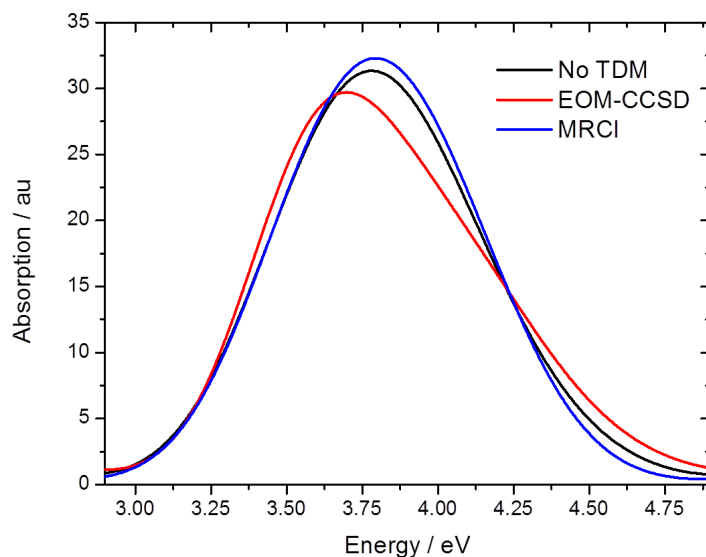
Figure 3.23: Absorption spectra calculated from wavepacket propagations on the 2 $^1A'$ state. The black line is from when no TDM function was used, the red is with EOM-CCSD TDMs and the blue is with MRCI TDMs.

NO vibrational distribution

NO product state distributions were found by analysing the quantum flux passing into the CAP [110], as discussed in section 2.2.1. To obtain the NO vibrational states it was first necessary to calculate the NO potential energy curve at the same level of theory as the ClNO PESs, i.e. at the MRCI/AVQZ level using a full-valence active space. The *ab initio* points were then fitted to an Extended Rydberg function of the form

$$V_{NO}(r) = -D_e \left(1 + \sum_{k=1}^{6} a_k \rho^k \right) e^{-b\rho} + V_{min} \tag{3.4}$$

where $\rho = r - r_e$. The fitted coeffcients were as follows: $a_1 = 1.8213$, $a_2 = -0.5283$, $a_3 = 0.1264$, $a_4 = 0.1564$, $a_5 = 0.1182$, $a_6 = -0.0136$, $b = -1.802$ and $V_{min} = 0.2384$ hartree. The *ab initio* points and fit are shown in figure 3.24. The value for r_e obtained from this curve matches the experimental value of 2.18 bohr, and the value of 6.49 eV for the dissociation energy D_e is near-identical to the experimental value of 6.48 eV [143]. From this function the NO vibrational eigenstates could be found and then projected onto the asymptotic flux. As shown in table 3.6, the energies of the calculated eigenstates agreed very well with experimental values, and so this curve can be considered accurate.
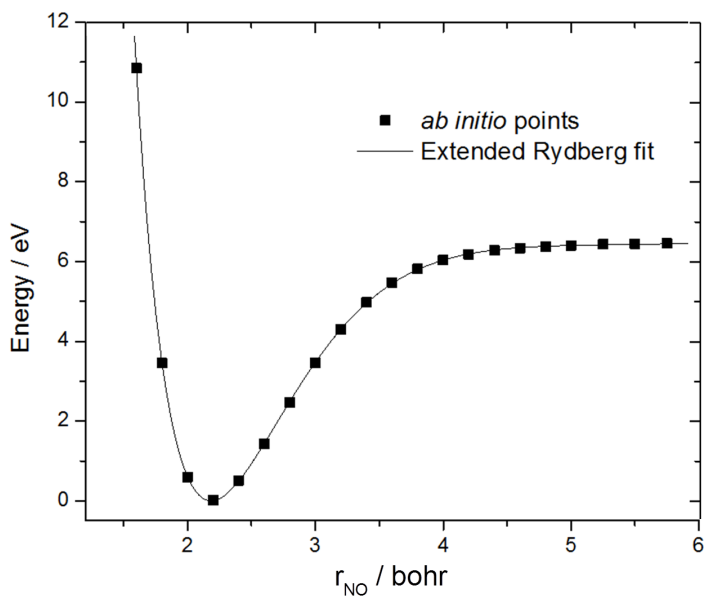
Figure 3.24: The potential energy curve for NO calculated at the MRCI/AVQZ level, and an extended Rydberg fit to the *ab initio* points.

NO v	Energy / cm^{-1}	
	Calculated	Experimental
0	946.6	948.6
1	2824	2825
2	4675	4673
3	6498	6492
4	8295	8284

Table 3.6: The energies of the NO vibrational states, derived from the NO potential energy curve calculated here, and derived from the experimental constants of $\omega_e = 1904.2$ cm^{-1}, $\omega_e x_e = 14.075$ cm^{-1}.

NO v	% of total		
	no TDMs	MRCI TDMs	EOM-CCSD TDMS
0	78.9	91.2	62.8
1	17.4	8.30	28.0
2	3.1	0.38	7.26
3	0.53	0.11	1.55
4	0.09	0.04	0.03

Table 3.7: The proportion of the total flux going into each product NO vibrational state for wavepacket propagations with no TDM function, with MRCI level TDMs and with EOM-CCSD level TDMs.

Figure 3.25 shows the energy distribution of the quantum flux passing into each NO vibrational state and table 3.7 gives the proportion of the total flux going into each state for the whole range of energies contained in the initial wavepacket. The total flux distribution is, as would be expected, broad and featureless like the absorption spectrum (Figure 3.23). The flux distributions into the individual vibrational states are similarly-shaped, with the peaks shifted slightly in energy. When the MRCI TDMs are used, the vast majority of NO is formed in v = 0, with only 8% in v = 1, and with the populations of higher excited states negligible. The photodissociation process is therefore essentially adiabatic with respect to the NO stretch. The proportion of the flux going into each vibrational state is obtained by numerical integration using the trapezium rule, with 500 points across the energy range of interest.

However, if TDMs are not employed in the initial excitation and the relaxed wavepacket is simply placed 'as-is' on the 2 $^1A'$ state, the calculated NO vibrational distribution is different. As shown in table 3.7, although most NO is still formed in v = 0, the proportion in v = 1 is more than doubled. This is because the MRCI TDM operator has the effect of shifting more wavepacket density closer to the minimum in the r_{NO} coordinate, hence giving less impetus in the direction of longer r_{NO}, as shown earlier in figure 3.21. When TDMs calculated at the EOM-CCSD level are used and the initial wavepacket is shifted further away from the r_{NO} minimum the effect is even greater, with more than a third of the NO being formed in excited vibrational states. The choice of TDMs hence has a significant effect on the dynamics.
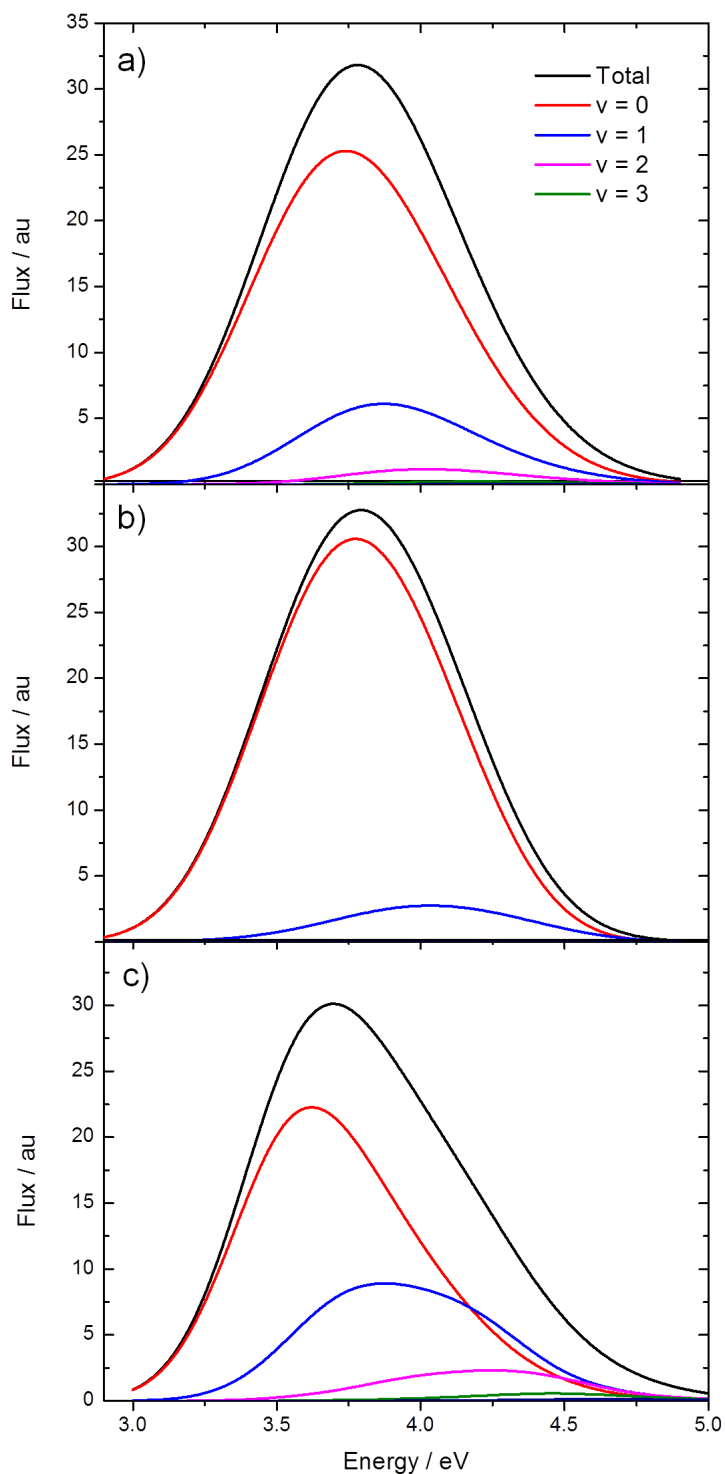
Figure 3.25: NO vibrational flux energy distributions obtained following wavepacket propagations on the 2 ^{1}A′ state. Panel a) shows the flux when no TDM function is included, panel b) shows the flux when the MRCI TDM function operates on the initial wavepacket, and panel c) shows the same for the EOM-CCSD TDM function.

NO rotational distribution

To find the NO rotational state populations the quantum flux was projected onto spherical harmonic functions. This gives the flux distribution for each value of j, the NO rotational quantum number. These, like the absorption spectrum, are single peaks and vary very little other than in amplitude and central energy. Integrating the individual distributions across all energies gives the overall NO rotational distribution, which is narrow and Gaussian-shaped. The incorporation of the TDM functions has a small effect upon the NO rotational distributions, shown in figure 3.26. Overall, when no TDM function is used the distribution peaks at $j = 51$ and has a full-width half-maximum (FWHM) of $15.7\,j$. When the MRCI level TDM function is used, the distribution still peaks at $j = 51$, but it is very slightly narrower, with a FWHM of $15.1\,j$. The biggest difference is once again seen when the EOM-CCSD TDMs are used: here, the distribution peaks $1\,j$ lower at $j = 50$, and is wider, with a FWHM of $16.5\,j$. However, these differences are still very small, showing the TDM has little impact upon the extent of NO rotational excitation.

The distributions can be explained simply by inspection of the PES shown in panel b) of figure 3.20 and employing an impulsive model. The slope of the surface at the FC geometry points steeply towards smaller values of γ, causing significant torque to be imparted upon the NO fragment as the ClNO dissociates, hence leading to a high level of rotational excitation. There are no other features on the PES which would cause the wavepacket to split or spread out in any significant way, and hence it remains well-localised throughout the photodissociation, and so the NO rotational distribution remains narrow. The NO product state distributions for individual energies are considered later, in section 3.7, where comparison with experiment gives an indication of the validity of each set of results.
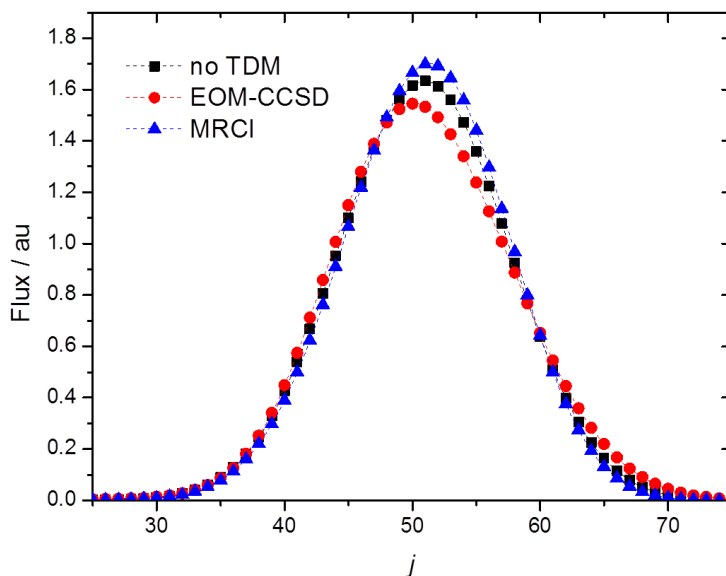
Figure 3.26: Rotational distributions obtained following wavepacket propagations on the $2\,^1A'$ state. Distributions are shown when no TDM function is included, and when the EOM-CCSD and MRCI TDM functions operate on the initial wavepacket.

3.6 Classical trajectories

To run classical trajectory calculations, software written by George McBane, Reinhard Schinke and co-workers [116, 144] was taken and adapted for ClNO. The main reasons for investigating this system using classical in addition to quantum mechanics were to enable the conical intersection between the 1 and $2\,^1A'$ states to be modelled more easily, and to allow β parameters to be calculated.

Trajectories were run at a single energy, plus or minus a small range, here set to $\Delta E = 0.01$ eV. Random numbers were used to help generate the starting conditions, based on a portion of an initial wavepacket on the ground state being excited up onto the $2\,^1A'$ state. Each trajectory therefore has initial positions and momenta in each of the three coordinates, and propagates across the $2\,^1A'$ PES according to Hamilton's equations. The time-step is 2 atomic units of time, equal to $2 \times 2.4188 \times 10^{-17}$ s. The trajectories were stopped when they reached a geometry with $R = 8.5$ bohr, from which point onwards the PESs were considered flat and the dissociation process over. In order to represent the motion of an entire wavepacket, a large number of trajectories (here 50 000) are run at each energy and then averaged.

Product state distributions are found by comparing the final energy of each trajectory with a list of energies of the NO eigenstates calculated from experimental constants, added to the calculated ClNO dissociation energy of 1.619 eV. The rotational quantum number is found by taking the integer closest to the non-integer classical rotational number, which is equal to the momentum in the angular coordinate in atomic units. Overall product state distributions are then found by binning the quantum numbers for all 50 000 trajectories. Note that the TDM functions are used only for the derivation of β parameters, and not in the excitation process itself.

The PESs for each state were once again created using cubic splines of the *ab initio* points, and Jacobi coordinates were used to describe the trajectories. Note that here instead of γ the angular coordinate is in terms of ϕ, where $\phi = 180° - \gamma$; this was done to avoid making more substantial changes to the existing code. A function was written to calculate the energy derivatives of the PESs in Jacobi coordinates from the derivatives of the binding coordinate PESs using the following equations:

$$\frac{dV}{dR} = \frac{dV}{dr_{ClN}}\frac{dr_{ClN}}{dR} + \frac{dV}{dr_{NO}}\frac{dr_{NO}}{dR} + \frac{dV}{d\theta}\frac{d\theta}{dR} \tag{3.5}$$

$$\frac{dV}{dr} = \frac{dV}{dr_{ClN}}\frac{dr_{ClN}}{dr} + \frac{dV}{dr_{NO}}\frac{dr_{NO}}{dr} + \frac{dV}{d\theta}\frac{d\theta}{dr} \tag{3.6}$$

$$\frac{dV}{d\phi} = \frac{dV}{dr_{ClN}}\frac{dr_{ClN}}{d\phi} + \frac{dV}{dr_{NO}}\frac{dr_{NO}}{d\phi} + \frac{dV}{d\theta}\frac{d\theta}{d\phi}. \tag{3.7}$$

The individual derivatives are:

$$\frac{dr_{ClN}}{dR} = (R - ar\cos\phi) \times A \tag{3.8}$$

$$\frac{dr_{ClN}}{dr} = (a^2 r - aR\cos\phi) \times A \tag{3.9}$$

$$\frac{dr_{ClN}}{d\phi} = arR\sin\phi \times A \tag{3.10}$$

$$\frac{dr_{NO}}{dR} = 0 \tag{3.11}$$

$$\frac{dr_{NO}}{dr} = 1 \tag{3.12}$$

$$\frac{dr_{NO}}{d\phi} = 0 \tag{3.13}$$

$$\frac{d\theta}{dR} = B \times \left(\cos\phi A + (ar - R\cos\phi)(R - ar\cos\phi) A^3 \right) \tag{3.14}$$

$$\frac{d\theta}{dr} = - \left(aA - (ar - R\cos\phi)(2a^2 r - 2aR\cos\phi) A^{\frac{3}{2}} \right) / \left(1 - (ar - R\cos\phi)^2 \right)^{-\frac{1}{2}} \tag{3.15}$$

$$\frac{d\theta}{d\theta} = B \times \left(R\sin\phi A \left(1 - A^2 ar (ar - R\cos\phi) \right) \right) \tag{3.16}$$

using

$$A = \left(R^2 + (ar)^2 - 2Rar\cos\phi \right)^{-\frac{1}{2}} \tag{3.17}$$

$$B = \left(1 - ((ar - R\cos\phi) A)^2 \right)^{-\frac{1}{2}}. \tag{3.18}$$

The constant $a = 0.533205$ once again represents the centre of mass of the r_{NO} bond.

3.6.1 Initial wavefunction

The initial wavefunction was a six-dimensional Wigner distribution function prepared by George McBane to represent the lowest vibrational state on the $1\,^1A'$ state PES. This was a product of six Gaussians in the phase space of the Jacobi coordinates and their momenta. For each individual coordinate the vibration was treated as a harmonic oscillator, giving a Wigner distribution of the form [18]:

$$P_W^{(0)}(x, P_x) = (\pi\hbar)^{-1} \exp\left(\frac{-2\alpha(x - x_e)}{\hbar} \right) \exp\left(\frac{-P^2}{2\alpha\hbar} \right) \tag{3.19}$$

for coordinate x (with an equilibrium value of x_e), where

$$\alpha = \frac{m\omega_x^{HO}}{2}. \tag{3.20}$$
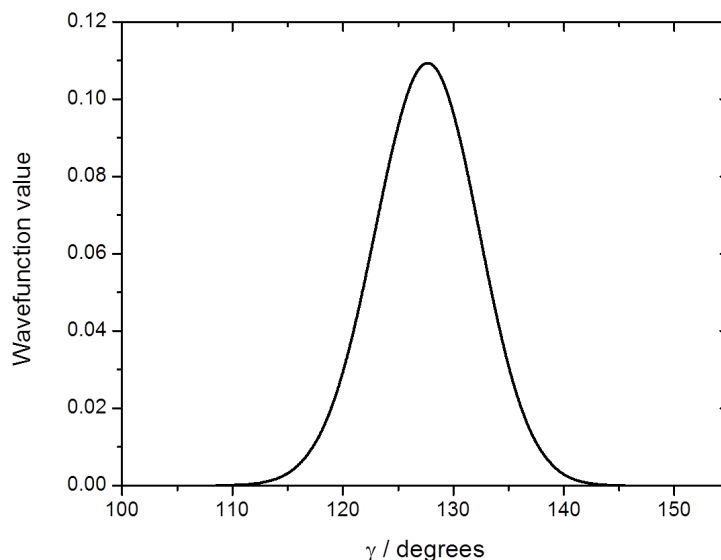
Figure 3.27: A cut through the classical initial wavepacket on the 1 ^{1}A$'$ state at the FC geometry of $R = 4.34$ bohr, $r = 2.15$ bohr.

Figure 3.27 shows a cut through this initial wavefunction, showing that it has a similar form to that produced fully quantum mechanically. The mean positions in each Jacobi coordinate were:

- $R = 4.350$, $dR = 0.148$ bohr
- $r = 2.168$, $dr = 0.0941$ bohr
- $\phi = 52.4°$, $d\phi = 4.62°$, equivalent to $\gamma = 127.6°$

These values are similar, but not identical, to those in the quantum wavepacket: the classical wavefunction has a longer mean r_{NO} bond length and is slightly wider in all coordinates.

3.6.2   Single-surface trajectories

Single-surface trajectories were run on the 2 ^{1}A$'$ state at a variety of energies: every 0.1 eV from 3.0 to 4.0 eV, at 3.283 eV (corresponding to the centre of the NO Q branch in 3D REMPI experiments described later in section 3.7), 3.348 eV (centre of R branch in 3D REMPI experiments) and 3.493 eV (experiments by Reisler *et al.* at 355 nm [69, 75]) and 3.573 eV (experiments by Busch and Wilson [71]). NO product state distributions were extracted. The paths of several individual trajectories were examined in more detail and
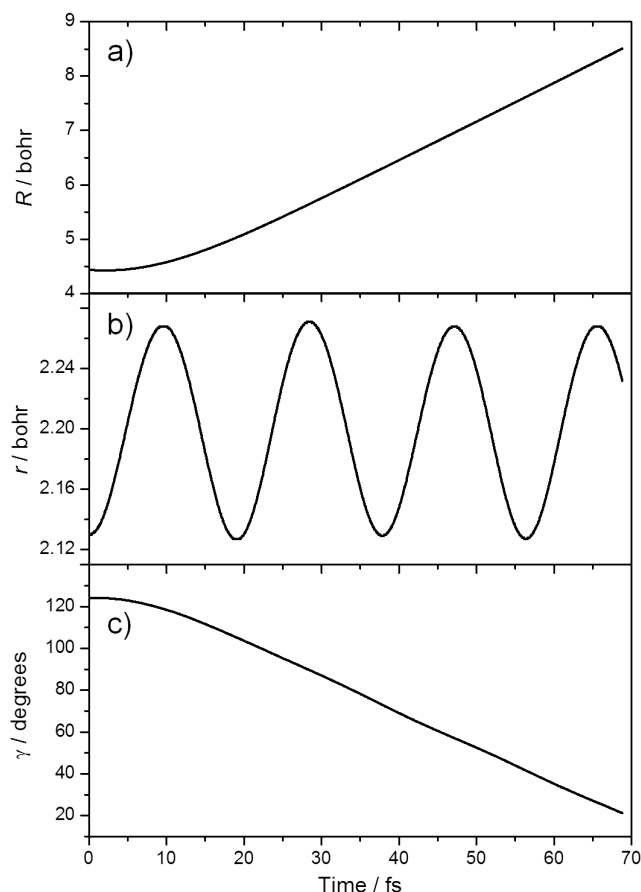
Figure 3.28: The variation in each of the Jacobi coordinates with time for an example trajectory on the $2\,^1A'$ surface. In this case an excitation energy of 3.283 eV was used.

were found to propagate sensibly across the PES; these paths are shown in figure 3.28 for a sample trajectory. An average propagation ran for $\sim$1400 steps, equating to $\sim$60 fs.

Figure 3.29 shows the variation of the NO product vibrational distribution with excitation energy. The majority of NO is formed in v = 0, with the proportion in v = 1 and 2 increasing as the energy increases; this is as would be expected given the quantum results and the lack of any features on the PES to force the trajectory to move significantly in the r_{NO} direction.

Figure 3.30 gives NO rotational distributions for a few excitation energies. As with the quantum distributions, these peak at high j, are Gaussian-shaped and narrow. Figure 3.31 shows how the peak j and FWHM of the NO rotational distribution vary as the excitation energy is changed. As the energy increases, the peak j increases and the distributions become wider, again as would be expected.
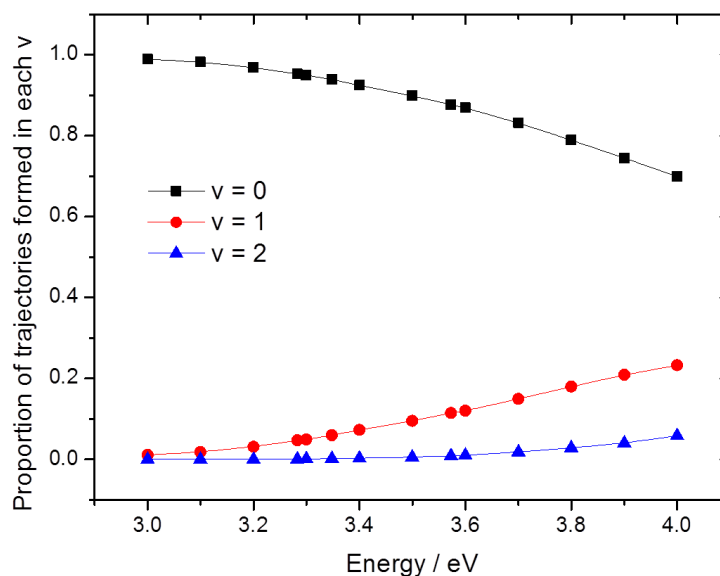
Figure 3.29: The proportion of trajectories ending in each NO vibrational state following dissociation on the $2\,^1A'$ surface for a range of energies.
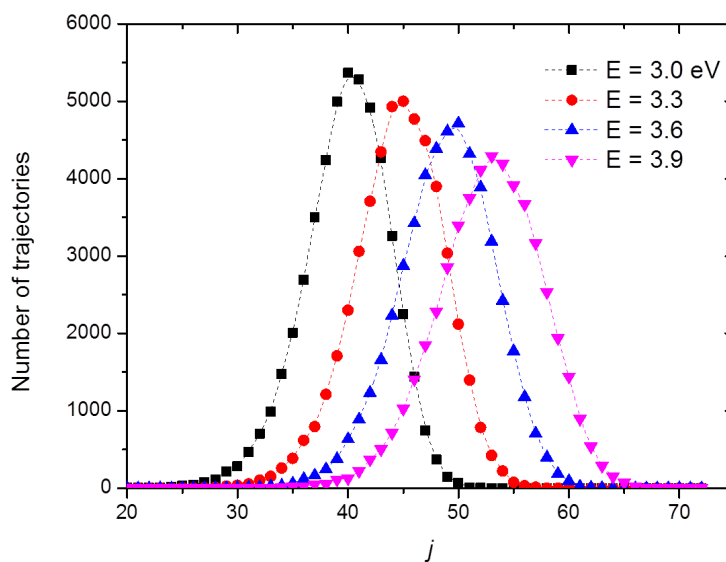
Figure 3.30: NO rotational distributions generated from classical trajectory calculations on the $2\,^1A'$ state for different excitation energies. The number of trajectories (out of a total 50 000) ending in each rotational state is shown for each enegy.
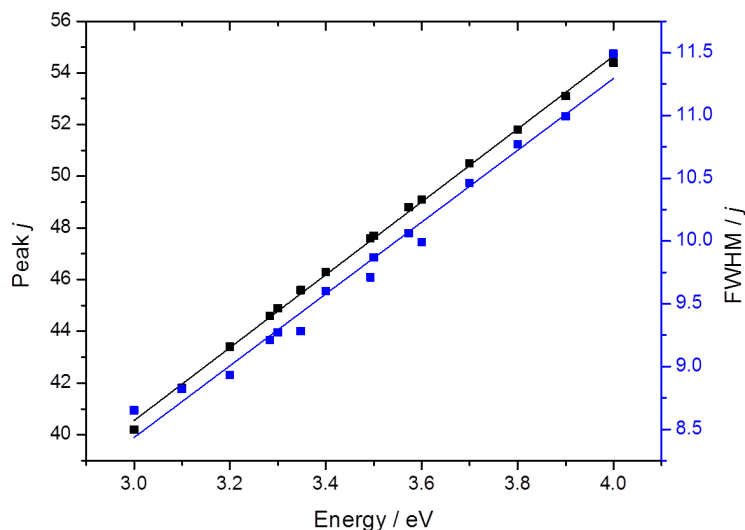
Figure 3.31: The variation of the peak j and the FWHM of the NO rotational distributions generated from classical trajectory calculations at different energies.

The results above imply that these single-surface calculations are behaving sensibly and giving results very close to the quantum equivalents. This shows they are a valid basis on which to build more complicated calculations. Their accuracy is likely due to the fact that the photodissociation on the 2 ^{1}A$'$ state is rapid and direct, and so is essentially a classical process.

3.6.3   Beta parameter calculations

As described in section 2.2.2, β anisotropy parameters can be calculated using classical trajectory results combined with TDMs. These can then be used to derive further information about the photodissociation process: if there is a change in β upon changing energy or product quantum state, it implies a change in the photodissociation dynamics. Here, the values of β are found for the trajectories producing each NO rotational state.

TDM surfaces in body-fixed y and z coordinates were, like the PESs, created using 3D cubic splines of the *ab initio* results. Both the MRCI and EOM-CCSD level TDMs were used. Before fitting the splines the TDM values were first multiplied by a factor of $\sqrt{\sin\phi}$. This is for two reasons: firstly, it serves as a weighting function when the β parameters are calculated, and secondly it tends to damp out sharp changes in the TDM functions, leading to smoother spline fits. The results were binned according to NO rotational state
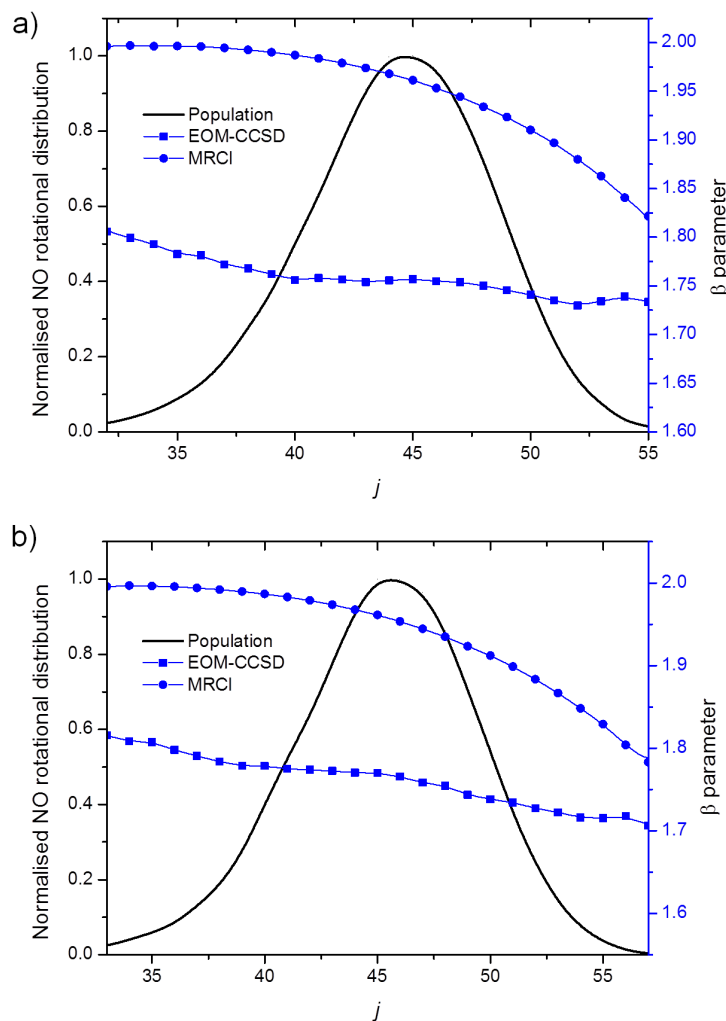
Figure 3.32: The variation of β with NO rotational state, using TDMs calculated at the MRCI and EOM-CCSD levels. These curves are superimposed with the NO rotational distributions. Panel a) shows the results for an excitation energy of 3.283 eV (Q branch) and panel b) shows results for 3.3485 eV (R branch).

and then averaged.

Figure 3.32 shows the variation of β with j for excitation energies of 3.283 (experimental Q branch) and 3.3485 eV (experimental R branch). The values for β are always positive and high, but there are nonetheless significant differences between those produced using the different TDM functions. Those for the MRCI TDMs are very close to 2, tailing off slightly at high j, whereas those for the EOM-CCSD TDMs are smaller, flatter and slightly less smooth. There are no dramatic changes in β, implying the photodissociation dynamics are very similar for all the trajectories.

To work out which set of β parameters is most valid, its expected value needs to

be considered. As the 2 ^{1}A$'$ state dissociates rapidly, β should be close to a limiting value, either 2 or -1. Which of these is more likely can be found by considering the vector correlation between μ, the direction of the TDM, and v, the photofragment recoil velocity. If these are fully parallel, β will be 2, whereas if they are fully perpendicular it will be -1. Here, it has been shown that μ lies almost entirely along the dissociative R coordinate, and so $\beta = 2$ is expected.

The tailing off of β at high j can be explained on simple kinetic grounds: the more energy that goes into rotation, the less there is available to go into translational motion, and hence the photodissociation process will slow down. This can be tested by comparing the dissociation times (i.e. the time over which the trajectory is propagated, until R reaches 8.5 bohr) for trajectories producing NO in higher and lower j. For an excitation energy of 3.283 eV, the average dissociation time for $j = 40$ is 65 fs, and that for $j = 50$ is 69 fs. Similarly, for an energy of 3.3485 eV, the time for $j = 38$ is 64 fs, whereas that for $j = 53$ is 69 fs. This change is small, but so is the decrease in β at high j, and so this seems a reasonable explanation. Again, this observation lends support to the MRCI level TDMs as, particularly for the 3.283 eV results, this tailing off is more marked.

Results for other excitation energies are very similar to those shown. The variation of β with NO vibrational state was also investigated, but no real difference was found. Similarly, in surface-hopping calculations no significant difference was found between the results for trajectories which did or did not pass through the conical intersection.

3.6.4 Surface-hopping calculations

Tully's fewest switches surface-hopping algorithm as described in section 3.6.4, but using electronic state amplitudes instead of density matrices to find the state populations, was used to model the transitions between the electronic states. The electronic state amplitudes for both the 1 and 2 ^{1}A$'$ states were calculated at each point along each trajectory; if the coupling was strong enough a hop may have taken place. It is common for multiple hops to occur on the same trajectory.

There are several ways to adjust the momenta to enable the total energy to be con-

served after a hop has taken place. The methods implemented in the software used were a 'democratic' prescription, whereby the momenta in each Jacobi coordinate are changed equally [116] and the 'g' prescription, in which the momentum is adjusted along the gradient of the energy difference between the two states [145]. For the first approach, if there is insufficient momentum in any of these coordinates when an upward hop takes place, it is deemed frustrated and does not occur. Both methods were tested, and the results were very similar, with few hops being frustrated. The democratic prescription was therefore used for simplicity.

The overall coupling between the states is taken as:

$$\chi = \frac{dR}{dt}\left\langle \Psi_1 \left| \frac{\partial}{\partial R} \right| \Psi_2 \right\rangle + \frac{dr}{dt}\left\langle \Psi_1 \left| \frac{\partial}{\partial r} \right| \Psi_2 \right\rangle + \frac{d\phi}{dt}\left\langle \Psi_1 \left| \frac{\partial}{\partial \phi} \right| \Psi_2 \right\rangle \tag{3.21}$$

where the $\langle \Psi_1 | \frac{\partial}{\partial x} | \Psi_2 \rangle$ are the NACMEs calculated in the direction of coordinate x. When they occured, transitions took place in the region where the CoIn was seen to be present from the PESs, i.e. at around $R = 6.5$ to 7.5 bohr, $r \sim 2.2$ bohr and $\gamma \sim 80°$, after ~ 40 fs.

Figure 3.33 shows how the proportion of trajectories ending in the lower $1\ ^1A'$ state varies with excitation energy: the proportion is never very high, being at most 12%, and decreases as the energy increases. This is in agreement with what would be expected from the simple 1D Landau-Zener model [20]. In this, the non-adiabatic crossing probability P is given as a function of the energy difference $V_1 - V_2$ between the two *diabatic* states, the coupling V_{12} between them and the velocity v along coordinate x:

$$P = \exp\left(-\frac{2\pi V_{12}^2}{\hbar v \frac{\partial (V_1 - V_2)}{\partial x}}\right) \tag{3.22}$$

As the excitation energy increases, the velocity of the trajectory will increase, leading to a reduction in P, as has been seen here. Intuitively this is sensible: a wavepacket that is moving more quickly is less likely to become caught in the cone of a conical intersection.

The NO vibrational state distributions are similar for trajectories ending in both states, with the majority formed in v = 0. The proportion of NO produced in higher vibrational
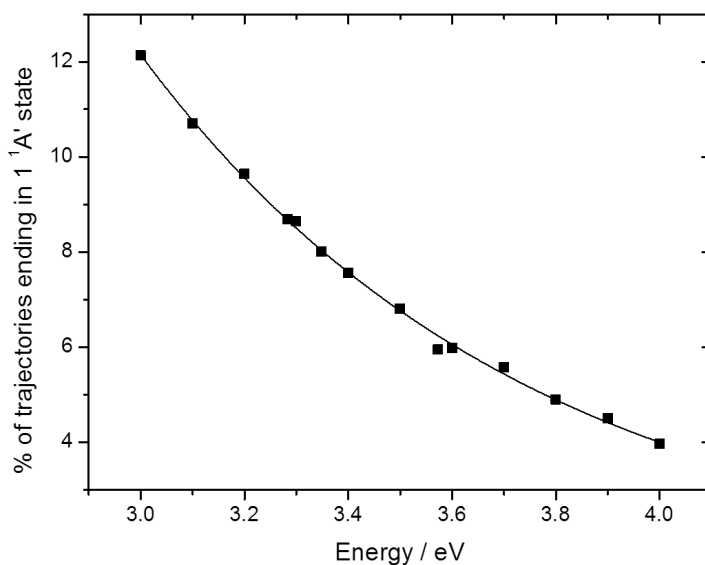
Figure 3.33: The percentage of classical trajectories ending in the 1 ^{1}A$'$ state across a range of energies.

states does of course increase with excitation energy, but even at 3.8 eV nearly 80% of the NO is still in its ground state. The results for a few sample energies are shown in table 3.8. Note that for higher energies the proportion of NO in excited vibrational states increases more rapidly for the trajectories ending on the 1 ^{1}A$'$ state than the 2 ^{1}A$'$, but the difference is not large.

The difference between the NO rotational distributions ending in the different states is more marked. The distributions have very similar widths and shapes, but those from trajectories ending in the 1 ^{1}A$'$ state are shifted to lower j. For example, at an excitation

Energy / eV	Vibrational state					
	0	0	1	1	2	2
3	0.987	0.989	0.013	0.011	0.000	0.000
3.1	0.975	0.980	0.025	0.020	0.000	0.000
3.283	0.937	0.953	0.061	0.046	0.002	0.001
3.3485	0.928	0.938	0.070	0.061	0.002	0.001
3.493	0.874	0.904	0.118	0.090	0.007	0.005
3.8	0.717	0.795	0.237	0.176	0.042	0.027

Table 3.8: The proportion of NO formed in each vibrational state v for a range of energies following trajectory surface hopping calculations. The columns shaded white are for trajectories ending in the 1 ^{1}A$'$ state, and those shaded grey are for trajectories ending in the 2 ^{1}A$'$ state. The energies of 3.283, 3.3485 and 3.493 eV correspond to energies used in experiments.

energy of 3.283 eV (equivalent to the Q branch energy in 3D REMPI experiments considered later), the rotational distribution for trajectories ending on the $1\,^1A'$ state is shifted $3j$ lower than that for trajectories ending on the $2\,^1A'$ state. The normalised rotational distributions for 3.283 and 3.8 eV are given in figure 3.34. Note that the distributions for the $1\,^1A'$ state are less smooth as they are based on fewer trajectories, particularly at higher energies.

There are two possible explanations for this, albeit small, difference in the NO rotational distributions. The first is that the topology of the $1\,^1A'$ PES causes the trajectories which pass through the CoIn to lose momentum in the γ coordinate, when compared to those which remain on the $2\,^1A'$ surface. The second is that the location of the CoIn seam is such that only trajectories which have lower momentum in the γ coordinate are likely to come near it.

Figure 3.35 shows cuts through the 2 PESs in Jacobi coordinates for a fixed $r = 2.2$ bohr, the value for which the coupling is greatest. The energies of the PESs do not change dramatically in this area, but there are some features which could potentially have an effect upon the trajectories. If the trajectory remains on the $2\,^1A'$ state, then the slope is essentially downhill all the way, and so would be expected to continue in the same direction in which it arrived in the asymptotic region. However, on the $1\,^1A'$ state there is a small downwards slope in the γ coordinate, corresponding to the edge of the well leading to the ClON isomer. This could initially give the trajectory further impetus in the γ direction, but upon hitting the other side of the well it could straighten out, leading to a lower eventual angular velocity. As out in the asymptotic region the well is not very deep, this would only have a small effect, but as the NO rotational distribution for trajectories ending on the ground state is only lowered by $3j$, this seems feasible.

It is impossible to thoroughly check the paths of all the trajectories and hence see if their paths are indeed altered significantly after passing through the CoIn. However, a small portion of the trajectories ending in each state have been investigated in more detail, and no significant change is seen. This implies the second of the two explanations is more likely. Figure 3.36 shows the paths of two example trajectories ending in the 1 and $2\,^1A'$ states in terms of the γ and R coordinates. The excitation energy was 3.283 eV in both
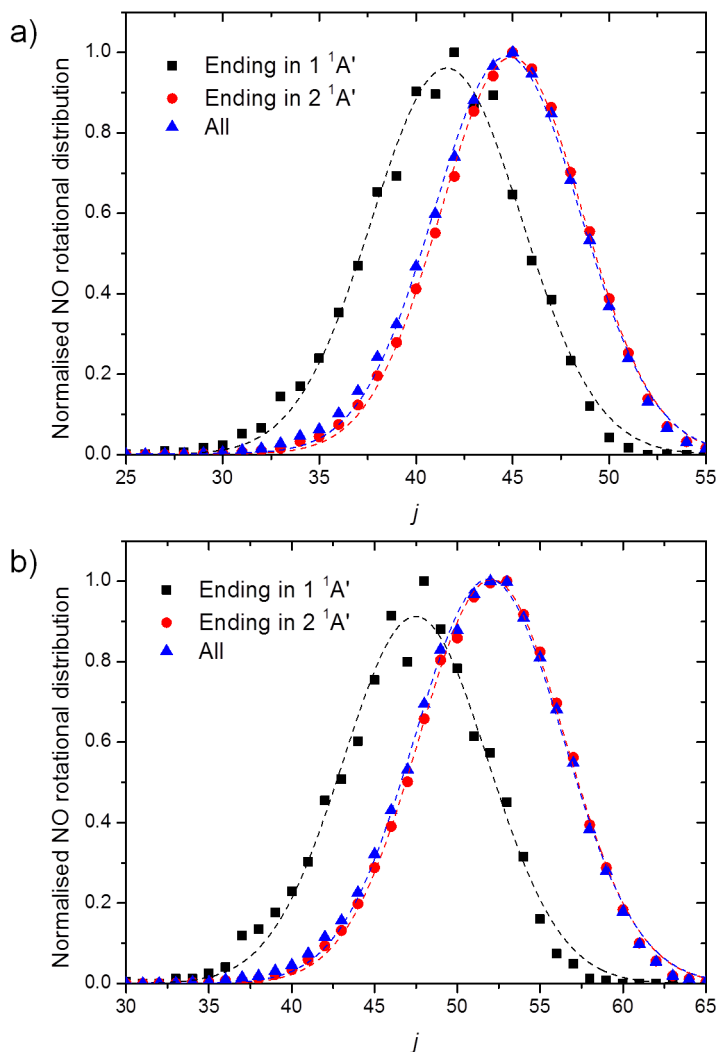
Figure 3.34: NO rotational distributions produced from trajectory surface hopping calculations, for trajectories ending in the 1 and 2 ^{1}A$'$ states. Panel a) shows results for an excitation energy of 3.283 eV, panel b) shows results for an excitation energy of 3.8 eV. The distributions have been fitted with Gaussian functions.
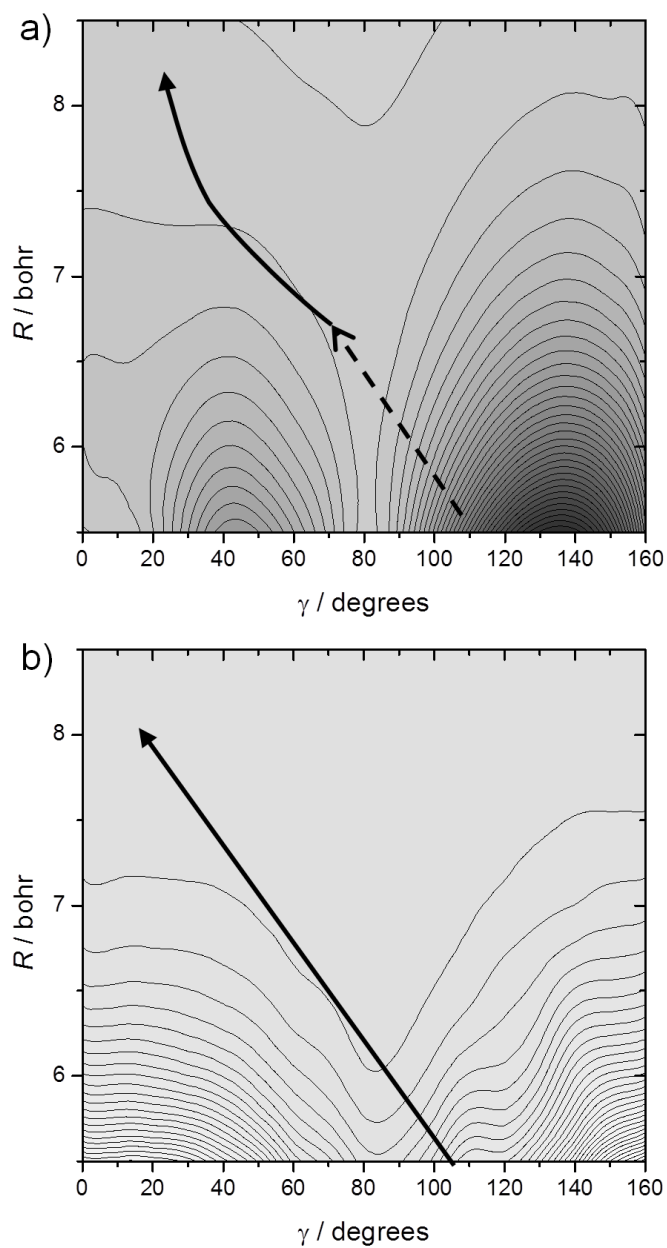
Figure 3.35: Cuts through the 1 (panel a)) and 2 (panel b)) $^1\text{A}'$ PESs in the γ and R coordinates for a fixed r of 2.2 bohr. The sketched lines show how the paths of trajectories could potentially be modified by the ground state surface after passing through the CoIn. Contour lines are 0.025 eV apart, with darker shades corresponding to lower energies.
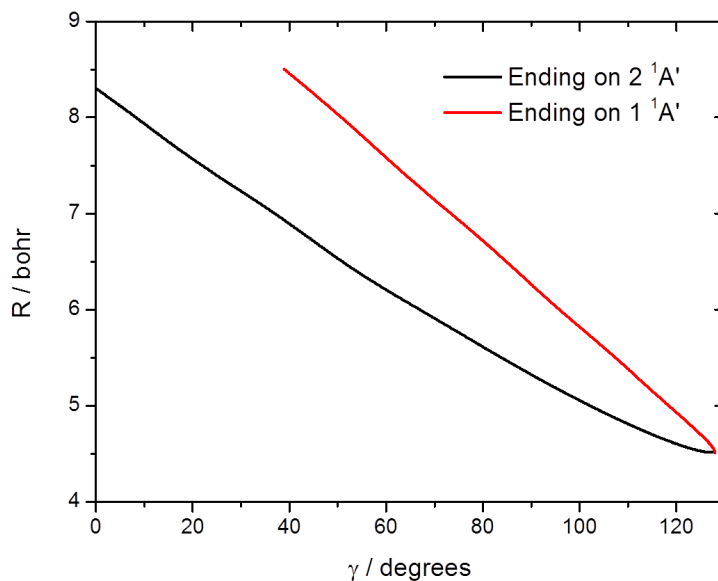
Figure 3.36: The paths of example trajectories ending in the 1 and 2 ^{1}A$'$ states in the γ and R coordinates. The excitation energy was 3.283 eV in both cases, and the starting geometries of the trajectories were very similar.

cases, and the starting geometries of the trajectories were very similar. The change in γ for the trajectory which did pass through the CoIn is considerably less than for the trajectory which did not, resulting in a final NO rotational state of $j = 45$ as opposed to $j = 51$. The trajectory which remained on the 2 ^{1}A$'$ surface throughout does not enter the region where the non-adiabatic coupling is highest. The paths of both trajectories are smooth; there is no kink when the CoIn region is reached. Note that as only a small proportion of trajectories end on the ground state, the effect of the CoIn is unlikely to be seen clearly in the experimental NO rotational distributions.

3.7 Comparison with experiment

3.7.1 3D REMPI spectrum

Velocity resolved REMPI spectra, produced using a variant of velocity map imaging, were recorded by Alan Sage and Jadwiga Milkiewicz to investigate photodissociation on the 2 ^{1}A$'$ state of ClNO experimentally [120]. The ClNO was excited using nanosecond lasers in the range 369 to 379 nm, where the wavelength spans a number of (two-photon)

rotational transitions in the D $^2\Sigma \leftarrow$ X $^2\Pi$ (0,0) and C $^2\Pi \leftarrow$ X $^2\Pi$ (0,0) bands of NO (figure 3.37 panels b) and a) respectively). The spectra shown are comprised of several shorter scans which have been 'stitched' together. In order to assign the 3D REMPI spectrum, the wavelengths of each of the possible rotationally resolved REMPI transitions were calculated from the well known spectroscopic constants of the D $^2\Sigma$, C $^2\Pi$ and X $^2\Pi$ states of NO [146, 147].
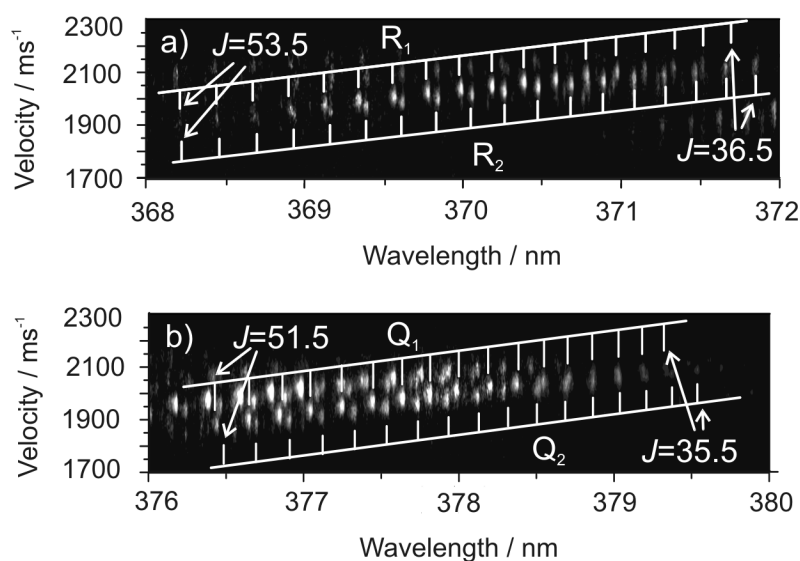
Figure 3.37: Experimental 3D REMPI spectra obtained and assigned by Alan Sage and Jadwiga Milkiewicz. Panel a) shows results obtained via the Q_1 (circles) and Q_2 (triangles) branches of the C $\leftarrow$ X transition in NO. Panel b) shows results obtained via the R_1 (circles) and R_2 (triangles) branches of the D $\leftarrow$ X transition

As the experiment is one-colour, i.e. the same laser pulse is used to both dissociate the ClNO and probe the NO product, the different rotational branches are probed at slightly different wavelengths. The branches for the C and D states of NO therefore need to be considered separately. The C state is predissociative and so gives rise to larger linewidths than the D state.

In figure 3.37, portions of the experimental spectrum are overlaid with expected peak positions. The agreement between these is good, implying that the assignment is reliable. It also shows that the NO fragments are produced highly rotationally excited and in a narrow distribution, which is in agreement with the computational results. From the intensities of the peaks in the the rotational distributions can be extracted, and then

compared with those calculated.

The experiment yields rotational distributions in terms of *J*, the total angular momentum quantum number. To make direct comparison with the computational results these have been converted to give distributions in terms of *j*. To achieve this, Hund's coupling case (b) has been invoked as the spin-orbit coupling constant for NO is small (123 cm^{-1} [59]) and the degree of rotational excitation is high. More detail on the experiments can be found in the Master's thesis of Jadwiga Milkiewicz [148].

3.7.2   NO vibrational distributions

In the 3D REMPI experiment, all the NO was found to be in its lowest vibrational state. Similarly, Reisler *et. al.* found only NO in v = 0 in photofragment yield spectroscopy experiments [69]. The proportion of NO produced in v = 0 following photodissociation at the energies used in these experiments has been calculated from the wavepacket propagations using both the MRCI and EOM-CCSD TDM functions. The results are given in table 3.9, and show clearly that the agreement is better when the MRCI TDM function is used, as only a negligible amount of vibrationally excited NO is produced. When the EOM-CCSD function is used, up to 17% of the NO is formed in excited vibrational states, a proportion that would have been detectable in the experiments, particularly those of Reisler.

Energy	% of NO formed in v = 0	
	MRCI	EOM-CCSD
Q branch	98	91
R branch	97	89
355 nm	97	83

Table 3.9: The proportion of NO formed in v = 0 calculated from wavepacket propagations using the MRCI and EOM-CCSD TDMs, at energies corresponding to the Q and R branches of the 3D REMPI spectra, and Reisler's experiments (355 nm).

3.7.3   NO rotational distributions

The R_1 and R_2 branches of the $D \leftarrow X$ transition in NO were probed experimentally between 368.9 and 371.5 nm (equivalent to 3.34 to 3.36 eV). Rotational distributions for both spin-orbit states of NO are shown in panel b) of figure 3.38 with those from the R_1 branch ($^2\Pi_{1/2}$) marked by squares and those from the R_2 branch ($^2\Pi_{3/2}$) marked by triangles. Both distributions have similar FWHM values of about $9j$, with the R_1 distribution centred at $j = 46$ and the R_2 centred a little lower at $j = 43$. These results are overlaid with the calculated distributions for this small energy range, both quantum and classical. The quantum distribution when the MRCI TDMs were used peaks at $j = 45$ and has a FWHM of $9.5j$; when EOM-CCSD TDMs were used the distribution has the same width but peaks $\sim 1.5j$ lower. The classical distribution also shows the same shape but peaks at $j = 46$.

The distributions resulting from the Q_1 ($^2\Pi_{1/2}$, squares) and Q_2 ($^2\Pi_{3/2}$, triangles) branches of the $C \leftarrow X$ transition between 376.6 to 378.7 nm (3.27 to 3.29 eV) are plotted in panel a) of figure 3.38. Due to the pre-dissociative nature of the C state the distributions are noisier than those for the D state, but still exhibit similar features. The widths of the distributions are similar to those for the D state, being ~ 8-$9j$ and the Q_2 distribution is shifted a little lower than that for the Q_1 branch, being centred at $j \sim 44$ as opposed to $j \sim 45$. The calculated quantum distribution for the C state energy range using the MRCI TDMs has a peak at $j = 44$ and a FWHM of $9.5j$, and the classical distribution has the same width but again peaks $1j$ higher at $j = 45$. The quantum distribution using the EOM-CCSD TDMs is very similar to the classical distribution, but slightly wider.

Despite some noise in the experimental distributions it is evident that the agreement between the experimental and computational results is very good. The theory recreates the overall shape and widths of the distributions well, with the maxima of the rotational distributions agreeing to within 1-3 quanta. The quantum results when the MRCI TDMs are used are better than the classical distributions, but the difference is only $1j$. For the R branch, the results when the EOM-CCSD TDMs are used are perhaps slightly better than those for the MRCI TDMs, but for the Q branch they are slightly worse. It is therefore
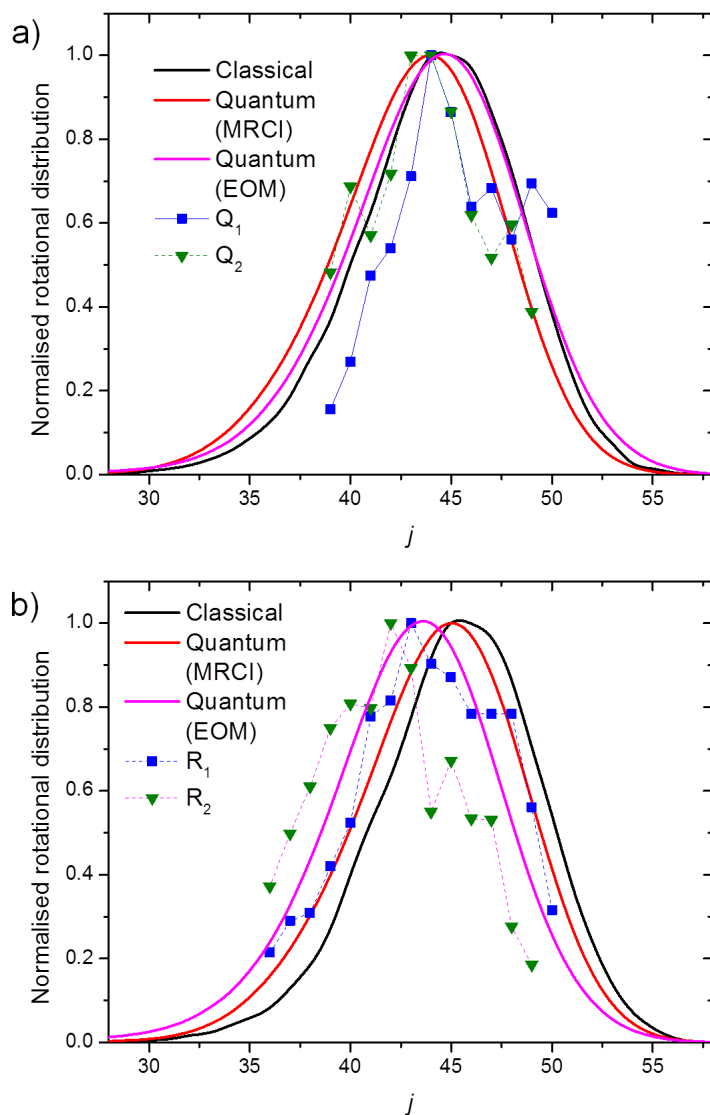
Figure 3.38: Comparison of calculated (quantum and classical) and experimental NO rotational distributions. Panel a) shows results obtained via the Q_1 (squares) and Q_2 (triangles) branches of the $C \leftarrow X$ transition in NO. Panel b) shows results obtained via the R_1 (squares) and R_2 (triangles) branches of the $D \leftarrow X$ transition.

difficult to determine which function is most valid from the rotational distributions. The energy difference between the C and D state transitions is small, but nonetheless appears to cause a shift in the NO rotational distribution of ~1 quanta towards higher j for the shorter-wavelength D state. The signal to noise in the experimental results is not sufficient to confirm this effect, but the corresponding shift in the calculated distributions suggests it is real. In addition, the experimental results suggest that the rotational distributions arising from the excited spin-orbit state of NO, $^2\Pi_{3/2}$, are shifted 1-2j higher than those from its ground $^2\Pi_{1/2}$ state, an observation that may be qualitatively explained on energetic grounds.

Previous studies on the photodissociation of the $2\,^1A'$ state of ClNO have been carried out at the slightly lower wavelength of 355 nm. Quantum results using the MRCI TDMs at the equivalent energy predict an NO rotational distribution that peaks at $j = 47$ with a shape and FWHM very similar to the distributions presented above. This is in good agreement with the distribution measured by Torres, Pipes and Baugh [77]. The calculation also reproduces the shape of the distribution obtained by Reisler and co-workers, although the calculated peak is a few quanta higher than the measurement [69]. There is very little difference in the distributions in the two NO spin-orbit states in the observations reported by Torres *et al.*, whereas the results reported by Reisler appear to show a slight shift of the NO $^2\Pi_{3/2}$ distribution to lower j, which is similar to what has been observed in the 3D REMPI experiment.

3.7.4 β parameters

Despite the noise in the 3D-REMPI data, β parameters were extracted from the images following angular integration, using a program written by Alan Sage. The results are shown in figure 3.39. The first point to note is that the values of β for each J across the bands are not the same, immediately casting doubt upon their validity. The values from the Q branches vary only across a small range, but average at about 0.6, which intuitively seems too low for such a rapid photodissociation. The values for the R branches vary much more wildly, averaging about 1.2, which again is rather low. This large variation
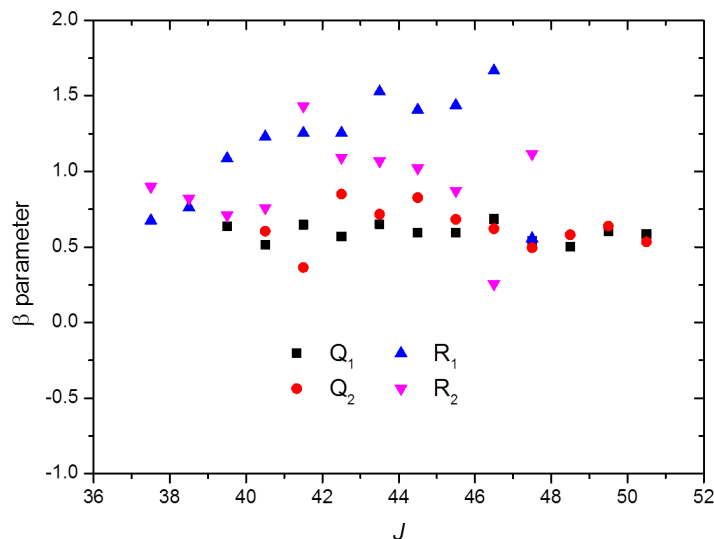
Figure 3.39: β parameters for different values of total angular momentum J extracted from the R and Q branches of the 3D REMPI data.

is not altogether surprising given the quality of the experimental data - to extract such information reliably it is necessary to collect single images over a large number of laser shots, as opposed to the quick scans employed in the 3D REMPI method. The values of β shown here cannot therefore be considered reliable.

Other groups have also extracted values of β from experimental data. For example, Busch and Wilson found it to be 1.76 ± 0.08 in 1972 using results from photofragment spectroscopy experiments at 347 nm. Reisler and coworkers used a more advanced form of a similar technique to produce a value of $\beta = 1.8 \pm 0.2$ for photodissociation at 355 nm, and Cao *et. al.* obtained values of 1.63 ± 0.1 (when ground spin-orbit Cl was formed) and 1.78 ± 0.1 (for Cl*) at the same photolysis wavelength. At 355 nm (3.493 eV), the values of β calculated here are 1.93 (MRCI TDMs) and 1.75 (EOM-CCSD TDMs); the results using the EOM-CCSD TDMs agree slightly better with experiment, although there is little real difference. At 347 nm, the MRCI TDMs give $\beta = 1.92$ and the EOM-CCSD TDMs give $\beta = 1.73$, so once again the EOM-CCSD method gives results closer to experiment.

3.8 Conclusions

The photodissociation of ClNO on the $2\,^1A'$ state of ClNO has been studied computationally in more detail than before, both fully quantum-mechanically and semi-classically. TDM functions have been used to more realistically model the transference of the wavepacket from the ground to excited state, however it is not obvious as to whether the MRCI or EOM-CCSD method produces the most accurate functions. The EOM-CCSD function leads to β parameters which match better with experiment, whereas the MRCI function leads to more accurate NO vibrational distributions. Given the greater smoothness of the MRCI functions, and the greater reliability of the experimental vibrational state measurements over those for β parameters, it is likely that the MRCI method is better here, but further work is necessary to confirm this.

A conical intersection in the asymptotic region has been discovered between the 1 and $2\,^1A'$ states. Classical trajectory surface hopping calculations have shown that a small proportion of the wavepacket can be expected to pass through this, but that it has little effect upon the overall dynamics. The NO rotational distribution for trajectories which end on the $1\,^1A'$ is however shifted slightly towards lower j.

As found in previous work [69, 71, 75, 77], the NO product is produced highly rotationally excited, but mostly in its ground vibrational state. Calculated NO product state distributions agree very well with experimental results, both from the Whitaker group and others. The classical and quantum results are very similar, showing that the photodissociation on the $2\,^1A'$ state is essentially a classical process. Further experimental work is necessary to determine the accuracy of the calculated β parameters, but the values obtained by use of TDMs calculated at both the MRCI and EOM-CCSD methods both appear reasonable.

3.8.1 Future work

The photodissociation of the $2\,^1A'$ state of ClNO in the gas phase is a problem that has essentially been solved, barring full understanding of the spin-orbit product branching ratios as discussed later in chapter 6. However, it would be interesting to investigate the system

further in solution. Reid *et al.* carried out experiments investigating the photochemistry of ClNO in the solution phase [149, 150]. When ClNO is photolysed at 266 nm after being dissolved in acetonitrile, geminate recombination occurs, leading to ground state ClNO being re-formed. Interestingly, the ClON isomer is also formed, with a quantum yield of 0.07. Although the excitation energy is higher than those considered here for the $2\,^1A'$ state, it may be possible for the system to pass through the conical intersection between the 1 and $2\,^1A'$ states as the fragments recombine, moving along the asymptotic region of the PESs. Depending upon the path taken, some wavepacket density could then pass into the minimum corresponding to the ClON isomer, as seen in figure 3.7. Note however that no geminate recombination is seen when cyclohexane is used as a solvent, and that there are many factors at play [151].

Further calculations would be necessary to test this highly speculative hypothesis. For example, such solution phase dynamics could be modelled by building a barrier in the asymptotic region of the ClNO excited state PESs. The wavepacket could hit this barrier and be reflected, returning to the region of the CoIn. The position and character of this barrier could be adjusted depending on the solvent being investigated. Calculations could also be undertaken to study more accurately the effect of the solvent cage upon the energies and topologies of the excited state PESs, and hence to see if the geometry of the CoIn varies, or indeed if other such interactions exist between higher energy states.

Chapter 4

Photodissociation on the 1 ^{3}A$''$ state of ClNO

4.1 Summary

The PES of the 1 ^{3}A$''$ state of ClNO has been calculated and used in both wavepacket dynamics and classical trajectory calculations. Transition dipole moment surfaces have been calculated for the excitation from the ground 1 ^{1}A$'$ state by taking account of spin-orbit coupling. NO product state distributions have been calculated, and the provenance of these has been investigated in considerable detail. The agreement with both experiment and previous theoretical results is good, showing that the PES can reliably be used as a basis for coherent control calculations.

4.2 Potential energy surfaces

As for the singlet states, it was possible to calculate the 1 ^{3}A$''$ PES at an advanced level of theory. Once again the AVQZ basis set was used, and a full valence active space was chosen for the CAS step. The states included in the state-averaging were varied, with the best results found when the first three states of ^{3}A$''$ symmetry were used. These all converge on the lowest energy asymptote, corresponding to NO and Cl in their ground electronic states. The problem of the N 1s orbital being rotated into the active space in
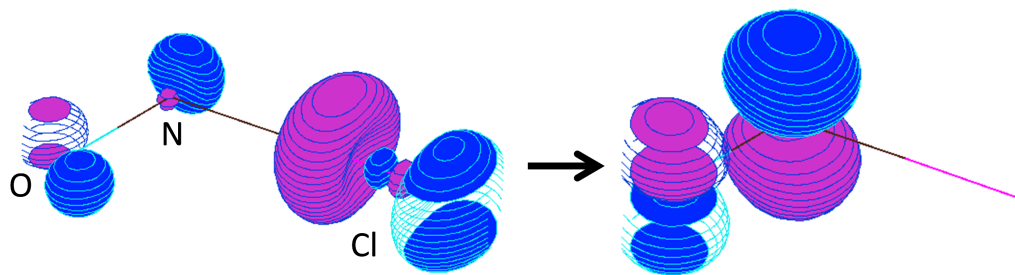
Figure 4.1: A visualisation of the orbitals involved in the excitation from the 1 $^1A'$ to 1 $^3A''$ state, pictured using Molden [126] following a single-point calculation at the CASSCF/STO-3G level. The predominant excitation is out of a Cl $3p_z$ orbital into an NO $(2p_x)$ π^* orbital.

the asymptotic region of the PES was also found for these triplet states. Therefore, the same technique of using a restricted active space in these regions was employed. This led to smooth curves.

The CAS results reproduced all the key features of the PES, namely a well in the r_{NO} coordinate and a fairly shallow slope towards the exit channel in the FC region. This latter feature is crucial in determining the dissociation dynamics: the flatter this is, the longer the wavepacket will persist in the excited state. As also found by Schinke [64] this gradient was insufficiently small on the the CAS PES, and the excitation energies were too high, meaning the more expensive MRCI method was necessary. In the MRCI step of the PES calculations, only the 1 $^3A''$ state was calculated.

The primary excitation from the 1 $^1A'$ to 1 $^3A''$ state involves the promotion of an electron from a predominantly Cl $3p_x$ orbital to an NO $(2p_x)$ π^* orbital; these orbitals are illustrated in figure 4.1. As the excited state is a triplet, the single electrons in both of these orbitals then have the same spin. Although other electronic configurations play some part, this configuration contributes 95% of the whole to the CAS wavefunction.

4.2.1   MRCI level PES

Ab initio energies were calculated at 3360 points across the following geometries:

- r_{NO}: every 0.2 bohr from 1.8 to 3.0 bohr
- r_{ClN}: every 0.25 bohr from 2.75 to 10.0 bohr

- **bond angle θ:** every $10°$ from $20°$ to $170°$.

The Davidson correction using relaxed reference functions was used to approximate the contribution of quadruple excitations. The energies at individual points were then formed into a surface using 3D splines.

The dissociation energy of the 1 $^3A''$ state was calculated by taking the difference between the energy at the FC geometry and that at the same values of θ and r_{NO} but with r_{ClN} equal to 10 bohr, is -0.563 eV. This compares reasonably well with the value of D_e = -0.524 eV obtained from experimental data by Schinke *et al.* [64]. As the ground state was not calculated at the same time as the 1 $^3A''$ state, it is not possible to directly compare the energies of the two. Instead, the 1 $^3A''$ PES has been positioned in energy such that the vertical energy difference between it and the ground state at the FC geometry is equal to the experimentally-derived T_e of 2.193 eV [64]. After this adjustment has been applied the asymptotic energy is 1.613 eV, in excellent agreement both with experiment and the results in the preceding chapter from the $^1A'$ states.
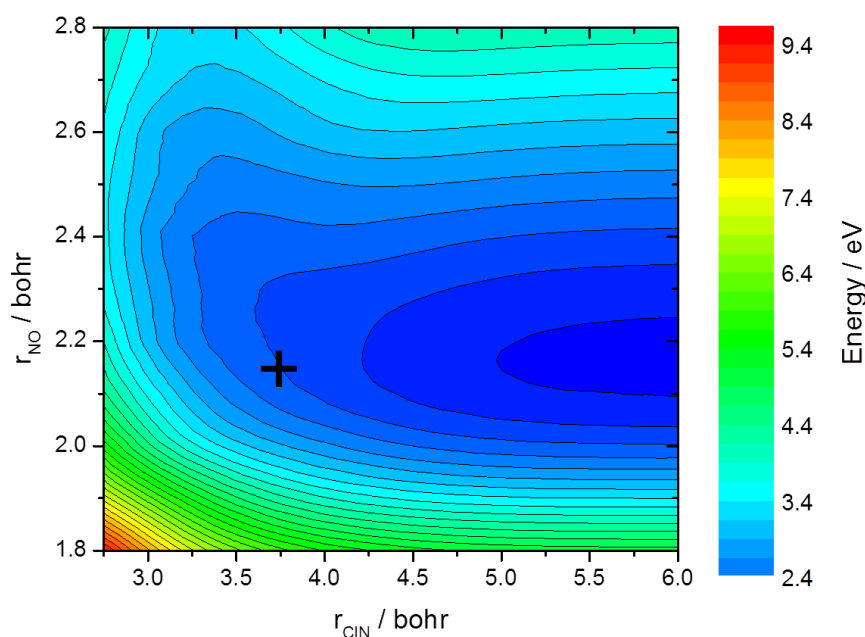
Figure 4.2: A cut through the 1 $^3A''$ PES for a fixed bond angle θ of $110°$. Contour lines are 0.25 eV apart. The cross marks the FC point.

A cut through the PES at $\theta = 110°$ is given in figure 4.2. Note that due to the downwards slope in the r_{NO} coordinate, an excited wavepacket will have some initial momen-

tum towards longer r_{NO}. The well in this direction is quite marked, although it is at a considerably higher energy than the exit channel. Figure 4.3 shows cuts through the surface for two values of r_{NO}. As the r_{NO} bond length is increased a minimum appears in the surface at ever-decreasing bond angles. This implies that some wavepacket density could become temporarily trapped in this well around the turning point of its oscillation in the the r_{NO} coordinate.
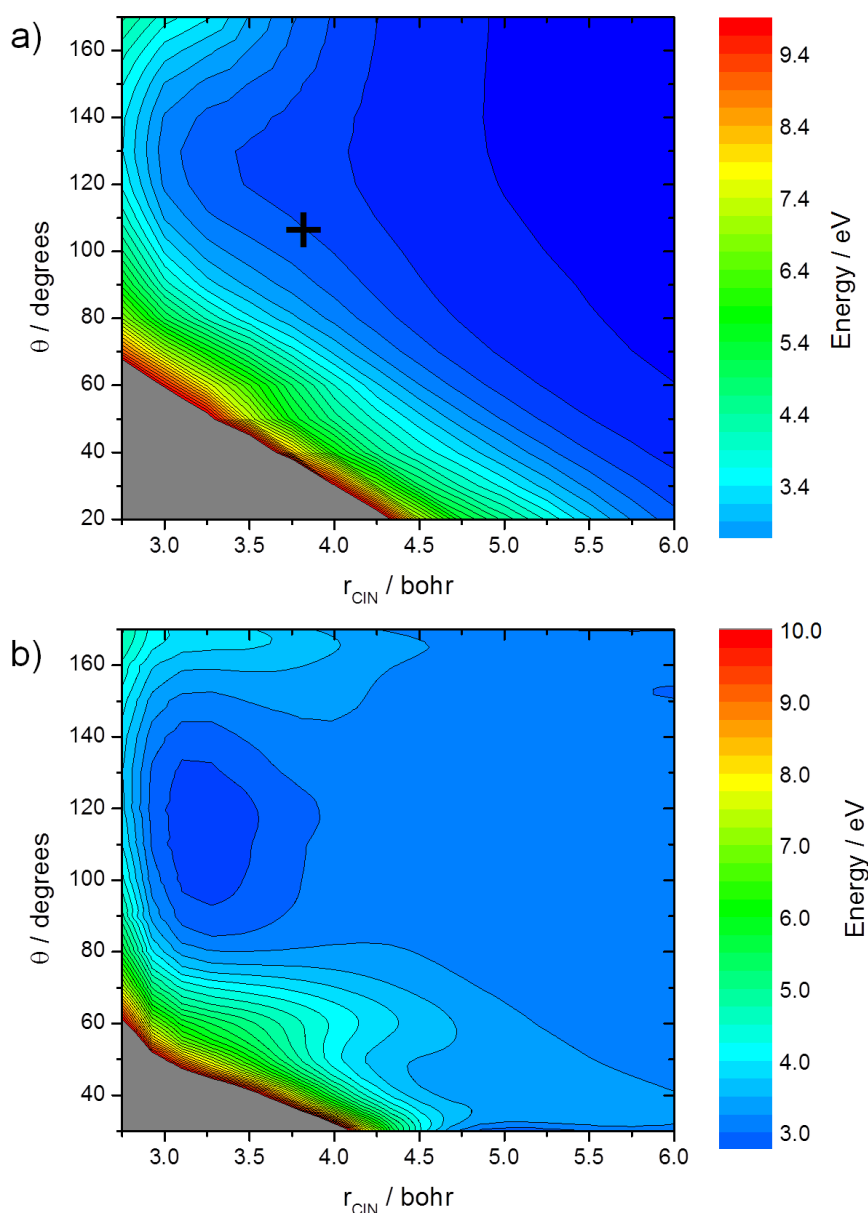
Figure 4.3: Cuts through the 1 $^3A''$ PES for fixed r_{NO} bond distances of 2.2 bohr (panel a)) and 2.6 bohr (panel b)). Contour lines are 0.25 eV apart. The cross marks the approximate FC point. Note the minimum which appears at around $\theta = 115°$ for the higher r_{NO} bond length.

4.3 Transition dipole moments

Viewed without consideration of spin-orbit coupling, the transition between the ground $1\ ^1A'$ state and the $1\ ^3A''$ state is forbidden as it involves a change of spin. However, the fact that the absorption spectrum for the state can be observed experimentally shows that the transition is indeed possible, mediated by spin-orbit coupling. Calculating the transition dipole moments for spin-forbidden transitions is difficult: when the standard BO Hamiltonian is employed, they will always be zero. Therefore to obtain the TDMs in this case, spin-orbit coupling needs to be taken into account by use of the Breit-Pauli Hamiltonian.

Further details of the calculations involving spin-orbit coupling will be given in the next chapter. Briefly, all 12 zeroth-order states converging on the lowest energy asymptote (NO and Cl in their ground electronic states) were included: $3 \times\ ^1A'$, $3 \times\ ^1A''$, $3 \times\ ^3A'$ and $3 \times\ ^3A''$. These combined to produced 24 spin-orbit states, 12 for each symmetry. All calculations were carried out at the CAS/AVTZ level.

Each triplet state splits into three spin-orbit states. Considered in a basis of the zeroth-order wavefunctions, the spin-orbit states corresponding to the original $1\ ^3A''$ state are the second and third A' states and the first A'' state, ordered according to their energies at the FC geometry. By comparison with the spin-orbit states considered in a symmetry-adapted basis, it was found that the first of these mostly derives from the T_- component of the triplet, the second mostly from the T_0 and the third mostly from the T_+.

The TDMs with the ground state for each of the spin-orbit states derived from the original $1\ ^3A''$ state are given in table 4.1 for a cut along the r_{ClN} coordinate in the FC region. The values for the 3 A' state are an order of magnitude or more greater than those for the 2 A' state. The values for the 1 A'' state are very small. It was therefore assumed the TDMs for the 2 A' and 1 A'' states could be neglected, as the contribution from the 3 A' state would dominate. The TDMs for state 3 A' were calculated across a reasonably dense grid in the FC region, giving 1287 *ab initio* points in total:

- r_{ClN}: every 0.125 bohr from 3.5 to 5.0 bohr

- r_{NO}: every 0.05 bohr from 1.95 to 2.45 bohr

r_{ClN} / bohr	TDM $\times 10^4$ / au				
	z, 2 A$'$	z, 3 A$'$	y, 2 A$'$	y, 3 A$'$	x, 1 A$''$
3.5	-2.06	27.3	-1.24	-4.89	1.70
3.75	-2.40	43.0	-0.40	-1.88	1.29
4	-2.70	62.1	0.15	1.19	1.09
4.25	-2.73	83.5	0.44	3.90	1.03
4.5	-2.55	105	0.57	6.01	1.02
4.75	-2.40	125	0.63	7.39	1.02
5	-2.61	141	0.66	7.97	0.99

Table 4.1: Transition dipole moments between the ground state and the 3 spin-orbit states corresponding to the original 1 ^{3}A$''$ state, along the z, y and x directions. The values are shown for a range of r_{ClN} bond lengths, with r_{NO} fixed at 2.15 bohr and θ fixed at 115°.

- Bond angle $\boldsymbol{\theta}$: every 5° from 90° to 130°.

There was some variation in the signs of the TDMs, and so these were modified where necessary to ensure smooth curves.

Figure 4.4 shows cuts through the TDM surface. As with the TDMs between the zeroth-order 1 and 2 ^{1}A$'$ states, the z component of the TDMs is rather larger than the y component, again showing that it mostly lies along the dissociative R coordinate, and implying that the resultant of the two components can safely be used in quantum dynamics calculations. Panel a) of figure 4.4 shows that the overall TDM is fairly flat along the angular coordinate, raising slightly at lower angles, and panel c) shows that there is only a small variation as the r_{NO} bond length is varied. More marked is the change as the r_{ClN} bond is stretched, as given in panel b): the TDM increases fairly linearly as the bond becomes longer. This likely reflects the transition from a ClNO molecule to a separated pair of photofragments, in which the singlet - triplet description is less valid, and hence the transition is less strictly forbidden. The TDM function can therefore be expected to act on the initial wavepacket by shifting density slightly towards longer r_{ClN} lengths. Note that given the variation in TDMs with the method used seen in the previous chapter, these TDMs may not necessarily be accurate. It was not feasible to calculate them at a more advanced (e.g. MRCI) level, and so no comparison between methods has been performed. As a counter to these reservations, the TDMs as calculated do produce a smooth surface and appear sensible.
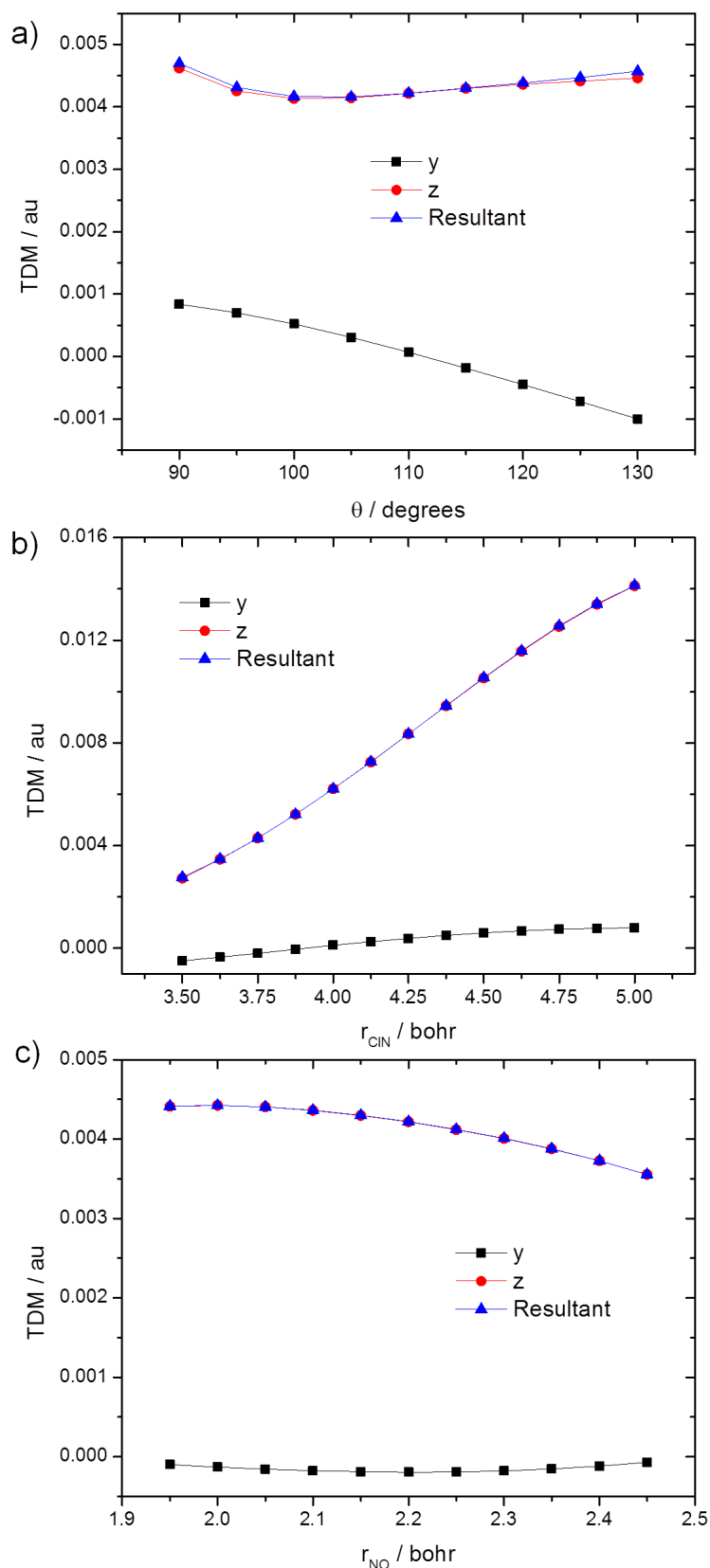
Figure 4.4: TDM surfaces for the transition between the 1 and 3 A′ spin-orbit states of ClNO (corresponding to the zeroth-order $1\,^1A'$ and $1\,^3A''$ states), calculated at the CAS/AVTZ level. The y and z components of the TDMs, as well as their resultants, are shown. Panel a) shows a cut at $r_{ClN} = 3.75$ bohr and $r_{NO} = 2.15$ bohr; panel b) shows a cut at $r_{NO} = 2.15$ bohr and $\theta = 115°$; panel c) shows a cut at $r_{ClN} = 3.75$ bohr and $\theta = 115°$.

4.4 Wavepacket dynamics

4.4.1 Propagation on the 1 ^{3}A$''$ state

The MCTDH method was employed for all quantum wavepacket propagations on the 1 ^{3}A$''$ PES. The initial wavepacket used in these calculations was the same as in the previous chapter. This was operated on by the TDM function and then allowed to propagate for 180 fs. The same numbers of SPFs and DVR grid points were used as for the singlet calculations, but the CAP parameters needed to be adjusted to avoid back-reflections: in this case, values of 0.1 and 3 were found to be appropriate for the strength and order respectively, with the CAP placed on the R coordinate at 7.5 bohr.

Figures 4.5 and 4.6 show snapshots of the wavepacket propagation at different times, for a fixed γ of 127° and a fixed r bond length of 2.15 bohr respectively. These plots immediately show that the photodissociation dynamics are more complicated than on the 2 ^{1}A$'$ surface. Figure 4.5 shows that, as expected, the PES at the FC point imparts an impetus towards longer r, so the wavepacket moves initially in this direction. The slope towards longer R distances is much shallower, so movement in this direction for the first few 10s of fs is less pronounced. The wavepacket stretches out and becomes asymmetric, with a portion becoming briefly caught in the well in the r_{NO} coordinate. After around 40 fs the wavepacket forms two distinct parts because of this entrapment, then proceeds down the exit channel with the r_{NO} bond oscillating gently.

Figure 4.6 shows that the movement in the angular coordinate is a little simpler: the slope towards the exit channel is again small, and so the wavepacket moves only slowly. There is a small downwards gradient in the direction of lower values of γ, and so the wavepacket initially moves slightly in this direction before stretching out significantly and curving towards smaller angles. By 50 fs the wavepacket is rather long, covering about 2 bohr in the R coordinate. As the propagation continues, the wavepacket fans out further in the γ coordinate, becoming spread across the whole angular range.
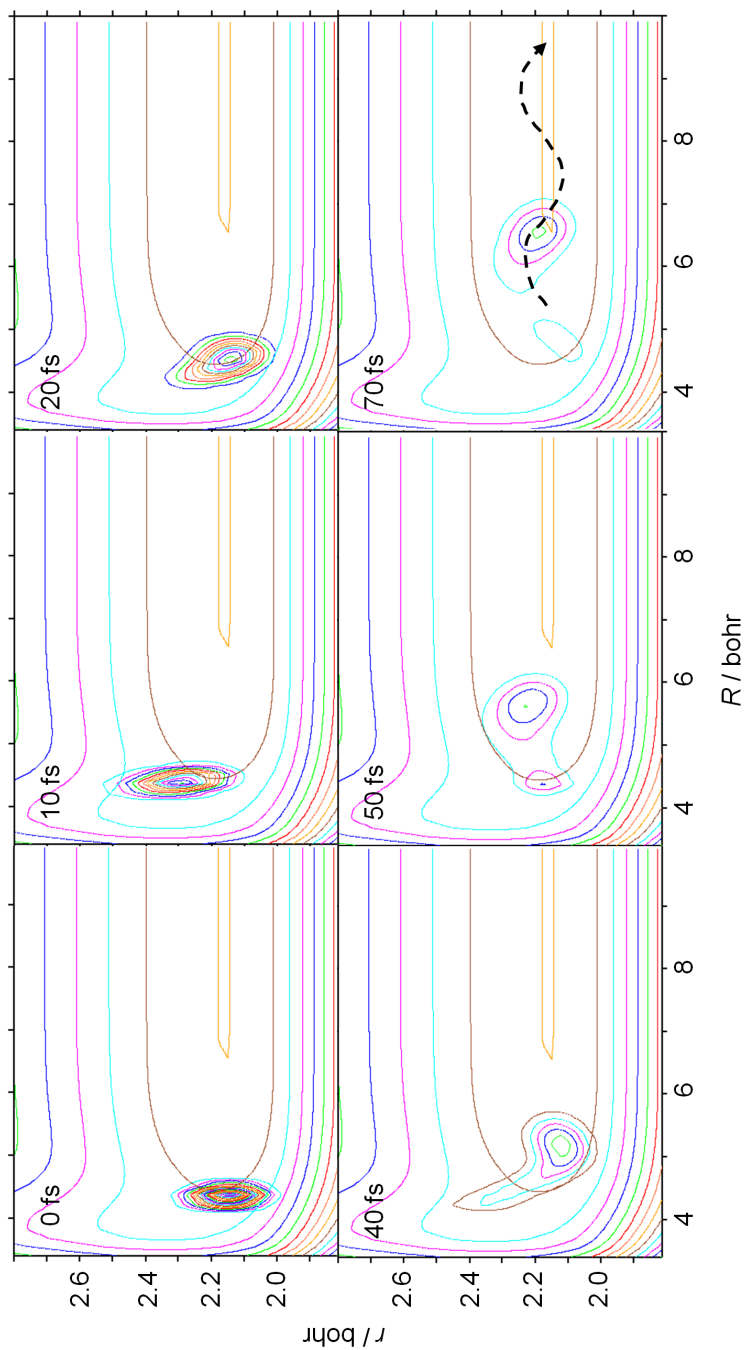
Figure 4.5: Snapshots of the wavepacket propagation on the $1\ ^3A''$ state of ClNO at 0, 10, 20, 40, 50 and 70 fs after excitation from the ground state. In these cuts, γ is fixed at its FC value of $127°$ and the contour lines on the PES are 0.5 eV apart.
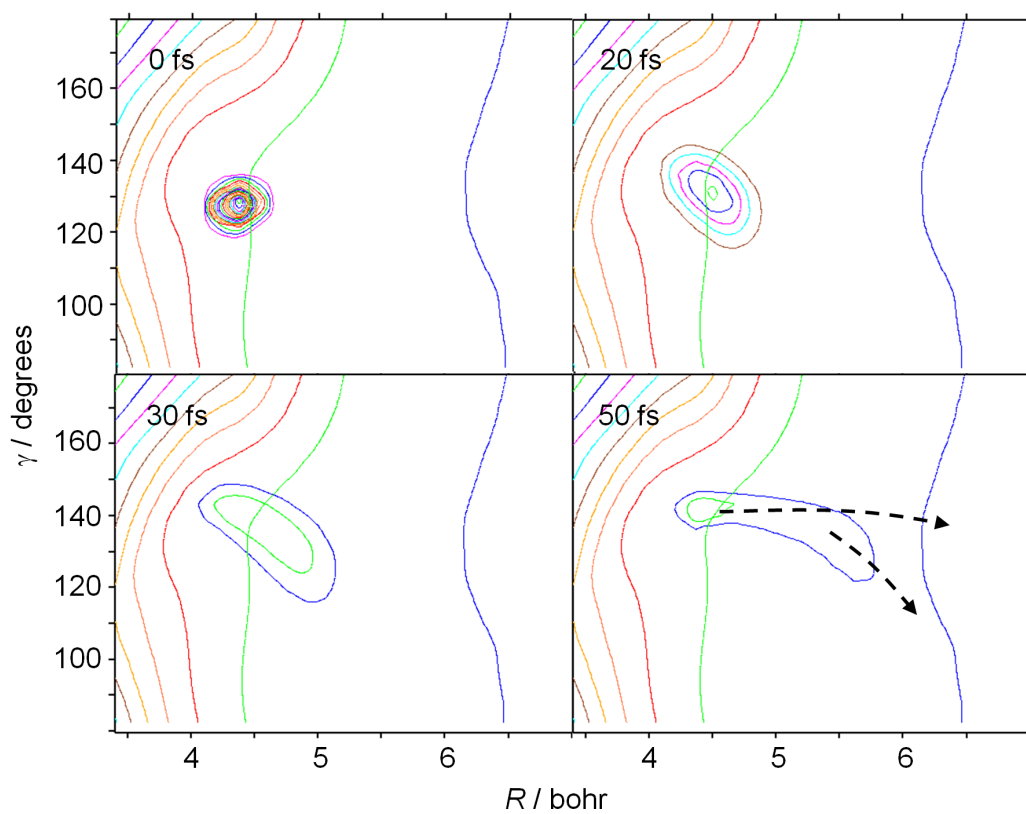
Figure 4.6: Snapshots of the wavepacket propagation on the $1\,^3A''$ state of ClNO at 0, 20, 30, and 50 fs after excitation from the ground state. In these cuts, r is fixed at its FC value of 2.15 bohr and the contour lines on the PES are 0.5 eV apart.

4.4.2   Autocorrelation and absorption spectrum

The autocorrelation and spectrum, for calculations both with and without the TDM function, are given in figures 4.7 and 4.8. The autocorrelation shows clear structure, with the main partial recurrences seen at $\sim$18 fs and $\sim$70 fs. It follows that the spectrum is also structured: there are three main peaks, each of which are divided into three sub-peaks. Previous work has shown that these are due to different quanta populated in the NO stretch (v*, main peaks) and bend (n*, sub-peaks) of the excited state complex [64, 79]. The differences between the spectra with and without the TDM function are small. All the peaks appear in very nearly the same locations, although those when TDMs are included are shifted to slightly lower energy. This is likely due to the shifting of the initial wavepacket on the excited state surface to slightly longer r_{ClN} bond lengths (from 3.71 to 3.79 bohr): the PES slopes downwards in this coordinate. The peak heights are similar but not identical: when the TDM function is used, the first main peak is weaker and the subsequent peaks are a little stronger.

The peak energies of the first six peaks are given, along with experimental energies, in table 4.2. The agreement is good, with all energies matching experiment to within 0.02 eV. The energies between the peaks can be used to obtain averaged NO stretch and bend vibrational frequencies. These are calculated as 1420 cm^{-1} and 365 cm^{-1} respectively, in reasonable agreement with the experimental values of 1520 cm^{-1} and 387 cm^{-1} [64, 79]. There are however discrepancies between the overall absorption spectrum calculated here, and that found both experimentally and in earlier calculations by Schinke and co-workers. The major difference is that in the first main peak, the highest sub-peak is that corresponding to n* = 0, where n* denotes the number of quanta in the bend, whereas in the other results the highest sub-peak is that corresponding to n* = 1. In addition, the sub-peaks are less clearly defined. This shows there are some small deficiencies in the PES calculated here. However, it is worth noting that in order to achieve a good match with the experimental absorption spectrum, Schinke *et al.* applied a scaling factor to their *ab initio* results; without this their spectrum did not show any structure from the bend. Here, no such manipulations have been used.
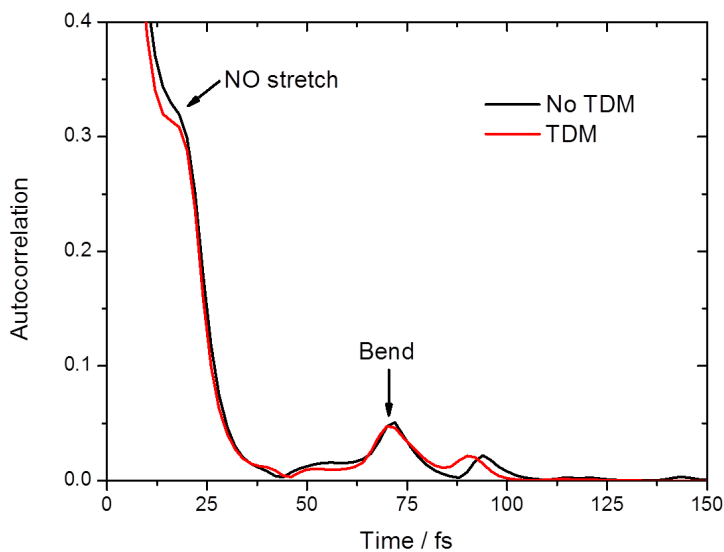
Figure 4.7: Autocorrelations calculated from wavepacket propagations on the 1 ^{3}A$''$ state of ClNO. The black line results when no TDM function is used, the red line results when it is. The recurrences at ∼18 fs derive from the NO stretch and those at ∼70 fs from the bending vibration in the excited state.
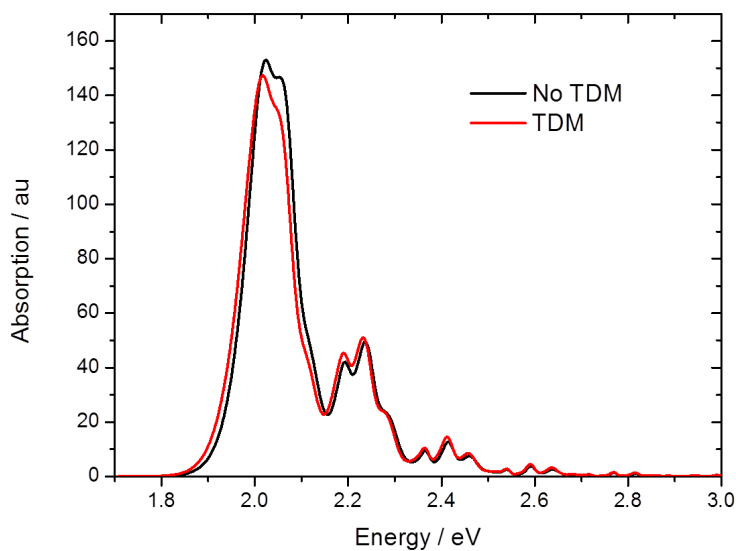
Figure 4.8: Absorption spectra calculated from wavepacket propagations on the 1 ^{3}A$''$ state of ClNO. The black line results when no TDM function is used, the red line results when it is. The main peaks derive from the NO stretch and the sub-peaks derive from the bending vibration.

v* (NO)	n* (bend)	Peak energy / eV		
		Experiment	No TDM	TDM
0	0	2.009	2.024	2.017
0	1	2.060	2.056	2.048
0	2	2.112	2.12	2.11
1	0	2.198	2.193	2.191
1	1	2.246	2.238	2.232
1	2	2.296	2.283	2.279

Table 4.2: The energies of the first 6 peaks in the absorption spectrum of the $1\ ^3A''$ state of ClNO, calculated from wavepacket propagations both with and without a TDM function, compared to experimental results from Reisler *et al.* [79]. The peaks are assigned according to the number of quanta in the NO stretch and the bend in the excited ClNO complex.

4.4.3 NO product state distributions

NO vibrational state distribution

NO vibrational distributions were found by projecting the quantum flux entering the CAP onto the eigenstates of lone NO, in the same way as in the previous chapter. Figure 4.9 shows the flux passing into each NO vibrational state for the propagation including TDMs. This shows very clearly how each of the main peaks corresponds to NO in a different vibrational state, and hence shows that the photodissociation occurs essentially adiabatically with respect to the NO stretch, i.e. the vast majority of the NO in $v = 0$ comes from $v* = 0$ in the excited state, etc. Overall, 72.7% of the NO is formed in $v = 0$, 21.0% in $v = 1$, 4.8% in $v = 2$ and 1.2% in $v = 3$. The populations of higher excited vibrational states are negligible. If TDMs are not included, these proportions are only slightly different: 76.3% in $v = 0$, 19.6% in $v = 1$, 3.4% in $v = 2$ and 0.6% in $v = 3$.

NO rotational state distribution

NO rotational state distributions were again found by projecting the quantum flux entering the CAP onto the spherical harmonics. The distribution for the calculation including TDMs is shown in figure 4.10. The majority is produced at low j, with a smaller peak at higher j, centred at around $j = 17$. Note that the oscillations at low j are due to quantum mechanical interferences, as there are multiple pathways by which the rotational states can be formed. These oscillations were also observed by Schinke and co-workers
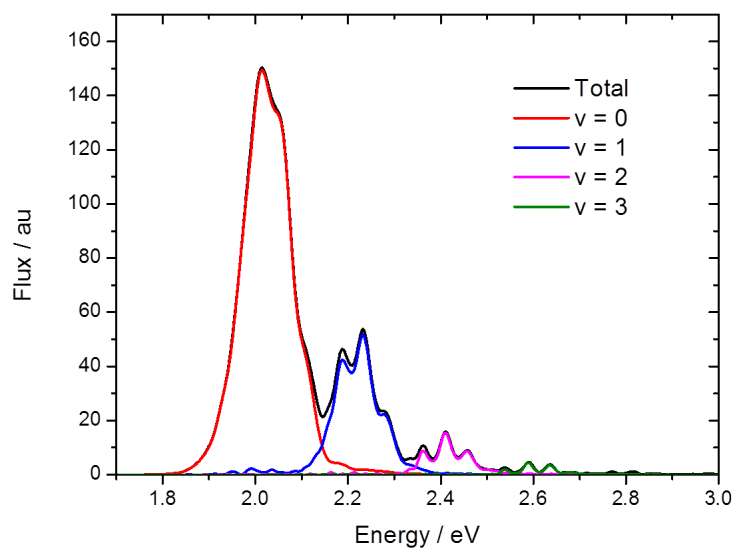
Figure 4.9: NO vibrational flux distributions obtained following a wavepacket propagation on the $1\,^3A''$ state. The results are from a calculation in which TDMs were used.
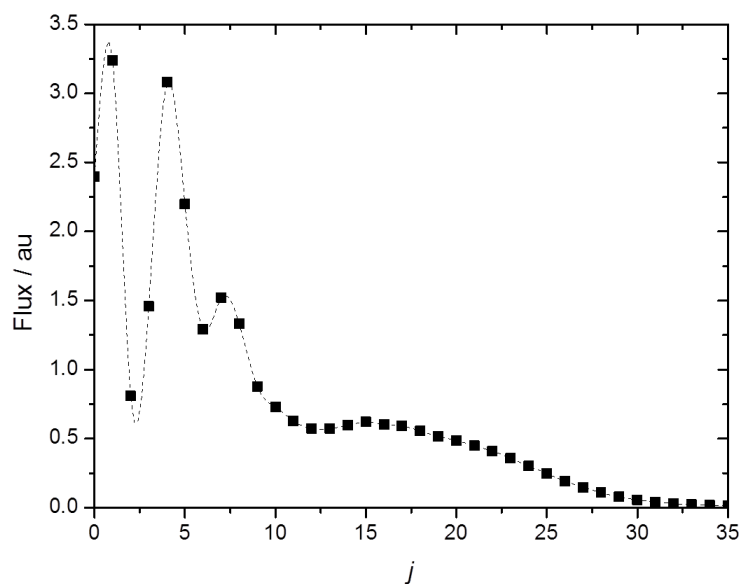
Figure 4.10: NO rotational distribution obtained following a wavepacket propagation on the $1\,^3A''$ state. The results are from a calculation in which TDMs were used.

[64], but they do not appear in experimental results. This is because the temperature of the molecular beam in the experiments is not 0 K, and hence the parent molecule will be rotating and so total angular momentum states other than $J = 0$ will occur. The oscillations will therefore become averaged out. In addition, averaging can occur due to the different spin-orbit and Λ-doublet states of NO, the effects of which are not accounted for in the calculations. This distribution cannot be directly compared with experiments using narrowband ns lasers as it includes NO produced at every energy contained within the wavepacket. Distributions for individual energies will be considered later in section 4.6.1.

Analysis

To explain these product state distributions, the wavepacket propagation has been examined in more detail. The flux entering the CAP has been measured every 5 fs from 40 to 125 fs, after which point very little further change is seen. At each time step product state distributions have been calculated, thus allowing more information about how the final distributions build up to be extracted. Figure 4.11 shows the total flux passing into the CAP during each 5 fs period. This illustrates clearly how the wavepacket splits into two distinct parts, with the bulk dissociating within the first 80 fs after excitation, but with a substantial portion taking up to 120 fs to reach $R = 7.5$ bohr.

Figure 4.12 shows the flux ending in each NO vibrational state during each 5 fs time-bin. The shape of the curve for $v = 0$ mirrors that for the total flux, with most being formed in the first part of the wavepacket. For NO produced in $v = 1$, there is again more formed in the first part of the wavepacket, but the proportion formed from the second part of the wavepacket is much higher. In addition, there is a slight dip at 60-65 fs. Zooming in, as shown in the inset on the figure, it can be seen that the $v = 2$ results have a similar overall trend to those for $v = 1$, but with the initial dip in the first peak shifted to 65-70 fs and with the proportion formed in each portion of the wavepacket fairly equal. Almost all of the NO ending up in $v = 3$ (admittedly a very small quantity) is formed in the second part of the wavepacket. Overall, this plot shows how the second portion of the wavepacket is much more vibrationally excited by the first, which is logical. The second portion was
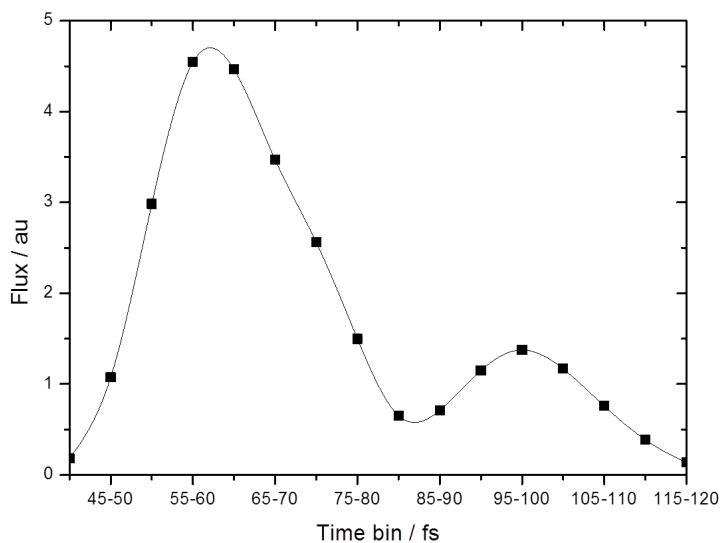
Figure 4.11: The flux entering the CAP in the asymptotic region of the PES in 5 fs wide time-bins during a wavepacket propagation on the $1\,^3A''$ state.
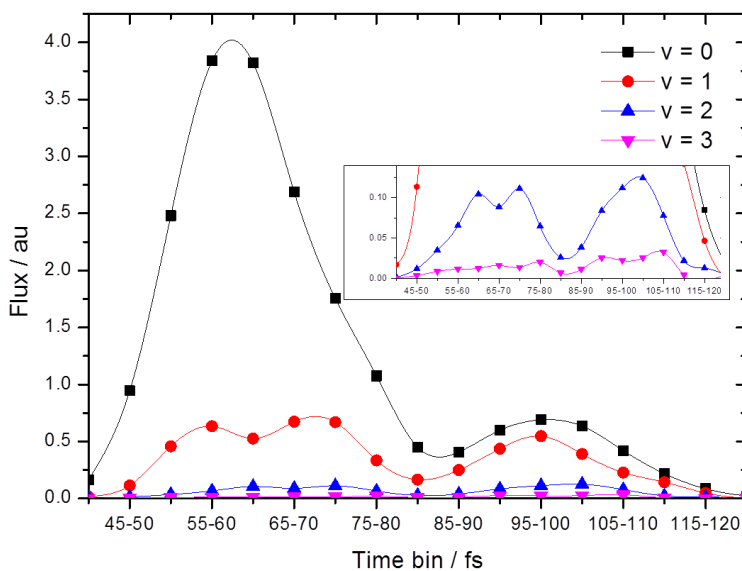
Figure 4.12: The flux ending in each NO vibrational state during 5 fs wide time-bins during a wavepacket propagation on the $1\,^3A''$ state. The inset is a magnified view of the results for v = 2 and v = 3.
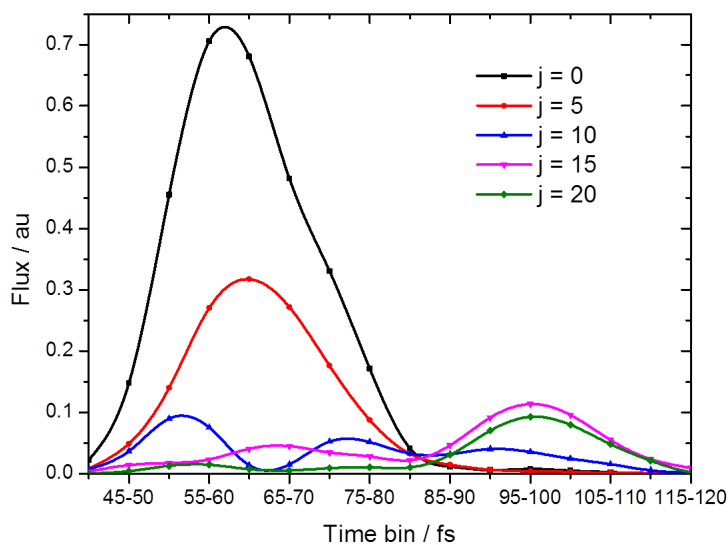
Figure 4.13: The flux ending in selected NO rotational states during 5 fs wide time-bins during a wavepacket propagation on the $1\ ^3A''$ state.

originally trapped in the slight well in the r coordinate; the parts of the wavepacket with the most momentum in this direction are more likely to have become temporarily caught there, and hence have taken longer to dissociate.

Figure 4.13 shows the flux ending in NO rotational states of $j = 0$, 5, 10, 15 and 20 during each 5 fs time-bin. Almost all of the NO produced in $j = 0$ or 5 is formed from the first part of the wavepacket. In contrast, most of the NO produced in the higher rotational states of $j = 15$ and 20 comes from the second portion of the wavepacket. This implies that the second part, which takes longer to dissociate, has more time to spread out over the angular coordinate, and hence has greater momentum in this direction, resulting in NO that is rotating more rapidly.

By projecting the flux entering the CAP onto the lone NO vibrational eigenstates and the spherical harmonics at the same time, the rotational distribution for each vibrational state can be found. These are given in figure 4.14. As would be expected from the previous two plots, NO that is vibrationally excited is more likely to be rotationally excited: for NO in $v = 0$ the hump in the distribution at higher j is small, whereas for NO in $v = 3$ it dominates.
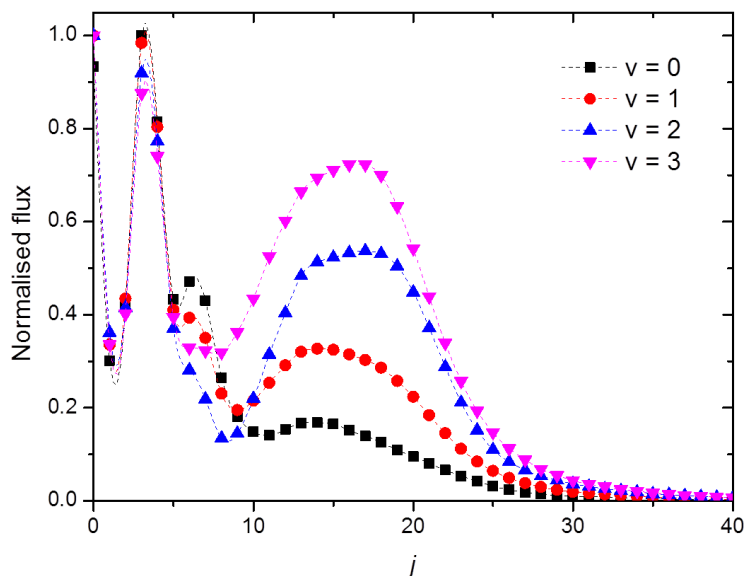
Figure 4.14: The NO rotational distributions for each NO vibrational state following a wavepacket propagation on the $1\,^3A''$ state. To allow for easier comparison, all the distributions have been normalised.

4.5 Classical trajectories

4.5.1 Single-surface trajectories

Single surface classical trajectory calculations were carried out using the same methods as detailed in section 3.6. The same initial wavepacket was used in all cases. Trajectories were run at a range of excitation energies: every 0.1 eV from 1.9 to 2.7 eV, and at the energies corresponding to the maxima of the first six peaks in the absorption spectrum as calculated using the MCTDH method without the TDM function.

Figure 4.15 shows the path of a sample trajectory in each of the three Jacobi coordinates, for an excitation energy of 2.0 eV. Panel b) shows clearly how the trajectory initially moves into the well towards longer values of r, but then returns to oscillate closer to the FC value as the dissociation progresses. Figure 4.16 gives the variation in γ for trajectories ending in different NO rotational states: as expected, trajectories in which the change in the angular coordinate is most extreme result in the most highly rotationally excited NO. The time taken to for the trajectories to complete, i.e. to reach $R = 8.5$ bohr, varied depending on the precise path taken, but was normally in a range between 110 and 165 fs, with the longer times corresponding to a larger change in γ.
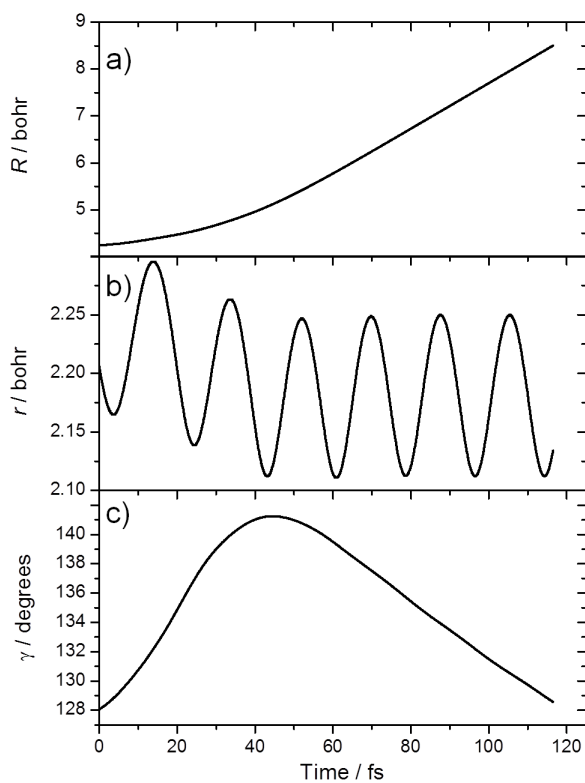
Figure 4.15: Panels a) to c) show the variation in each of the Jacobi coordinates with time for an example classical trajectory on the $1\,^3A''$ surface, for an excitation energy of 2.0 eV.
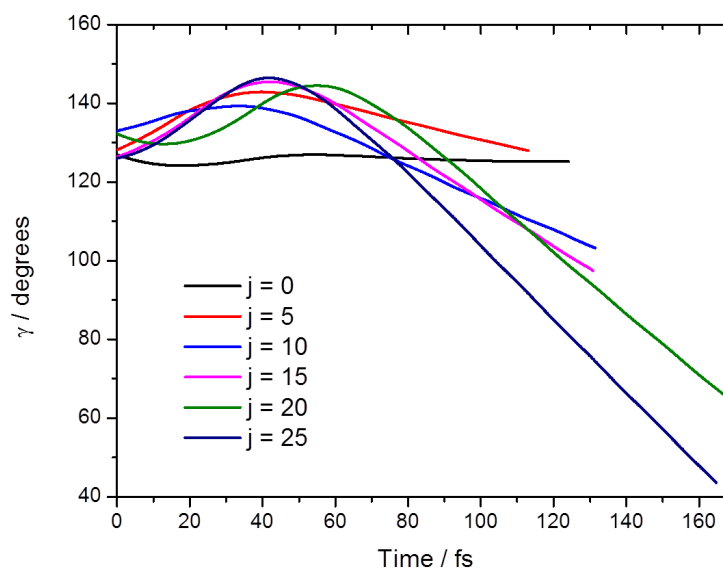
Figure 4.16: The variation in γ for sample classical trajectories on the $1\,^3A''$ surface ending in a range of NO rotational states, for an excitation energy of 2.0 eV.
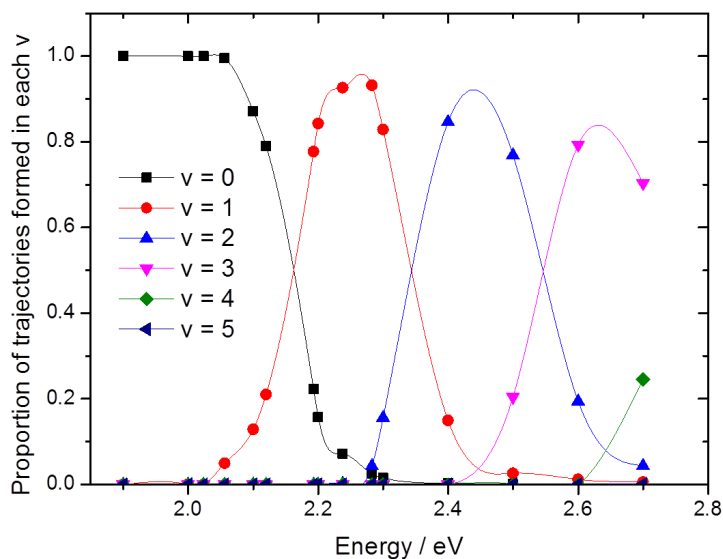
Figure 4.17: The proportion of trajectories ending in each NO vibrational state following dissociation on the $1\,^3A''$ surface for a range of energies.

The variation in the NO product vibrational state distribution with excitation energy is shown in figure 4.17. The most populated vibrational state varies considerably with energy, reflecting the absorption spectrum seen in figure 4.8 well. The agreement with the equivalent quantum results is good, as shown in table 4.3. There is however slightly more overlap between the vibrational states in the classical calculations; as the energy changes the quantum distribution changes more sharply. This effect is nonetheless small, and so the classical trajectories can be said to reproduce the NO vibrational motion well.

Figure 4.18 shows NO product rotational state distributions following trajectories with

v^* (NO)	n^* (bend)	Proportion of NO ending in each vibrational state / %					
		0	0	1	1	2	2
0	0	100	99.4	0	0.5	0	0.1
0	1	99.5	99.2	0.5	0.75	0	0
0	2	79.0	93.6	21.0	6.4	0	0.1
1	0	22.3	8.0	77.7	91.5	0	0.6
1	1	7.2	3.6	92.6	96.3	0.2	0.2
1	2	2.5	5.1	93.2	95.0	4.3	1.6

Table 4.3: The proportion of NO ending up in each vibrational state v at the energies of the first 6 peaks in the absorption spectrum of the $1\,^3A''$ state, corresponding to $n^* = 0$, 1 and 2 for $v^* = 0$ and 1. Results for classical trajectories are in the unshaded columns, those for a quantum wavepacket propagation including the TDM function are shaded grey.
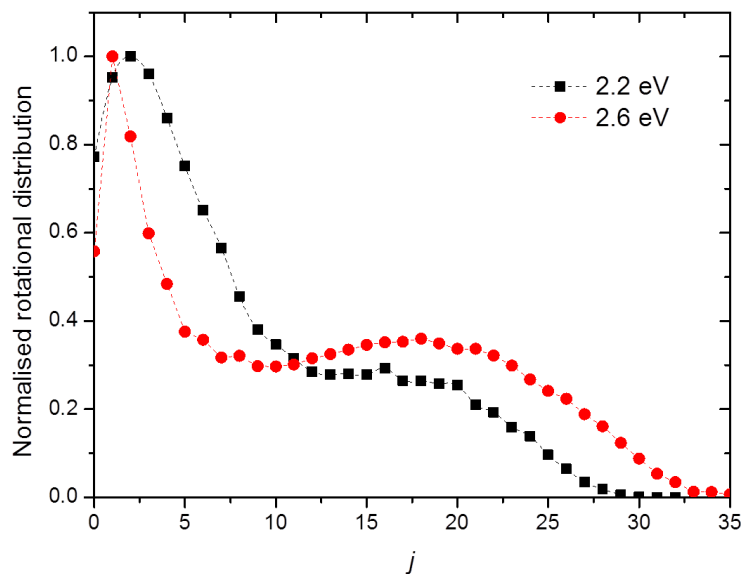
Figure 4.18: Normalised NO rotational state distributions obtained from classical trajectory calculations on the $1\,^3A''$ state, for excitation energies of 2.0 and 2.6 eV.

excitation energies of 2.0 and 2.6 eV; note the absence of oscillations at low j due to quantum interferences. Similarly to the quantum results, there is a peak at very low j followed by a wide hump in the distribution centred around $j = 18$; this hump increases in size as the energy increases. This more rotationally excited NO is most likely formed from trajectories which have become caught in the slight well in the r coordinate for longer, thus giving more time to spread in the angular coordinate, again as suggested by the quantum results and figure 4.16. Further rotational distributions will be considered in section 4.6.1.

4.5.2 β parameter calculations

Calculations to find the anisotropy parameter β for NO rotational state j were carried out as detailed in section 3.6.3. The variation of β with j is more complicated for the $1\,^3A''$ than for the $2\,^1A'$ state of ClNO. However, the value is always close to 2, reflecting the fast dissociation process. This result is sensible as again μ is aligned mostly along the R coordinate.

The variation of β with j, superimposed upon the NO rotational distributions, is shown in figure 4.19 for excitation energies corresponding to the first six peaks in the
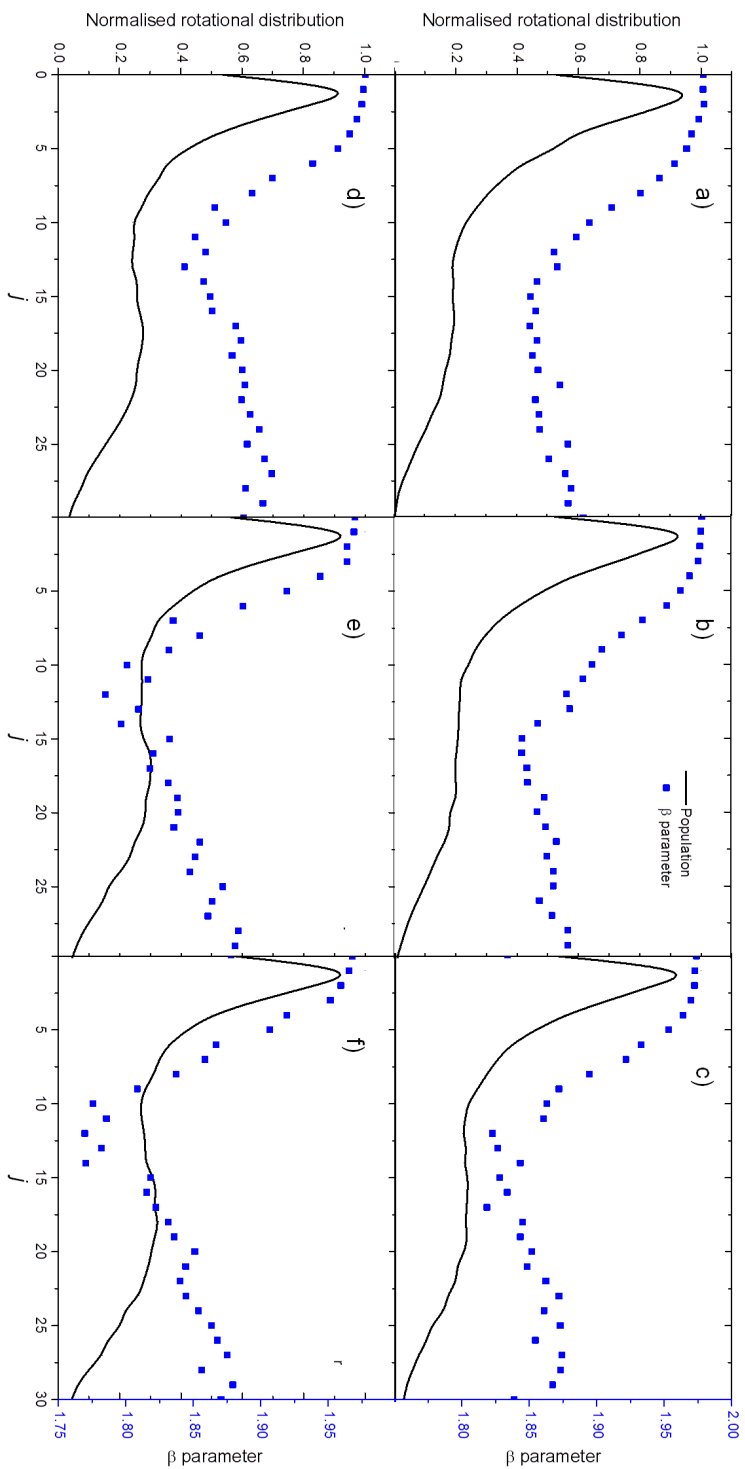
Figure 4.19: The variation of β with j superimposed onto normalised NO rotational state distributions obtained from classical trajectory calculations on the $1\,{}^3A''$ state. Panel a) corresponds to v* = 0, n* = 0 (2.024 eV), b) to v* = 0, n* = 1 (2.056 eV), c) to v* = 0, n* = 2 (2.012 eV), d) to v* = 1, n* = 0 (2.193 eV), e) to v* = 1, n* = 1 (2.238 eV) and f) to v* = 1, n* = 2 (2.283 eV).

absorption spectrum (i.e. for $v^* = 0$ and 1). There are two main trends in this data: firstly, as the number of quanta in the excited bending vibration n^* increases, the values of β decrease. Secondly, β starts very close to 2 at low j, then falls to a minimum at around $j \sim 12$, then increases slightly as j increases. Both these trends are more marked when the NO stretching vibration is more excited, i.e. when $v^* = 1$.

β is calculated by taking the angle θ_m between the direction of μ at the starting geometry for the trajectory and the velocity of the departing Cl atom. As the TDM is essentially flat along the r and γ coordinates in the FC region, the major influence on β will be the photofragment velocity. The initial decrease in β can be explained on kinetic grounds as the more rotationally excited NO comes from ClNO that has taken longer to dissociate, as already seen. However, this does not explain the subsequent, albeit smaller, rise in β as j increases further. The decrease in β as the number of quanta in the NO stretch increase can be explained as the greater the oscillation in the r coordinate, the more likely the trajectory is to become temporarily stuck in the well in this direction, and hence the longer the photodissociation process will take. Similarly, the greater the excitation in the bending vibration, the more likely the trajectory will reach larger values of γ, resulting in more rotationally excited NO as seen in figure 4.16. The times taken for the dissociation process to finish at the six energies shown in figure 4.19 are 124 ± 19, 125 ± 20, 130 ± 23, 135 ± 26, 138 ± 28 and 142 ± 30 fs, supporting these observations.

The slight increase in β for higher values of j may be explained with reference to figure 4.20, which shows the rotational distributions associated with each NO product vibrational state for an excitation energy of 2.283 eV. Although the distributions for $v = 0$ and 2 are not smooth due to the small number of trajectories they are averaged over, it is clear that NO in $v = 0$ is more likely to be formed at high j, and that in $v = 2$ at low j. The mean dissociation times for $v = 0$, 1 and 2 are 129 ± 21, 142 ± 30 and 152 ± 43 fs respectively. It would therefore appear that the decrease in photodissociation time due to the NO vibrational state is out-competing the increase expected from the increased angular motion for high j, resulting in a slight rise in β. The variation in β is however rather small, with a maximum deviation from the limiting value of less than 0.25.
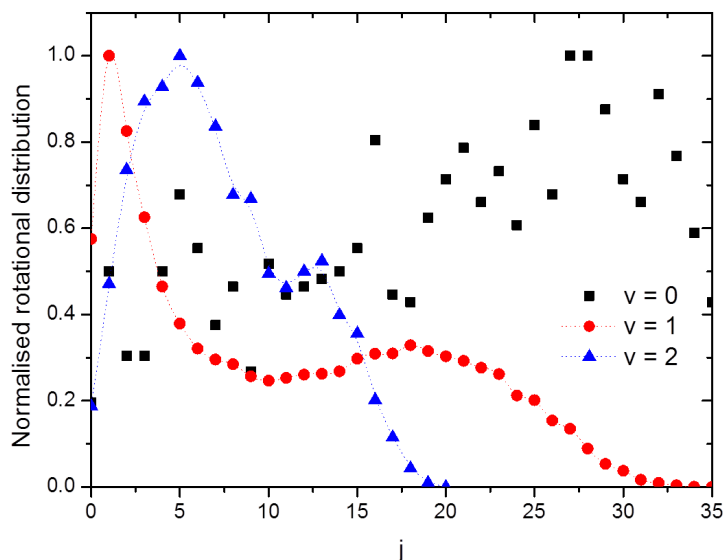
Figure 4.20: NO rotational distributions for each NO product vibrational state following dissociation on the 1 $^3A''$ with an excitation energy of 2.283 eV.

4.6 Comparison between experimental and computational results

The photodissociation of the 1 $^3A''$ state of ClNO has been studied before, primarily by the groups of Reisler, who investigated the process using photofragment absorption spectroscopy, and Schinke, who used computational methods. The validity of the results obtained here can therefore be determined by comparison with these older studies. The comparison with experimental and calculated absorption spectra has already been discussed in section 4.4.2, with the agreement found to be reasonable.

4.6.1   NO rotational distributions

Figure 4.21 shows the rotational distributions for energies across the first main peak in the absorption spectrum, where v* = 0. Results from both the classical and quantum calculations performed here are given in addition to experimental results taken from [79]. To allow for clearer comparison with experiment, the flux values for each *j* in the quantum distribution have been averaged over 3 points, which smooths out the low *j* oscillations. Figure 4.22 shows the same for the second main peak in the spectrum, with v* = 1.
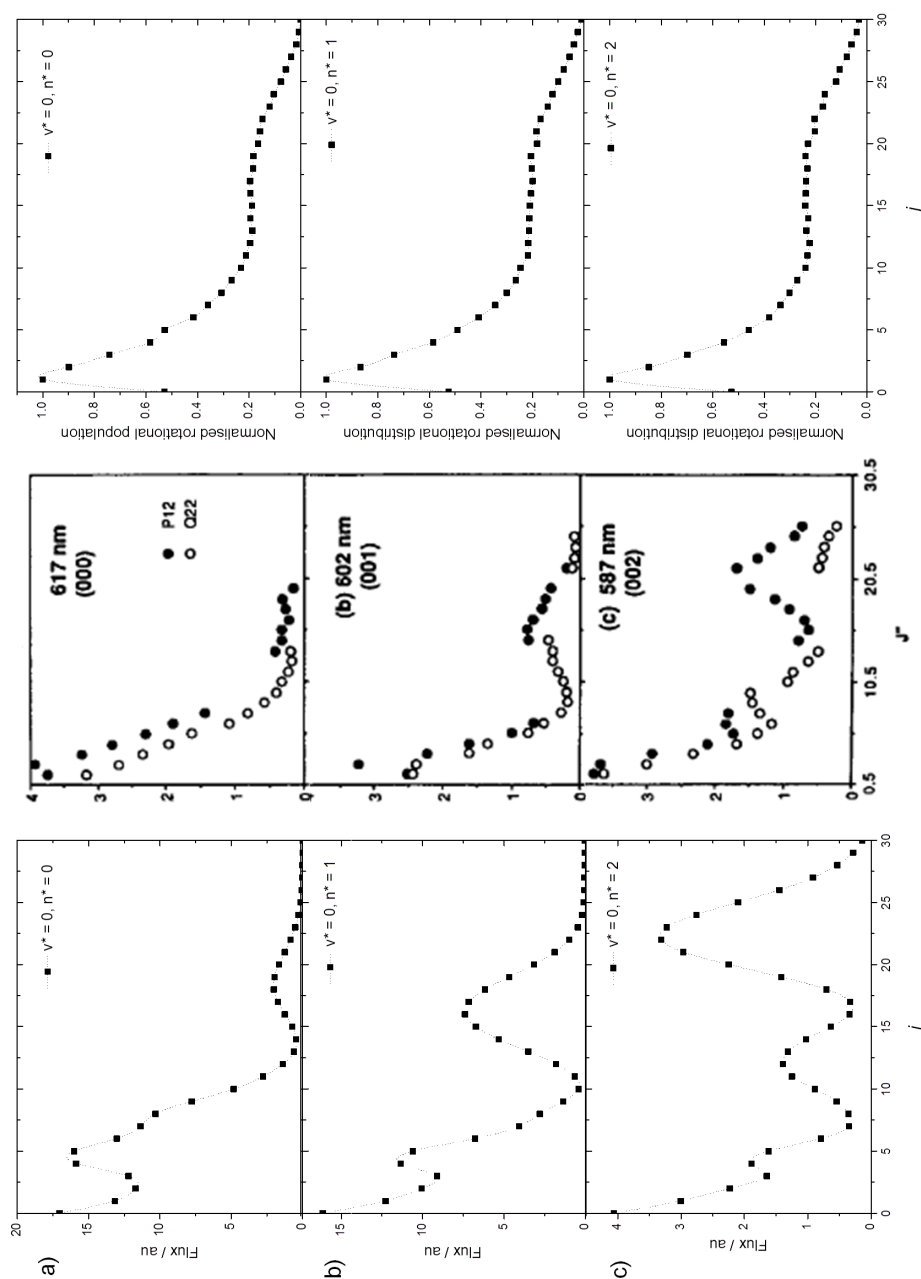
Figure 4.21: NO rotational distributions following dissociation on the 1 $^3A''$ for energies across the first main peak in the absorption spectrum. Row a) corresponds to the sub-peak with $v^* = 0$, $n^* = 0$, row b) to the sub-peak with $v^* = 0$, $n^* = 1$ and row c) to the sub-peak with $v^* = 0$, $n^* = 2$. The first plot in each row shows the distribution obtained from the quantum wavepacket propagation including the TDM function. To allow for clearer comparison with experiment, the flux values for each j have been averaged over 3 points, which smooths out the low j oscillations. The second plot in each row shows experimental results taken from [79]. The third plot shows distributions obtained from classical trajectory calculations.
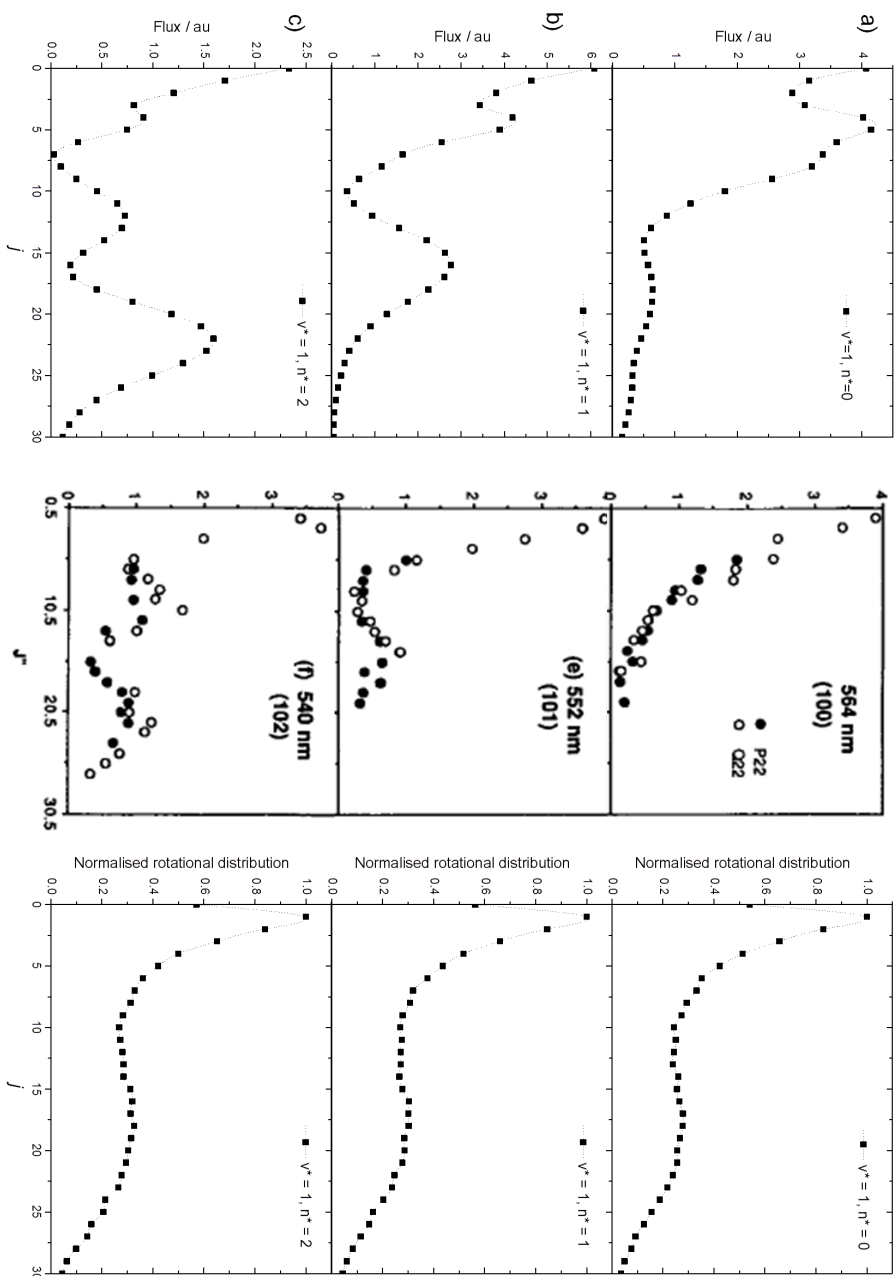
Figure 4.22: NO rotational distributions following dissociation on the $1\,^3A''$ for energies across the second main peak in the absorption spectrum. Row a) corresponds to the sub-peak with $v^* = 1$, $n^* = 0$, row b) to the sub-peak with $v^* = 1$, $n^* = 1$ and row c) to the sub-peak with $v^* = 1$, $n^* = 2$. The first plot in each row shows the distribution obtained from the quantum wavepacket propagation including the TDM function. The flux values for each j have been averaged over three points. The second plot in each row shows experimental results taken from [79]. The third plot shows distributions obtained from classical trajectory calculations.

It is immediately clear that the agreement between the quantum results and experiment is fair: the overall shape of the distributions is reproduced reasonably well, with the correct number of nodes seen, apart from perhaps when n* = 0, where a small peak at higher *j* is present in the calculated results but not in the experiment. The heights of the various peaks in the rotational distributions do not match exactly, with the population in higher rotational states being rather over-estimated. The peak positions for n* = 2 are also slightly too high, by ∼3-5*j*. This implies there are problems with the PES in the angular coordinate: it is likely too steep leading away from the FC region. This is perhaps not unexpected given the differences between the experimental and calculated absorption spectra, as the sub-peaks for each value of n* are insufficiently clearly defined.

In contrast, the classical rotational distributions show none of the relevant features: each distribution consists of a peak at low *j*, followed by an additional broad peak centred around *j* ∼18. The height of this second peak increases with excitation energy, but the shape of the distribution does not change. This implies the photodissociation of the 1 ^{3}A$''$ state has too much quantum character to be accurately modelled using semi-classical methods.

The rotational distributions calculated by Schinke and co-workers match experiment slightly better than those calculated quantum mechanically here: the peak heights at high *j* are lower in magnitude, although the degree of rotational excitation is still slightly too high, especially for n* = 0. Schinke *et al.* used the rotational reflection principle outlined in section 1.4.3 to explain these results. Briefly, the rotational distributions reflect the stationary dissociation wavefunctions for the different values of n*: the wavefunction for n* = 0 has no nodes and hence the rotational distribution consists of one peak, the wavefunction for n* = 1 has one node leading to two peaks, and so on. The results here are also consistent with this explanation.

4.6.2 β parameters

Reisler *et al.* obtained a value for β of 1.9 ± 0.1. This is in excellent agreement with the overall calculated values. No experimental results are available regarding the variation of

β with j, and so the validity of these more detailed results cannot be confirmed, but their behaviour seems sensible, even if the results are slightly noisy. The major problem with these data however is the classical NO rotational distributions themselves, which do not match well with experiment.

4.7   Conclusions

A new PES for the 1 ^{3}A$''$ state of ClNO has been calculated. Transition dipole moments for the excitation from the ground state have been calculated and used for the first time. Quantum wavepacket propagations have been run on the surface using the MCTDH method, and these have been examined in detail to show which part of the wavepacket leads to each product state. NO vibrational and rotational product state distributions have been found, and these agree reasonably well with experiment [79], although not quite as well as those of Schinke *et al.* [64]. However, in these older calculations an arbitrary shift was applied to the PES in order to improve the results; no such manipulation has been performed here. The quantum results are considered accurate enough to use as the basis for coherent control calculations, described in the next chapter. Classical trajectory calculations have also been run, and although these reproduce NO vibrational distributions and values of the β parameter well, they do not reproduce the NO rotational distributions to any reasonable degree of accuracy. Semi-classical methods are therefore not suitable for studying this state of this system.

Chapter 5

Coherent control on the $1\,^3A''$ state of ClNO

5.1 Summary

Calculations using the MCTDH method have been used to model coherent control experiments on the $1\,^3A''$ state of ClNO. Pairs of laser pulses at a variety of energies have been used to excite the system. If the relative phases of the two pulses are set so that they can interfere freely, by varying the delay between the two laser pulses the NO product state distributions can be controlled. The control exhibited lies between the extremes of the Brumer-Shapiro and Tannor-Rice-Kosloff schemes detailed earlier in section 1.3. It should be possible to test these wavepacket interferometry schemes in the laboratory. The linear chirp (in the temporal domain) of the pulses has also been varied. This however has a much smaller effect on the results: the key factor in the control is the delay, and this overrides any other effects which may have been present. The degree of control achievable is limited by the nature of the photodissociation in this system: as the process is complete in $\sim$150 fs, it is difficult to enact more complicated schemes controlling a greater range of outcomes.

The results detailed here show that the MCTDH method in concert with accurate PESs can be used to plan coherent control experiments prior to their implementation. Although some 'optimal control' calculations have been run using MCTDH [152–155], in which

the electric field of a laser pulse has been optimised in order to maximise the population of a particular final state, it has not previously been used in a more closed-loop study such as this. Hopefully in the future similar calculations can be run on more complex systems to help understand experimental results.

5.2   Aims

Considering the $1\,^3A''$ state in isolation, the clear variables to be controlled are the NO product state distributions. The NO vibrational state distribution is strongly linked to the proportion of the wavepacket which becomes temporarily 'trapped' in the well in the r_{NO} coordinate on the PES in the FC region, and so if more wavepacket can be forced into this region, more highly excited NO should be produced. The NO rotational state distribution reflects the distribution of the wavepacket in the asymptotic region when viewed along the γ coordinate, hence by changing the shape of the wavepackets along this axis the rotational states formed should be controllable. In addition, the dissociation time could potentially be controlled: for example, the more wavepacket entering the r_{NO} well, the longer the system takes to break apart.

Any control on the $1\,^3A''$ state can also be viewed as a possible precursor to excitation to higher-lying excited states. Although not considered here as these higher states have not been calculated at an accurate level of theory, it may be possible to use multi-photon processes to effect some control on the population of these states, or indeed the likelihood of eventual ionisation versus dissociation. A further, eventual goal could be the formation of the ClON isomer.

The initial reason for studying the $1\,^3A''$ state of ClNO was that it absorbs in a wavelength region which is convenient for experimental study in our laboratory. Shaped ultrashort laser pulses of > 20 fs duration can be produced using an acousto-optic programmable dispersive filter (the Dazzler^{TM} [156, 157]) in the wavelength range 540 to 720 nm [158]. Pulses that are shorter still could be produced using our non-linear optical parametric amplifier, but it would not be possible to shape these. The aim therefore has been to formulate control schemes which could be tested experimentally, thus giving a

good indication as to the reliability of the theoretical techniques used.

In order for interferences to occur, more than one laser pulse is normally required. Often, this is achieved using multiphoton excitation: see for example, our group's previous work on I_2 [159, 160]. As the pulse energies that can be produced in our laboratory are in the region of the 1 $^3A''$ state excitation energy, only a single photon is required for excitation. The obvious experiments to run for this system are therefore those involving pulse pairs, with the second pulse arriving some variable time after the first. By controlling this delay, the interference between the initial wavepacket and the second pulse can be varied. As the photodissociation process is fast, the delay will need to be fairly short in order to effect control before the wavepacket has moved completely from the FC region. An alternative method to achieve similar effects would be to keep the delay constant but to vary the absolute phase of the second pulse; here however just the delay has been varied.

To start, transform limited (TL) pulses, i.e. those with the shortest possible duration for the given bandwidth and pulse envelope, have been used. Following on from this, pulses with varying degrees of linear chirp have been applied, either in pairs of identical pulses or with a TL second pulse. Lastly, some pulses with quadratic chirp have been used.

5.3 Methodology

5.3.1 The Hamiltonian

In order to treat the absorption of a photon, the Hamiltonian for the system needs to be modified. The simplest way to do this is to consider the electric field as a perturbation onto the field-free Hamiltonian using the semi-classical dipole approximation [161], i.e.

$$\hat{H} = \hat{H}_0 - E(t) \cdot \hat{\mu}. \tag{5.1}$$

$\hat{H}_0$ is the Hamiltonian operator without the pulse as used previously, $E(t)$ is the electric field and $\hat{\mu}$ is the dipole moment operator. For a two state system such as that studied

here, in matrix form this gives:

$$\hat{H} = \begin{pmatrix} \hat{T} + \hat{V}_1 & -\hat{\mu}E(t) \\ -\hat{\mu}E(t) & \hat{T} + \hat{V}_2 \end{pmatrix}.$$ (5.2)

The kinetic energy operator $\hat{T}$ is the same as that used in equation 2.55 and the potential energy operators $\hat{V}_1$ and $\hat{V}_2$ are the PESs for the $1\ ^1A'$ and $1\ ^3A''$ states. $\hat{\mu}$ is the TDM operator as described in section 4.3. As in earlier chapters it is assumed that the total angular momentum $J = 0$, and that the laser light is polarised parallel to the TDM.

5.3.2 Laser pulses

Gaussian pulse envelopes have been used throughout as these are slightly easier to work with than sech^2 functions and are a reasonable description of a typical ultrafast laser pulse. To include the pulses in the Hamiltonian, the following mathematical form has been used:

$$E(t) = S \times \frac{\sqrt{4\ln 2}}{\sqrt{\pi}w} \exp\left(-\frac{4\ln 2}{w^2}(t - t_0)^2\right) \cos\left(\omega(t - t_0)\right)$$ (5.3)

This includes a strength factor S reflecting the power of the laser pulse, the normalised intensity of the pulse (i.e. the Gaussian envelope squared) and the oscillating field. w is the temporal FWHM of the pulse, t_0 is the time the pulse is centred at, and ω is the frequency.

When more than one pulse is used, the second pulse is centred at time t_{0b}. If the pulses are allowed to interfere both constructively and destructively, this new time needs to be used in both the envelope and field parts of the pulse. In this situation the pulses are referred to as 'freely interfering'. The alternative is to keep the phases of the two pulses in sync with each other: to do this, the central time of the second pulse envelope is changed to t_{0b}, but the field remains relative to t_0. These pulses are referred to as 'phase-locked'. Figure 5.1 illustrates these two situations for a pair of pulses 21 fs apart. The Dazzler can be programmed to operate in both modes.
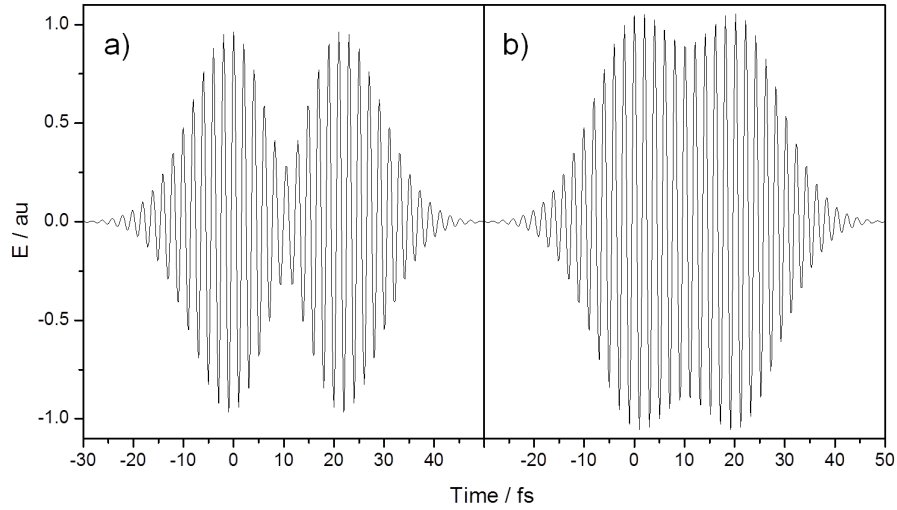
Figure 5.1: The variation in the electric field produced a pair of laser pulses centred at an energy of 2.048 eV and separated by 21 fs, a) when the field of the second pulse is taken relative to t_{0b} (here 21 fs), and b) when the fields are both relative to the same time t_0. In this second case the pulses are able to interfere destructively.

Linear chirp

For pulses with linear chirp, the following description has been used:

$$E(t) = S \times \frac{\sqrt{4\ln 2}}{\sqrt{\pi}w} \exp\left(-\frac{4\ln 2}{w^2}(t-t_0)^2\right) \cos\left(\omega(t-t_0) + \alpha(t-t_0)^2\right) \qquad (5.4)$$

where α is the degree of chirp. This gives a linear variation in frequency with time. The resulting instantaneous frequency is:

$$\omega_{inst} = \omega_0 - \frac{d\phi}{dt} = \omega_0 + 2\alpha(t-t_0) \qquad (5.5)$$

where ω_0 is the central frequency of the pulse. Figure 5.2 shows an example pulse with linear chirp; the pulse is centred at an energy of 2.048 eV (equivalent to $\omega_0 = 3.111$ fs^{-1}) and has $\alpha = +10$ cm^{-1} fs^{-1} (equivalent to 1.884×10^{-3} fs^{-2}). Note that fs^{-2} is a more commonly used unit of chirp, but here cm^{-1} fs^{-1} has been used for ease of calculation. Similarly, central frequencies have been quoted in eV to allow easier comparison with the energies used in previous chapters. If the pulses are freely interfering, the oscillating field of the second pulse needs to be centred at time t_{0b}, i.e. the field has the form
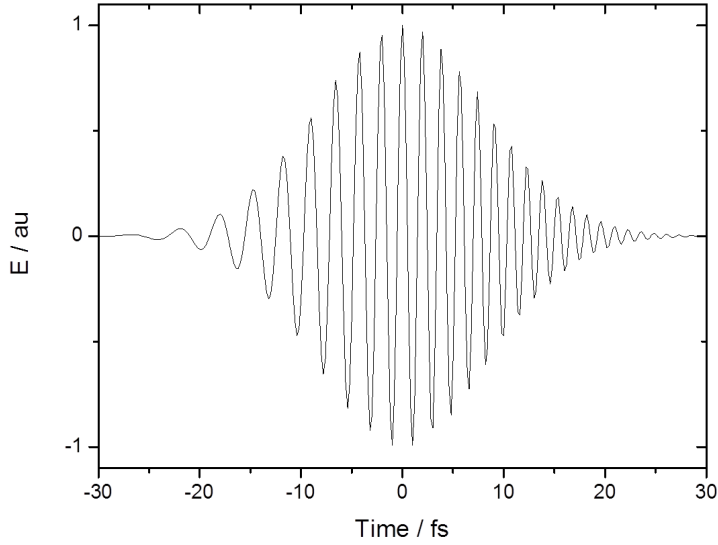
Figure 5.2: The electric field of a linearly-chirped Gaussian pulse centred at an energy of 2.048 eV with $\alpha = +10 \text{ cm}^{-1} \text{ fs}^{-1}$.

$\cos\left(\omega(t - t_{0b}) + \alpha(t - t_{0b})^2\right)$. However, if the pulses are phase-locked the field of the second pulse needs to be $\cos\left(\omega(t - t_0) + \alpha(t - t_{0b})^2\right)$.

Quadratic chirp

Some calculations have also been run using pulses with quadratic chirp. These have the form:

$$E(t) = S \times \frac{\sqrt{4\ln 2}}{\sqrt{\pi}w} \exp\left(-\frac{4\ln 2}{w^2}(t - t_0)^2\right) \cos\left(\omega(t - t_0) + \beta(t - t_0)^3\right) \qquad (5.6)$$

where β is the degree of quadratic chirp. Note that no linear chirp has been included in these pulses. This results in an instantaneous frequency of

$$\omega_{inst} = \omega_0 - \frac{d\phi}{dt} = \omega_0 + 3\beta(t - t_0)^2. \qquad (5.7)$$

For freely interfering pulse pairs, the carrier wave of the second pulse has the form $\cos\left(\omega(t - t_{0b}) + \beta(t - t_{0b})^3\right)$, whereas for phase-locked pulses it is $\cos\left(\omega(t - t_0) + \beta(t - t_{0b})^3\right)$.

Pulse strength

Test calculations were carried out to find the optimum strength of the laser pulse, which can have a marked effect upon the results of a wavepacket propagation, particularly if the pulse energy is not completely resonant with one of the peaks in the excited state absorption spectrum. If the strength is too low, only a negligible portion of the wavepacket will be excited onto the upper electronic state surface. The population on this state also will not increase smoothly, showing unphysical decreases as wavepacket density is transferred back to the ground state. Spurious peaks in the flux spectrum can then occur. The cause of these problems is not clear, but they could result either from highly vibrationally excited levels of the ground state becoming populated, or more simply from numerical errors in the calculation. In contrast, if the strength is too high, the population on the upper electronic state becomes tied to the oscillating field of the laser pulse, and moves up and down with it. This can also result in spurious peaks well outside the energy range of the exciting pulse, rendering the results virtually meaningless. In addition, if the pulse strength is too high then the perturbation theory used is no longer valid.

In experiments, only a very small proportion of the ground state wavepacket is likely to be excited onto the upper electronic state. This cannot be modelled realistically in the calculations. Therefore a compromise needs to be made: enough population needs to be excited to avoid spurious results and to allow sufficient wavepacket density for valid analysis, without using intensities so high as to produce unphysical results. To this end, laser strengths which result in around 10 to 30% of the ground state population being excited seem reasonable. For calculations involving a single laser pulse this meant $S = 350$ was a good choice, and for double pulses $S = 175$ was used.

5.3.3 Calculation set-up

All control calculations have been carried out using the MCTDH method. The PESs for the $1\,^1A'$ and $1\,^3A''$ states are those used in chapter 4. The same numbers of DVR grid points and the same CAP parameters were used, but in order to improve calculation times the number of SPFs were changed as follows:

- R coordinate: 3 on 1 ^{1}A$'$ state, 8 on 1 ^{3}A$''$ state

- r coordinate: 3 on 1 ^{1}A$'$ state, 6 on 1 ^{3}A$''$ state

- γ coordinate: 3 on 1 ^{1}A$'$ state, 8 on 1 ^{3}A$''$ state.

Although using a lower number of SPFs makes the calculations less accurate, the differences in test calculations compared to those with 10 SPFs for each state and mode were very small.

In order to more accurately model the excitation process, the laser pulse is operated on by the TDM function. The form of the laser pulses used has already been discussed. To capture the complete photodissociation process even with substantial delays, the propagations were run from -40 to 240 fs in most cases, with the first pulse centred at $t_0 = 0$ fs. Once the propagations had completed, the NO product state distributions were found by analysing the quantum flux passing into the CAP, as before. The population of each state, i.e. the proportion of the wavepacket lying on the 1 ^{1}A$'$ and 1 ^{3}A$''$ surfaces, was also calculated every 1 fs. This is found from the norm of the MCTDH expansion coefficients for each state, i.e. from $\sqrt{\sum A^2_{j_1 \dots j_f}(t)}$ [93].

5.4   Excitation with single pulses

To test the calculation set-up, wavepacket propagations were run using single pulses at energies corresponding to the peaks in the absorption spectrum. For these calculations, a pulse width w of 25 fs was used. Figure 5.3 shows the quantum flux distributions for pulses centred at 2.017, 2.048, 2.11 eV and 2.232 eV, corresponding to the peaks for v* = 0 with n* = 0, 1, and 2, and v* = 0 with n* = 1. The pulses are sufficiently wide in bandwidth that peaks corresponding to multiple values of n* appear in all cases. For an energy of 2.11 eV there is a small, higher-energy peak corresponding to NO produced in v = 1, and for 2.232 eV there is a larger peak at lower energy showing that a reasonable proportion of NO in v = 0 is produced.
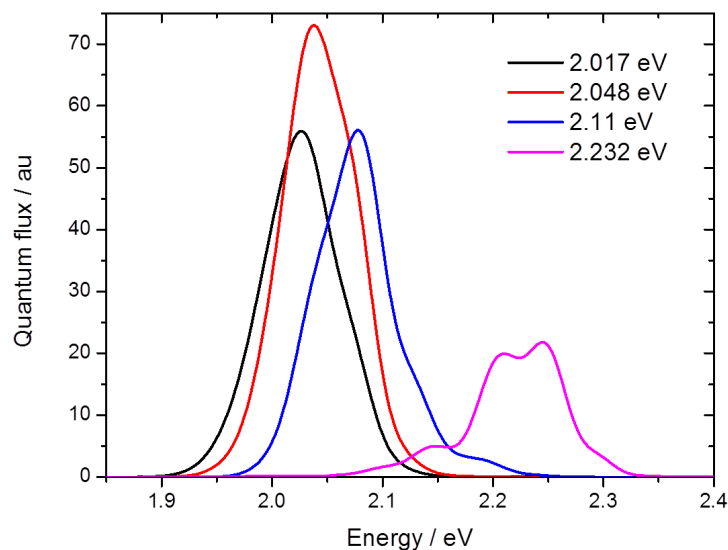
Figure 5.3: The energy distributions of the quantum flux entering the CAP following excitation with a single 25 fs laser pulse at a range of energies.

Note that the bandwidths of the quantum flux distributions are a little wider than would be expected for transform limited pulses. This is an artefact due to the time-to-energy Fourier transformation carried out at each time-step during the wavepacket propagation. The time-step is normally set at 0.25 fs; reducing this gives a reduction in bandwidth but at the expense of a considerably increased calculation time.

At a central frequency corresponding to 2.048 eV, calculations were also run with a variety of pulse widths. As shown in figure 5.4, these behave as expected: the bandwidth of the quantum flux entering the CAP increases as the pulse length decreases, with corresponding changes in NO vibrational and rotational distributions as more vibrational states on the $1\,^3A''$ electronic state are accessed. For the 5 fs pulse, the NO stretching vibration is not just in $v^* = 0$; a significant amount in $v^* = 1$ is also formed, whereas for the 40 fs pulse only $v^* = 0$ is populated. The NO rotational state distributions imply that for the 40 fs pulse the majority of the flux ends up in $n^* = 1$, but as the pulse length decreases the distribution averages out and peaks corresponding to particular values of n^* are no longer clear.
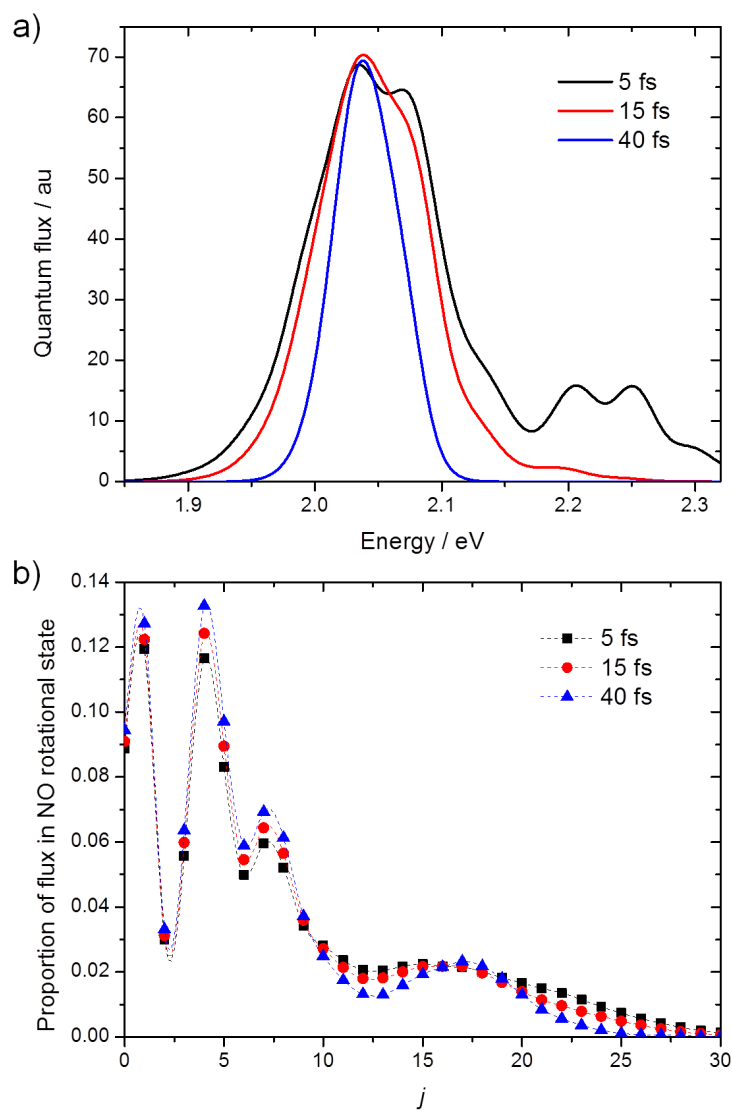
Figure 5.4: Results from wavepacket propagations including a single laser pulse at 2.048 eV, for pulse widths of 5, 15 and 40 fs. Panel a) shows the energy distributions of the quantum flux entering the CAP, and panel b) shows the NO rotational distributions.

5.5   Energies for control

In order to effect control using ultrashort laser pulses, multiple states (in this case vibrational) need to be excited. Therefore, the bandwidth of the laser pulses used needs to be such that multiple peaks in the absorption spectrum are encompassed. To attempt to control NO rotational distributions it is therefore desirable to use a bandwidth which covers all of the sub-peaks due to the different quanta of the excited ClNO bending vibration, n*, for each value of v*, the NO stretching vibration. Only n* = 0, 1 and 2 are observed in the absorption spectrum of the 1 ^{3}A$''$ state; the energy from this mode goes into NO rotational motion whereas that from v* is essentially adiabatic with respect to the product NO stretch, v.

For the main peak corresponding to v* = 0, the energy difference between the sub-peaks is 0.093 eV, or 750 cm^{-1}. To produce this bandwidth from a TL Gaussian pulse, a pulse length of <20 fs is needed. These pulses need to be centred on the central energy of the main peaks corresponding to each value of v*, i.e. on the sub-peak corresponding to n* = 1. In order to attempt control on the NO vibrational state distributions, a wider energy gap of 0.176 eV, or 1420 cm^{-1} is required. This corresponds to a TL pulse length of <10 fs. These pulses need to have a central energy in between that of the two main peaks of interest, where for a longer pulse the absorption cross-section would be rather low.

Given these observations, control has been investigated with the following laser pulses:

- 20 fs long pulses centred at 2.048 eV, which excites the 1 ^{3}A$''$ (0,1) ← 1 ^{1}A$'$ transition (where (0,0) denotes (v*,n*)), to control the NO rotational state when v* = 0

- 20 fs long pulses centred at 2.232 eV, which excites the 1 ^{3}A$''$ (1,1) ← 1 ^{1}A$'$ transition, to control the NO rotational state when v* = 1

- 10 fs long pulses centred at 2.151 eV, between the 1 ^{3}A$''$ (0,1) ← 1 ^{1}A$'$ and 1 ^{3}A$''$ (1,1) ← 1 ^{1}A$'$ transitions, to control the NO vibrational state.

5.6   Transform limited pulse pairs

To begin, simple TL laser pulses were used. Wavepacket propagations were run in two ways: firstly, with phase-locked pulses, and secondly with freely interfering pulses. Propagations were carried out for values of the delay τ every 3 fs from 0 to 30 fs, and at 40 and 50 fs, in addition to any other delays deemed necessary. For longer delays the bulk of the wavepacket would have moved out of the FC region before the second pulse arrived.

5.6.1 $1\,^{3}A''$ (0,1) $\leftarrow$ $1\,^{1}A'$ transition (2.048 eV)

At an excitation energy of 2.048 eV, centred on the $1\,^{3}A''$ (0,1) $\leftarrow$ $1\,^{1}A'$ transition, in the region of 98% of product NO is formed in v = 0. Therefore, only NO rotational distributions should be controllable, and so the analysis is simpler than for other energies which encompass a greater range of states. With pulses of 20 fs duration, the bandwidth should be sufficient that the n* = 0, 1, and 2 bending modes are all excited.

Phase-locked pulses

Keeping the oscillating field of both pulses locked to t_0 and varying the delay τ yields NO rotational distributions as shown in figure 5.5. The distributions appear to mostly be a mix of those corresponding to excitation to n* = 0 and 1 on the $1\,^{3}A''$ state (refer to the distributions shown earlier in figure 4.21). The magnitude of the higher j peak varies slightly, decreasing by a small amount as the delay increases, but there is nothing to suggest that completely different photodissociation pathways are being accessed. Instead, examination of the energy distribution of the quantum flux given in figure 5.6 shows that the flux becomes centred at lower energies at longer delays. This means the proportion of excited ClNO formed in n* = 1 will decrease slightly.

    The total flux excited onto the upper state surface decreases as the τ increases, before levelling out at longer delays. For all delays, between 98.2 and 98.7% of NO was formed in v = 0. This variation is negligible, and there is effectively no control.
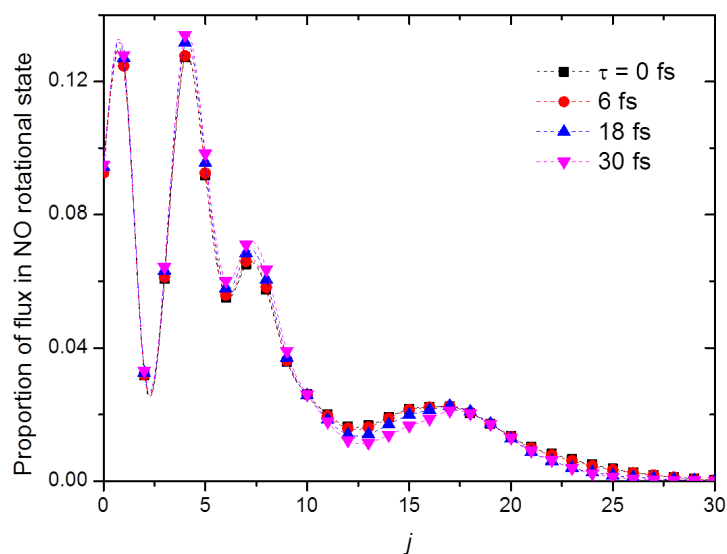
Figure 5.5: NO rotational distributions following wavepacket propagations on the $1\,^3A''$ state, including pairs of 20 fs long laser pulses centred at an energy of 2.048 eV separated by a range of delays, τ. The oscillating fields of both pulses were locked to t_0.
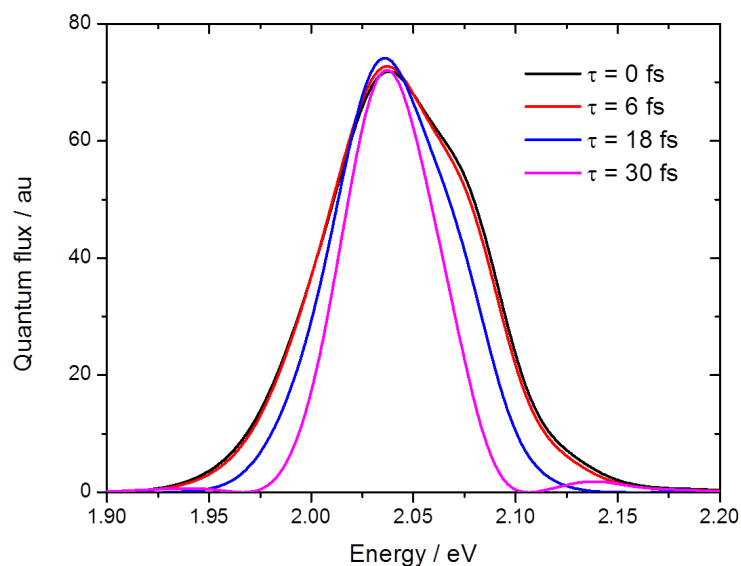
Figure 5.6: The energy distributions of the quantum flux entering the CAP for wavepacket propagations involving a pair of 20 fs laser pulses centred at 2.048 eV. The oscillating fields of both pulses were locked to t_0.

Freely interfering pulses

Allowing the pulses to interfere freely yields a much greater change in NO rotational distribution with delay. Figure 5.7 shows the distributions for a range of delays. It is immediately clear that there are two main dissociation channels, resulting in two patterns of rotational distribution. For even values of τ, there is a peak centred at $j \sim 17$, and reduced population at lower and higher j. For odd values of τ there is a minimum at $j \sim 17$; instead the major features are increased population at lower j and a smaller hump centred around $j \sim 22$. Note that for longer delays, especially those greater than $\tau = 70$ fs, the rotational distributions are virtually identical to those for when the delay is 0 fs, showing that the wavepacket excited by the first pulse has moved completely out of the FC region by this point.
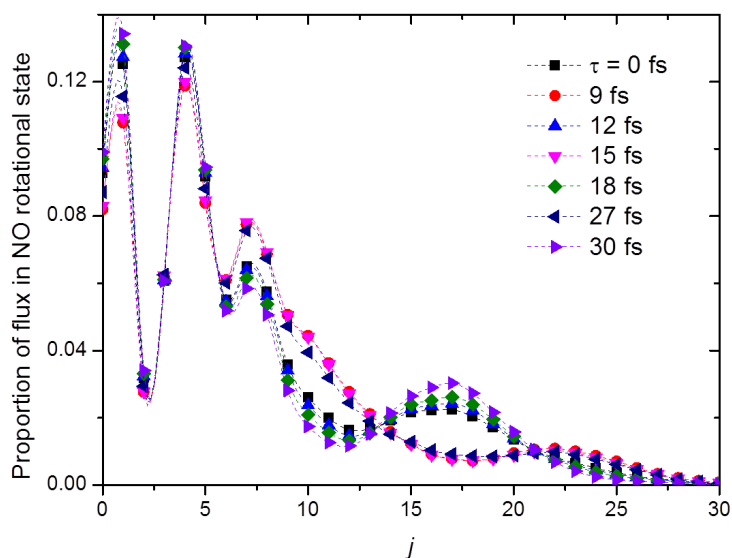
Figure 5.7: NO rotational distributions following wavepacket propagations on the 1 $^3A''$ state, including pairs of 20 fs long laser pulses centred at an energy of 2.048 eV separated by a range of delays, τ. The pulses were allowed to interfere freely.

The total flux excited onto the 1 $^3A''$ state varies dramatically according to the degree of destructive interference. The variation in the total quantum flux with τ is given in figure 5.8, showing that the flux oscillates with a period of ~ 2 fs, which is the same as the period of the electric field of each of the exciting pulses. The total flux for even values of τ (giving the hump at $j \sim 17$) is high, whereas that for odd values of τ (giving no hump at
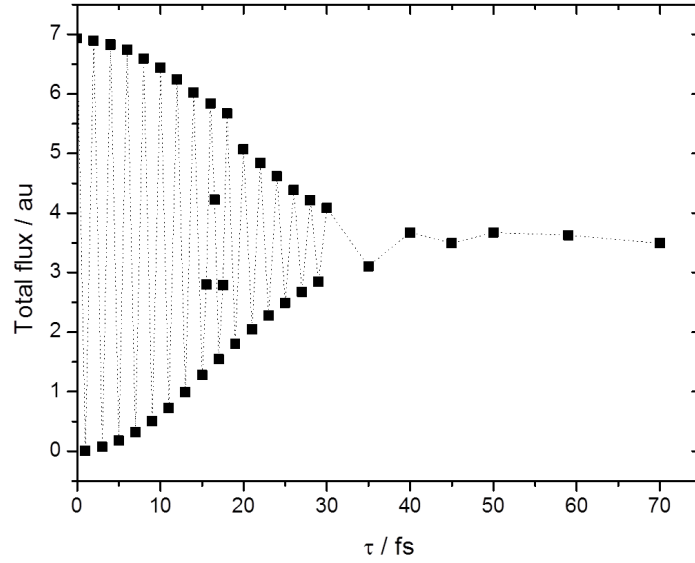
Figure 5.8: The total quantum flux excited onto the $1\,^3A''$ state by pairs of 20 fs long laser pulses centred at an energy of 2.048 eV separated by a range of delays, τ.

$j \sim 17$) is low, until longer delays when it levels out at a value half that for when $\tau = 0$ fs.

The variation in the total flux can be explained as follows. The degree of absorption is proportional to the intensity of the exciting light pulse, i.e. to the square of the electric field. In a situation with a pulse pair, the overall intensity is given by

$$I = I_1 + I_2 + 2\sqrt{I_1 I_2}\mathrm{Re}\{\gamma_{12}(\tau)\}. \tag{5.8}$$

Here, $\gamma_{12}(\tau)$ is the complex degree of coherence, which relates to the phase difference between the pulses and is given as

$$\gamma_{12}(\tau) = \frac{\langle E_1(t+\tau)E_2^*(t)\rangle}{\sqrt{\langle |E_1(t)|^2 |E_2(t)|^2\rangle}}. \tag{5.9}$$

When the pulses are completely in-phase, i.e. $\mathrm{Re}\{\gamma_{12}(\tau)\} = 1$, they will interfere constructively. Assuming the pulses are identical, the overall intensity will then be four times that of a single pulse, or double that of two non-interacting pulses. In contrast, if the pulses are completely out of phase, i.e. $\mathrm{Re}\{\gamma_{12}(\tau)\} = -1$, they will interfere destructively and the intensity will drop to zero. In between these two extremes when $\mathrm{Re}\{\gamma_{12}(\tau)\} = 0$,

the behaviour will be identical to that of two completely separate pulses [162]. Since the optical period of a pulse centred at 2.048 eV is $\sim$2 fs, even values of τ give pulses that are very nearly in phase, whereas for odd values of τ they are out of phase.

In order to ensure that the differences in the NO rotational distributions were not purely due to the lower proportion of ground state wavepacket being excited onto the $1\,^3A''$ state, calculations for $\tau = 9$, 15 and 18 fs were re-run with higher pulse strengths. The NO rotational distributions produced were virtually identical regardless of the value of S (barring pulses clearly too weak or too strong as discussed earlier), and therefore it can be safely assumed that the differences are real. In addition, calculations for a range of pulse strengths for $\tau = 0$ fs were run. These found that the results varied very little for strengths leading to more than $\sim$0.5 au of quantum flux being excited to the upper state. This implies that the results obtained here for $\tau = 1$, 3, 5 and 7 fs may be dubious as less than 0.5 au of flux was excited in these cases, but all others should be valid.

By inspection of the wavepacket in the asymptotic region, the origin of the rotational distributions can be found. As examples, results for $\tau = 15$ fs, which results in a distribution without a hump centred at $j \sim 17$, and $\tau = 18$ fs, which yields a distribution with it, are now considered in more detail. Figure 5.9 shows how the wavepacket density varies with R and γ for a fixed r bond length of 2.15 bohr. Schinke's rotation-reflection principle states that the NO rotational distribution reflects the angular distribution of the wavepacket in the γ coordinate. By inspecting the wavepackets in the asymptotic region as they hit the CAP, the reason for the difference in rotational distributions becomes clear: for $\tau = 18$ fs, the shape of the wavepacket is simpler and results in two clear peaks. In contrast, for $\tau = 15$ fs, the wavepacket is more structured, having the main peak, but then smaller peaks appearing at lower γ than for $\tau = 18$ fs. The shapes in the γ coordinate reflects those of the rotational distributions near-perfectly.

As previously shown in chapter 4, the shape of each NO rotational distribution derives from the populations of the different bending quanta, n*, on the excited $1\,^3A''$ state. For $j < 11$, the majority of the flux derives from ClNO in n* = 0, for $14 < j < 20$ it is from n* = 1, and for $j > 24$ the majority corresponds to n* = 2. Hence, when the hump in the rotational distribution centred at around $j = 17$ disappears, this is due to the suppression
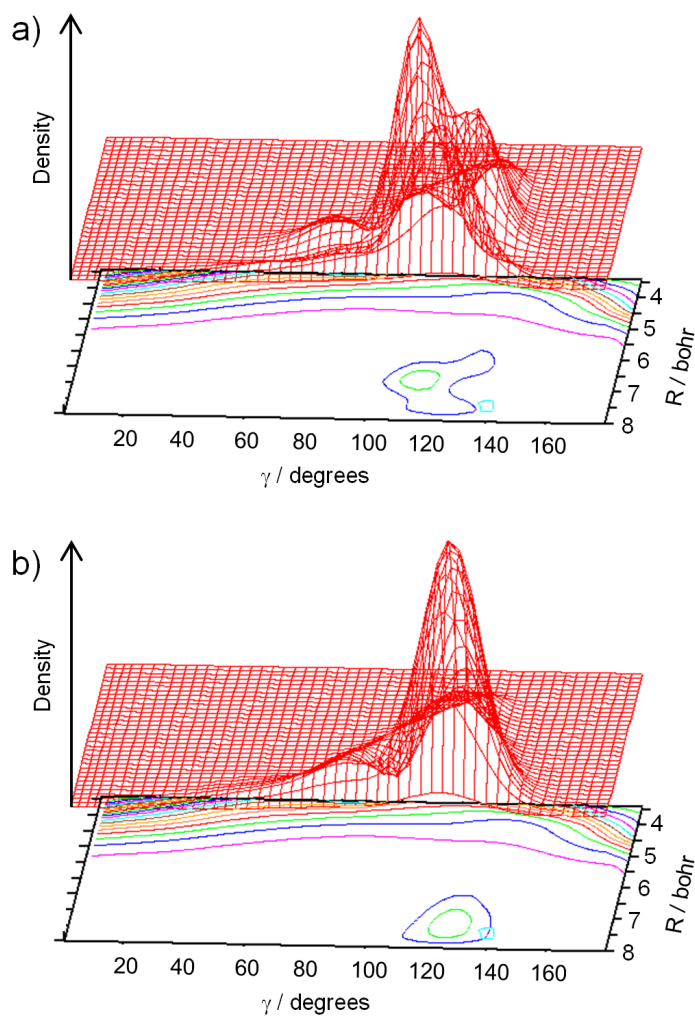
Figure 5.9: A visualisation of the wavepackets during propagations on the $1\ ^3A''$ state, for a cut through the PES with $r = 2.15$ bohr. The pair of laser pulses used were 20 fs in duration and centred at an energy of 2.048 eV. Panel a) shows the wavepacket at $t = 90$ fs when $\tau = 15$ fs, and panel b) shows the wavepacket at $t = 100$ fs when $\tau = 18$ fs. Clear differences can be seen between the two wavepackets.

of the portions of the wavepacket with n* = 1. The proportion of NO formed in low j is similarly linked to the amount of wavepacket in n* = 0. The population of n* = 2 is always considerably lower, and so any effects from this are harder to see.

The question of why the NO rotational distributions vary is hence equivalent to that of how the n* distribution in the 1 ^{3}A″ state comes about. There are two potential explanations for the variation with delay: firstly, the second pulse is interfering with the wavepacket excited by the first pulse in a way which changes the excited state bending quanta occupied, or secondly that the two pulses are combining in such a way that only certain energies are excited in the first place. To find the most likely reason, the results for a range of delays spaced every 0.5 fs from 15 to 18 fs have been examined in more detail.

NO rotational distributions for these delays are shown in figure 5.10. The distributions for values of τ 2 fs apart are very similar, with $\tau = 17$ fs giving almost the same results as for $\tau = 15$ fs as seen earlier, and $\tau = 16$ fs near-identical to $\tau = 18$ fs. For $\tau = 15.5$, 16.5 and 17.5 fs, which give values of the total quantum flux between the extremes, the rotational distributions are different: those for $\tau = 15.5$ and 17.5 fs have a significant hump centred at around $j \sim 16$ with rather smaller populations at lower j, whereas that for $\tau = 16.5$ fs has a smaller hump at $j \sim 17$ with more population at lower j. These suggest that the distributions of the bending vibration n* on the 1 ^{3}A″ state are as follows:

- $\tau = 15$ fs: mostly n* = 0

- $\tau = 15.5$ and 17.5 fs: mostly n* = 1, with some n* = 0 and 2

- $\tau = 16$ and 18 fs: mostly n* = 1, but with a substantial population in n* = 0

- $\tau = 16.5$ fs: mix of n* = 0 and 1.

The electric fields of the combined pulses for $\tau = 15$, 15.5, 16 and 16.5 fs are given in figure 5.11, showing how the variation in delay causes significant changes in the overall field. For $\tau = 15$ fs, there is significantly more destructive interference, resulting in a pulse pair with much lower overall amplitude, and hence to a small amount of quantum flux being excited onto the upper state surface. In contrast, for $\tau = 16$ fs, the interference is more constructive, giving a pulse pair with a larger overall amplitude which excites 4.5 times more flux.
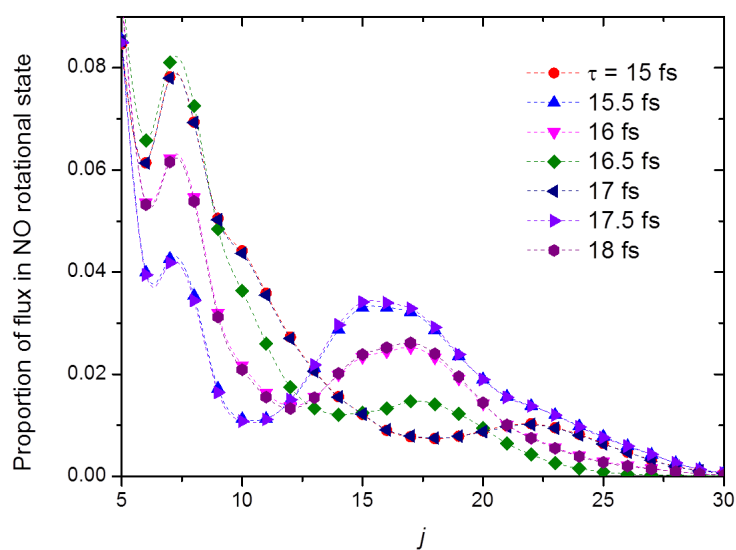
Figure 5.10: Parts of the NO rotational distributions following wavepacket propagations on the $1\,^3A''$ state, including pairs of 20 fs long laser pulses centred at an energy of 2.048 eV separated by a range of delays, τ spaced every 0.5 fs from 15 to 18 fs. The pulses were allowed to interfere freely.
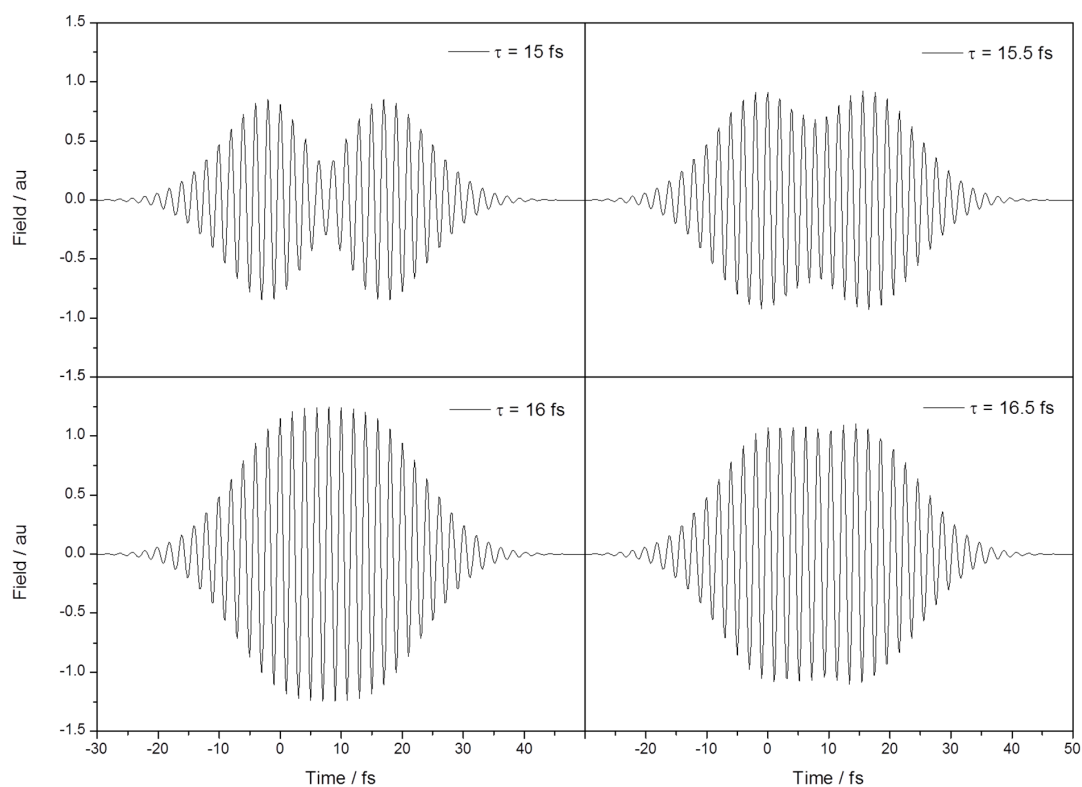
Figure 5.11: Plots of the pulse electric field for pairs of freely interfering pulses separated by delays of $\tau = 15$, 15.5, 16 and 16.5 fs.

To help understand how these fields result in the different NO distributions, they were Fourier transformed into the energy domain. Recall that the centres of the peaks for v* = 0 corresponding to n* = 0, 1 and 2 lie at 2.017, 2.048 and 2.11 eV respectively. By examining the positions of the peaks in the energy distribution of the pulses, it is therefore possible to see which n* states will be excited. The energy distributions of the pulse pairs given in figure 5.11 are shown in figure 5.12. The peaks are centred as follows:

- τ = 15 fs: peaks at 1.99 and 2.13 eV, implying n* = 0 most populated, then n* = 2, with less n* = 1

- τ = 15.5 fs: small peak at 1.94 eV, larger peak at 2.09 eV, implying a mix of n* states, but with less n* = 0.

- τ = 16 fs: large, broad main peak at 2.05 eV, implying the most populated state will be n* = 1, but still with significant population in n* = 0 and 2 due to its breadth

- τ = 16.5 fs: main broad peak at 2.03 eV, implying n* = 0 and 1 will both be populated.

Of course, these predictions will be tempered by the absorption spectrum of the 1 ^{3}A″ state, but they nonetheless match well with those qualitatively derived from the NO rotational distributions above. To further support this observation, figure 5.13 shows the energy distribution of the quantum flux for these propagations. For τ = 15 fs, it can clearly be seen that the central energy portion of the wavepacket has been cancelled out by the interference between the pair of pulses, whereas for τ = 16 fs the flux spectrum consists of a single broad peak spanning all n* energies.

A further piece of information obtainable from the wavepacket propagations is the total population on the 1 ^{3}A″ surface for each time step. For τ = 15, 15.5, 16 and 16.5 fs the change in population over 60 fs of the propagation from t = -20 to 40 fs is given in figure 5.14. This is the period during which the bulk of the absorption occurs for these short delays, and during which no wavepacket density has reached the CAP and hence been absorbed by it. It can be seen that the population in the upper state increases smoothly for τ = 16 and 16.5 fs, but for the other delays this is not the case. For τ = 15.5 fs the slope of the population increase becomes less steep in a similar time period to that when the amplitude of the overall electric field as shown in figure 5.11 is smaller. Most interesting
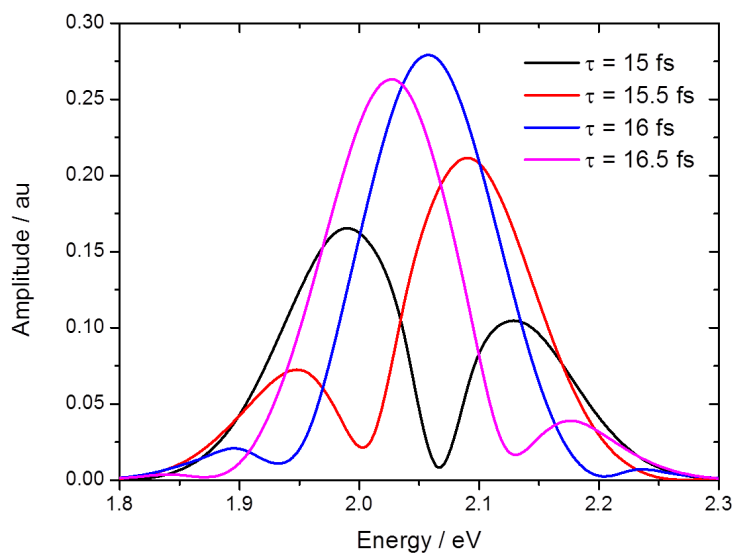
Figure 5.12: The energy distribution of the pulse pairs given in figure 5.11, obtained via Fourier transformation.
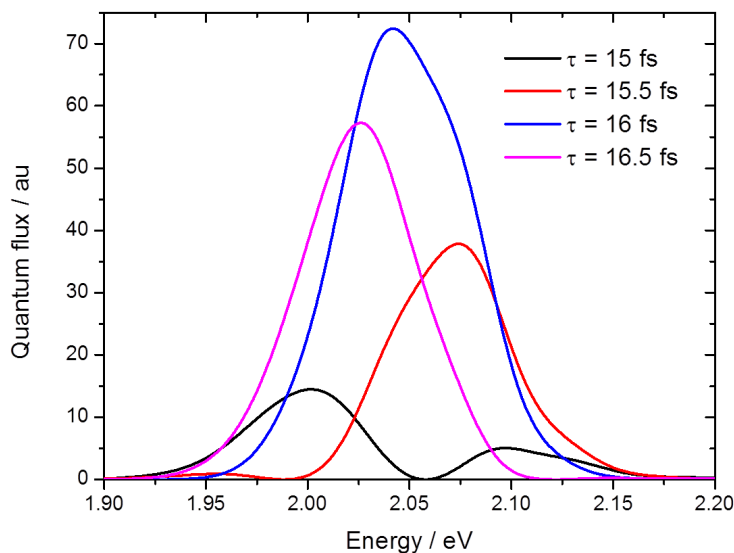
Figure 5.13: The energy distributions of the quantum flux entering the CAP for wavepacket propagations involving a pair of 20 fs laser pulses centred at 2.048 eV. Results are shown for τ = 15, 15.5, 16 and 16.5 fs.
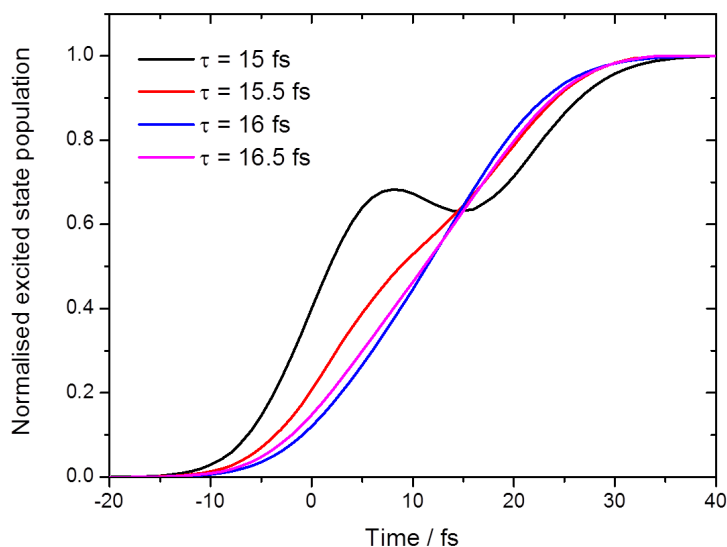
Figure 5.14: The normalised total populations on the 1 ^{3}A″ state from -20 to +40 fs for wavepacket propagations involving a pair of 20 fs laser pulses centred at 2.048 eV. Results are shown for τ = 15, 15.5, 16 and 16.5 fs.

though is the change in population for τ = 15 fs, which shows a marked decrease after 8 fs, before rising again from ∼15 fs. This decrease implies that there is some destructive interference between the wavepacket excited by the first pulse and the electric field of the second - if the only interaction was between the pulses themselves, and not with the wavepacket, this would not be expected.

It must be noted that the total quantum flux excited onto the 1 ^{3}A″ state varies considerably across this range of delays. Therefore, although the proportion of NO produced at a particular j may be enhanced considerably, the amount produced may not change in the same way. For example, consider the flux into the rotational states $j = 7$ and 17 (indicative of the populations in n* = 0 and 1 respectively) at delays of 15 and 16 fs. For $\tau = 15$ fs, 7.8% of NO is produced in $j = 7$, as opposed to 6.2% for $\tau = 16$ fs, a 26% difference. However, the total flux into $j = 7$ is just 0.100 au for $\tau = 15$ fs as opposed to 0.364 au for $\tau = 16$ fs, so despite the fact that a greater proportion of the NO is formed in this state for the shorter delay, the actual population is only 27% of that produced at the longer delay. Similarly, for $\tau = 15$ fs 0.8% of the total flux is produced in $j = 17$, whereas for $\tau = 16$ fs this rises more than threefold to 2.5%. Looking at the total populations this difference becomes even more marked: only 0.010 au of flux enters $j = 17$ for $\tau = 15$ fs, compared
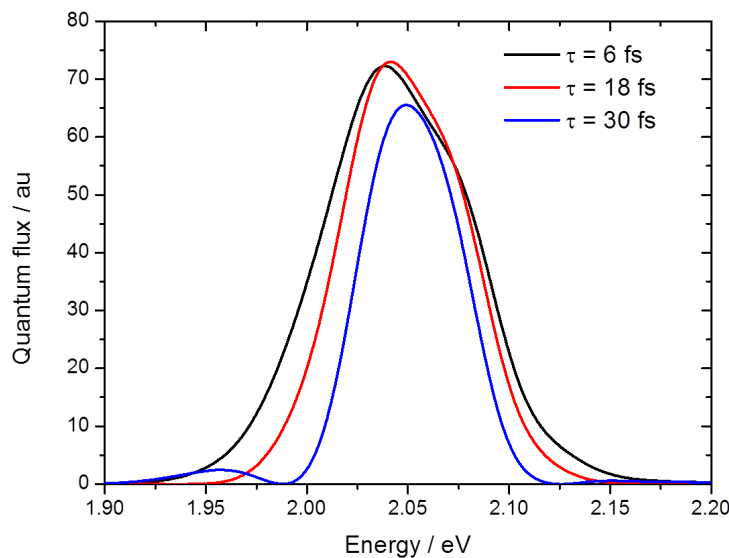
Figure 5.15: The energy distributions of the quantum flux entering the CAP for wavepacket propagations involving a pair of 20 fs laser pulses centred at 2.048 eV for delays of 6, 18 and 30 fs.

with 0.147 au, i.e. 14.7 times as much NO is formed in this state.

The other trend present in the rotational distributions for even delays is that as τ increases, the proportion of NO formed at higher j increases, until the wavepackets excited by each pulse are no longer able to interact. This implies that as the delay increases, a greater proportion of the quantum flux on the 1 $^3A''$ surface ends up in n* = 1. By examining the energy distribution of the quantum flux for τ = 6, 18 and 30 fs, as given in figure 5.15, the reason for this becomes clear: the flux becomes centred at higher energies for longer delays.

The results presented here show that number of quanta in the bending vibration on the 1 $^3A''$ state, and hence the shape of the product NO rotational distribution, can be controlled by 20 fs pulse pairs separated by varying delays. The mechanism is mostly due to the range of frequencies contained in the exciting pulse pair; however there is also a degree of interference between the wavepacket excited by the first pulse and the electric field of the second pulse, showing that the picture is more complicated than just this simple effect. For shorter delays where there is considerable destructive interference care needs to be taken to ensure the total amount of NO produced is not negligible.

5.6.2   1 ^{3}A″ (1,1) ← 1 ^{1}A′ transition (2.232 eV)

The excitation energy of 2.232 eV is centred on the 1 ^{3}A″ (1,1) ← 1 ^{1}A′ transition. Following the absorption of a 20 fs long pulse, most NO is formed in v = 1, but a small proportion in v = 0 is also produced. The picture is therefore slightly more complicated than for an excitation energy of 2.048 eV.

Phase-locked pulses

For these calculations, the oscillating fields of both pulses were locked to t_0. Varying the delay τ results in a change in both the NO vibrational and rotational distributions. Figure 5.16 shows how the proportion of the NO formed in v = 0 and v = 1 varies with τ. When both pulses arrive at the same time the split is around 4:1 for v = 1 to 0, but as the delay increases the proportion in the excited vibrational state increases until it reaches a maximum of 87.5% at τ = 18 fs. As the delay becomes still longer it decreases again, returning to $\sim$ 80% by the time the wavepackets produced by the pulses are no longer interacting significantly. As the period of the NO stretching oscillation in the 1 ^{3}A″ state of ClNO is $\sim$ 18 fs it would appear that the second pulse is providing additional momentum to the initial wavepacket in the r_{NO} direction. This effect is not large, but is clearly present. The relative total flux excited onto the 1 ^{3}A″ surface is also shown in the figure; once again tests were run to ensure the effects seen were not purely down to the laser strength.

There is also a change in the NO rotational distribution as τ is varied, as shown for a few sample delays in figure 5.17. Overall, the rotational distributions appear to derive from ClNO with mixture of excited bending quanta. As the delay increases, the size of the hump at $j \sim 22$ decreases, with a corresponding increase in the size of that at $j \sim 17$. This can in part be explained by the corresponding decrease in v = 0 population: on energy grounds any NO produced in v = 0 is most likely to derive from excited ClNO with n* = 2. However, this would not account for the continuing decrease of the n* = 2 population for larger τ. Instead it is likely that this results from changes in the quantum flux spectra: figure 5.18 shows these for τ = 0 and 18 fs. At τ = 18 fs, the flux is concentrated in a

narrower range of energies, with clearly less in the v = 1, n* = 2 region. At longer delays from $j \sim 40$ fs onwards, the NO rotational distribution once again resembles that for when the pulses arrive together.
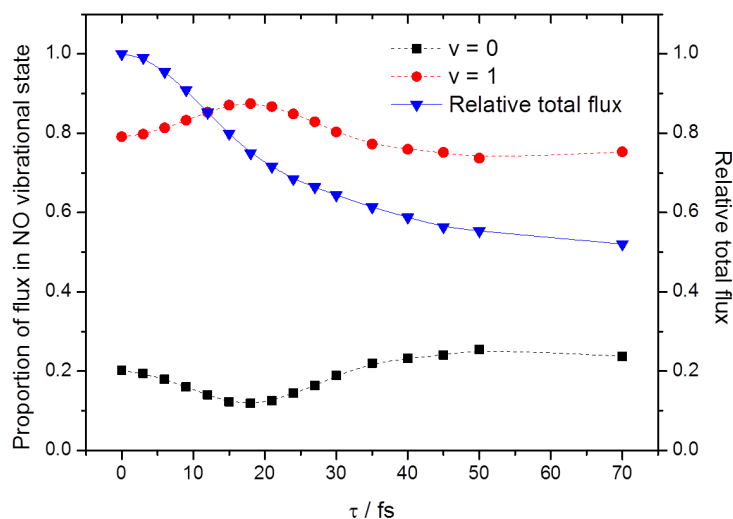
Figure 5.16: The variation in NO vibrational distribution, and total quantum flux, with delay τ following wavepacket propagations involving a pair of 20 fs laser pulses centred at 2.232 eV.
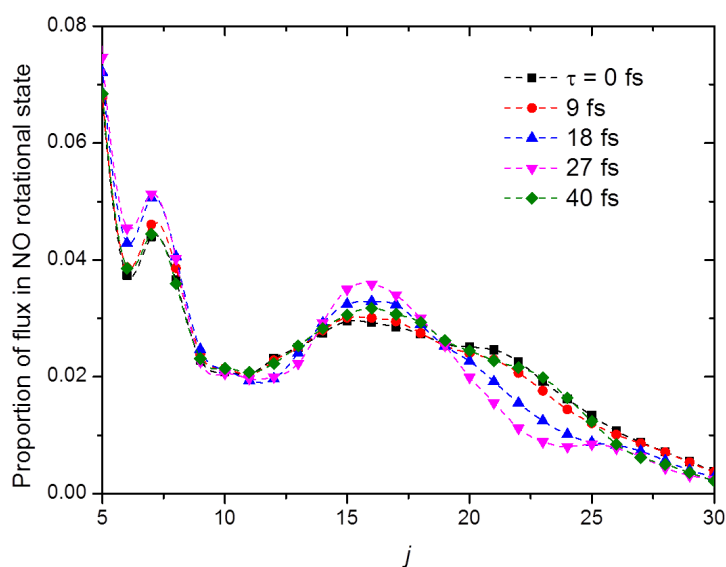
Figure 5.17: Parts of the NO rotational distributions for several values of the delay τ following wavepacket propagations involving a pair of 20 fs laser pulses centred at 2.232 eV.
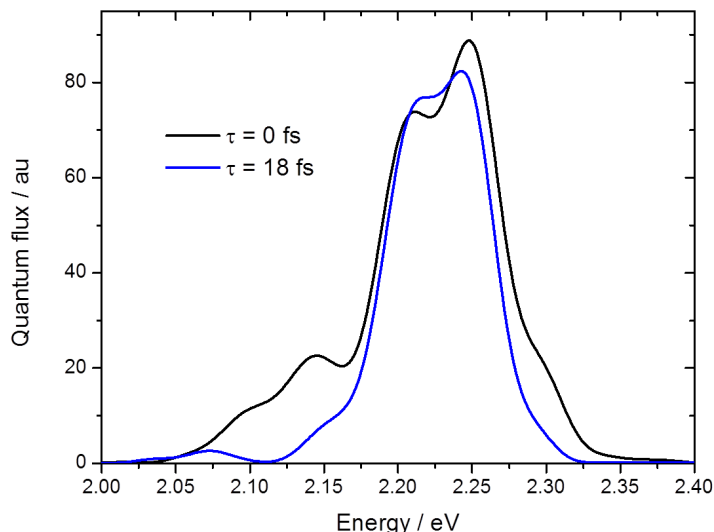
Figure 5.18: The energy distributions of the quantum flux entering the CAP for wavepacket propagations involving a pair of 20 fs laser pulses centred at 2.232 eV, for delays of 0 and 18 fs.

Freely interfering pulses

The situation for freely interfering pulses centred on the $1\ ^3A''$ (1,1) $\leftarrow 1\ ^1A'$ transition is rather more complicated. As shown in figure 5.19, for most delays, the majority of NO (between 62 and 89%) is formed in v = 1. However, the exact proportion does vary significantly, and in the case of τ = 12 fs it drops to only 35%. For delays greater than ~ 40 fs however, the distributions remain reasonably constant.

Panel a) of figure 5.20 shows the NO rotational distributions for 12 values of the delay τ. These differ quite dramatically, implying that there are various dissociation channels involved. Specifically, the shapes of the distributions imply that a large range of combinations of different bending quanta n* are being populated on the $1\ ^3A''$ surface as τ is varied.

To understand these results, consider the wavepacket $\Psi(q,t)$ on the excited state. This can be viewed as a superposition of the n vibrational eigenstates (ψ_n) on this surface, with the form

$$|\Psi(q,t)\rangle = \sum_n c_n |\psi_n(q)\rangle \exp\left(-i(\omega_n t - \phi_n)\right). \tag{5.10}$$
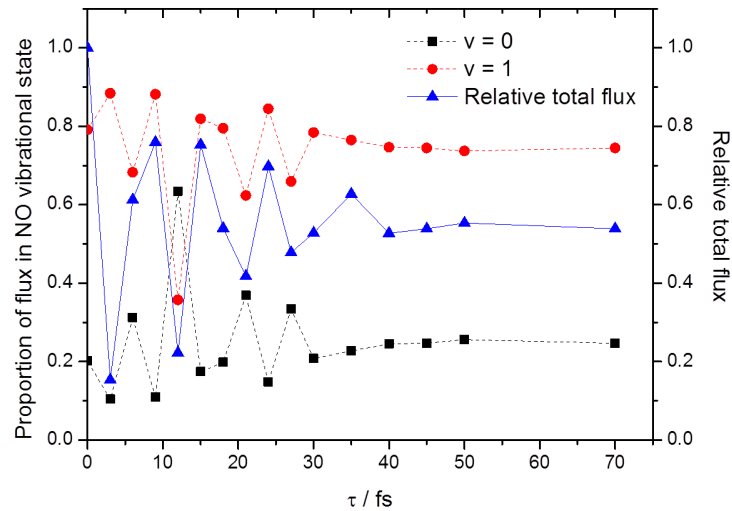
Figure 5.19: The variation in NO vibrational distribution, and total quantum flux, with delay τ following wavepacket propagations involving a pair of freely interfering 20 fs laser pulses centred at 2.232 eV.

The c_n give the amplitudes, the ϕ_n give the phases and the ω_n give the transition frequencies of each vibrational level. As broad bandwidth light is being used, several levels will be excited concurrently and the relative amplitudes and phases of each will be in part controlled by the exciting laser pulse(s).

For a pair of otherwise identical pulses separated by a delay τ, the overall field is:

$$E_{total}(t, \tau) = E_0(t) \cos(\omega_0 t) + E_0(t - \tau) \cos(\omega_0(t - \tau)). \tag{5.11}$$

Following on from equation 5.10, this pulse pair will produce an excited (electronic) state wavefunction with the form

$$|\Psi(q,t)\rangle = \sum_n c_n |\psi_n(q)\rangle \exp(-i(\omega_n t - \phi_n)) + \sum_n c_n |\psi_n(q)\rangle \exp(-i(\omega_n(t - \tau) - \phi_n)). \tag{5.12}$$

From this wavefunction, the population of each vibrational level can be obtained by taking
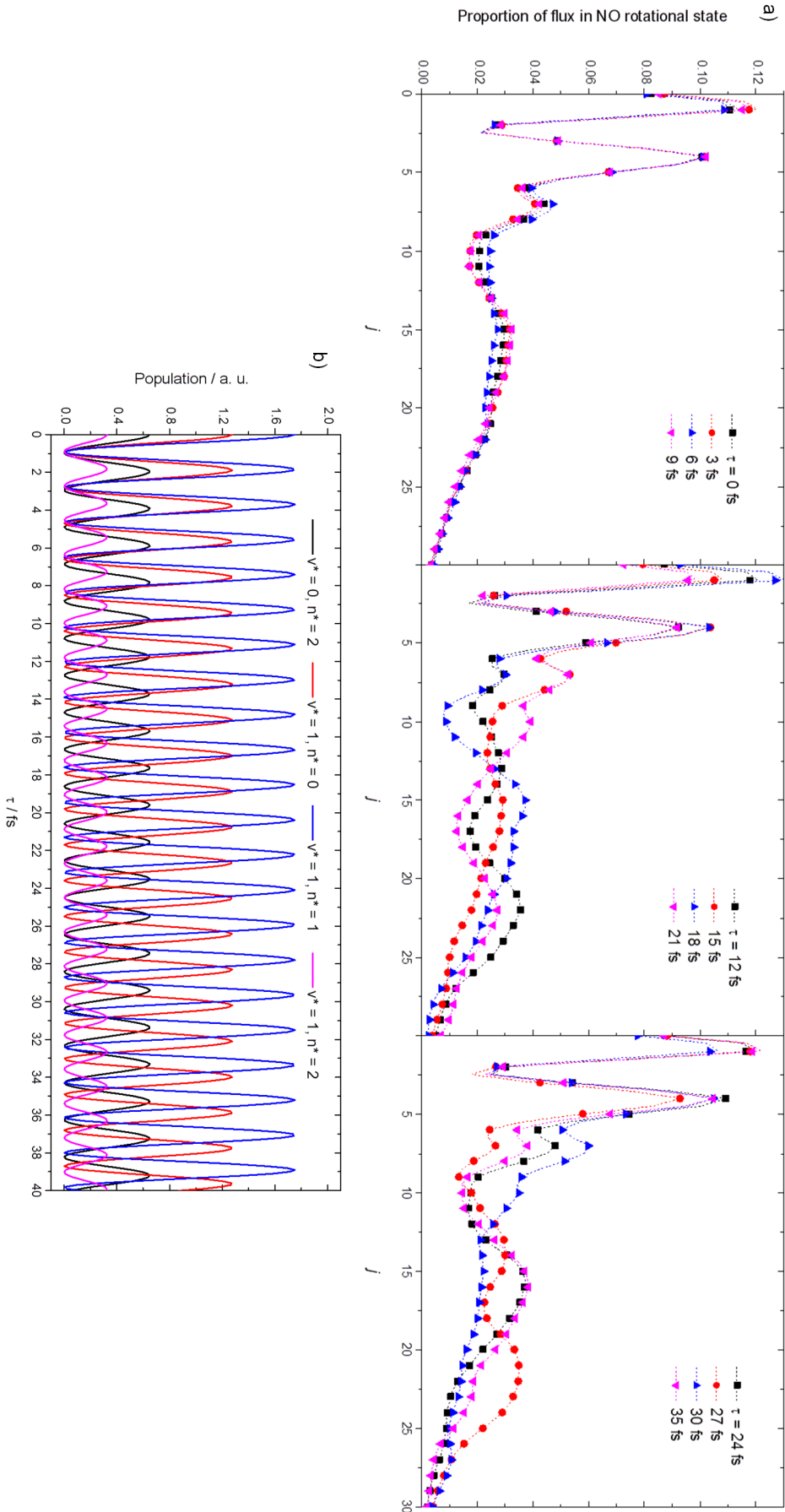
Figure 5.20: Panel a) shows NO rotational distributions following wavepacket propagations on the $1\,^3A''$ state, including pairs of freely interfering 20 fs long laser pulses centred at an energy of 2.232 eV separated by a range of delays, τ. Panel b) shows the predicted populations of the bending vibrations on the excited $1\,^3A''$ state of ClNO for $\tau = 0$ to 40 fs, as calculated using equation 5.13. The relative populations of $n^* = 0$, 1 and 2 for $v^* = 1$, and $n^* = 2$ for $v^* = 0$ are given.

the square of its pulse-mediated amplitude, i.e.

$$
\begin{aligned}
\rho_n &= c_n^2 \left| \exp(-i\omega_n t) + \exp\left(-i\omega_n(t-\tau)\right) \right|^2 \\
&= c_n^2 \left| 1 + \exp(i\omega_n \tau) \right|^2 \\
&= c_n^2 \left(2 + 2\cos\left(\omega_n \tau\right) \right).
\end{aligned}
\tag{5.13}
$$

Note that this assumes the system is bound and that the wavepacket oscillates back and forth along each vibrational mode. It therefore results in populations ρ_n which oscillate at the rate $2\pi/\omega_n$ as the inter-pulse delay is varied [44].

Given this, by taking the angular frequencies of the sub-peaks for all values of n* for v* = 0 and 1 and calculating approximate values of c_n, the expected excited state ClNO vibrational populations for different delays can be found. From these, insight into the final product state distributions can be obtained. Panel b) of figure 5.20 plots expected relative populations for those ClNO 1 $^3A''$ vibrational states states likely to be occupied for an excitation energy of 2.232 eV, namely n* = 2 (v* = 0), and n* = 0, 1 and 2 (v* = 1). To obtain values for the c_n, the flux spectrum for the propagation with $\tau = 0$ fs was taken, and the area under each peak was found by integration. The c_n^2 values were then taken to be the area of each individual peak divided by the total area under the spectrum.

Table 5.1 lists the apparent ClNO excited vibrational state distributions for each value of τ, both as inferred from the NO rotational state distributions shown in panel a) of figure 5.20 and predicted from panel b) of the same figure. The agreement between the inferred and predicted n* distribution is reasonable, up until delays of $\sim$40 fs and greater. This is due to the fact that at these longer delays the wavepacket will have moved sufficiently far away from the FC point to invalidate the model. The agreement for v*, the NO stretch, is less good however, even for shorter delays, implying either that the model is too simplistic to describe the NO stretching motion, or that the system behaves considerably less adiabatically than previously thought.

τ / fs	n* inferred from NO rotational distribution	Proportion of NO in v = 0 / %	(v*,n*) populations predicted from equation 5.13 / %			
			(0,2)	(1,0)	(1,1)	(1,2)
0	Mix of 0, 1, 2, most in 1	20.1	16.2	31.9	43.8	8.1
3	As for τ = 0, but more in 1	10.4	1.5	24.0	57.5	17.0
6	Mix of 0, 1, 2	31.2	24.2	35.3	36.4	4.1
9	Mix, most in 1	11.0	2.1	28.4	56.8	12.7
12	Most in 2	63.4	66.0	28.3	1.1	4.6
15	Mix, most in 0	17.5	4.4	39.7	51.2	4.7
18	Most in 1 and 2	19.8	31.3	1.1	46.8	20.8
21	2 and 0	36.9	14.1	60.7	24.2	0.9
24	1	14.8	12.3	18.2	62.7	6.8
27	2	33.5	32.2	36.4	7.5	23.9
30	Mix, more in 0	20.8	8.4	44.7	46.8	0.1
35	1, some in 2	22.7	23.7	1.0	69.7	5.6
40	Mix, less 0	24.5	3.9	63.4	9.5	23.2
45	Mix	24.7	25.5	39.1	27.0	8.4
50	Mix	25.6	0.0	0.1	99.4	0.5
70	Mix	24.7	10.1	47.7	41.5	0.7

Table 5.1: The vibrational states accessed on the 1 ^{3}A$''$ surface of ClNO, for wavepacket propagations involving a pair of freely-interfering 20 fs laser pulses centred at 2.232 eV separated by variable delays τ. In the second column the n* vibrational state distributions have been inferred by inspecting the shape of the NO rotational distribution for each delay, as shown in panel a) of figure 5.20. These are compared with the distributions predicted from equation 5.13, given in the final four columns. The proportion of NO produced in v = 0 following the wavepacket propagations is also given.

5.6.3   2.151 eV, between the $1\,^3A''\,(0,1) \leftarrow 1\,^1A'$ and $1\,^3A''\,(1,1) \leftarrow 1\,^1A'$ transitions

The excitation energy of 2.151 eV lies halfway between the $1\,^3A''\,(0,1) \leftarrow 1\,^1A'$ and $1\,^3A''\,(1,1) \leftarrow 1\,^1A'$ transitions. By using pulses of 10 fs in duration, all the peaks in the absorption spectrum for v* = 0 and 1, with n* = 0, 1 and 2 can be covered simultaneously.

Phase-locked pulses

At 2.151 eV, when the oscillating fields of both pulses are locked to t_0 there is little change in the NO vibrational distributions as the delay between the pulses is varied. At $\tau = 0$ fs, 78% is formed in v = 0, with the vast majority of the remaining 22% formed in v = 1. As illustrated in figure 5.21, this distribution remains reasonably constant: there is a slight rise in the proportion of NO in v = 0 to 82% at $\tau = 21$ fs, which corresponds to a small decrease in the total quantum flux, and so is likely the result of some minor destructive interference. Despite the excitation energy being halfway between the two main peaks in the absorption spectrum, the proportion of the wavepacket ending up in v* = 0 is much larger than that in v = 1 due to the relative heights of the peaks.
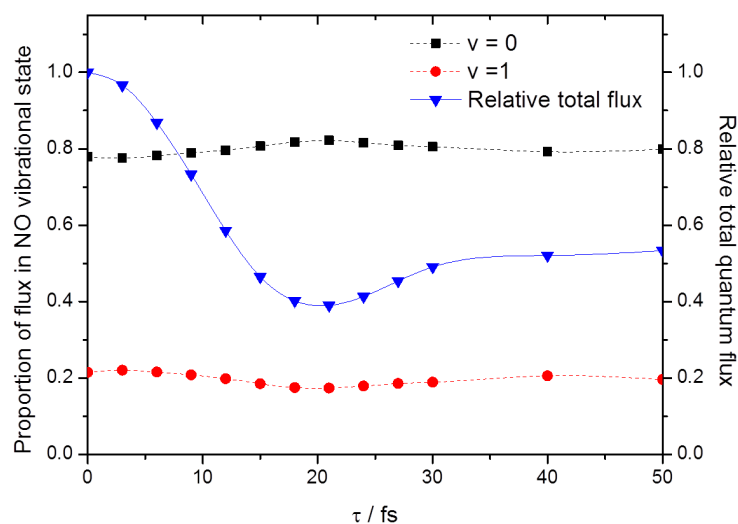
Figure 5.21: The variation in NO vibrational distribution, and total quantum flux, with delay τ following wavepacket propagations involving a pair of 10 fs laser pulses centred at 2.151 eV.

Selected NO rotational distributions are shown in figure 5.22. In contrast to the other
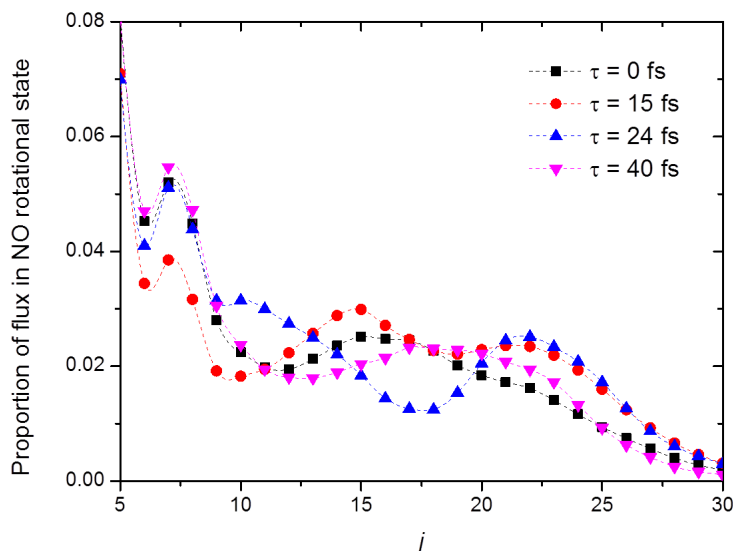
Figure 5.22: NO rotational distributions for several values of the delay τ following wavepacket propagations involving a pair of 10 fs laser pulses centred at 2.151 eV.

energies studied so far with phase-locked pulses, there is a marked variation with τ. When both pulses arrive at the same time, the distribution appears to come from a mixture of excited ClNO bending vibrational states, with more contribution from $n^* = 0$ and 1. As τ increases, it appears that the contribution from $n^* = 0$ decreases and those from $n^* = 1$ and 2 increase, until $\tau \sim 18$ fs. From this point onwards the proportions of $n^* = 2$ and 0 increase, and the hump in the distribution at $j \sim 17$ disappears, implying negligible contribution from $n^* = 1$. At longer delays the distribution moves back to resemble that at $\tau = 0$ fs.

The reason for this variation can once again be found by examination of the energy distribution of the quantum flux entering the CAP. Figure 5.23 shows the flux spectra for $\tau = 0$, 15 and 24 fs. At $\tau = 0$ fs, sub-peaks corresponding to $n^* = 0$ and 1 are more populated than those for $n^* = 2$. At $\tau = 15$ fs in contrast, the main peaks populated are those corresponding to $n^* = 1$ and 2 for $v^* = 0$, and $n^* = 0$ for $v^* = 1$. As the $v^* = 1$ peak is considerably lower in amplitude than that for $v^* = 0$, the effect from the more excited bending vibrations wins out, and the NO rotational distribution resembles most strongly that from $n^* = 1$. Finally, at $\tau = 24$ fs there is little flux in either sub-peak for $n^* = 2$. As with those centred at an energy of 2.048 eV, the exciting pulse pairs can be Fourier transformed to yield spectra which closely resemble the flux spectra given here, showing
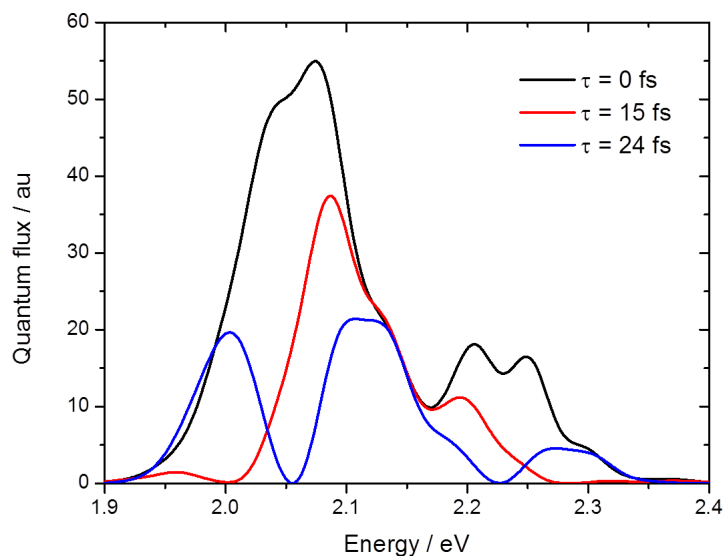
Figure 5.23: The energy distributions of the quantum flux entering the CAP for wavepacket propagations involving a pair of 10 fs laser pulses centred at 2.151 eV, for delays of 0, 15 and 24 fs.

that the overall effect is predominantly due to spectral control.

Freely interfering pulses

As expected given the results at other energies, considerably more control can be elicited when the pulses are freely interfering. As shown in figure 5.24, there is now a marked variation in NO vibrational state with delay. Note that the results at $\tau = 3$ fs may be dubious due to the small amount of quantum flux excited onto the $1\,^3A''$ state, but all others should be valid. The proportion of NO produced in v = 0 varies from a low of 35% when $\tau = 9$ fs to a high of 95% when $\tau = 12$ fs. As seen previously, the distribution levels off at longer τ when less interference can occur.

There is also a significant change in NO rotational distribution with τ. Example distributions for $\tau = 0$, 15, 21 and 24 fs are shown in panel a) of figure 5.25, and the associated flux spectra are given in panel b). When $\tau = 15$ and 21 fs, there is a significant hump in the rotational distribution at $\sim j = 22$, as well as a large population at low j, implying the bending quanta n* = 0 and 2 were dominant on the $1\,^3A''$ surface. In contrast, for $\tau = 24$ fs the main feature in the rotational distribution is the peak at $\sim j = 17$, implying the majority of the excited wavepacket was in n* = 1.
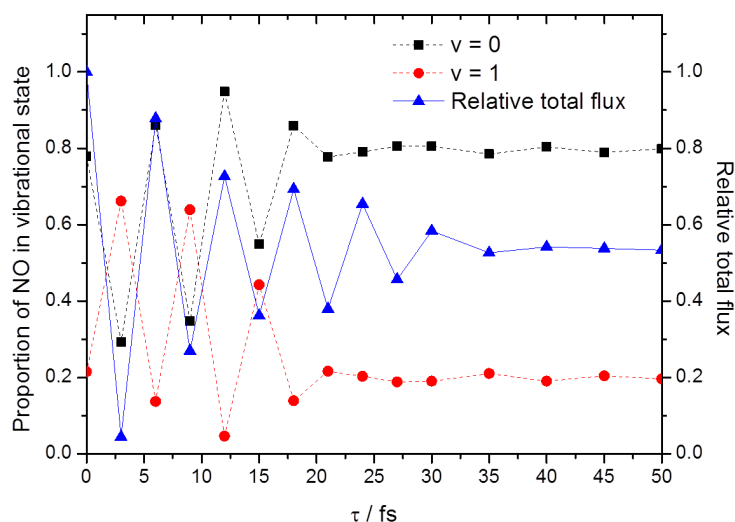
Figure 5.24: The variation in NO vibrational distribution, and total quantum flux, with delay τ following wavepacket propagations involving a pair of 10 fs laser pulses centred at 2.151 eV. The pulses were allowed to interfere freely.

These results can again be partly understood by predicting the vibrational state populations using equation 5.13. However, the situation is rather complicated as six sub-peaks can be accessed. As before, the values of the amplitude coefficients for each vibrational state, c_n^2, have been estimated by integrating the peaks in the flux spectrum at $\tau = 0$ fs. The total expected population in each of the two NO stretching quanta v* has then been found by summing the populations for all n*. Similarly, the total expected population in each of the bending quanta n* has been found by summing the populations for both v*.

Panel b) of figure 5.25 shows the energy distribution of the flux for $\tau = 9$, 12 and 15 fs. When $\tau = 9$ fs, 64% of NO is formed in v = 0, when $\tau = 12$ fs this drops to only 5%, before rising back to 55% when $\tau = 15$ fs. These varying distributions can be understood using both the flux distributions and the predicted populations given in panel c) of the figure. In this case, the results match well, albeit not perfectly, with the predicted populations. For example:

- For $\tau = 0$ fs, 77.9% of NO is formed in v = 0 and 21.5% is formed in v = 1; the predicted proportions are 78.7% and 21.3%.

- For $\tau = 9$ fs, 34.9% of NO is in v = 0 and 63.9% is in v = 1; the predicted proportions are 26.2% and 73.8%.

- For $\tau = 12$ fs, 94.8% of NO is in v = 0 and 4.6% is in v = 1; the predicted proportions are 96.6% and 3.4%.

- For $\tau = 15$ fs, 55.0% of NO is in v = 0 and 44.3% is in v = 1; the predicted proportions are 42.8% and 57.1%.

It is likely that at least some of the differences are due to the rather crude estimation of the amplitudes c_n used in equation 5.13; non-adiabaticity may also play a part.

The predictions of the rotational distributions are less accurate, but still give a fair reflection of the observed NO rotational distributions. Panel a) of figure 5.25 gives the NO rotational distributions for a few example delays, panel b) gives the corresponding flux spectra and panel c) shows how the populations of each bending state n* are expected to vary as calculated using equation 5.13. These give rise to the following observations:

- For $\tau = 0$ fs the NO distribution appears to derive from a mix of n* = 0, 1 and 2. The predicted n* population is 42.2% in n* = 0, 40.9% in n* = 1 and 16.9% in n* = 2

- For $\tau = 15$ fs the NO distribution appears to derive from n* = 0 and 2. The predicted n* population is 60.9% in n* = 0, 25.8% in n* = 1 and 13.2% in n* = 2

- For $\tau = 21$ fs the NO distribution appears to derive from n* = 0 and 2. The predicted n* population is 70.8% in n* = 0, 14.0% in n* = 1 and 15.2% in n* = 2

- For $\tau = 24$ fs the NO distribution appears to derive mostly from n* = 1. The predicted n* population is 25.5% in n* = 0, 59.9% in n* = 1 and 14.6% in n* = 2

It is impossible to obtain precise n* populations by visual inspection of the NO rotational distributions. However, it would appear that there are some errors in the predicted populations of the n* quanta, despite them being qualitatively reasonable. The flux spectra can be related once again to the Fourier transformation of the pulse pairs, showing that spectral shaping of the overall exciting field is important to the control.
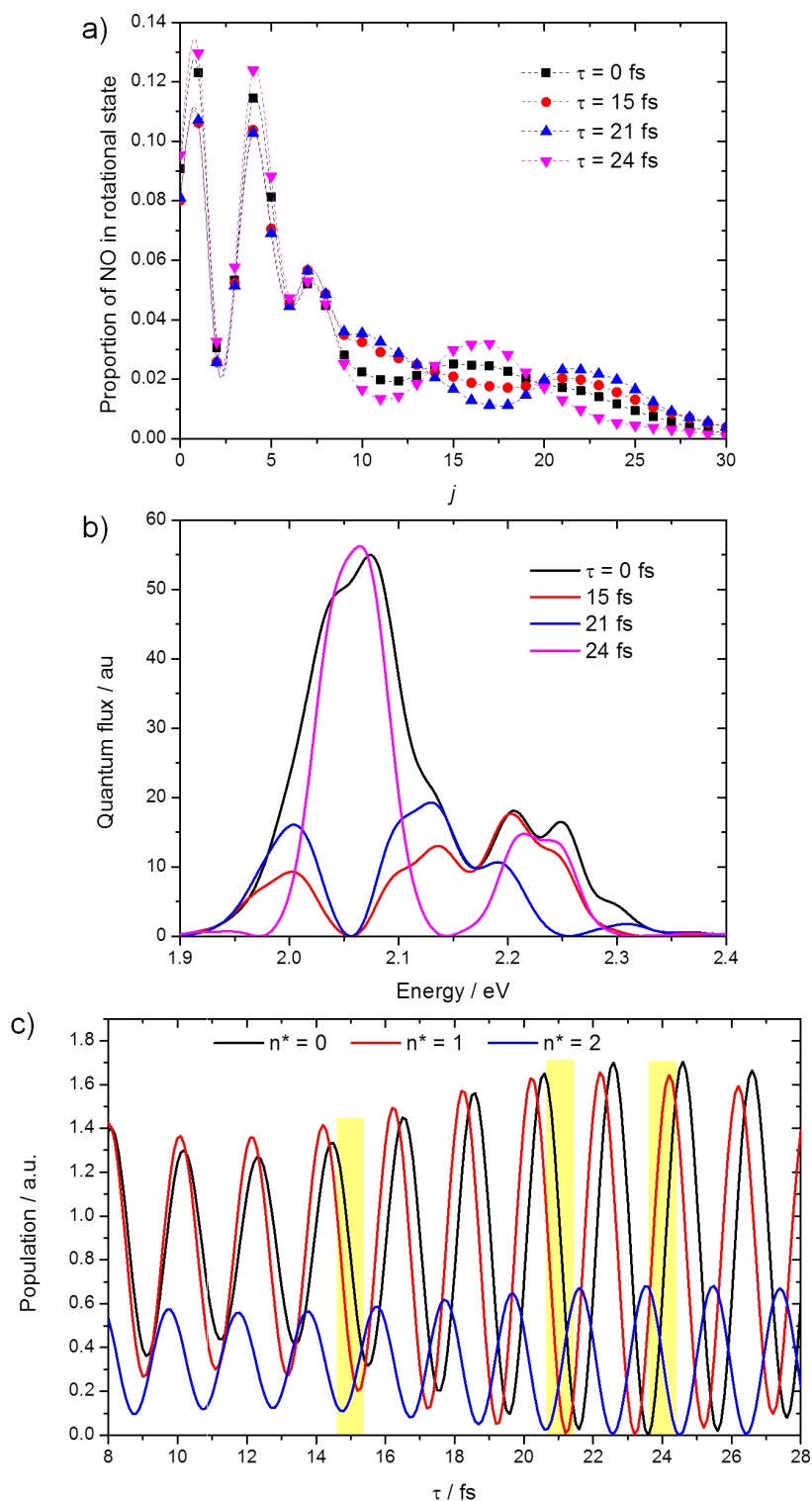
Figure 5.25: Panel a) gives NO rotational distributions following wavepacket prop-
agations on the 1 ^{3}A″ state, including pairs of 10 fs long laser pulses centred at an
energy of 2.151 eV separated by a range of delays, τ. The pulses were allowed to
interfere freely. Panel b) shows the energy distribution of the quantum flux for $\tau = 0$,
15, 21 and 24 fs. Panel c) shows the predicted populations of the NO stretching vi-
brations on the excited 1 ^{3}A″ for $\tau = 8$ to 28 fs, as calculated using equation 5.13.
The relative populations of n* = 0, 1 and 2 are given, and the results for $\tau = 15$, 21
and 24 fs are highlighted in yellow.

5.7   Linearly chirped pulse pairs

For energies of 2.232 and 2.151 eV, centred on the $1\,^3A''$ (1,1) $\leftarrow$ $1\,^1A'$ transition and between the $1\,^3A''$ (0,1) $\leftarrow$ $1\,^1A'$ and $1\,^3A''$ (1,1) $\leftarrow$ $1\,^1A'$ transitions respectively, a significant amount of control was possible simply by varying the delay between the two excitation pulses. For an energy of 2.048 eV, centred on the $1\,^3A''$ (0,1) $\leftarrow$ $1\,^1A'$ transition, the effect was more simple as just one NO vibrational state was spanned, and the NO rotational distributions were dominated by the quantum flux entering two different bending vibrational states, n* = 0 and 1. To see if any further control was possible at this energy, linearly chirped 20 fs pulses of the form given in equation 5.4 have been used, and the product state distributions examined.

As seen earlier in section 5.6.1, figure 5.7, when pulses are allowed to interfere freely the NO rotational distributions for delays of 15 and 18 fs look very different, with that at $\tau = 15$ fs resulting mainly from excited state ClNO in n* = 0, and that at $\tau = 18$ fs due mostly to ClNO in n* = 1. Therefore, calculations with chirped pulses have been predominantly run at these two delays.

5.7.1   Phase-locked pulses

First, identical phase-locked pulse pairs were used. When TL limited pulses are used, the NO rotational distributions for these delays are near-identical. However, by altering the linear chirp differences can be introduced. Panel a) of figure 5.26 shows a portion of the NO rotational distribution for $\tau = 15$ fs. The linear chirp is varied from $\alpha = -10$ cm^{-1} fs^{-1} to $+10$ cm^{-1} fs^{-1}. As the degree of chirp increases, the greater the deviation from the original distribution becomes, with positive chirp leading to an increased peak at $j \sim 17$ (implying greater population of n* = 1), and negative chirp leading to a decrease in amplitude of this peak (implying a greater population of n* = 0). Panel b) of the figure shows the distributions for $\tau = 18$ fs, this time for a greater number of α values. Here the same trend is seen, but it is more marked.

Inspection of the quantum flux spectra for the various chirps shows that with positive chirp, the flux distribution is shifted towards higher energies, and with negative chirp it
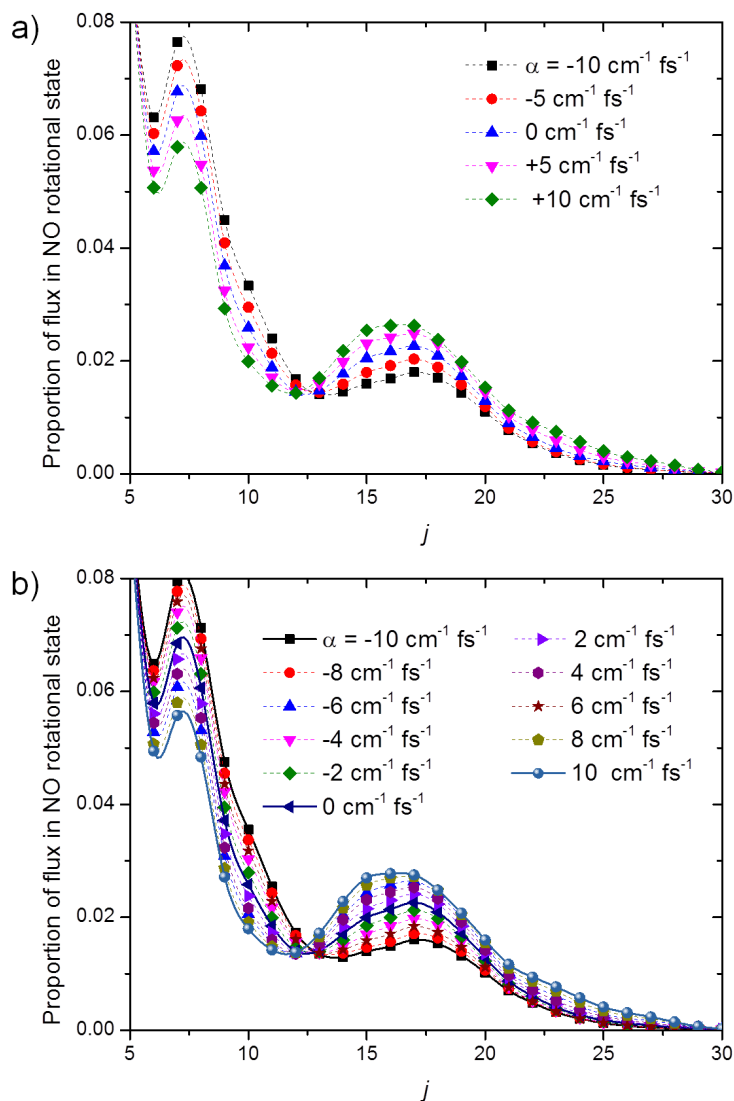
Figure 5.26: Parts of the NO rotational distributions produced following wavepacket propagations on the 1 ^{3}A″ state, including pairs of 20 fs long linearly chirped laser pulses centred at an energy of 2.048 eV. Panel a) shows the distributions for $\tau = 15$ fs. Panel b) shows the distribution for $\tau = 18$ fs, with the linear chirp α varied from -10 to $+10$ cm^{-1} fs^{-1}, every 2 cm^{-1} fs^{-1}. The distributions for $\alpha = -10$, 0 and $+10$ cm^{-1} fs^{-1} are given in bold.
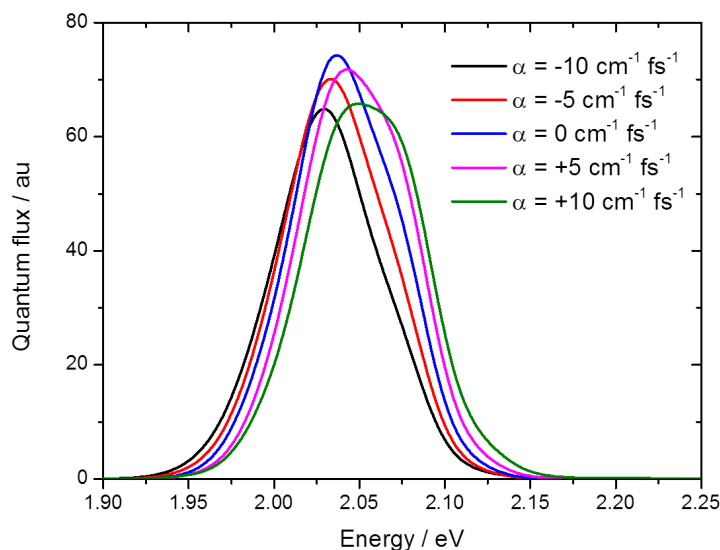
Figure 5.27: The energy distribution of the quantum flux excited onto the 1 ^{3}A″ surface by a pair of 20 fs linearly chirped laser pulses centred at 2.048 eV separated by a delay of 15 fs. Results are shown for α = -10, -5, 0, +5 and +10 cm^{-1} fs^{-1}.

is shifted lower. This effect is shown for $\tau = 15$ fs in figure 5.27; the change is not large but it is enough to shift the proportions of n* = 0 and 1 occupied. A similar situation is found for $\tau = 18$ fs (not shown). To check that the variation in flux distribution was not due simply to the degree of chirp, without any interference, calculations were run with single pulses across a range of α values. These yielded NO rotational distributions with only negligible differences between them, implying that the changes seen here must be a result of interference effects.

5.7.2 Freely interfering pulses

Secondly, identical freely interfering pulse pairs were used. A range of chirps from $\alpha = -15$ to $+15$ cm^{-1} fs^{-1} were used, but the resulting differences in NO rotational distributions were negligible; all were virtually identical to those shown in figure 5.7. The NO vibrational distributions also remained constant. This method is therefore no more effective for achieving control than using transform limited pulses. By Fourier transforming the linearly chirped pulse pairs it is clear why: the spectra are very similar to those produced when TL pulses are used.

5.7.3   Chirped pulse followed by TL pulse

Given the lack of success with a pair of chirped pulses, calculations were run where the initial pulse was linearly chirped, but the second was transform limited. The field of the first pulse was locked to t_0, whereas that of the second was locked to t_{0b}, thus allowing free interference. However, once again this led to very little difference in the resulting NO rotational or vibrational distributions as compared to equivalent propagations using a pair of TL pulses, even across a very large range of chirps from $\alpha = -20$ to $+20$ cm^{-1} fs^{-1}.

5.8   Quadratically chirped pulses

As with the linearly chirped pulse pairs, an energy of 2.048 eV, centred on the $1\,^3A''$ (0,1) $\leftarrow 1\,^1A'$ transition has been used for the investigation of quadratically chirped pulse pairs. Delays of 15 and 18 fs have again been chosen, as these give rise to very different NO rotational distributions when simpler TL pulses are employed.

5.8.1   Single pulses

Pulses with quadratic chirp behave quite differently to those with linear chirp: 'beats' appear in their frequency distributions, and so a degree of spectral control can be obtained even with a single pulse. Figure 5.28 shows examples of this, for pulses with the degree of quadratic chirp $\beta = +2$ and $+5$ cm^{-1} fs^{-2}.

Wavepacket propagations were run using single pulses with a range of β values, every 1 cm^{-1} fs^{-2} from -5 to +5. Selected results are shown in figure 5.29. The NO rotational distributions given in panel a) show that positive values of β result in enhancement of the n* = 1 and 2 populations on the $1\,^3A''$ state, whereas when negative values are used the proportion formed in n* = 0 increases compared to an unchirped pulse. This effect is caused by the beats in the spectrum of the pulses: for positive β these occur towards higher energies, whereas for those with negative β they occur at lower energies. This is reflected in the energy distributions of the total quantum flux entering the CAP as shown in panel b) of the figure. Note that for the largest positive value of β given here the bandwidth of the
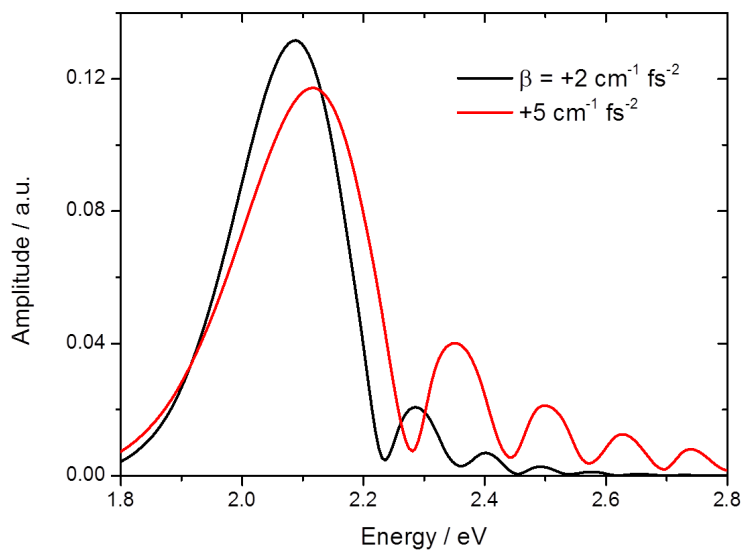
Figure 5.28: The energy distribution of quadratically chirped 20 fs long pulses cen-
tred at an energy of 2.048 eV, obtained via Fourier transformation.

pulse increases to the extent that a small amount of the excited NO stretch, v* = 1, is also

formed. Note also that due to the destructive interferences occurring within the pulses, the

total flux excited is lower for chirped than unchirped pulses: that for $\beta = +5$ cm^{-1} fs^{-2} is

only 75% that of the TL pulse. The decrease is more marked for negative chirps as there

is increased amplitude at lower energies where the $1\,^3A''$ state does not absorb.

5.8.2   Phase-locked pulses

Phase-locked pulse pairs were investigated for delays of 15 and 18 fs. Regardless of

delay, the same effects were seen as for the single pulses: positive values of β lead to an

enhancement in the populations of n* = 1 and 2, whereas negative values of β lead to a

decrease in these. Once again, this was due to the differences in the FTs of the pulse pairs;

as no new effects were seen these were not investigated further.

5.8.3   Freely interfering pulses

When TL pulse pairs are used, a delay of 15 fs results in an NO rotational distribution

deriving mostly from n* = 0, and a delay of 18 fs results in a distribution deriving more

from n* = 1. For τ = 18 fs the trend is much as that seen for single pulses, but to a lesser
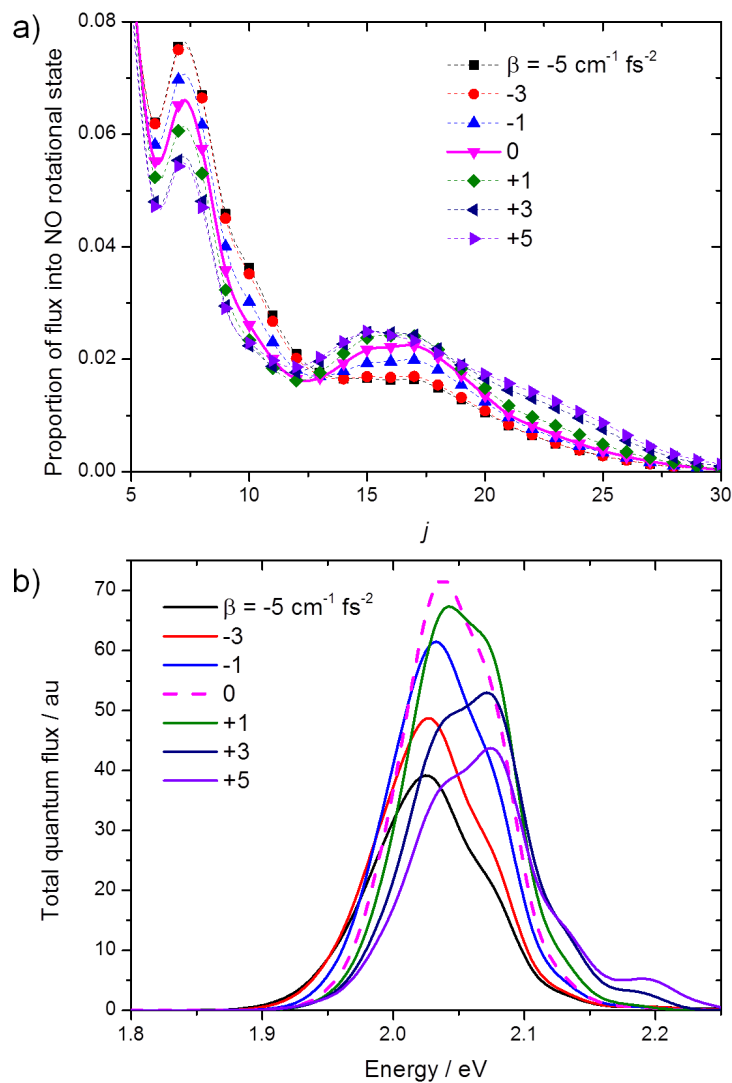
Figure 5.29: Panel a) shows parts of the NO rotational distributions produced following wavepacket propagations on the $1\,^3A''$ state, including single 20 fs long quadratically chirped laser pulses centred at an energy of 2.048 eV. Panel b) shows the energy distributions of the quantum flux obtained from the same calculations.

extent: there is only a small change in the NO rotational distributions (for example, the population of NO formed in $j = 17$ varies from 2.1 to 2.8% across the whole range of β used, from -5 to +5 cm^{-1} fs^{-2}).

For $\tau = 15$ fs however, where much more destructive interference occurs, the effect is considerably greater. The NO rotational distributions and quantum flux spectra for this delay are shown in figure 5.30. Here, as the degree of positive chirp increases, the proportion of excited state ClNO formed in n* = 2 appears to increase considerably. The change for negative values of β is less marked, but does result in a slight suppression of the hump in the rotational distribution centred at $j \sim 22$. For example, with $\beta = -5$ cm^{-1} fs^{-2} only 0.6% of NO is produced in $j = 22$, whereas with $\beta = +5$ cm^{-1} fs^{-2} 2.1% is formed in this state. The quantum flux spectra show that although in all cases there is little to no wavepacket density in the central region corresponding to n* = 1, the proportion at energies matching those for n* = 0 and 2 varies considerably with β. The variation again reflects the spectra of the pulse pairs. There is however a small decrease in the 1 ^{3}A$''$ state population when the second pulse arrives, showing once more that there is also some wavepacket interference occurring. Note that the total flux excited onto the 1 ^{3}A$''$ state also varies to an extent with quadratic chirp. The peak flux occurs for $\beta = -2$ cm^{-1} fs^{-2}, at which point it is 1.2 times that for a TL pulse pair.
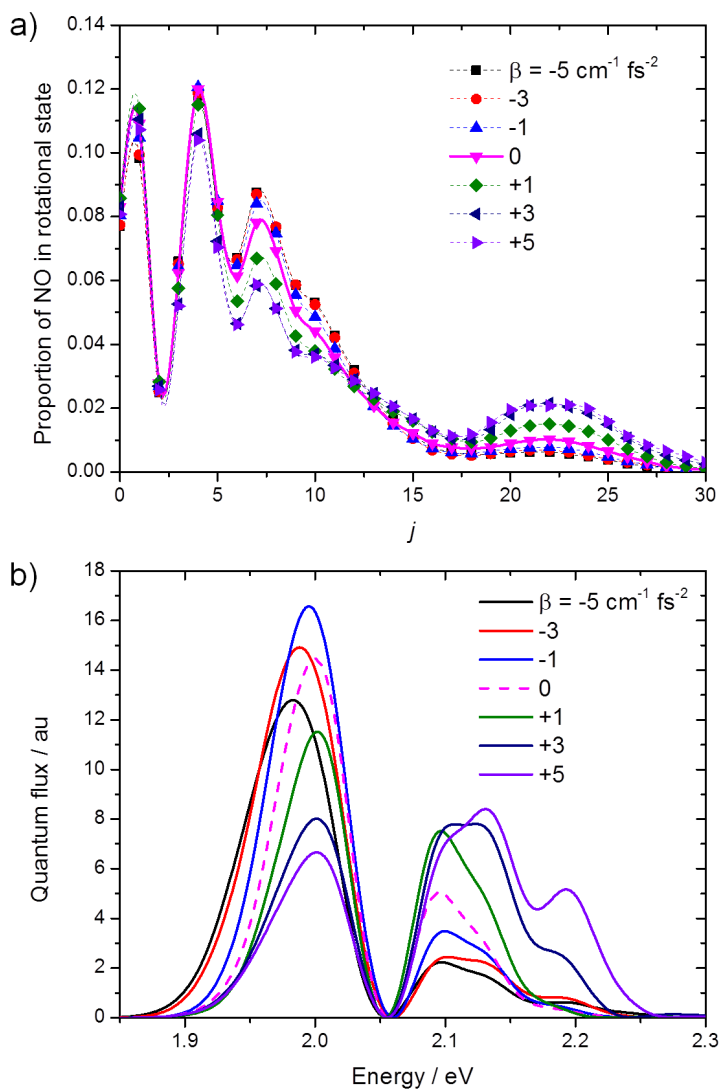
Figure 5.30: Panel a) shows parts of the NO rotational distributions produced following wavepacket propagations on the 1 $^3A''$ state, including pairs of freely-interfering 20 fs long quadratically chirped laser pulses centred at an energy of 2.048 eV and separated by a delay of 15 fs. Panel b) shows the energy distributions of the quantum flux obtained from the same calculations.

5.9   Conclusions

It has been shown that coherent control should be possible on the 1 $^3A''$ state of ClNO, by using pairs of ultrashort laser pulses and varying the delay between them in order to select a desired NO product state distribution. This may in turn provide a basis for further control experiments involving higher excited states. The control is mostly derived from spectral shaping resulting in varying populations of the bending vibrational states on the 1 $^3A''$ surface. The simplest way to obtain some control over the NO rotational or vibrational distribution is to use a narrow band laser; however this would only permit a few neighbouring states to be produced concurrently. Here, ranges of states can be produced, and using destructive interference whole regions of the distributions can be enhanced or suppressed across the entire energy range spanned by the ultrashort laser pulse.

The work presented here can be compared with other examples of control performed via wavepacket interferometry, of which reviews can be found in references [44] and [163]. An illustrative study was performed by Scherer *et al.* [164]. They controlled the population on the excited B state of I_2 using pairs of phase-locked ultrashort pulses, which produced vibrational wavepackets on the excited state. By varying the time delay between these, the wavepacket interference was either constructive or destructive depending on the position of the wavepacket as it oscillated along vibrational modes. The major difference to the current study is that the 1 $^3A''$ state of ClNO is dissociative, and hence any control needs to be exerted over very short time-scales as the excited state wavepacket will not return to its FC location other than very briefly due to the slight motion in the r_{NO} coordinate.

This work has shown that the MCTDH method, combined with a thorough analysis of the quantum flux entering the exit channel, is a suitable technique for formulating control strategies before they are tested in the laboratory, or to help explain existing results. It is hoped that the same approach will be used to study more complex systems in the future.

5.10 Future work

Clearly, it would be useful to verify these predicted control effects experimentally. Given the equipment available in our laboratory, it should be straightforward to run experiments probing different NO rotational states and varying the excitation energy and inter-pulse delay. A suggested set-up would be to create fs pulse pairs using the Dazzler^{TM} pulse shaper, and use these to photodissociate ClNO in a molecular beam. The NO product could then be ionised and detected using a ns laser via REMPI-TOF schemes similar to those used in our group's 3D-REMPI experiments. The major difficulty is likely to be ensuring sufficient absorption to the $1\,^3A''$ state whilst minimising multi-photon absorption effects. Given the results seen here at 2.048 eV, it is unlikely to be worthwhile to vary the linear chirp of the pulses; freely interfering transform limited pulses should be used first. Using the Dazzler^{TM} it will also be possible to produce single pulses with varying degrees of quadratic chirp. Care needs to be taken throughout to ensure that any enhancement of a particular NO rotational or vibrational state is not outweighed by a decrease in the overall absorption.

From a computational perspective, it would be desirable to calculate the PESs for higher energy states of ClNO, to investigate if more complex control is possible via multi-photon absorption. In particular, it would be interesting to see if there were pathways by which the ClON isomer could be produced. This may require the use of different pulse energies, and could involve the conical intersection seen between the 1 and $2\,^1A'$ states. Finally, if the understanding of the spin-orbit branching ratios discussed in the next chapter could be improved, these would also make good control targets.

Chapter 6

Spin-orbit coupled states of ClNO

6.1 Overview

PESs for the spin-orbit coupled states have been calculated in order to help explain experimental product state distributions, namely the proportions of NO in its $^2\Pi_{1/2}$ and $^2\Pi_{3/2}$ states and Cl in its $^2P_{3/2}$ and $^2P_{1/2}$ states, following photodissociation on the zeroth-order $2\,^1A'$ surface. Complete spin-orbit matrices have been calculated and used in a 2 dimensional (r coordinate kept fixed) wavepacket propagation on the spin-orbit state most closely correlating to the $2\,^1A'$. This preliminary calculation yields product state distributions which agree well with the available experimental data.

6.2 Potential energy surfaces and spin-orbit matrices

6.2.1 Choosing a method

There are 12 zeroth-order electronic states of ClNO which converge on the lowest energy asymptote giving NO and Cl in their ground electronic states. These comprise $3 \times {}^1A'$, $3 \times {}^1A''$, $3 \times {}^3A'$ and $3 \times {}^3A''$ states. The primary states of interest here are the $2\,^1A'$ and the $1\,^3A''$. As discussed in section 1.1.3, the triplet states split into three sub-levels. Therefore, 24 spin-orbit states (12 of each symmetry) will be formed from the original 12 zeroth-order states. These are expected to converge upon four separate asymptotes,

corresponding to NO + Cl, NO* + Cl, NO + Cl* and NO* + Cl*. The experimental separation between the NO spin-orbit states is 123 cm^{-1}, and that between the Cl states is 881 cm^{-1} [59].

Molpro has been used to carry out the calculations including spin-orbit coupling [165] using the Breit-Pauli Hamiltonian. Initial calculations were carried out at the CAS level as follows:

- Calculate the CAS wavefunction state-averaged over selected zeroth-order states
- Save the CAS wavefunctions for each spin-symmetry using the MRCI program (required for the spin-orbit step)
- Calculate the one and two-electron spin-orbit integrals
- Calculate and diagonalise the spin-orbit matrix.

Various combinations of zeroth-order states were used, however sensible results were only obtained when all 12 states were included: with fewer states erroneous minima and asymptotes were produced.

A full-valence active space was used throughout. In preliminary calculations, the spin-orbit splitting of the lone Cl atom was calculated. In order to obtain an accurate energy split (within 10 cm^{-1} of the experimental value) between the Cl $^2P_{3/2}$ and $^2P_{1/2}$ states, it was necessary to include the $3d$ orbitals in the active space. Therefore, to try to improve the asymptotic energies for the ClNO calculations, the ClNO molecular orbitals were inspected to find those corresponding most to the Cl $3d$ with a view to including these in the active space. However, adding these orbitals on to the full-valence active space proved difficult, and so it was not feasible to include them.

Figure 6.1 shows cuts through the PESs of 12 spin-orbit states of A$'$ symmetry at a fixed r_{NO} of 2.15 bohr and a fixed θ of 113.4°, calculated at the CAS/AVTZ level. Panel a) shows the region close to the FC geometry: all the states barring the ground are dissociative and the surfaces are smooth. Panel b) gives the same surfaces closer to the asymptotic region, showing clearly how the states converge on the four different asymptotes. However, it is also clear that the asymptotes are centred around an energy of ~ 1 eV, which is far too low given the experimental value of 1.615 eV.
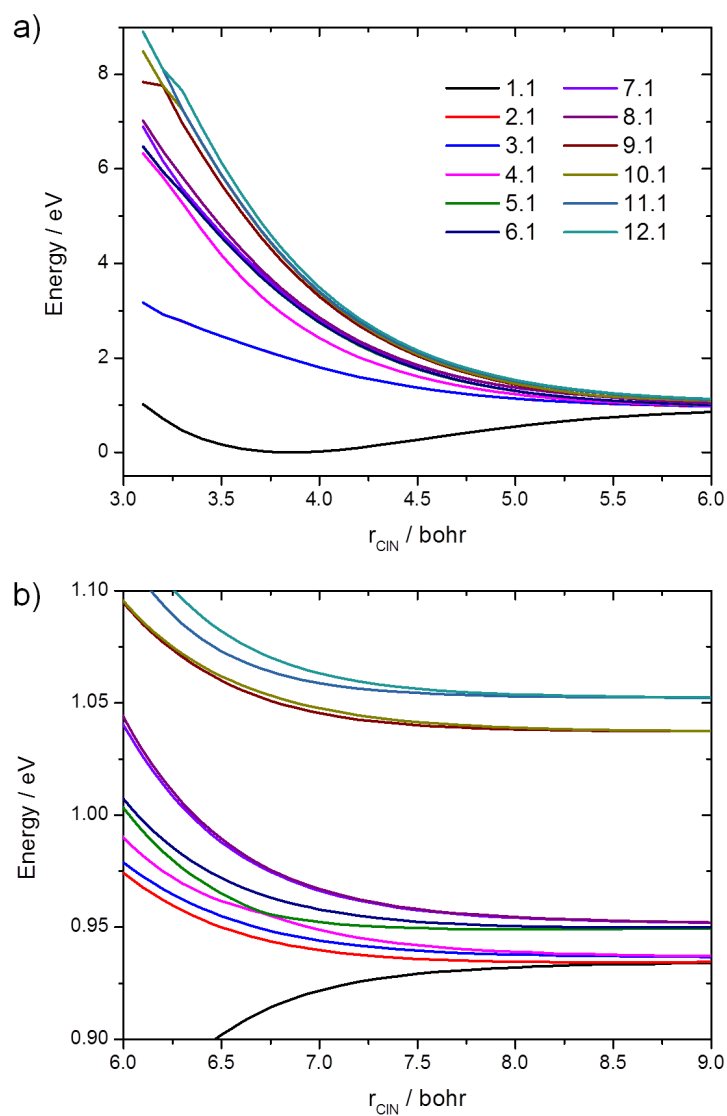
Figure 6.1: Cuts through the PESs of the 12 spin-orbit states of A′ symmetry at a fixed r_{NO} of 2.15 bohr and a fixed θ of 113.4°, calculated at the CAS/AVTZ level. Panel a) shows the region close to the FC geometry, and panel b) shows the asymptotic region, where the states are clearly converging on four separate asymptotes.

A very long way out into the asymptotic region, at $r_{ClN} = 50$ bohr, the energies of the asymptotes and the spin-orbit states converging on them are as follows:

- 0 cm^{-1}, corresponding to NO + Cl. States: 1.1, 2.1, 3.1, 4.1, 1.2, 2.2, 3.2, 4.2
- 121 cm^{-1}, corresponding to NO* + Cl. States: 5.1, 6.1, 7.1, 8.1, 5.2, 6.2, 7.2, 8.2
- 818 cm^{-1}, corresponding to NO + Cl*. States: 9.1, 10.1, 9.2, 10.2
- 942 cm^{-1}, corresponding to NO* + Cl*. States: 11.1, 12.1, 11.2, 12.2.

The states are labelled according to their energy ordering and their symmetry, with '.1' denoting A$'$ and '.2' denoting A$''$. The asymptotic energies give averages of 123 cm^{-1} for the NO-NO* split, which matches perfectly with experiment, and 820 cm^{-1} for the Cl-Cl* split, which is 61 cm^{-1} too low, but still reasonable. This implies the spin-orbit effects are being reproduced with a fair degree of accuracy. However, as shown next, there are errors in the excitation energies as well as with the overall dissociation energy.

FC energies

The excitation energies of the spin-orbit states at the CAS/AVTZ level, found at the minimum energy geometry for this level of theory ($r_{ClN} = 3.9$ bohr, $r_{NO} = 2.16$ bohr, and $\theta = 113.4°$), are given in table 6.1, to be compared with the energies of the zeroth-order states taken from the literature as given in table 6.2. It would be expected that some, though not all, of the excitation energies would match. This is clearly not the case, implying the CAS energies are not reliable at this point.

To obtain more accurate energies, the spin-orbit states were calculated at the MRCI/AVQZ level, just at the FC geometry of $r_{ClN} = 3.75$ bohr, $r_{NO} = 2.15$ bohr and bond angle $\theta = 113.4°$. The energies of the states, and their transition dipole moments with the ground state, are given in tables 6.3 (for states of A$'$ symmetry) and 6.4 (for states of A$''$ symmetry). These results can also be compared with table 6.2, which gives significantly better agreement than for the CAS-level results, and yields the following assignments for the zeroth-order states which contribute significantly to the absorption spectrum:

- State 3.1 is the major contributor to the zeroth-order 1 ^{3}A$''$ state
- State 2.2 corresponds to the 1 ^{1}A$''$ state

SO states	Energy / eV
1.1	0
2.1, 3.1, 1.2	1.92
2.2	2.22
4.1, 3.2, 4.2	2.67
5.2, 5.1	3.03
6.1, 6.2	3.05
7.1, 7.2	3.11
8.2	3.12
8.1	3.15
9.1, 9.2, 10.2	3.67
10.1, 11.1, 11.2	3.78
12.1	3.9
12.2	3.94

Table 6.1: Excitation energies for the 24 spin-orbit states of ClNO. The values are shown for the FC geometry at the CAS/AVTZ level, with r_{ClN} = 3.9 bohr, r_{NO} = 2.15 bohr and θ = 113.4°.

Zeroth-order state	Energy / eV
$1\,^1A'$	0
$1\,^3A''$	2.06^a
$1\,^1A''$	2.64^a
$1\,^3A'$	3.34^b
$2\,^3A''$	3.61^b
$2\,^1A''$	3.62^b
$2\,^3A'$	3.7^b
$2\,^1A'$	3.72^a
$3\,^3A'$	4.45^b
$3\,^1A''$	4.62^b
$3\,^1A'$	4.77^b
$3\,^1A''$	4.86^b

Table 6.2: Excitation energies for the 12 zeroth-order states of ClNO. The values marked [a] are experimental results taken from reference [69], and those marked [b] are calculated results taken from reference [68].

- State 8.1 gives the major contribution to the $2\,^1A'$, with some contribution from state 6.1 at lower energies

- State 12.1 gives the major contribution to the $3\,^1A'$ state

- State 12.2 corresponds to the zeroth-order $3\,^1A''$ state.

The excitation energies for these selected states are in excellent agreement with experiment; for higher states there is greater disparity between the energies calculated here and in the literature [68].

Clearly, the ideal approach would be to calculate entire PESs at the MRCI/AVQZ level. However, due to the large number of states involved, this was not feasible. Therefore, the CAS method has been used, which means the energies of the states will not be as reliable. However, the qualitative features of the PESs should still be reproduced: both the vertical excitation energies and the dissociation energy are too low, and so the gradients of the states may well be reasonable. In particular, the energy of spin-orbit state 8.1 is 0.57 eV too low, which is similar to the error of ∼0.6 eV in the dissociation energy. There was virtually no difference in the relative energies of the spin-orbit states depending on

SO state	TDM$_y$ / 10^{-2} au	TDM$_z$ / 10^{-2} au	Energy / eV	Wavelength / nm
1.1	-	-	0	-
2.1	0.005	0.024	2.173	570.76
3.1	0.014	0.499	2.173	570.68
4.1	0.096	0.086	3.255	380.98
5.1	0.002	0.009	3.540	350.26
6.1	0.031	2.229	3.550	349.32
7.1	0.029	0.051	3.622	342.32
8.1	0.110	9.321	3.712	334.04
9.1	0.029	0.539	4.371	283.69
10.1	0.930	1.113	4.517	274.53
11.1	0.015	0.690	4.532	273.64
12.1	3.747	4.562	4.659	266.14

Table 6.3: Excitation energies and transition dipole moments with the ground state (both y and z components) for the 12 spin-orbit states of ClNO of A$'$ symmetry, calculated at the MRCI/AVQZ level. The states with an appreciable TDM are highlighted in orange. The values are shown for the FC geometry, with r_{ClN} = 3.75 bohr, r_{NO} = 2.15 bohr and θ = 113.4°.

SO state	TDM$_x$ / 10^{-2} au	Energy / eV	Wavelength / nm
1.2	0.0045	2.173	570.76
2.2	4.6695	2.608	475.52
3.2	0.0087	3.254	381.01
4.2	0.2022	3.255	380.98
5.2	0.0828	3.540	350.26
6.2	0.1749	3.563	348.07
7.2	0.1188	3.623	342.27
8.2	0.1321	3.631	341.55
9.2	0.0033	4.372	283.65
10.2	0.4678	4.376	283.39
11.2	0.0055	4.532	273.59
12.2	5.0404	4.748	261.19

Table 6.4: Excitation energies and transition dipole moments with the ground state (x component only) for the 12 spin-orbit states of ClNO of A$''$ symmetry, calculated at the MRCI/AVQZ level. The states with an appreciable TDM are highlighted in orange. The values are shown for the FC geometry, with r_{ClN} = 3.75 bohr, r_{NO} = 2.15 bohr and θ = 113.4°.

whether the AVTZ or AVQZ basis set was used; therefore the smaller triple-zeta basis set was chosen in order to improve the calculation time.

6.2.2   CAS/AVTZ surfaces

Full PESs and spin-orbit coupling matrices (SOMs) were calculated at the CAS/AVTZ level, at 3876 *ab initio* points across the following geometries:

- r_{ClN}: every 0.25 bohr from 2.75 to 12.0 bohr

- r_{NO}: every 0.2 bohr from 1.8 to 2.8 bohr

- Bond angle θ: every $10°$ from $10°$ to $170°$.

The eigenvalues of the SOMs at each point were taken and used as the adiabatic PESs for each state.

Figures 6.2 and 6.3 show cuts through the PESs of all states of A' symmetry for a fixed r_{NO} bond distance of 2.2 bohr. In the former, r_{ClN} is fixed at 4, 6 and 8 bohr so that the variation with θ can be seen. At low r_{ClN} there is a very large variation in energy across the angular coordinate, which decreases as the molecule dissociates and the states converge upon the four spin-orbit asymptotes. As expected from the zeroth-order 1 and 2 $^1A'$ surfaces, there is a significant interaction between the ground and higher lying states at $\sim \theta = 70°$ which persists, albeit at smaller angles, out into the asymptotic region until $r_{ClN} \sim 10$ bohr. This interaction can help explain partitioning between the different spin-orbit products for ClNO excited states, such as the 2 $^1A'$, which are anisotropic in the angular coordinate to the extent that a large change in θ is expected during their dissociation. The strength of the coupling between individual states, as well as the path of the wavepacket, will influence the effect of these intersections on the final results.

In figure 6.3, θ is fixed at 70, 110 and $150°$ so that the variation in energy with r_{ClN} can be seen. With the exception of the ground state, all states are dissociative at all angles. The crossings between the states are less clear from this perspective, however they do exist. The figure shows a zoomed-in portion of the PES cuts at $110°$, which reveals an interaction involving states 7.1 and 8.1 and states 9.1 and 10.1 at $r_{ClN} \sim 5.3$ bohr. This is not present at the other angles shown; however a crossing between states 4.1 and 5.1 (and
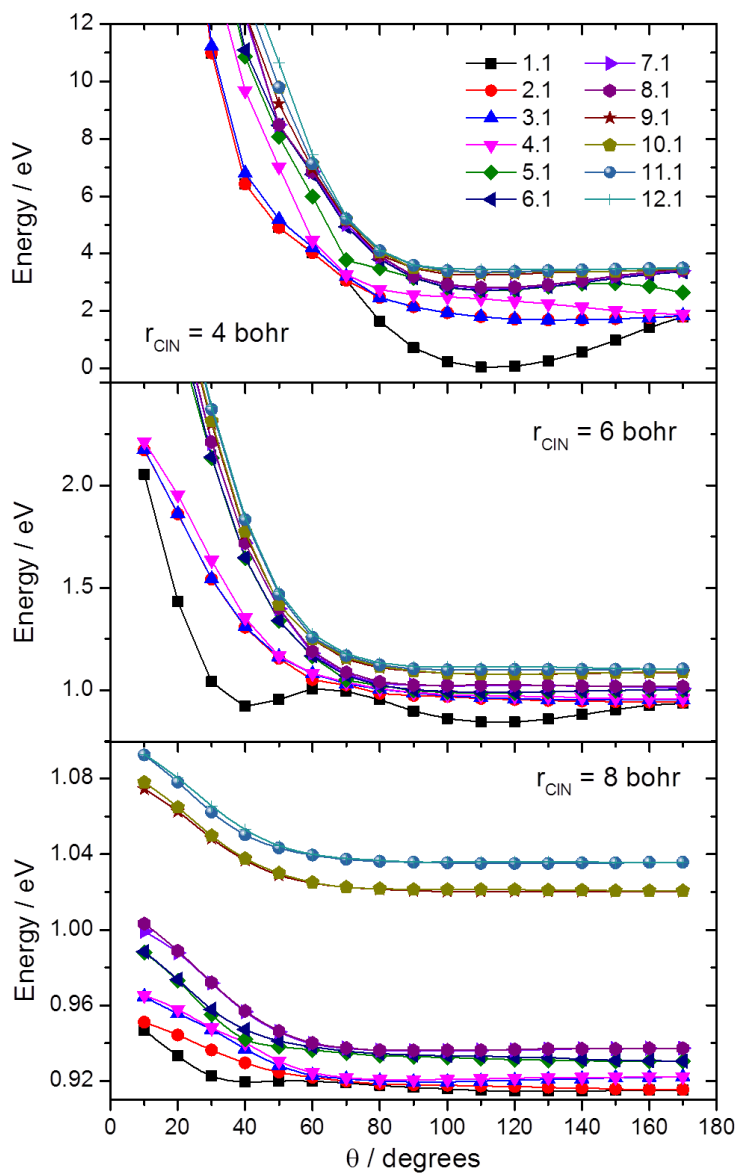
Figure 6.2: Cuts through the PESs of the 12 spin-orbit states of A′ symmetry calculated at the CAS/AVTZ level. The top panel shows cuts for $r_{ClN} = 4$ bohr, the middle for $r_{ClN} = 6$ bohr and the bottom for $r_{ClN} = 8$ bohr; r_{NO} is fixed at 2.2 bohr in all cases. Note the intersections between various states in the $\theta \sim 70°$ region.
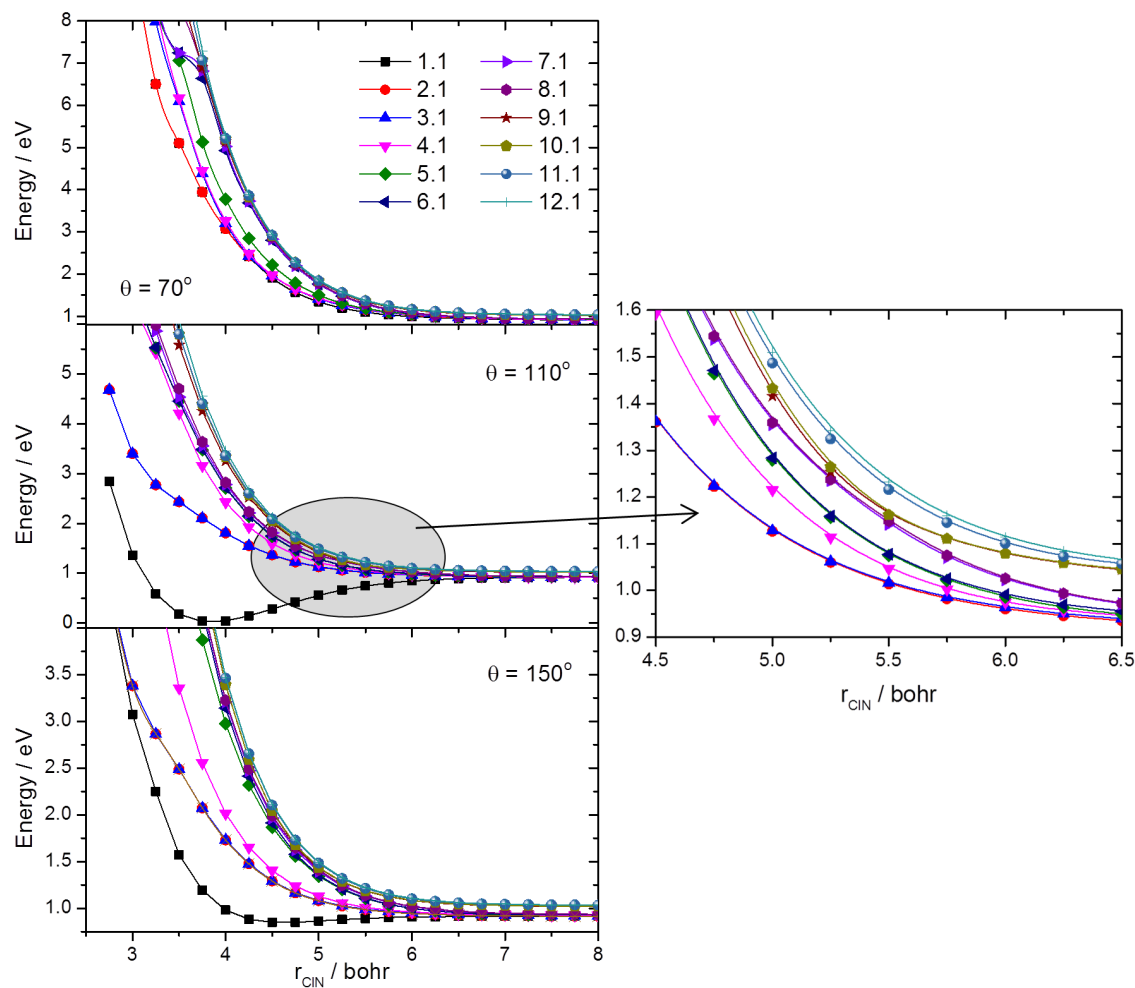
Figure 6.3: Cuts through the PESs of the 12 spin-orbit states of A′ symmetry calculated at the CAS/AVTZ level. The top panel shows cuts for $\theta = 70°$, the middle for $\theta = 110°$ and the bottom for $\theta = 150°$; r_{NO} is fixed at 2.2 bohr in all cases. A zoomed-in view at 110° is also given to show the interaction of states 7.1 and 8.1 with states 9.1 and 10.1 at this angle.

to a lesser extent 6.1), as visible in panel b) of figure 6.1, is common to all angles. At $\theta = 70°$ this occurs at $r_{ClN} \sim 6.3$ bohr, for $\theta = 110°$ it is positioned slightly further out at $r_{ClN} \sim 6.6$ bohr, and at $\theta = 150°$ it is at $r_{ClN} \sim 7.2$ bohr.

Movement in the r_{NO} coordinate is much less likely to have an impact upon the final product state distribution: figure 6.4 gives cuts through the PESs for a fixed r_{ClN} bond length and a fixed angle θ. The behaviour seen here is fairly typical for the whole surface: all states follow a similar pattern to the lone NO molecule, with very few if any obvious interactions in the vicinity of the minimum r_{NO} bond length where wavepackets are most likely to be found.
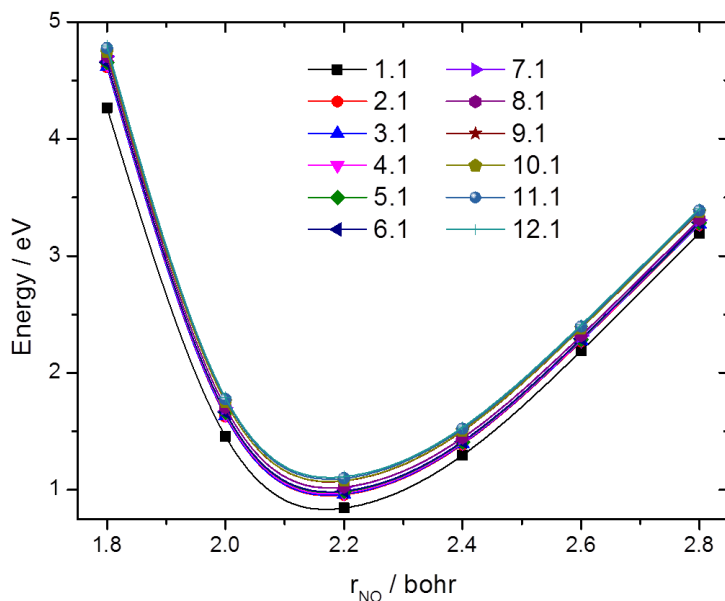
Figure 6.4: Cuts through the PESs of the 12 spin-orbit states of A′ symmetry calculated at the CAS/AVTZ level, for $r_{ClN} = 6$ bohr and $\theta = 110^{circ}$. This picture is typical of the variation in energy with r_{NO} bond length across the PESs: all states follow a similar pattern to the lone NO molecule, with little to no apparent interactions in the vicinity of the minimum r_{NO} bond length.

In all asymptotic regions of the PES, the same number of states of each symmetry converge on each of the four asymptotes, and due to the fact that the states calculated are adiabatic, their labelling remains the same. To understand which initial states lead to which final states it is therefore necessary to consider the entire spin-orbit matrix, the off-diagonal terms of which represent the couplings between the spin-orbit states. Molpro outputs the SOMs both in the basis of the zeroth-order wavefunctions, and in symmetry-adapted bases. Here, the zeroth-order basis has been used; this choice should make no difference to the results.

6.2.3   Spin-orbit coupling matrix elements

The SOM in the basis of the zeroth-order wavefunctions is a 24 by 24 matrix, i.e. it has 576 elements, namely 24 diagonals and 552 coupling terms. These coupling terms are often zero on symmetry grounds. The SOM is complex, and so each individual SOCME may be either real or imaginary. The real-valued SOCMEs are symmetric, i.e. matrix element x-y is identical to matrix element y-x. The imaginary-valued SOCMEs are anti-
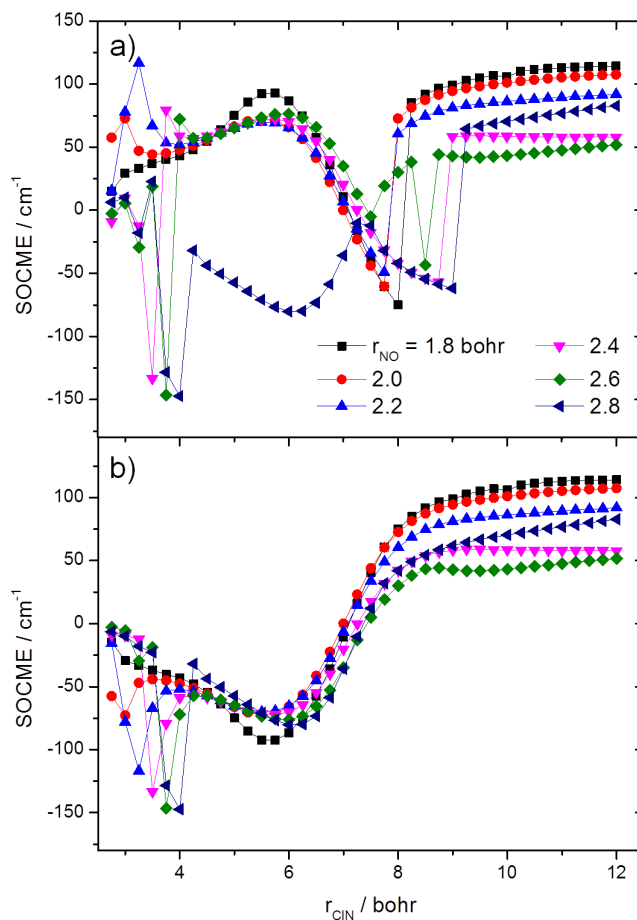
Figure 6.5: Values of the SOCME between states 18 and 11 (labelled here s18-11) for a fixed bond angle $\theta = 110°$. Panel a) shows the raw values; there are several places in which the sign flips erroneously. Panel b) shows the corrected values as produced by the sign-sorting algorithm.

symmetric, i.e. matrix element x-y has the same value but opposite sign to matrix element y-x.

The major problem with the SOCMEs calculated by Molpro is that their signs are not consistent moving from one geometry to another across the PES. This is because the sign of the wavefunction itself is arbitrary, and so will vary from point to point. Panel a) of figure 6.5 shows a set of raw SOCME values across a small range of geometries. There are several places in which the sign flips, leading to SOCME surfaces that are not smooth; without these erroneous changes the values appear sensible for r_{ClN} bond lengths above $\sim$4 bohr.

Before using the SOMs in dynamics calculations, the sign variation needs to be recti-

fied. Even after discounting the SOCMEs that are zero-valued everywhere, and allowing for the symmetry of SOCMEs on opposite sides of the matrix, there are still 168 for which the signs potentially need to be adjusted. As the SOMs have been calculated at 3786 geometries, and the signs need to be consistent along three degrees of freedom, this is too large a problem to treat manually. The signs have therefore been sorted using a home-made algorithm as detailed in appendix A. Panel b) of figure 6.5 shows SOCMEs that have been adjusted by the algorithm. Note that due to the very high dimensionality of the problem, it is not possible to predict what the SOCME curves should look like along each degree of freedom, and so the main criterion in assessing their validity is whether they vary smoothly across the whole range of geometries.

In order to find the correct signs, a starting point is needed at which the signs can be assumed correct. This then acts as the reference from which all other values are determined. The starting point used here was chosen to be the geometry r_{ClN} = 12 bohr, r_{NO} = 2.2 bohr and $\theta = 110°$ for the following reasons: it is out in the asymptotic region, where the PESs and SOCMEs vary little, and the r_{NO} and θ values are close to their FC positions, meaning results should be more reliable.

6.3   Qualitative observations on the 2 ^{1}A$'$ product state distribution

It is possible to obtain a qualitative picture of expected the spin-orbit product state distributions following dissociation on each zeroth-order PES by inspection of the spin-orbit PESs, and the interactions between them. Here, the product state distribution expected from dissociation on the 2 ^{1}A$'$ state is considered.

From the information given in tables 6.3 and 6.4, the zeroth-order 2 ^{1}A$'$ state corresponds most strongly to the SO state labelled 8.1. However, depending on the exact excitation energy used, there may also be a contribution from the SO state 6.1, which peaks 0.16 eV lower than state 8.1, but still has an appreciable TDM with the ground state. By examining the PESs for these states, and their interactions with neighbouring

states, a qualitative idea of the spin-orbit product state distribution can be obtained.

In order to do this, the SO surfaces were calculated along the mean path of a wavepacket propagation run on the zeroth-order 2 ^{1}A′ state. The expectation value for each mode (R, r, and γ) was taken every 3 fs and converted to binding coordinates for use in Molpro. Towards the end of the propagation the expectation values, and hence the PESs, become slightly distorted due to the presence of the CAP, but up until ~ 45 fs they should be reliable.

Figure 6.6 shows cuts through the resulting SO PESs in the region from $r_{ClN} = 4.25$ to 6.25 bohr, for states 6.1 and 8.1 in addition to those states of A′ symmetry which appear to interact with state 8.1, namely 9.1 and 10.1. From these surfaces, it seems likely that wavepacket density will transfer from state 8.1 to either 9.1, 10.1 or both at geometries in the region of $r_{ClN} = 5$ bohr, $r_{NO} = 2.15$ bohr, $\theta = 90°$. This shows that pathways exist towards states which end on asymptotes corresponding to both Cl and Cl*, and so depending on the strength of the coupling, both of these spin-orbit product states should be seen. In contrast, state 6.1 has no clear intersections with other states, implying it may lead to a greater proportion of Cl being formed. It does however remain very close in energy to neighbouring states, and so it is likely that some wavepacket density will be transferred despite this.

The interactions between the states further out into the asymptotic region are obscured by the effects of the CAP and the motion in the r_{NO} coordinate. However, by inspection of the PESs calculated in section 6.2.2, more information can be obtained. Figure 6.7 shows a cut through the lowest 8 states of A′ symmetry for $r_{NO} = 2.2$ bohr and $r_{ClN} = 7.0$ bohr. Clear interactions between several states can be seen, namely states 7.1 and 8.1 with 4.1 and 3.1 at at $\sim 75°$, and subsequently states 3.1 and 4.1 with 5.1 and 6.1 at $\sim 60°$. The first interaction persists throughout a range of r_{ClN} distances, and so provides an opportunity for population on state 8.1 to be transferred to lower energy states. The wavepacket enters the region of the latter interaction after ~ 35 fs, and so any density on state 6.1 is likely to split onto states correlating to both the NO + Cl and NO* + Cl asymptotes. Any interactions between the higher energy states, 9.1 to 12.1, are less distinct. However, these states are very close in energy, particularly in the region with $\theta = 90$ to $50°$, and so
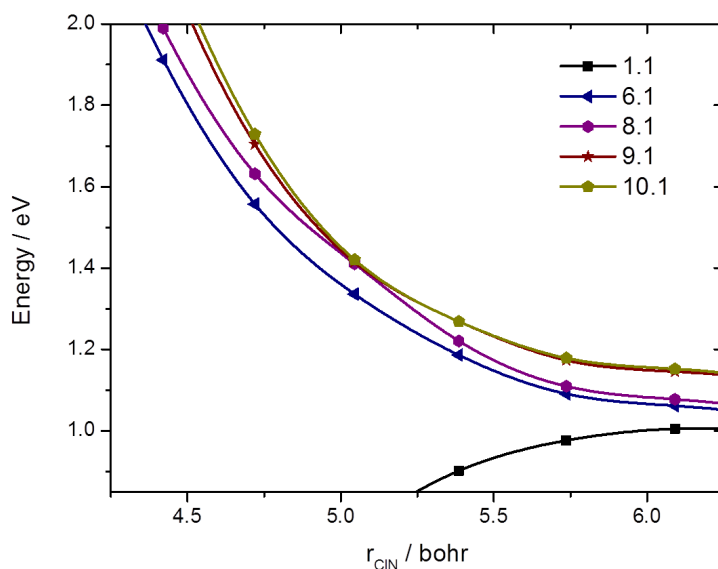
Figure 6.6: Cuts through the PESs of 5 spin-orbit states of A' symmetry calculated at the CASSCF/AVTZ level. The geometries used correspond to the expectation values of each binding coordinate from a wavepacket propagation on the 2 $^1A'$ state. State 8.1, which on energetic grounds corresponds most closely to the zeroth-order 2 $^1A'$ state, appears to interact with states 9.1 and 10.1.
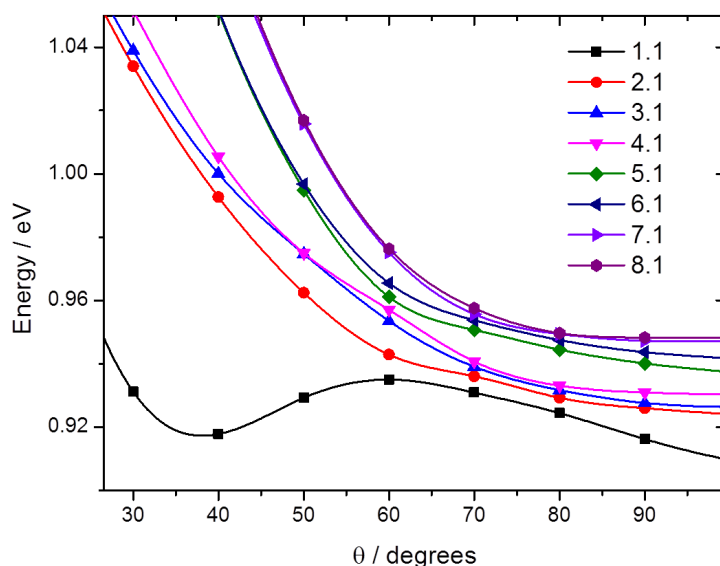
Figure 6.7: Cuts through the PESs of 8 spin-orbit states of A' symmetry calculated at the CASSCF/AVTZ level, for $r_{NO} = 2.2$ bohr and $r_{ClN} = 7.0$ bohr.

wavepacket density is likely to transfer between them, opening channels to NO + Cl* and NO* + Cl*.

6.4   Prelimary wavepacket dynamics on the 2 ^{1}A$'$ state

In order to obtain a better picture of the dynamics leading to the experimentally observed spin-orbit product distributions following dissociation on the 2 ^{1}A$'$ state, computational methods can be used. Here, a preliminary 2D wavepacket propagation has been run, paving the way for future calculations on the full 3D spin-orbit surfaces. A 2D rather than 3D calculation has been chosen with the dual aims of reducing computational expense and providing a simpler test of the validity of the method. As it is the change in the dissociation R and angular γ coordinates which has the greatest effect upon the dynamics, the r coordinate has been kept fixed at $r = 2.2$ bohr which is close to both the FC value and the equilibrium bond length of lone NO.

6.4.1   Calculation set-up

The wavepacket propagation has been run using the latest version of the Heidelberg MCTDH suite of programs [166], but in this instance it has been performed using the exact method rather than MCTDH. This allows for easier analysis of the results, and improves accuracy. DVRs have been used on each coordinate as before; to reduce computational cost fewer points in the R and γ coordinates were initially tested, but this led to errors. A CAP has been placed on each of the diagonal terms of the SOM at $R = 7.5$ bohr to prevent the wavepacket hitting the end of the grid. The initial wavepacket was Gaussian-shaped at the FC geometry on the ground state surface. This was then placed on the excited state surface corresponding most closely to the zeroth order 2 ^{1}A$'$ state. The propagation was run for 70 fs, after which time the vast majority of the wavepacket density had been absorbed.

Hamiltonian

The Hamiltonian used here is rather more complicated than in previous calculations due to the inclusion of the whole SOM. Overall, the Hamiltonian is:

$$\hat{H} = \hat{T} + \hat{V}_{SO} \tag{6.1}$$

where the spin-orbit operator $\hat{V}_{SO}$ is

$$\begin{pmatrix} V_{1,1} & V_{1,2} & \dots & V_{1,24} \\ V_{2,1} & V_{2,2} & \dots & V_{2,24} \\ \vdots & \vdots & \ddots & \vdots \\ V_{24,1} & V_{1,2} & \dots & V_{24,24} \end{pmatrix}. \tag{6.2}$$

The $V_{n,n}$ are the diagonal elements of the SOM, which are referred to here as the 'diabatic' states, and the $V_{n,m}$, $n \neq m$ are the off-diagonal elements which describe the coupling. These off-diagonal elements can be either real or imaginary; if they are real then $V_{n,m} = V_{m,n}$, if they are imaginary then $V_{n,m} = -V_{m,n}$. Each of the 168 distinct, non-zero SOCME surfaces have been fitted using a 2D spline, then where necessary multiplied by i or $-i$. As the calculation is run exactly, these surfaces do not need to be converted into product form. Note that after application of the sign-sorting algorithm, the SOCMEs appeared to vary smoothly in all dimensions, with the exception of those points at $r_{CIN} < 4.0$ bohr, which appeared erroneous. To counter this, the SOCMEs in this region were all set to zero. This approximation seems valid as there is little difference between the diabatic and adiabatic states in this part of the PESs, and the SOCMEs before this point were tending to zero.

The kinetic energy operator is once again formulated in Jacobi coordinates with the total angular momentum $J = 0$, but this time is in 2D:

$$\hat{T}(R,\gamma) = -\frac{\hbar^2}{2\mu_R} \frac{\partial^2}{\partial R^2} - \frac{1}{2} \left(\frac{1}{\mu_R R^2} + \frac{1}{\mu_r r_{fix}^2} \right) \frac{1}{\sin\gamma} \frac{\partial}{\partial\gamma} \sin\gamma \frac{\partial}{\partial\gamma}. \tag{6.3}$$

Here, r_{fix} is a constant, equal to 2.2 bohr.

Choice of initial state

It has been shown using tables 6.1 and 6.3 that the spin-orbit state most closely corresponding to the zeroth-order 2 ^{1}A′ state is that labelled 8.1. At the FC point, the diabatic and adiabatic states have very similar energies. The diabatic state labelled '2' by Molpro has an energy which very closes matches that of the adiabatic state 8.1. The calculation has been run in the diabatic basis, and so the propagation was started on this diabatic state.

Ideally, the transition dipole moments of all the relevant spin-orbit states would be taken into account and excitation would occur with wavepacket density being transferred onto multiple states. However, in this preliminary calculation the initial wavepacket has simply been placed on the single PES of interest. This is partially justified by the fact that most of the states close in energy to the adiabatic state 8.1 have considerably smaller TDMs with the ground state, as shown in tables 6.3 and 6.4. However, there is one exception: state 6.1, which lies 0.1 eV below state 8.1, and has an overall TDM that is 24% of that for state 8.1, and so can be expected to contribute to a reasonable extent if a broadband laser pulse is used in the excitation. In the experimental results discussed later, nanosecond laser pulses have been used, and so the majority of the absorption should be to the 8.1 state. This deficiency in the calculations does however need to be borne in mind when considering the results.

Adiabatic state analysis

As already mentioned, the propagation proceeds along the diabatic states. However, to find the spin-orbit product state distributions the proportion of the wavepacket ending on each of the adiabatic states (i.e. those found from the eigenvalues of the SOM) need to be found. These adiabatic states converge onto the four asymptotes corresponding to the possible NO/NO* and Cl/Cl* combinations. First, the diabatic wavefunction needs to be converted into the adiabatic form. This is achieved by diagonalising the diabatic PES matrix. Next, a flux operator is applied to each adiabatic PES in the asymptotic region (here the points at $R = 7.5$ bohr have been used). The time evolution of the expectation value of these flux operators are recorded, giving the quantum flux into each. By integrating

across the whole propagation time, the total flux ending on each adiabatic state can be found. Note that the total flux ending on each diabatic state can similarly be calculated by using flux operators with the diabatic wavefunction.

6.4.2 Results

Diabatic state populations

Consider first the diabatic state populations, as given in figure 6.8 for those states which have a non-negligible population during the dissociation process. These are states 2, 7, 8, 13, 14, 16, 19, 20, 21 and 22, numbered according to their positions in the SOM as produced by Molpro. The considerable number of states involved shows that the picture is complicated, with multiple transitions occuring between the different spin-orbit surfaces. This is perhaps expected as many interactions between the PESs of the states occur towards the asymptotic region where the states become very close in energy, making transitions between them more likely.

The total population starts to decrease after about 32 fs, when the first of the wavepacket hits the CAPs, and reaches virtually zero by 50 fs as by this point it has all been absorbed. This shows that the photodissociation is still fast and direct when spin-orbit coupling is included. In the first 20 fs of the propagation wavepacket density is transferred from the initial state, 2, onto state 20. At 20 fs, the expectation values of the R and γ coordinates on each state are $\sim$ 5.5 bohr and $\sim 95°$ respectively (equivalent to r_{ClN} = 5.5 bohr and $\theta = 83°$). Inspection of the PESs for this pair of states shows that they are extremely close in energy at the FC point, then move slightly further apart as the bond angle decreases; at $\theta = 110°$ for $r_{ClN} < 5.5$ bohr, state 2 is higher in energy than state 20, whereas at $\theta = 80°$ for $r_{ClN} < 6.5$ bohr state 20 is higher. The states clearly cross along the path of the wavepacket, hence allowing wavepacket density to be transferred between them. This crossing is comparable with that between the adiabatic states 8.1 and 9.1/10.1, as shown earlier in figure 6.6, implying that diabatic state 20 correlates to adiabatic state 9.1 or 10.1 in this region.

Further understanding can be obtained from a cut through the PESs of the relevant
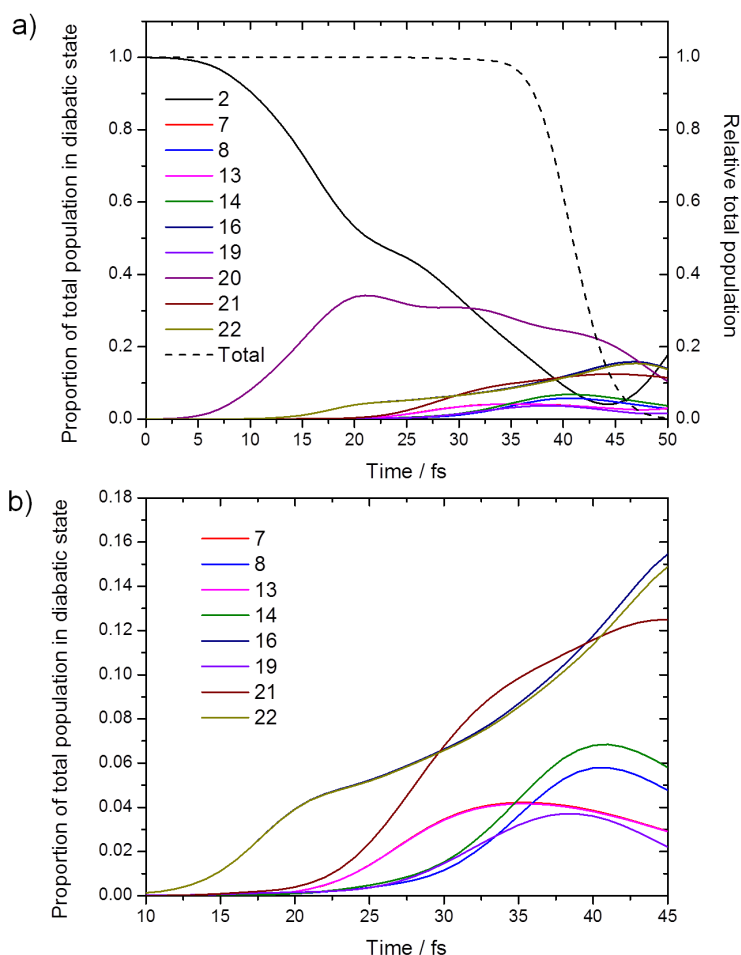
Figure 6.8: The variation in the population of diabatic states with time following a wavepacket propagation on the spin-orbit surfaces of ClNO. The proportion of the total wavepacket in each state is given so that the effect of the CAPs does not complicate the picture. Panel a) shows the complete view; panel b) gives a magnified view of the less populated states.
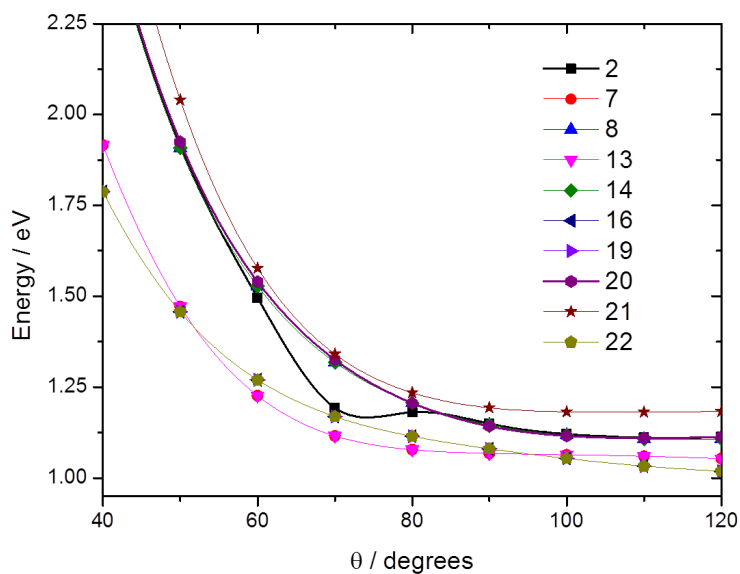
Figure 6.9: A cut through the PESs of the relevant diabatic spin-orbit states for fixed r_{ClN} and r_{NO} bond lengths of 2.2 and 5.5 bohr respectively. The most important states, 2 and 20, are highlighted in bold.

diabatic states at a fixed r_{ClN} bond distance of 5.5 bohr, as shown in figure 6.9. Although at longer r_{ClN} values the states all become closer in energy, the general features visible here persist until at least the point at which the CAP is placed. The surfaces clearly show the reasons for the transfers between the different states: certain states are very close in energy, and others cross.

Once population has been transferred onto state 20, it can move onto further states. When the wavepacket is in the region of $\theta = 70°$, after $\sim$25 fs, state 21 becomes very close in energy and some transfer occurs, shown by the gradual increase in its population after $\sim$ 20 fs. This increase seems to correspond to the slight decrease in the state 20 population at the same time. The PES of state 21 does not appear to interact further with any others, hence its population shows no decrease with time. States 8 and 14 are very close in energy to state 20 through the whole extent of the PESs, and so their smaller populations are also likely to derive from this state.

The population remaining on state 2 can also move on further. Around $\theta = 70°$, state 2 becomes close in energy to states 16, 19 and 22. The populations of states 16 and 22 increase quite early on, from about 12 fs, showing that there is some transfer even before this interaction region is reached. The population of state 19 increases at later times (from

around 25 fs), implying that its population could derive from states 16 and 22 rather than just state 2. The populations of states 7 and 13 do not start to rise until after ~ 25 fs, and remain low. Figure 6.9 shows that these intersect with states 16, 19 and 22 at $\theta \sim 50°$ (the angle of this crossing decreases as r_{ClN} increases), and so it is likely that the population derives from these states rather than state 2 directly.

The minimum on the state 2 surface at around $\theta = 70°$ is caused by its interaction with the ground state (not shown on figure 6.9). No population transfer is seen due to this interaction as it results from vibronic rather than spin-orbit coupling, and hence is not included in this calculation. As seen from the classical trajectory calculations in section 3.6, a small but not insignificant portion of the wavepacket is expected to pass through this intersection onto the ground state. This portion would almost certainly end on one of the asymptotes corresponding to ground state Cl, hence the predicted proportions of these are likely to be underestimated.

The wavepacket divides at the crossing between states 2 and 20 (correlating to that between adiabatic states 8.1 and 9.1/10.1), which appears to be responsible for the majority of the partitioning between Cl and Cl*. Then, these two portions of the wavepacket are divided further by interactions extending into the asymptotic region (some of which can be seen in panel b) of figure 6.1), which dictate the NO:NO* ratio. In this region the diabatic states correlate less clearly to the adiabatic, and so it is not possible to see directly which diabatic states lead to which asymptotes.

Diabatic flux

In addition to the state populations, the total flux into the flux operator on the asymptotes of each diabatic state has been determined. Those states onto which more than 3% of the quantum flux passes are given in table 6.5. This shows that nearly a quarter of the flux ends on state 20, with sizeable proportions also ending on states 2, 16, 21 and 22. Note that 7.4% of the flux is spread between the states not listed, but in negligible proportions.

Diabatic state label	Proportion of flux / %
2	14.5
7	3.9
8	4.4
13	3.8
14	5.3
16	11.1
19	3.1
20	24.6
21	11.0
22	10.8

Table 6.5: The proportion of the total quantum flux ending on the diabatic spin-orbit states following a wavepacket propagation starting on state 2.

Adiabatic state	Proportion of flux / %	Asymptote
12	3.1	NO* + Cl
15	7.4	NO* + Cl
16	5.6	NO* + Cl
17	12.4	NO + Cl*
18	13.2	NO + Cl*
19	11.3	NO + Cl*
20	11.9	NO + Cl*
21	9.8	NO* + Cl*
22	5.7	NO* + Cl*
23	10.5	NO* + Cl*

Table 6.6: The proportion of the total quantum flux ending on the adiabatic spin-orbit states. Note here that the state numbering is simply in order of energy.

Adiabatic flux

More important is the distribution of the quantum flux into each of the adiabatic states in the asymptotic region, as from this the spin-orbit product distribution can be obtained. Table 6.6 gives the 10 adiabatic states onto which more than 3% of the quantum flux passes, in addition to the asymptote each state correlates to. The states are here simply ordered by energy, and so with reference to the results in section 6.2.1, the first 8 will converge on NO + Cl, the next 8 on NO* + Cl, the next 4 on NO + Cl*, and the final 4 on NO* + Cl*. By summing the total flux across all states (including those not listed in the table), the flux ending on each asymptote can hence be found as:

- NO + Cl: 5.2%
- NO* + Cl: 20.0%
- NO + Cl*: 48.8%
- NO* + Cl*: 26.0 %.

The dominant pathway is therefore that ending in NO + Cl*, and very little NO + Cl is expected. Overall, this gives spin-orbit product ratios of:

- NO:NO* $\sim$ 1:1
- Cl:Cl* = 1:3.

Therefore, more spin-orbit excited Cl* is expected to be observed, but the proportions of the NO spin-orbit states should be about equal.

6.4.3   Discussion and conclusions

Some experimental spin-orbit state distributions have already been given in table 1.1. Work from Reisler *et al.* found the NO:NO* ratio following photodissociation at 355 nm to be approximately 1:1, with a slight preference for NO, which is in excellent agreement with the calculated distribution [69]. In addition, Torres and Baugh obtained a 1:1 ratio at 355 nm, providing further support for the validity of the calculated results [77]. For the Cl:Cl* ratio, there is more disagreement in the literature. Cao *et al.* used a REMPI-TOF technique to obtain a Cl:Cl* ratio of $\sim$1:1 at 355 nm [61], which is in contrast to the

preference for the excited spin-orbit state found here. However, Chichinin *et al.* found the ratio to be ~1:9 at the slightly different wavelength of 351 nm [76]. It would be surprising if the distribution changed by such a large extent over such a small energy range, and so these values may not be reliable. It should also be noted that at 355 nm there may be a significant degree of excitation to the adiabatic spin-orbit state 6.1, which has not been included here, and which may give rise to different product state distributions.

Bearing in mind the same caveat, the calculated results can also be compared with experimental data from our own group. In the 3D REMPI experiments described in section 3.7, which were analysed fully in the wavelength range 369 to 379 nm, the NO:NO* ratio was again found to be approximately 1:1, with slightly more NO observed. However, this ratio was not found to be constant across the whole range of the NO rotational distributions: as the NO rotational state became more excited, the proportion of NO formed became higher, with the ratio reaching 3:1 for NO in $j = 50$ [148]. It has not been possible to extract similar information from the current calculation, but with some modifications it should be possible to verify if this is indeed the case, or if the effect is simply down to noise in the experimental data.

Further data concerning the Cl:Cl* partitioning was also obtained. At the shortest wavelengths investigated, from 345 to 355 nm (corresponding to the NO D (v = 1) ← X (v = 0) band), Cl* was found to be dominant, although some Cl was present. All four product channels were observed. At longer wavelengths from 369 to 370 nm (corresponding to the NO D (v = 0) ← X (v = 0) band), Cl* remained dominant and the NO + Cl channel disappeared completely. For the NO C (v = 0) ← X (v = 0) band from 376 to 380 nm, the channels from ground spin-orbit Cl were no longer observed. Additional two colour REMPI experiments were performed in which the ionisation laser was tuned to a strong transition in the NO C (v = 0) ← X (v = 0) band, and the photodissociation laser was tuned from 353 - 355 nm and 360 - 362 nm. Here, only Cl* was seen, showing there is some uncertainty around the branching ratios at these energies [148].

The overall trend seen in our group's experimental results agrees with that calculated here, in that Cl* is dominant, and the NO + Cl channel contributes very little. To investigate the detailed energy dependence of the product state distributions would require a

calculation that does not contain such a broad range of energies in the initial wavepacket. However, the changes seen suggest that varying the excitation energy across the B band of ClNO does have an effect upon the product channels accessed. This could be due in part to the varying proportions of the adiabatic states 6.1 and 8.1 excited. To be sure, further computational work is necessary.

The calculation performed here has several shortcomings, which must be taken into account when assessing the validity of the results. Firstly, the r_{NO} bond length is kept fixed, meaning the contribution of this coordinate to the dynamics is neglected. For modelling photodissociation on the zeroth-order 2 ^{1}A′ state this is a reasonable assumption, however for states such as the 1 ^{3}A″ where motion along the r_{NO} bond is more crucial to the dynamics, this is not valid. The SOMs have only been calculated at the CAS/AVTZ level. Although for many states this should produce good qualitative surfaces, and the couplings should be reasonable, the energies are clearly not accurate enough for fully quantitative analysis. The excitation process has also not been well modelled, as the initial wavepacket has simply been placed on the excited state of interest and no others. The results are obtained for the whole range of energies contained in this wavepacket, and so cannot be compared directly with results from experiments where narrow band nanosecond duration lasers were used. Finally, the conical intersection between the 1 and 2 ^{1}A′ states has not been included; incorporation of this could result in a greater proportion of NO and Cl being found in their ground spin-orbit states.

However, many positives can also be taken from this preliminary calculation. Firstly, there is reasonable agreement between the calculated spin-orbit product distributions and those found experimentally both by our group and others. Secondly, the calculation appears to be running sensibly: the diabatic state populations are believable given the topologies of the spin-orbit PESs involved. Thirdly, it has shown that it is possible to follow the flow of energy through the system as the photodissociation progresses to a high level of detail. This implies that further calculations on this system using this method will be worthwhile and should yield a full picture of the photodissociation of ClNO. Similar calculations have been performed on different systems, for example by Balint-Kurti and coworkers on a range of hydrogen halides [167–169], but not before on ClNO.

6.5 Future work

There are many ways in which to build upon the work presented here and counter the shortcomings of the preliminary wavepacket propagation. Most obvious is to perform the propagation on the full 3D surfaces; due to computational and time constraints this has not been possible here, but is eminently feasible. It also should be fairly simple to implement an improved excitation process: the TDMs of each spin-orbit state with the ground state have already been calculated, and so laser pulses of various bandwidths could be used to trigger the photodissociation on a variety of states. In order to obtain more accurate energies, it may be possible to calculate some of the SOMs at the MRCI level and then apply a scaling factor to the CAS PESs. A further improvement would be to incorporate the NACMEs calculated in section 3.4.2, thus enabling vibronic coupling to be included.

With these improvements, it would be interesting to investigate the photodissociation processes on those zeroth-order states which have been extensively studied experimentally. The agreement with experimental spin-orbit product state distributions across a range of states and energies would give a real insight into the reliability of these calculations. If the method is shown to be successful it could then be extended to other small systems for which spin-orbit coupling is more crucial to the dynamics, and for which it is feasible to calculate multi-dimensional PESs.

Conclusions

The photodissociation of ClNO on its $2\,^1A'$ and $1\,^3A''$ states has been studied in considerable detail. New, purely *ab initio* potential energy surfaces have been calculated for these excited states and the ground state, and the dynamics on these have been investigated using both quantum mechanical wavepacket propagations and classical trajectories. For the first time full transition dipole moment functions have been calculated to better model the excitation processes involved; this has a small, but non-negligible effect upon the photodissociation dynamics for each state. To carry out the quantum dynamics calculations the MCTDH method has been used, both to reduce computational cost and to facilitate analysis of the results.

For the $2\,^1A'$ state, NO product state distributions have been calculated and have been shown to agree very well with experimental results, both from our group and from the literature. In addition, non-adiabatic coupling matrix elements have been calculated in order to model a conical intersection between the 1 and $2\,^1A'$ states in the asymptotic region. By incorporating these into trajectory surface hopping calculations, it has been shown that trajectories passing through the intersection lead to NO that is less rotationally excited than that produced from trajectories which remain on the $2\,^1A'$ state throughout. This effect is most marked at lower excitation energies. The anisotropy parameter (β) for the photodissociation process has been calculated and shown to be close to 2 for all NO rotational states; this is again in good agreement with experimental results.

For the $1\,^3A''$ state of ClNO, the photodissociation cannot be accurately modelled using classical dynamics: NO rotational state distributions produced from trajectories do not show the nodal structure present in experimental results. However, the wavepacket propagations reproduce the observed dynamical information well, showing that the PES

is accurate. The PES has therefore been used to investigate coherent control schemes, in which pairs of interfering ultrashort laser pulses have been shown to exhibit some control over the NO product state distributions. The effects seen derive mostly from spectral control; as the delay between pulse pairs is varied, the degree of interference, and hence the frequencies contained within the exciting field, change. The control obtained is quite basic, but provides groundwork for future control schemes in the ClNO system. In addition, the work here has shown that the MCTDH method can be used with success when investigating closed-loop control.

PESs for 24 spin-orbit coupled states of ClNO have been calculated across a wide range of geometries. The spin-orbit matrices have been used in a preliminary 2D calculation to investigate the origin of the NO:NO* and Cl:Cl* ratios observed following dissociation on the zeroth-order $2\,^1A'$ state. This 2D calculation can be improved upon considerably, but nonetheless reproduces experimental spin-orbit product state distributions well, and allows the passage of the quantum flux from state to state to be studied in fine detail. Again, the MCTDH method has been shown to be a valuable tool for investigating these processes.

Future work will build upon the calculations involving spin-orbit coupling. There is scope to extend these to run wavepacket propagations on the full 3D surfaces, incorporating transition dipole moment functions and studying a wide range of initial states. Another area of interest is the dissociation of ClNO in the solution phase; non-adiabatic coupling may play a more important role here. Regarding coherent control, the next step would be to try to facilitate the formation of the ClON isomer, which has been observed in solution.

Appendix A

SOCME sign-sorting algorithm

In this appendix the algorithm used to ensure that the signs of the SOCMEs are consistent across the extent of the surfaces is described.

A.1 Overall algorithm

The values of the SOCMEs have been assumed to be correct, and so only the signs have been adjusted. Each degree of freedom is considered in turn, starting with the r_{ClN} bond length. Briefly, the algorithm works as follows, for each individual non-zero off-diagonal SOCME:

- Take the sign at $r_{ClN} = 12$ bohr, $r_{NO} = 2.2$ bohr, $\theta = 110°$ to be correct, and make the signs of adjacent points the same

- For each r_{NO} distance at $\theta = 110°$, sort the signs at each r_{ClN} distance using the CheckGradient method in the r_{ClN} coordinate

- For each r_{NO} distance, cycle through the values of θ, first working out from 120 to 170°, and then working in from 100 to 10°. Then starting at $r_{ClN} = 12$ bohr and working inwards, sort the sign using the CheckGradient method

- The signs should now all be consistent along each cut along the r_{ClN} coordinate.

- Consider the signs at $r_{ClN} = 12$ bohr. For each r_{NO} distance, assume the sign at $\theta = 110°$ is correct, and the sign at 120° is the same. Work from $\theta = 130°$ upwards,

243

using the CheckBeta method to sort the sign of each point. If the sign needs to change at r_{ClN} = 12 bohr, change it at all values of r_{ClN} for the current θ and r_{NO}.

- Sort the signs in the same way for values of θ moving downwards from 100 to 10°.

- The signs should now all be consistent for each cut along the θ coordinate.

- Consider the signs at r_{ClN} = 12 bohr, $\theta = 110°$. Use the CheckGradient method to sort the signs along the r_{NO} coordinate. If the signs need to be switched, they should change for all points with the current r_{NO} value across the surface.

- The signs should now all be consistent across each of the three degrees of freedom.

The main assumptions here are that the starting point is correct, that neighbouring geometries will have SOCMEs with the same sign as it, and that the signs of each SOCME can be adjusted in such a way as to give smooth variation across each degree of freedom.

A.2   Sign checking methods

The two methods used to check the sign are CheckGradient and CheckBeta. CheckGradient is used for the r_{ClN} and r_{NO} coordinates and works as follows:

- Take the value of the current point and the two preceding points: points 1, 2 and 3

- Calculate the gradient between points 2 and 3

- Calculate the gradient between points 1 and 2, with both the original sign of point 1 and the opposite sign

- Use whichever sign gives the lowest absolute difference between the current and previous gradients.

CheckBeta is used for the θ coordinate, over which the SOCMEs tend to change sign more rapidly in a way that is not correctly dealt with by the CheckGradient method. It proceeds as follows:

- Take the value of the current point and the two preceding points: points 1, 2 and 3

- Calculate the angle A, which is the angle between the line from point 3 to point 2 and the x axis
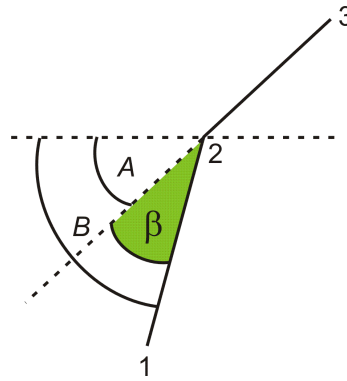
Figure A.1: The definition of the angle β (highlighted in green) used in the Check-Beta method. In this example, β is the difference between the angles A and B, which are respectively the angle the line from points 3 to 2 makes with the x axis, and the angle the line from points 2 to 1 makes with the x axis.

- Calculate the angle B, which is the angle between the line from point 2 to point 1 and the x axis, with both the original sign of point 1 and the opposite sign

- Calculate the angle β, shown in figure A.1, which is the angle between the line from point 3 to 2 and the line from point 2 to 1, for both values of B

- Use whichever sign gives the smallest value of β.

Note that the calculation of β varies slightly depending on the relative positions of points 1, 2 and 3.

References

[1] Wayne, R. P. *Chemistry of atmospheres;* Clarendon Press, Oxford, 1993.

[2] Monks, P. S. *Chem. Soc. Rev.* **2005**, *34*, 376–395.

[3] Chambreau, S. D.; Townsend, D.; Lahankara, S. A.; Lee, S. K.; Suits, A. G. *Phys. Scr.* **2006**, *73*, C89.

[4] Lahankara, S. A.; Goncharova, V.; Suits, F.; Farnumc, J. D.; Bowman, J. M.; Suits, A. G. *Chem. Phys.* **2008**, *347*, 288–299.

[5] Arnon, D. I. *Proc. Nat. Acad. Sci.* **1971**, *68*, 2883–2892.

[6] Herbst, E. *Chem. Soc. Rev.* **2001**, *30*, 168–176.

[7] Born, M.; Oppenheimer, J. R. *Annalen der Physik* **1927**, *389*, 457–484.

[8] Reisler, H. *Annu. Rev. Phys. Chem.* **2009**, *60*, 39–59.

[9] Whitaker, B. J., Ed. *Imaging in molecular dynamics, technology and applications;* Cambridge University Press, 2003.

[10] Reid, G. D.; Wynne, K. In *Encyclopedia of analytical chemistry*; Meyers, R. A., Ed.; John Wiley and Sons Ltd, 2000.

[11] Rosker, M. J.; Dantus, M.; Zewail, A. H.

[12] Zewail, A. H. *Science* **1988**, *242*, 1645–1653.

[13] Zewail, A. H. *Angew. Chem. Int. Ed.* **2000**, *39*, 2586–2631.

[14] Scherer, N. F.; Knee, J. L.; Smith, D. D.; Zewail, A. H. *J. Phys. Chem.* **1985**, *89*, 5141–5143.

[15] Dantus, M.; Rosker, M. J.; Zewail, A. H. *J. Chem. Phys.* **1988**, *89*, 6128–6140.

[16] Carley, R. E.; Heesel, E.; Fielding, H. H. *Chem. Soc. Rev.* **2005**, *34*, 949–969.

[17] Elles, C. G.; Crim, F. F. *Annu. Rev. Phys. Chem.* **2006**, *57*, 273–302.

[18] Schinke, R. *Photodissociation Dynamics;* Cambridge University Press, 1993.

[19] Untch, A.; Hennig, S.; Schinke, R. *Chem. Phys.* **1988**, *126*, 181–190.

[20] Brouard, M., Vallance, C., Eds. *Tutorials in molecular reaction dynamics;* RSC Publishing, 2004.

[21] Worth, G. A.; Cederbaum, L. S. *Annu. Rev. Phys. Chem.* **2004**, *55*, 127.

[22] Domcke, W.; Yarkony, D. R.; Koppel, H. In *Advanced Series in Physical Chemistry;* World Scientific, Singapore, 2004.

[23] Federov, D. G.; Koseki, S.; Schmidt, M. W.; Gordon, M. S. *Int. Rev. Phys. Chem.* **2003**, *22*, 551–592.

[24] Trebino, R. *Frequency-Resolved Optical Gating: The Measurement of Ultrashort Laser Pulses;* Springer, 2002.

[25] Diels, J. C.; Rudolph, W. *Ultrashort Laser Pulse Phenomena;* Academic Press, 2006.

[26] Bar, I.; Cohen, Y.; David, D.; Arusi-Parpar, T.; Rosenwaks, S.; Valentini, J. J. *J. Chem. Phys.* **1991**, *95*, 3341–3346.

[27] Tonomura, A.; Endo, J.; Matsuda, T.; Kawasaki, T.; Ezawa, H. *Am. J. Phys.* **1989**, *57*, 117–120.

[28] Arndt, M.; Nairz, O.; Vos-Andreae, J.; Keller, C.; van der Zouw, G.; Zeilinger, A. *Nature* **1999**, *401*, 680–682.

[29] Brumer, P.; Shapiro, M. *Chem. Phys. Lett.* **1986**, *126*, 541–546.

[30] Brumer, P.; Hepburn, J. W.; Shapiro, M. *Chem. Phys. Lett.* **1988**, *149*, 451–454.

[31] Zhu, L.; Kleiman, V.; Li, X.; Lu, S. P.; Trentelman, K.; Gordon, R. J. *Science* **1995**, *270*, 77–80.

[32] Zhu, L.; Kleiman, V.; Li, X.; Lu, S. P.; Trentelman, K.; Gordon, R. J. *Phys. Rev. Lett.* **1997**, *79*, 4108–4111.

[33] Fiss, J. A.; Zhu, L.; Suto, K.; He, G.; Gordon, R. J. *Chem. Phys.* **1998**, *233*, 335–341.

[34] Tannor, D. J.; Rice, S. A. *J. Chem. Phys.* **1985**, *83*, 5013–5018.

[35] Tannor, D. J.; Kosloff, R.; Rice, S. A. *J. Chem. Phys.* **1985**, *85*, 5805–5820.

[36] Baumert, T.; Grosser, M.; Thalweiser, R.; Gerber, G. *Phys. Rev. Lett.* **1991**, *67*, 3753–3756.

[37] Baumert, T.; Grosser, M.; Thalweiser, R.; Weiss, V.; Wiedenmann, E.; Gerber, G. *J. Phys Chem.* **1991**, *95*, 8103–8110.

[38] Judson, R. S.; Rabitz, H. *Phys. Rev. Lett.* **1992**, *68*, 1500–1503.

[39] Assion, A.; Baumert, T.; Helbing, J.; Seyfried, V.; Gerber, G. *Chem. Phys. Lett.* **1996**, *259*, 488–494.

[40] Brixner, T.; Gerber, G. *Chem. Phys. Chem.* **2003**, *4*, 418–328.

[41] Herek, J. L.; Wohlleben, W.; Cogdell, R. J.; Zeidler, D.; Motzkus, M. *Nature* **2002**, *417*, 533–535.

[42] Shapiro, M.; Brumer, P. *Rep. Prog. Phys.* **2003**, *66*, 487–511.

[43] Brif, C.; Chakrabarti, R.; Rabitz, H. *New J. Phys.* **2010**, *12*, 075008.

[44] Ohmori, K. *Ann. Rev. Phys. Chem.* **2009**, *60*, 487–511.

[45] Meshulach, D.; Silberberg, Y. *Phys. Rev. A.* **1999**, *60*, 1287–1292.

[46] Vogt, G.; Krampert, G.; Niklaus, P.; Nuernberger, P.; Gerber, G. *Phys. Rev. Lett.* **2005**, *94*, 068305.

[47] Hoki, K.; Brumer, P. *Phys. Rev. Lett.* **2005**, *95*, 168305.

[48] Kistiakowsky, G. B. *J. Am. Chem. Soc.* **1930**, *52*, 102.

[49] Beckham, L. J.; Fessler, W. A.; Kise, M. A. *Chemical Reviews* **1951**, *48*, 319–396.

[50] Finlayson Pitts, B. J. *Nature* **1983**, *306*, 676–677.

[51] Keene, W. C.; Pszenny, A. A. P.; Jacob, D. J.; Duce, R. A.; Galloway, J. N.; Schultz-Tokos, J. J.; Sievering, H.; Boatman, J. F. *Global Biogeochem. Cy.* **1990**, *4*, 407–430.

[52] Weis, D. D.; Ewing, G. E. *J. Phys. Chem. A* **1999**, *103*, 4865–4873.

[53] Schroede, W. H.; Urone, P. *Environ. Sci. Technol.* **1974**, *8*, 756–758.

[54] Njegic, B.; Raff, J. D.; Finlayson Pitts, B. J.; Gordon, M. S.; Gerber, R. B. *J. Phys. Chem. A* **2010**, *114*, 4609.

[55] Cazzoli, G.; Esposti, C.; Palmieri, P.; Simeone, S. *J. Mol. Spectrosc.* **1983**, *97*, 165–185.

[56] Lacombe, S.; Loudet, M.; Dargelos, A.; Camou, J. *Chem. Phys.* **2000**, *258*, 1–12.

[57] Coriani, S.; Marchesan, D.; Gauss, J.; Hattig, C.; Helgaker, T.; Jorgensen, P. *J. Chem. Phys.* **2005**, *123*, 184107.

[58] Demaison, J.; Császár, A. G.; Dehayem-Kamadjeu, A. *J. Phys. Chem. A* **2006**, *110*, 1360913617.

[59] Chase, M.; Davies, C.; Downey, J.; Frurip, D.; McDonald, R.; Syverud, A. NIST JANAF Thermochemical Tables. See http://kinetics.nist.gov/janaf/, **1985**.

[60] Jones, L. H.; Ryan, R. R.; Asprey, L. B. *J. Chem. Phys.* **1968**, *49*, 581–585.

[61] Cao, J. Y.; Wang, Y. F.; Qian, C. X. W. *J. Chem. Phys.* **1995**, *103*, 9653–9660.

[62] Ogai, A.; Qian, C. X. W.; Reisler, H. *J. Chem. Phys.* **1990**, *93*, 1107–1115.

[63] Schinke, R.; Nonella, M.; Sueter, H. U.; Huber, J. R. *J. Chem. Phys.* **1990**, *93*, 1098–1106.

[64] Solter, D.; Werner, H. J.; Vondirke, M.; Untch, A.; Vegiri, A.; Schinke, R. *J. Chem. Phys.* **1992**, *97*, 3357–3374.

[65] Goodeve, C. F.; Katz, S. *Proc. R. Soc. A.* **1939**, *172*, 0432–0444.

[66] Chemical kinetics and photochemical data for use in atmospheric studies, evaluation number 17. Sander, S. P.; Abbatt, J.; Barker, J. R.; Burkholder, J. B.; Friedl, R. R.; Golden, D. M.; Huie, R. E.; Kolb, C. E.; Kurylo, M. J.; Moortgat, G. K.; Orkin, V. L.; Wine, P. H. JPL Publication 10-6. See http://jpldataeval.jpl.nasa.gov.

[67] Roehl, C. M.; Orlando, J. J.; Calvert, J. G. *J. Photochem. Photobiol. A. Chem.* **1992**, *69*, 1–5.

[68] Yamashita, T.; Kato, S. *J. Chem. Phys.* **2004**, *121*, 2105–2116.

[69] Bai, Y.; Ogai, A.; Qian, C.; Iwata, L.; Segal, G.; Reisler, H. *J. Chem. Phys.* **1989**, *90*, 3903–3914.

[70] Untch, A.; Weide, K.; Schinke, R. *Journal of Chemical Physics* **1991**, *95*, 6496–6507.

[71] Busch, G. E.; Wilson, K. R. *J. Chem. Phys.* **1972**, *56*, 3655.

[72] Bruno, A.; Bruhlmann, U.; Huber, J. R. *Chem. Phys.* **1988**, *120*, 155–167.

[73] Ticktin, A.; Bruno, A. E.; Bruhlmann, U.; Huber, J. R. *Chem. Phys.* **1988**, *125*, 403–413.

[74] Solgadi, D.; Lahmani, F.; Lardeux, C.; Flament, J. P. *Chem. Phys.* **1983**, *79*, 225–233.

[75] Ogai, A.; Qian, C. X. W.; Iwata, L.; Reisler, H. *Chem. Phys. Lett.* **1988**, *146*, 367–374.

[76] Chichinin, A. I. *Chem. Phys. Lett.* **1993**, *209*, 459–463.

[77] Torres, E.; Pipes, L.; Baugh, D. *Faraday Discuss.* **1999**, *113*, 279–290.

[78] Qian, C. X. W.; Ogai, A.; Iwata, L.; Reisler, H. *J. Chem. Phys.* **1988**, *89*, 6547–6548.

[79] Qian, C. X. W.; Ogai, A.; Iwata, L.; Reisler, H. *J. Chem. Phys.* **1990**, *92*, 4296–4307.

[80] Qian, C. X. W.; Ogai, A.; Brandon, J.; Bai, Y. Y.; Reisler, H. *J. Chem. Phys.* **1991**, *95*, 6763–6774.

[81] Morse, M. D.; Freed, K. F. *J. Chem. Phys.* **1983**, *78*, 6045–6065.

[82] Morse, M. D.; Freed, K. F. *J. Chem. Phys.* **1981**, *74*, 4395–4417.

[83] Vegiri, A.; Alexander, M. H. *J. Chem. Phys.* **1994**, *101*, 4722–4734.

[84] Grinberg, H.; Freed, K. F.; Williams, C. J. *J. Chem. Phys.* **1997**, *107*, 1849–1860.

[85] Grinberg, H.; Freed, K. F.; Williams, C. J. *Chem. Phys. Lett.* **1991**, *182*, 297–303.

[86] Grinberg, H.; Williams, C. J.; Freed, K. F. *J. Chem. Phys.* **1994**, *100*, 9215–9227.

[87] Jensen, F. *Introduction to Computational Chemistry, Second Edition;* Wiley, 2007.

[88] Molpro, version 2010.1, a package of ab initio programs. Werner, H.-J.; Knowles, P. J.; Knizia, G.; Manby, F. R.; Schütz, M.; Celani, P.; Korona, T.; Lindh, R.; Mitrushenkov, A.; Rauhut, G.; Shamasundar, K. R.; Adler, T. B.; Amos, R. D.; Bernhardsson, A.; Berning, A.; Cooper, D. L.; Deegan, M. J. O.; Dobbyn, A. J.; Eckert, F.; Goll, E.; Hampel, C.; Hesselmann, A.; Hetzer, G.; Hrenar, T.; Jansen, G.; Köppl, C.; Liu, Y.; Lloyd, A. W.; Mata, R. A.; May, A. J.; McNicholas, S. J.; Meyer, W.; Mura, M. E.; Nicklass, A.; O'Neill, D. P.; Palmieri, P.; Peng, D.; Pflüger, K.; Pitzer, R.; Reiher, M.; Shiozaki, T.; Stoll, H.; Stone, A. J.; Tarroni, R.; Thorsteinsson, T.; Wang, M. **2010**.

[89] Gaussian 09 Revision D.01. Frisch, M. J.; Trucks, G. W.; Schlegel, H. B.; Scuseria, G. E.; Robb, M. A.; Cheeseman, J. R.; Scalmani, G.; Barone, V.; Mennucci, B.; Petersson, G. A.; Nakatsuji, H.; Caricato, M.; Li, X.; Hratchian, H. P.; Izmaylov, A. F.; Bloino, J.; Zheng, G.; Sonnenberg, J. L.; Hada, M.; Ehara, M.; Toyota, K.; Fukuda, R.; Hasegawa, J.; Ishida, M.; Nakajima, T.; Honda, Y.; Kitao, O.; Nakai, H.; Vreven, T.; Montgomery, Jr., J. A.; Peralta, J. E.; Ogliaro, F.; Bearpark, M.; Heyd, J. J.; Brothers, E.; Kudin, K. N.; Staroverov, V. N.; Kobayashi, R.; Normand, J.; Raghavachari, K.; Rendell, A.; Burant, J. C.; Iyengar, S. S.; Tomasi, J.; Cossi, M.; Rega, N.; Millam, J. M.; Klene, M.; Knox, J. E.; Cross, J. B.; Bakken, V.; Adamo, C.; Jaramillo, J.; Gomperts, R.; Stratmann, R. E.; Yazyev, O.; Austin, A. J.; Cammi, R.; Pomelli, C.; Ochterski, J. W.; Martin, R. L.; Morokuma, K.; Zakrzewski, V. G.; Voth, G. A.; Salvador, P.; Dannenberg, J. J.; Dapprich, S.; Daniels, A. D.; Farkas, O.; Foresman, J. B.; Ortiz, J. V.; Cioslowski, J.; Fox, D. J. **2009**.

[90] Dunning, T. H. *J. Chem. Phys.* **1989**, *90*, 1007–1023.

[91] Stanton, J. F.; Bartlett, R. J. *J. Chem. Phys.* **1993**, *98*, 7029–7039.

[92] Tannor, D. J. *Introduction to quantum mechanics, a time-dependent perspective;* University Science Books, 2007.

[93] Beck, M. H.; Jäckle, A.; Worth, G. A.; Meyer, H.-D. *Phys. Rep.* **2000**, *324*, 1–105.

[94] Leforestier, C.; Bisseling, R. H.; Cerjan, C.; Feit, M. D.; Friesner, R.; Guildberg, A.; Hammerich, A.; Jolicard, G.; Karrlein, W.; Meyer, H. D.; Lipkin, N.; Roncero, O.; Kosloff, R. *J. Comp. Phys.* **1991**, *94*, 59.

[95] Tal-Ezer, H.; Kosloff, R. *J. Chem. Phys.* **1984**, *81*, 3967.

[96] Kosloff, R.; Tal-Ezer, H. *Chem. Phys. Lett.* **1986**, *127*, 223.

[97] Jäckle, A.; Meyer, H.-D. *J. Chem. Phys.* **1996**, *104*, 7974.

[98] Jäckle, A.; Meyer, H.-D. *J. Chem. Phys.* **1998**, *109*, 3772.

[99] Beck, M. H.; Meyer, H.-D. *Z Phys. D* **1997**, *42*, 113–129.

[100] Park, T. J.; Light, J. C. *J. Chem. Phys.* **1986**, *85*, 5870–5876.

[101] Press, W. H.; Teukolsky, S. A.; Vetterling, W. T.; Flannery, B. *Numerical Recipes;* Cambridge University Press, 1992.

[102] Manthe, U.; Meyer, H.-D.; Cederbaum, L. S. *J. Chem. Phys.* **1992**, *97*, 3199–3213.

[103] Rabb, A.; Worth, G. A.; Meyer, H.-D.; Cederbaum, L. S. *J. Chem. Phys.* **1999**, *110*, 936–946.

[104] Meyer, H.-D. *Wiley Interdisciplinary Reviews: Computational Molecular Science* **2012**, *2*, 351.

[105] Shalashilin, D. V.; Child, M. S. *J. Chem. Phys.* **2000**, *113*, 10028.

[106] Shalashilin, D. V.; Child, M. S. *Chem. Phys.* **2004**, *304*, 103.

[107] Ben-Nun, M.; Quenneville, J.; Martinez, T. J. *J. Phys. Chem. A* **2000**, *104*, 5161–5175.

[108] Kosloff, R.; Kosloff, D. *J. Comput. Phys.* **1986**, *63*, 363.

[109] Leforestier, C.; Wyatt, R. *J. Chem. Phys.* **1982**, *78*, 2334.

[110] Jäckle, A.; Meyer, H.-D. *J. Chem. Phys.* **1996**, *105*, 6778.

[111] Heller, E. *Acc. Chem. Res.* **1981**, *14*, 368–375.

[112] Engel, V. *Chem. Phys. Lett.* **1992**, *189*, 76–78.

[113] Tully, J. C.; Preston, R. K. *J. Chem. Phys* **1971**, *55*, 562–572.

[114] Tully, J. C. *J. Chem. Phys* **1990**, *93*, 1061–1071.

[115] Tully, J. C. *Wiley Interdisciplinary Reviews: Computational Molecular Science* **2011**, *1*, 620–633.

[116] Schinke, R.; McBane, G. C. *J. Chem. Phys.* **2010**, *132*, 044305.

[117] McBane, G. C.; Schmidt, J. A.; Johnson, M. S.; Schinke, R. *J. Chem. Phys.* **2013**, *138*, 094314.

[118] McBane, G. C.; Schinke, R. *J. Chem. Phys.* **2012**, *136*, 044314.

[119] Schmaunz, A.; Kensy, U.; Slenczka, A.; Dick, B. *Phys. Chem. Chem. Phys.* **2009**, *11*, 7115–7119.

[120] Jones, K. M.; Milkiewicz, J. A.; Whitaker, B. J.; Sage, A. G.; Worth, G. A. *Chem. Phys. Chem.* **2013**, *14*, 1479–1487.

[121] Eckert, F.; Pulay, P.; Werner, H. J. *J. Comp. Chem.* **1997**, *18*, 1473.

[122] Busch, T.; Degli Esposti, A.; Werner, H. J. *J. Chem. Phys.* **1991**, *94*, 6708.

[123] Kutateladze, A. G., Ed. *Computational Methods in Photochemistry;* Taylor and Francis, 2005.

[124] Langhoff, S. R.; Davidson, E. R. *Int. J. Quantum Chem.* **1974**, *8*, 61–72.

[125] Chapman, E. L. *Theoretical studies on the ultrafast photodissociation of molecules* PhD thesis, University of Birmingham, **2009**.

[126] Schaftenaar, G.; Noordik, J. H. *J. Comput. -Aided Mol. Design* **2000**, *14*, 123–134.

[127] Hallou, A.; Schriver-Mazzuoli, L.; Schriver, A.; Chaquin, P. *Chem. Phys.* **1998**, *237*, 251–264.

[128] Werner, H. J.; Knowles, P. J. *J. Chem. Phys.* **1985**, *82*, 5053.

[129] Knowles, P. J.; Werner, H. J. *Chem. Phys. Lett.* **1985**, *115*, 259.

[130] Werner, H. J.; Knowles, P. J. *J. Chem. Phys.* **1988**, *89*, 5803.

[131] Knowles, P. J.; Werner, H. J. *Chem. Phys. Lett.* **1988**, *145*, 514.

[132] Knowles, P. J.; Werner, H. J. *Theor. Chim. Acta* **1992**, *84*, 95.

[133] Varandas, A. J. C. *J. Molec. Struct.* **1985**, *120*, 401–424.

[134] Varandas, A. J. C.; da Silva, J. D. *J. Chem. Soc. Faraday Trans.* **1992**, *88*, 941–954.

[135] Varandas, A. J. C.; Rodrigues, S. P. J. *J. Phys. Chem. A* **2006**, *110*, 485–493.

[136] de Oliveira-Filho, A. G. S.; Aoto, Y. A.; Ornellas, F. R. *J. Chem. Phys.* **2011**, *135*, 044308.

[137] Yamashita, T.; Kato, S. *J. Chem. Phys.* **2003**, *119*, 4251–4261.

[138] Hampel, C.; Peterson, K.; Werner, H. J. *Chem. Phys. Lett.* **1992**, *190*, 1.

[139] Korona, T.; Werner, H. J. *J. Chem. Phys.* **2003**, *118*, 3006.

[140] Meyer, H.-D.; Manthe, U.; Cederbaum, L. S. *Chem. Phys. Lett.* **1990**, *165*, 73–78.

[141] Manthe, U.; Meyer, H.-D.; Cederbaum, L. S. *J. Chem. Phys.* **1992**, *97*, 3199–3213.

[142] Worth, G. A.; Beck, M. H.; Jäckle, A.; Meyer, H.-D. , The MCTDH Package, Version 9.0, (2012). H.-D. Meyer. See http://mctdh.uni-hd.de.

[143] Brook, M.; Kaplan, J. *Phys. Rev.* **1954**, *96*, 1540–1542.

[144] McBane, G. C.; Nguyen, L. T.; Schinke, R. *J. Chem. Phys.* **2010**, *133*, 144312.

[145] Blais, N. C.; Truhlar, D. G. *J. Chem. Phys.* **1983**, *79*, 1334–1342.

[146] Hippler, M.; Pfab, J. *Mol. Phys.* **1998**, *94*, 313–323.

[147] Cheung, A. S.-C.; Wong, A. L.; Lo, D. H.-Y.; Leung, K. W.-S.; Yoshino, K.; Thorne, A. P.; Murray, J. E.; Imajo, T.; Ito, K.; Matsui, T. *J. Chem. Phys.* **2003**, *119*, 8373–8378.

[148] Milkiewicz, J. A. Photodissociation of nitrosyl chloride Master's thesis, University of Leeds, **2013**.

[149] Cooksey, C. C.; Reid, P. J. *Photochem. Photobio.* **2004**, *80*, 3886–3894.

[150] Bixby, T. J.; Patterson, J. D.; Reid, P. J. *J. Phys. Chem. A.* **2009**, *113*, 3886–3894.

[151] Patterson, J. D.; Reid, P. J. *J. Phys. Chem. B.* **2012**, *116*, 10437–10443.

[152] Wang, L.; Meyer, H. D.; May, V. *J. Chem. Phys.* **2006**, *125*, 014102.

[153] Schröder, M.; Brown, A. *J. Chem. Phys.* **2009**, *131*, 034101.

[154] Worth, G. A.; Sanz, C. S. *Phys. Chem. Chem. Phys.* **2010**, *12*, 015570–15579.

[155] Bredtmann, T.; Manz, J. *J. Chem. Sci.* **2012**, *124*, 121–129.

[156] Tournois, P. *Opt. Commun.* **1997**, *140*, 245–249.

[157] Kaplan, D.; Tournois, P. *J. Phys. IV* **2002**, *12*, 69–75.

[158] Form, N. T.; Burbidge, R.; Ramon, J.; Whitaker, B. J. *J. Mod. Opt.* **2008**, *55*, 197–209.

[159] Form, N. T.; Whitaker, B. J.; Meier, C. *J. Phys. B-At. Mol. Opt. Phys.* **2008**, *41*, 074011.

[160] Form, N. T. *Molecular Coherent Control: A study of three-photon absorption in I2* PhD thesis, University of Leeds, **2008**.

[161] Principles of nonlinear optical spectroscopy: A practical approach. Hamm, P. **2005**.

[162] Demtröder, W. *Laser Spectroscopy, Volume 1: Basic Principles;* Springer, 2008.

[163] Cina, J. A. *Ann. Rev. Phys. Chem.* **2008**, *59*, 319–342.

[164] Scherer, N. F.; Carlson, R. J.; Matro, A.; Du, M.; Ruggiero, A. J.; Romero-Rochin, V.; Cina, J. A.; Fleming, G. R.; Rice, S. A. *J. Chem. Phys.* **1991**, *95*, 1487–1511.

[165] Berning, A.; Schweizer, M.; Werner, H. J.; Knowles, P. J.; Palmieri, P. *Mol. Phys.* **2000**, *98*, 1823.

[166] Worth, G. A.; Beck, M. H.; Jäckle, A.; Meyer, H.-D. The MCTDH Package, Version 10.1, (2014). Available from G. A. Worth, University of Birmingham.

[167] Brown, A.; Balint-Kurti, G. G. *J. Chem. Phys.* **2000**, *113*, 1870–1878.

[168] Brown, A.; Balint-Kurti, G. G. *J. Chem. Phys.* **2000**, *113*, 1879–1884.

[169] Smolin, A. G.; Vasyutinskii, O. S.; Balint-Kurti, G. G.; Brown, A. *J. Phys. Chem. A* **2006**, *110*, 5371–5378.